

**UNRAVELLING THE ANATECTIC HISTORY
OF THE LOWER CONTINENTAL CRUST
THROUGH THE PETROLOGY OF MELT
INCLUSIONS
AND LU-HF GARNET GEOCHRONOLOGY**

**A CASE STUDY FROM THE WESTERN ALPUJÁRRIDES
(BETIC CORDILLERA, S. SPAIN)**

Amel Barich



Editor: Universidad de Granada. Tesis Doctorales

Autor: Amel Barich

ISBN: 978-84-9125-481-2

URI: <http://hdl.handle.net/10481/42210>



**UNRAVELLING THE ANATECTIC HISTORY
OF THE LOWER CONTINENTAL CRUST
THROUGH THE PETROLOGY
OF MELT INCLUSIONS AND LU-HF GARNET
GEOCHRONOLOGY**

*A CASE STUDY FROM THE WESTERN ALPUJÁRRIDES
(BETIC CORDILLERA, S. SPAIN)*

AMEL BARICH

Ph.D. Thesis • Tesis Doctoral • Thèse Doctorale



*Memoria de Tesis Doctoral presentada por la Licenciada en Geología
Amel Barich para optar al Grado de Doctor por la Universidad de
Granada*

*Esta Tesis Doctoral ha sido dirigida por el
Dr. Antonio Acosta-Vigil y el Dr. Carlos Jesús Garrido Marín
del Instituto Andaluz de Ciencias de la Tierra (CSIC-UGR)*

Granada, 3 de noviembre de 2015

La doctoranda Amel Barich y los directores de la tesis Antonio Acosta-Vigil y Carlos Jesús Garrido Marín, garantizamos, al firmar esta tesis doctoral, que el trabajo ha sido realizado por el doctorando bajo la dirección de los directores de la tesis y, hasta donde nuestro conocimiento alcanza, en la realización del trabajo se han respetado los derechos de otros autores a ser citados, cuando se han utilizado sus resultados o publicaciones.

En Granada, 3 de noviembre de 2015

Directores de la Tesis

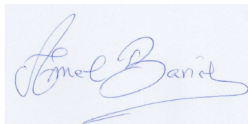


Fdo.: *Antonio Acosta-Vigil*



Fdo.: *Carlos J. Garrido Marín*

Doctoranda



Fdo: *Amel Barich*

*To him who called me Doctor before
everyone else, who taught me that
Science is everything;*

*To my Grand-papa, **Jameâ El
Ferdaous.***

All religions, arts and sciences are branches of the same tree. All these aspirations are directed toward ennobling man's life, lifting it from the sphere of mere physical existence and leading the individual towards freedom.

— Albert Einstein

« العلم نور »

Modern science has been a voyage into the unknown, with a lesson in humility waiting at every stop. Many passengers would rather have stayed home.

— Carl Sagan

Abstract

Partial melting (anatexis) plays a fundamental role in the generation, differentiation and the rheology of Earth's continental crust. "Migmatitic" terranes constitute the main geological record of crustal anatexis throughout Earth's history. Unravelling the mechanisms of crustal anatexis from these terranes has proven to be challenging particularly when it comes to unveiling the primary chemical composition of anatectic melts. The main aim of this thesis is to better understand lower crustal anatexis through the study of "*nanogranite inclusions*" —microscopic droplets of melt that formed *via* incongruent melting reactions— in metamorphic minerals, and its relationship with lithospheric scale tectonomagmatic processes. The originality of my Thesis resides in the combination of a petrological, thermodynamical and experimental study of anatexis on the basis of the study of nanogranite inclusions in garnets from high-pressure granulitic migmatites. The case study is migmatitic gneisses from the Jubrique unit, a complete —though strongly thinned— crustal section in the westernmost Alpujarrides (Betic Cordillera, S. Spain). These gneisses overlie the Ronda peridotites —the largest exposure of subcontinental lithospheric mantle on Earth— and provide a unique opportunity to investigate the nature and age of crustal melting events and their timing with mantle processes in the westernmost Mediterranean.

Melt inclusions ($\approx 30\text{-}40\ \mu\text{m}$) —now recrystallized to nanogranites— in Jubrique gneisses are present in garnet cores and rims throughout the entire sequence. Thermodynamic modeling and conventional thermobarometry provide peak conditions of $\approx 850\ \text{°C}$ and 1.2-1.4 GPa, corresponding to garnet cores with kyanite and rutile inclusions. Post-peak conditions of $\approx 800\text{-}850\ \text{°C}$ and c. 0.5 GPa are recorded in rims of garnet porphyroblast/clasts. The study of nanogranite inclusions shows that most garnet grew in the presence of melt. To constrain the primary composition and the P-T conditions of formation of nanogranitoids, we have carried out an experimental study of nanogranitoids in garnets, which were melted at 1.5 GPa and 850, 825 and 800 °C in a piston cylinder apparatus. Experiments show that anatexis and entrapment of nanogranites occurred at c. 800 °C. Electron microprobe and NanoSIMS analyses indicate that experimental glasses are leucogranitic and peraluminous and define two compositional groups: Type I corresponds to K-rich, Ca- and H₂O-poor leucogranitic melts, whereas type II represents K-poor, Ca- and H₂O-rich granodioritic to tonalitic melts. They are found, respectively, at cores and rims of garnet porphyroblasts/clasts, and show that Jubrique migmatites underwent two anatectic events under contrasting fluid regimes.

To determine the age of crustal melting events and their timing with lithospheric mantle processes, we have analyzed Lu-Hf in whole rocks and garnets of Jubrique gneisses and garnet pyroxenites from the Ronda peridotite. The Lu-Hf isochrons confirm that the growth of garnet in Jubrique gneisses occurred in the Early Permian (c. 289 Ma) during the latest stages of the Variscan orogeny, most likely in a context of continental collision and overthickened continental crust. We found no Alpine Lu-Hf

ages, indicating either that this event is not resolvable with our sampling and dating techniques, or that the Lu-Hf of garnet was not equilibrated in the Alpine orogeny. The Lu-Hf whole rock-garnet isochrons of mantle garnet pyroxenites provide Jurassic-Cretaceous (144 Ma), Paleogene (53 Ma) and Miocene (21 Ma) ages. We interpret early Miocene ages as recording the waning stages of an Alpine extensional-related thermal event before emplacement of peridotites. Mantle garnet pyroxenites do not record Lu-Hf Variscan ages that may suggest that this system was reset by later mantle events or that garnet in mantle rocks grew in geodynamic events later than the Variscan orogeny.

KEYWORDS: *nanogranites; crustal anatexis; migmatites; Betic Cordillera; Jubrique; gneiss; anatectic melts; piston cylinder; melt inclusions; Garnet Lu-Hf geochronology; garnet pyroxenites; Ronda peridotites.*

Resumen

La fusión parcial (“anatexia o anatexis”) desempeña un papel fundamental en la generación, la diferenciación y la reología de la corteza continental terrestre. Los terrenos “*migmatíticos*” constituyen el principal registro geológico de la anatexia cortical a largo de la historia de la Tierra. Desentrañar los mecanismos de la anatexis cortical en estos terrenos ha demostrado ser un reto, especialmente, cuando se trata de averiguar la composición química de los fundidos anatéticos. El objetivo principal de esta tesis doctoral es el de mejorar nuestra comprensión de la anatexis de la corteza inferior mediante el estudio de “*inclusiones de nanogranitos*” —gotas microscópicas de fundidos que se formaron en las reacciones de fusión incongruente— atrapadas en minerales metamórficos, y su relación con los procesos tectono-magmáticos a escala litosférica. La originalidad de mi tesis reside en la investigación de la anatexis cortical mediante la combinación del estudio petrológico, termodinámico y experimental de inclusiones de nanogranitos en granates de rocas migmatitas en facies de granulitas de alta presión. Con este objetivo, he investigado los gneises migmatíticos de la unidad de Jubrique; una sección cortical fuertemente adelgazada que aflora en la parte más occidental de las unidades Alpujárrides (Cordillera Bética, S. España). Estos gneises constituyen la cobertera de las peridotitas de Ronda —el mayor afloramiento mundial de peridotitas del manto litosférico subcontinental— y proporcionan una oportunidad única para investigar la naturaleza y la edad de los eventos de fusión cortical y su relación temporal con los procesos del manto en el Mediterráneo occidental.

Las inclusiones de fundidos anatéticos ($\approx 30\text{-}40\ \mu\text{m}$) —ahora recristalizadas a nanogranitos— aparecen en los núcleos y bordes de los granates de toda la secuencia gneílica de Jubrique. La modelización termodinámica y la geotermobarometría convencional proporcionan las condiciones del clímax metamórfico, que tuvo lugar a temperaturas entorno a los $850\ \text{°C}$ y a presiones de unos $1,2\text{--}1,4\ \text{GPa}$. Estas condiciones quedaron registradas en la composición química de los núcleos de los granates, donde también aparecen inclusiones de distena y rutilo. Las condiciones post-clímax metamórfico de unos $800\text{-}850\ \text{°C}$ y $0,5\ \text{GPa}$ se registran en los bordes de los porfiroclastos y porfiroblastos de granate. El estudio de las inclusiones de nanogranitos muestra que la mayor parte de los granates crecieron en presencia de fundidos. Para obtener la composición primaria y las condiciones de presión y temperatura de la formación de los nanogranitos, hemos llevado a cabo un estudio experimental de los nanogranitos incluidos en granates, que hemos fundido en un aparato tipo “piston cylinder” a presiones de $1,5\ \text{GPa}$ y a temperaturas de $850, 825$ y $800\ \text{°C}$. Los experimentos muestran que la anatexis y el atrapamiento de los nanogranitos ocurrieron a temperaturas de unos $800\ \text{°C}$. Los análisis de microsonda electrónica e iónica de los vidrios experimentales obtenidos por la fusión de nanogranitos poseen una composición de leucogranitoides peraluminosos que definen dos grupos de composicionales: las inclusiones de Tipo I corresponden a fundidos leucograníticos ricos en K, Ca y pobres en H_2O , mientras las inclusiones de Tipo II son fundidos granodioríticos a tonalíticos ricos en Ca y H_2O , y pobres en K. Las inclusiones se encuentran, respectivamente, en

los núcleos (Tipo I) y los bordes (Tipo II) de los porfiroblastos y porfiroclastos de granate. Este estudio demuestra que las migmatitas de Jubrique se generaron en al menos dos eventos anatéticos con regímenes contrastados de fluidos.

Para determinar la edad de la anatexis cortical y su relación temporal con los procesos del manto litosférico, hemos analizado el sistema isotópico Lu-Hf en la roca total y granates de los gneises de Jubrique y de piroxenitas con granate de las peridotitas Ronda. Las isócronas Lu-Hf confirman que el crecimiento del granate en los gneises de Jubrique se produjo en el Pérmico inferior (c. 289 Ma) durante las últimas etapas de la orogenia Varisca, muy probablemente en un contexto de colisión continental y corteza continental engrosada. No hemos encontrado en nuestro estudio edades Lu-Hf Alpinas, lo que indica bien que este evento no se puede resolver con nuestras técnicas de datación y muestreo de los granates, o que el sistema isotópico Lu-Hf en el granate no se equilibró durante la orogenia Alpina. Las isócronas Lu-Hf de roca total-granate en las piroxenitas con granate de las peridotitas de Ronda proporcionan edades del Jurásico-Cretácico (144 Ma), Paleógeno (53 Ma) y del Mioceno (21 Ma). Interpretamos las edades del Mioceno temprano como el registro geocronológico del ocaso de un evento térmico relacionado con la extensión del Dominio Alborán justo antes del emplazamiento intracortical de las peridotitas. Las piroxenitas con granate del manto no registran edades Lu-Hf variscas, que puede deberse a que este sistema isotópico requilibró durante acontecimientos del manto posteriores, o que el granate en las rocas del manto creció con posterioridad a la orogenia varisca.

PALABRAS CLAVE: *nanogranitos; anatexia cortical; migmatitas; Cordillera Bética; Alpujárrides; gneises de Jubrique; fundidos anatéticos; experimentos; inclusiones fundidas; geocronología de Lu-Hf; piroxenitas con granate; peridotitas de Ronda.*

Résumé

La fusion partielle (anatexie) joue un rôle fondamental dans la génération, la différenciation et la rhéologie de la croûte continentale terrestre. Les terrains dits «migmatitiques», constituent la principale figure de l'anatexie crustale à travers l'histoire de la Terre. Déchiffrer les mécanismes de l'anatexie crustale de ces roches s'avère difficile, particulièrement quand il s'agit de dévoiler la composition chimique primaire des fondus anatectiques. Le principal objectif de cette thèse est de mieux comprendre l'anatexie au niveau de la croûte inférieure à travers l'étude d'inclusions de «nanogranites» —des gouttelettes microscopiques de fondus qui se forment via des réactions de fusion incongrues— dans les minéraux métamorphiques, et leur relation avec les processus tectonométamorphiques à l'échelle de la lithosphère. L'originalité de ma thèse réside dans la combinaison d'études pétrologiques, thermodynamiques et expérimentales de l'anatexie, et ce en se basant sur les inclusions de nanogranites dans les grenats de migmatites granulitiques de haute pression. Le présent cas d'étude traite les gneiss migmatitiques de l'unité de Jubrique, une séquence crustale complète —bien que fortement amincie— dans les Alpujarrides occidentales (Cordillères Bétiques, S. Espagne). Ces gneiss surmontent les péridotites de Ronda —le plus large affleurement du manteau lithosphérique subcontinental sur Terre— et livrent une opportunité unique d'étudier de près la nature et l'âge des événements de fusion partielle de la croûte et leur lien temporel vis-à-vis des processus mantelliques dans la Méditerranée occidentale.

Les inclusions de fondu ($\approx 30\text{-}40\ \mu\text{m}$) – recristallisées en nanogranites – dans les gneiss de Jubrique sont présentes dans les cœurs et bordures des grenats tout au long de la séquence. Les modélisations thermodynamiques et la thermobarométrie conventionnelle donnent des conditions de pic métamorphique de $\approx 850\ \text{°C}$ et $1.2\text{-}1.4\ \text{GPa}$, correspondant aux cœurs des grenats également riches en inclusions de disthène et de rutile. Les conditions de post-pic métamorphique —correspondant à $\approx 800\text{-}850\ \text{°C}$ et c. $0.5\ \text{GPa}$ — sont enregistrées dans les bordures des porphyroblastes/clastes de grenats. L'étude des inclusions de nanogranites montre que la plupart des grenats sont cristallisés dans la présence du fondu. Afin de contraindre la composition primaire et les conditions P-T de la formation des nanogranitoïdes, nous avons entamé une étude expérimentale des nanogranitoïdes dans les grenats, que nous avons refondus à $1.5\ \text{GPa}$ et $850, 825$ and $800\ \text{°C}$ dans un appareil à piston cylindre. Les expérimentations montrent que l'anatexie et le piégeage des nanogranites s'est produit à c. $800\ \text{°C}$. Les analyses de microsonde et NanoSIMS indiquent que les verres expérimentaux sont leucogranitiques et peralumineux, et définissent deux groupes compositionnels: le type I correspond à des fondus leucogranitiques riches en K et Ca et pauvres en H_2O , tandis que le type II représente des fondus granodioritiques à tonalitiques pauvres en K et Ca et riches en H_2O . Ces fondus se trouvent, respectivement, dans les cœurs et bordures de porphyroblastes/clastes de grenats, et montrent que les migmatites de Jubrique ont subi deux événements anatectiques associés à deux régimes contrastés de fluides.

Afin de déterminer l'âge des événements de fusion crustale et leur lien temporel avec les processus du manteau lithosphérique, nous avons analysé le Lu-Hf dans les

roches totales et les grenats des gneiss de Jubrique et des pyroxénites à grenat des péridotites de Ronda. Les isochrones Lu-Hf confirment que la croissance du grenat dans les gneiss de Jubrique s'est passée pendant le Permien Inférieur (c. 289 Ma) durant les derniers stades de l'orogénèse Varisque, et ce, très probablement dans un contexte de collision continentale et d'une croûte surépaissie. Nous n'avons trouvé aucun âge Lu-Hf Alpin, ce qui indique que, soit cet événement n'est pas résoluble avec notre échantillonnage et nos techniques de datations, soit que le Lu-Hf dans les grenats n'a pas été équilibré pendant l'orogénèse Alpine. Les isochrones roche totale-grenat du Lu-Hf dans les pyroxénites à grenat du manteau donnent des âges Jurassique-Crétacé (144 Ma), Paléogène (53 Ma) et Miocène (21 Ma). Nous interprétons les âges du Miocène inférieur comme correspondant aux stades de déclin d'un événement thermique extensionnel Alpin, antérieur à la mise en place des péridotites. Par ailleurs, les pyroxénites à grenat du manteau n'enregistrent aucun âge Lu-Hf Varisques qui indiqueraient que ce système a été réinitialisé par des événements mantelliques postérieurs ou que le grenat des roches mantelliques aurait cristallisé pendant des événements géodynamiques postérieurs à l'orogénèse Varisque.

MOTS-CLÉS: *nanogranites; anatexie crustale; migmatites; Cordillères Bétiques; Jubrique; gneiss; fondus anatectiques; piston cylindre; inclusions de fondu; géochronologie du Lu-Hf; pyroxénites à grenats; péridotites de Ronda.*

Acknowledgements

... This part is perhaps the hardest part to write. Words are almost never eloquent enough for Gratitude...

First of all, I would like to thank all the people that I had the chance to know during this adventure, the ones who accompanied me in many ways at each of its stages. It's been a life-changing experience at all levels, and I'm grateful for what I've learned from it.

Mis agradecimientos van a mis dos directores de tesis **Dr. Carlos J. Garrido Marín** (*Instituto Andaluz de Ciencias de la Tierra UGR-CSIC, Spain*) y **Dr. Antonio Acosta-Vigil** (*Instituto Andaluz de Ciencias de la Tierra UGR-CSIC, Spain*). Gracias por la oportunidad, el apoyo y la implicación en este proyecto de tesis doctoral, y gracias por lo que he aprendido con vosotros.

My thanks go to the teams and individuals who collaborated to make this work feasible and with whom I learned a lot. To **Bernardo Cesare** (*Università degli studi di Padova, Italy*), **Omar Bartoli** (*Università degli studi di Padova, Italy*) and **Stefano Poli** (*Università degli studi di Milano, Italy*), grazie mille per tutto, e soprattutto per il supporto e per avermi iniziato alla petrologia sperimentale! My thanks go to **Robert Anczkiewicz** and his wonderful team in Krakow -**Marta Smędra** and **Darek Sala** – (Polish Academy of Sciences, Poland) for all their help and support, and the fruitful discussions, dziękuję bardzo! My thanks go also to **Lucie Tajčmanová** (*ETH, Zurich, Switzerland*) for her valuable contribution to this work.

From the *Instituto Andaluz de Ciencias de la Tierra* (IACT), I thank all the people who facilitated the realization of this work whether technically: **Chari, Miguel, Sonia, Gan & Jose Manuel, Alpiste, Karoly, Jose Alberto**, or administratively: **Ana, Juani, Amparo, Carolina, Cristina, Alejandro, Manolo, Carmen** and all the colleagues I had the chance to work and collaborate with. From *Centro de Instrumentacion Cientifica* (CIC), I thank **Isabel** (for the long but fun hours in chasing MI in SEM!) and **Miguel** for his assistance with the microprobe.

Mes remerciements vont aussi au laboratoire *Géosciences Montpellier (France)*, et spécialement à: **Jean-Louis, Nathalie, Alain, Andrea, Delphine, Pierre, Brigitte**, la communauté **Crystal2Plate** ainsi que tous ceux qui ont fait partie de cette aventure à un moment donné: **Takako, Fatna, Gregory, Vincent, Michael**.

A mis colegas y amigos de la UGR y del IACT, empezando por la **Granada Dream Team: Erwin** (le R'win, meilleur compagnon de terrain, Béni Bousera nous aura beaucoup appris!), **Claudio** (mon italien préféré! Merci pour ton amitié, ton écoute et tes conseils, et pour ta bonne humeur toujours contagieuse!), **Mary** (mi Mary! Gracias por tu tranquilidad y apoyo), **Karoly** (for your disponibility and precious help, köszönöm szépen!), **Zoltan** (for the Hungarian words!), **Nicole** (the sweet newcomer); **el Despacho 29 y UGR: Vanessa** (Mi Vane preciosa!), **Juan** (mi Juanillo!), **Vero, Aitor, Chema, Carmen, Patricia...** muchas gracias por todos los momentos bonitos que hemos compartido. Del IACT, no olvido **Laura, Mery, Carmina, Luis, Claudia, Giordana, Isaac, Tillo & Elena, Marga, Luis & Angeles, Cesar, Carola, Muhammed, Loubna, Rita, Ari, Enric**.

A **mi familia granadina**: **Chiara** (la mia miss sunshine!), **Kamar** (my Moon & sweeter self!), **Siham** (Sahoumti!), **Nieves** (Mi andaluz avanzado lo debo a ti!), **Gan** (for our crazy adventures), **Luis David** (pour ta précieuse amitié et la révélatrice “jazz synergy”), **Benny** (for your beautiful friendship and support), mi coro **Gospel Molotov** (por la cantoterapia y por ser lo que sois), **Willy’s Band** y los **Willy’s Orphans** (Willy, Luis-David, Alpiste, David y Chiara – we literally rocked/jazzed the IACT!), **Germán** (por tu optimismo y tu bondad), **Mery** (por las sorpresas siempre espectaculares!). Estoy muy agradecida por haberos conocido, por la amistad y el apoyo que me habéis aportado todos en cada momento, cada uno a su manera; esta aventura no hubiera podido ser la misma sin vosotros; y la nuestra, todavía tiene la vida por delante para seguir.

A **mes amis du Maroc (et MRE)**, merci de m’avoir soutenue malgré la distance, merci pour votre patience et vos encouragements. Ils m’ont été précieux durant ces années. Une pensée à **Hanane** (Mimi diali!), **Loubna** (ma Loulou), **Mouna** (ma Moni), **Mastere** (mon grand frère d’une autre maman), **Aniss**, **Wissal** (ma Wiss), **Brahim** (Bajocien), **Imane** (ma Emma), **Oussama**, **Mohamed** (Hmina), **Younes**.

To **my friends from other lands**, **Meiyin** (the magical soul), **Andre**, **Rafa**, **Will**, **Bachir**, **Tobias**, **Bianca**, my people in Krakow **Przemek**, **Ania**, **Kasia**, **Marta**, **Darek**, **Alise** (not forgetting **Nina**, **Kaska**, **Irena**, **Akik**, **Jérémie**); to my **YES & IUGS colleagues** and **mentors**: Thank you for being there, for being who you are and for everything we have shared and what I learned from you.

A **ma famille**, et en particulier mes chers parents **Amina** et **Mohamed**, mes frères **El Khalil** et **Mohsine**, ma grand-maman **Fatima**, je ne pense pas qu’il y ait de mots pour

exprimer à quel point je suis reconnaissante pour votre présence et votre amour inconditionnel et à toute épreuve. Grâce à vous je suis là où je suis et je suis qui je suis. Merci. Je vous aime !

A **mon grand-papa** qui nous a quittés tôt, à qui je n'ai pas pu dire au revoir; j'espère que de là-haut tu es fier de moi, cette thèse est en ta mémoire.

Last but not least, two words to resume it all: { الحمد لله }

Disclaimer: It is very likely that I may have missed some names (or many!); I apologize for it in advance, I wrote this in a rush. However, I promise I'll make it up to you!

Affectionately,

Amel Barich

FUNDING

My Ph.D. Thesis is supported by a "Formación del Personal Investigador-FPI" Fellowship (BES-2011-045283) funded by the Spanish Government (Ministerio de Economía y Competitividad). I also acknowledge an earlier MAE-AECID fellowship funded by the "Agencia Española de Cooperación Universitaria y Científica para el Desarrollo". The research of my Ph.D. Thesis has been funded by research grants from the "Ministerio de Economía y Competitividad" (Grants CGL2010-14848 and CGL2013-42349-P), Junta de Andalucía (research groups RNM-131 and Proyecto de Excelencia P09-RNM-4495), and has benefited from EU Cohesion Policy funds from the European Regional Development Fund (ERDF) and the European Social Fund (ESF) in support of human resources, innovation and research capacities, and research infrastructures.

Table of Contents

EXTENDED ABSTRACT	1
RESUMEN EXTENDIDO	7
RESUME ÉTENDU	13
PART I. INTRODUCTION, THESIS AIMS, STRUCTURE OF THE THESIS AND METHODOLOGY	19
<hr/>	
1 INTRODUCTION	21
1.1 EARTH STRUCTURE: THE LOWER CONTINENTAL CRUST	21
1.2 COMPOSITION, ANATEXIS AND DIFFERENTIATION OF THE CONTINENTAL CRUST	24
1.3 APPROACHES AND METHODOLOGIES TO INVESTIGATE ANATECTIC ROCKS	26
1.3.1 STRUCTURAL AND PETROLOGICAL STUDIES	26
1.3.2 EXPERIMENTAL APPROACH	27
1.3.3 THERMODYNAMIC MODELING APPROACH	27
1.3.4 STUDY OF NANOGRANITES AND MELT INCLUSIONS	28
1.4 GEOLOGICAL SETTING OF THE STUDY CASE	32
1.4.1 THE MALÁGUIDE COMPLEX	32
1.4.2 THE ALPUJARRIDES COMPLEX AND THE JUBRIQUE UNIT	32
1.4.2.1 STRUCTURE AND DEFORMATION	34
1.4.2.2 METAMORPHISM	34
1.4.3 THE RONDA PERIDOTITE MASSIF	35
2 AIMS AND STRUCTURE OF THE THESIS	37
2.1 BACKGROUND AND PROBLEM STATEMENT	37
2.2 AIMS OF THE THESIS	38
2.3 OUTLINE OF THE THESIS	38
3 METHODOLOGY	41
3.1 SAMPLING AND SAMPLE PREPARATION	41
3.1.1 SAMPLING	41
3.1.2 PREPARATION OF ROCK THIN AND THICK SECTIONS	41
3.1.3 PREPARATION OF WHOLE-ROCK POWDERS	42
3.2 INSTRUMENTAL ANALYTICAL TECHNIQUES	42
3.2.1 BULK ROCK ANALYSES: ENERGY DISPERSIVE X-RAY FLUORESCENCE (XRF)	42
3.2.2 MICRO-ANALYTICAL SPECTROSCOPY INSTRUMENTAL ANALYSIS	42
3.2.2.1 SCANNING ELECTRON MICROSCOPY (SEM) 42	
3.2.2.2 ELECTRON MICRO-PROBE ANALYSIS (EMPA)	44
3.2.2.2.1 FUNDAMENTALS	44
3.2.2.2.2 MAJOR ELEMENT ANALYSES	46
3.2.2.3 NANOSCALE SECONDARY ION MASS SPECTROMETRY (NANOSIMS)	47
3.2.2.3.1 FUNDAMENTALS	47
3.2.2.3.2 ANALYSES OF MELT INCLUSIONS	48

3.2.3	MASS SPECTROMETRY INSTRUMENTAL TECHNIQUES	50
3.2.4	LASER ABLATION COUPLED WITH INDUCTIVELY COUPLED PLASMA SOURCE MASS SPECTROMETRY (LA-ICP-MS)	50
3.2.5	MULTICollector-ICP-MS: ANALYSES OF LU-HF ISOTOPES IN GARNETS	52
3.2.5.1	SEPARATION OF GARNET CORES AND RIMS IN THICK SECTIONS	52
3.2.5.2	DIGESTION AND DISSOLUTION OF SAMPLES	53
3.2.5.3	CHROMATOGRAPHY	54
3.2.5.4	INSTRUMENTAL ANALYSIS	54
3.3	EXPERIMENTAL TECHNIQUES FOR THE REMELTING OF MELT INCLUSIONS	55
3.3.1	SAMPLE PREPARATION	55
3.3.2	PISTON-CYLINDER EXPERIMENTS	56

PART II. RESULTS 59

4	MICROSTRUCTURES AND PETROLOGY OF MELT INCLUSIONS IN THE ANATECTIC SEQUENCE OF JUBRIQUE (BETIC CORDILLERA, S SPAIN): IMPLICATIONS FOR CRUSTAL ANATEXIS	61
4.1	INTRODUCTION	61
4.2	SAMPLING, PETROGRAPHY AND COMPOSITION OF MINERALS	64
4.2.1	PETROGRAPHY AND MINERAL CHEMISTRY OF MYLONITIC GNEISSES	67
4.2.2	PETROGRAPHY AND MINERAL CHEMISTRY OF PORPHYROBLASTIC GNEISSES	73
4.3	MICROSTRUCTURES OF MELT INCLUSIONS	77
4.1	PHASE EQUILIBRIA MODELING AND CONVENTIONAL THERMOBAROMETRY	81
4.2	DISCUSSION	83
4.2.1	PRIMARY NATURE AND SIGNIFICANCE OF THE MI: COMPARISON WITH PREVIOUS STUDIES	83
4.2.2	P-T CONDITIONS OF MELTING AND IMPLICATIONS OF NANOGRANITES	86
5	THE COMPOSITION OF NANOGRANITOIDS IN MIGMATITES OVERLYING THE RONDA PERIDOTITES (BETIC CORDILLERA, S SPAIN): THE ANATECTIC HISTORY OF A POLYMETAMORPHIC BASEMENT	89
5.1	INTRODUCTION	89
5.2	PETROGRAPHY AND MICROSTRUCTURES OF MELT INCLUSIONS	91
5.3	RESULTS	93
5.3.1	MICROSTRUCTURES OF REMELTED NANOGRANITOIDS	93
5.3.2	COMPOSITION OF GLASS IN REMELTED NANOGRANITOIDS	99
5.4	DISCUSSION	105
5.4.1	P-T CONDITIONS OF ANATEXIS AT JUBRIQUE	105
5.4.2	SIGNIFICANCE OF GLASS COMPOSITIONS IN REMELTED NANOGRANITOIDS	106
5.4.3	IMPLICATIONS FOR THE GEODYNAMIC EVOLUTION OF LOWER CONTINENTAL CRUST IN THE BETIC CORDILLERA	108
5.4.4	SIGNIFICANCE FOR MELT INCLUSION STUDIES, CRUSTAL MELTING AND DIFFERENTIATION	110

6	UNRAVELING THE AGE OF THE POLYMETAMORPHIC EVOLUTION OF THE ALBORÁN BASEMENT: GARNET LU-Hf GEOCHRONOLOGY OF JUBRIQUE GNEISSES AND GARNET PYROXENITES FROM THE RONDA PERIDOTITE	113
6.1	INTRODUCTION	113
6.2	GEOLOGICAL SETTING	115
6.3	SAMPLING AND SAMPLE DESCRIPTION	116
6.4	SAMPLE PREPARATION AND ANALYTICAL PROCEDURES	118
6.5	RESULTS	119
6.5.1	GARNET CORE TO RIM LU AND HF CONCENTRATION PROFILES	119
6.5.2	LU-Hf ISOCHRONS	121
6.5.2.1	JUBRIQUE GNEISSES	121
6.5.2.2	RONDA GARNET PYROXENITES	123
6.6	DISCUSSION	125
6.6.1	COMPARISON WITH PREVIOUS GEOCHRONOLOGICAL STUDIES	125
6.6.2	UNRAVELING THE P-T-TIME EVOLUTION OF JUBRIQUE GNEISSES	131
6.6.2.1	TIMING AND GEODYNAMIC SETTING OF PEAK P-T METAMORPHIC CONDITIONS	133
6.6.2.2	TIMING AND GEODYNAMIC SETTING OF POST-PEAK P-T METAMORPHIC CONDITIONS	135
	PART III. CONCLUSIONS	139
7	CONCLUSIONS	141
7.1	PERSPECTIVE AND FUTURE WORK	144
	PART V. REFERENCES	147
8	REFERENCES	149

Extended Abstract

The main aim of this thesis is to uncover the processes of lower crustal anatexis through the study of nanogranite inclusions in metamorphic minerals in lower-crust gneisses, and their potential relationships with lithospheric mantle tectono-magmatic processes. With this aim, in this Ph.D. Thesis I investigated gneisses from the polymetamorphic Jubrique crustal sequence—a complete though strongly thinned crustal section in the westernmost Alpujarrides (Betic Cordillera, S. Spain). These gneisses overlie the ultramafic Ronda peridotite massif—the largest exposure of subcontinental mantle on Earth—and provide a unique opportunity to investigate the nature and age of crustal melting events and their timing with lithospheric mantle processes in the westernmost Mediterranean.

The study of the composition of primary melts during anatexis of high-pressure granulitic migmatites is relevant to understand the generation and differentiation of continental crust. Peritectic minerals in migmatites can trap droplets of melt that form via incongruent melting reactions during crustal anatexis. These melt inclusions commonly crystallize and form *nanogranitoids* upon slow cooling of the anatectic terrane. To obtain the primary compositions of crustal melts recorded in these nanogranitoids—including volatile concentrations and information on fluid regimes—they must be remelted and rehomogenized before analysis.

In this thesis, I report a new occurrence of melt inclusions in polymetamorphic granulitic gneisses of the Jubrique unit. The gneissic sequence is composed of mylonitic gneisses at the bottom and in contact with the peridotites, and porphyroblastic gneisses on top. Mylonitic gneisses are strongly deformed rocks with abundant garnet and rare biotite. Except for the presence of melt inclusions, microstructures indicating the former presence of melt are rare or absent. Upwards in the sequence garnet decreases whereas biotite increases in modal proportion. Melt inclusions are present from cores to rims of garnets throughout the entire sequence. Most of the former melt inclusions are now totally crystallized and correspond to nanogranites, whereas some of them are partially made of glass or, more rarely, are totally glassy. They show negative crystal shapes and range in size from ≈ 5 to 200 micrometers, with a mean size of ≈ 30 -40 micrometers.

Daughter phases in nanogranites and partially crystallized melt inclusions include quartz, feldspars, biotite and muscovite; accidental minerals include kyanite, graphite, zircon, monazite, rutile and ilmenite; glass has a granitic composition. Melt inclusions are mostly similar throughout all the gneissic sequence. Some fluid inclusions, of possible primary origin, are spatially associated with melt inclusions, indicating that at some point during the suprasolidus history of these rocks granitic melt and fluid coexisted. Thermodynamic modeling and conventional thermobarometry of mylonitic gneisses provide peak conditions of ≈ 850 °C and 12-14 kbar, corresponding to cores of large garnets with inclusions of kyanite and rutile. Post-peak conditions of ≈ 800 -850 °C and 5-6 kbar are represented by rim regions of large garnets with inclusions of sillimanite and ilmenite, cordierite-quartz-biotite coronas replacing garnet rims, and the matrix with oriented sillimanite. Previous conventional petrologic studies on these strongly deformed rocks have proposed that anatexis started during decompression from peak to post-peak conditions and in the field of sillimanite. The study of melt inclusions shows, however, that melt was already present in the system at peak conditions, and that most garnet grew in the presence of melt.

To further constrain the primary composition and the P-T conditions of formation of nanogranitoids, I have carried out a detail experimental study. Nanogranitoids within separated chips of cores and rims of large garnets from were remelted at 15 kbar and 850, 825 or 800 °C and dry (without added H₂O), during 24 hours, using a piston cylinder apparatus. Although all experiments show glass (former melt) within melt inclusions, the extent of rehomogenization depends on the experimental temperature. Experiments at 850-825 °C show abundant disequilibrium microstructures, whereas those at 800 °C show a relatively high proportion of rehomogenized nanogranitoids, indicating that anatexis and entrapment of melt inclusions in these rocks occurred likely close to 800 °C. Electron microprobe and NanoSIMS analyses show that experimental glasses are leucogranitoid and peraluminous, though define two distinct compositional groups. Type I corresponds to K-rich, Ca- and H₂O-poor leucogranitic melts, whereas type II represents K-poor, Ca- and H₂O-rich granodioritic to tonalitic melts. Type I and II melt inclusions are found in most cases at the cores and rims of large garnets, respectively. We tentatively suggest that these former migmatites underwent two melting events under contrasting fluid regimes, possibly during two different orogenic periods. This study demonstrates the

strong potential of melt inclusions studies in migmatites and granulites in order to unravel their anatectic history, particularly in strongly deformed rocks where most of the classical anatectic microstructures have been erased during deformation.

One of the main issues that prevents establishing reliable P-T-t paths to better constrain the potential geodynamic scenarios for the tectonic and metamorphic evolution of Alborán basement high-grade gneisses is the difficulty of relating zircon and monazite thermochronological ages with the crystallization of major mineral assemblages and, in particular, garnet and its MI. Another important issue to unravel the geodynamic evolution of this area is to establish the temporal links between the P-T-t paths of the mantle section with those of the rocks from its crustal envelope. To shed some light on the age of crystallization, we have analyzed Lu-Hf in whole rock and several garnet core and rim fractions, and have obtained isochrons in five samples of porphyroclastic and porphyroblastic gneisses of the Jubrique unit, and in three garnet pyroxenites from the garnet-spinel mylonites and the spinel tectonite domain of the Ronda peridotite.

Multipoint Lu-Hf isochrons of whole rock and different garnet core and rim fractions in mylonitic and porphyroblastic gneisses of Jubrique unit yield ages mostly comprised between the Early Permian and Early Jurassic Periods. Multipoint isochrones of garnets in Jubrique mylonitic gneisses provide Early Permian (289 Ma) to Middle-Late Triassic (236 Ma) ages, except for the combination of whole rock and rims in a sample that yields an age of 193 Ma. Multipoint isochrones of garnets in porphyroblastic gneisses provide Early-Middle Triassic (248 Ma) to Early Jurassic (191 Ma) ages, except for a two-point isochron made of whole rock and a single garnet from JU-20, yielding an age of 129 Ma. We interpret the oldest ages as recording garnet formation during de Variscan orogeny. We interpret the Lu-Hf ages between ≈ 260 -190 Ma and ≈ 129 Ma as due to partial reset of the Lu-Hf system by post-Variscan tectono-metamorphic events.

The Lu-Hf geochronology of Jubrique gneisses, together with previous thermochronological U-Pb studies in accessory minerals, highlights the polymetamorphic nature of high-grade rocks in the crustal envelope of the Betic-Rif peridotites. The Lu-Hf ages of the cores of garnet porphyroclasts and porphyroblasts confirm that the growth of garnet in Jubrique gneisses occurred in the Early Permian

during the latest stages of the Variscan orogeny. This inference poses major problems to the interpretation of the Alpine decompression P-T-t paths in the high-grade Jubrique gneisses, which rely on peak metamorphic conditions registered in the inclusions and the mineral chemistry of garnet cores. The presence of MI in garnet cores—which we have demonstrated experimentally to be formed c. 800 °C— in equilibrium with kyanite and rutile strongly supports a high-P and high-T (1.2–1.4 GPa and \approx 850 °C) melt-present environment during the growth of garnet in the Hercynian. These conditions are akin to that of granulitic rocks formed at the base of thickened continental crust during continental collision. As deduced by previous authors in equivalent gneisses of the Rif belt, we interpret that the anatexis and crystallization of garnet cores in the Jubrique unit took place in the Early Permian in a context of continental collision and overthickened continental crust.

Despite the U-Pb-Th thermochronological evidence for a sequence of Alpine events in the Jubrique units, we have found no Alpine Lu-Hf ages indicating either that this event is not resolvable with the present sampling and dating techniques, or that the Lu-Hf of garnet was not equilibrated during the Alpine orogeny. A possible interpretation of the Lu-Hf isochrons is that most of the garnet and fabrics of the Jubrique gneissic sequence is of Permian and/or Jurassic age. However, this interpretation is at odd with U-Pb-Th dating of zircon and monazite in garnet rims and matrix of the Jubrique gneissic sequence that yielded Alpine ages ranging from 34 to 20 Ma, or younger. These results indicate that garnet growth in Jubrique gneisses is polymetamorphic and grew in at least in two different geodynamic events; the latest event also involved anatexis of the sequence as attested by the presence of Ca-rich inclusions in garnet rims. The slow diffusion of REE and Hf in garnet may have preserved primary garnet growth ages without being reset in the Alpine orogeny at least at the scale we sampled them. Further detailed studies relating microstructure with high spatial resolution thermochronology are needed to unravel the role of the Alpine orogenic event in the development of the magmatic and ductile microstructures of the Jubrique gneissic sequence.

The Lu-Hf whole rock and garnets isochrons of Ronda garnet pyroxenites provide ages of the Jurassic-Cretaceous limit (144 Ma), the Lower-Middle Paleogene (53 Ma) and the Lower Neogene (21 Ma) Periods. We interpret Early Miocene ages as

recording the waning stages of the extensional-related thermal event leading to the melting of the base of the lithospheric mantle peridotites, the development of the Ronda peridotite recrystallization front, and the final intracrustal emplacement of the Betic-Rif peridotites. In this interpretation, the Lu-Hf ages of garnet pyroxenites in the Ronda garnet-spinel mylonite domain were not reset during this thermal event because this domain was substantially cooler than the rest of the peridotite massif, which allowed the preservation of Lu-Hf ages from early orogenic events since the Mesozoic.

A striking difference between the geochronological results in peridotites and rocks from their crustal envelop is that the Lu-Hf ages in rocks of the mantle section do not record any Variscan event, which is otherwise widespread in the Lu-Hf and U-Pb-Th thermochronological record of the overlying high-grade crustal rocks. This may reflect either that this Lu-Hf ages might have been reset by later mantle events or that garnet in mantle rocks grew in geodynamic events later than the Variscan. On the other hand, the coincidence of U-Pb-Th age in zircon mantle pyroxenites and of garnet Lu-Hf ages in the overlying crustal sections most likely reflects extraordinary thermal events that partially melted garnet pyroxenite in the mantle lithosphere and induced anatexis in the overlying lithospheric crustal section during the Variscan orogeny.

Resumen extendido

El principal objetivo principal de esta tesis doctoral es investigar los procesos de fusión parcial de la corteza inferior mediante el estudio de inclusiones de nano-granitoides presentes en los minerales metamórficos de gneises de la corteza inferior y sus posibles relaciones con los procesos tectono-magmáticos del manto litosférico. Con este objetivo, en esta tesis doctoral he investigado los gneises de la secuencia cortical polimetamórfica de Jubrique, una secuencia cortical fuertemente adelgazada que aflora en los Alpujárrides occidentales (Cordillera Bética, sur de España) a techo del macizo de peridotitas subcontinentales de Ronda —el afloramiento más grande del manto subcontinental expuesto en la superficie terrestre. Las inclusiones de nano-granitos en los minerales de estos gneises proporcionan una oportunidad única para investigar la naturaleza y la edad de los eventos de fusión parcial de la corteza terrestre, así como su posible relación espacio temporal con los procesos tectono-magmáticos registrados en el manto litosférico en el Mediterráneo occidental.

El estudio de la composición de los fundidos primarios formados durante la fusión parcial de alta presión registrada en rocas migmatíticas en facies de granulitas es fundamental para comprender la generación y diferenciación magmática de la corteza continental. Los minerales peritéticos que se forman en estas migmatitas pueden atrapar durante su crecimiento pequeñas gotas de fundidos formados por las reacciones de fusión parcial incongruente de las rocas corticales. Debido al enfriamiento lento característico de los terrenos anatócticos, estas inclusiones fundidas cristalizan en forma de “nano-granitoides”. Para poder obtener información de la composición de los fundidos primarios y las condiciones de fusión parcial, las inclusiones de nano-granitoides han de ser refundidas y homogeneizadas experimentalmente.

En esta tesis, presento el primer estudio de inclusiones de nano-granitoides en los minerales de los gneises granulíticos polimetamórficos de la unidad de Jubrique. La secuencia gnéisica de Jubrique está formada en su parte basal en contacto con las peridotitas de Ronda por gneises miloníticos sobre los que se sitúan a techo una secuencia de gneises porfiroblásticos. Los gneises miloníticos están intensamente deformados y contienen abundante granate y escasa biotita. Excepto por la presencia de inclusiones de nano-granitos y fundidos, las microestructuras magmáticas características

de migmatitas son escasas. En la parte superior de la secuencia gnéissica, la proporción modal de granate disminuye mientras aumenta la de la biotita. Las inclusiones de fundidos aparecen tanto en los núcleos como en los bordes de los granates en toda la secuencia gnéissica. La mayor parte de las inclusiones de fundidos han recristalizado y corresponden ahora a inclusiones de nano-granitos, aunque en algunas se preserva aún vidrio y, más raramente, pueden aparecer completamente vitrificadas. Estas inclusiones fundidas presentan morfologías cristalinas negativas y su tamaño varía entre ≈ 5 y 200 micrómetros, con un tamaño promedio de uno $\approx 30-40$ micrómetros. Las fases minerales que componen los nano-granitos y las inclusiones parcialmente cristalizadas son cuarzo, feldespatos, biotita y moscovita; los minerales accidentales (i.e., atrapados durante la fusión) incluyen cianita, grafito, circón, monacita, rutilo y la ilmenita; el vidrio, cuando está presente, tiene una composición granítica. Las inclusiones fundidas son en su mayoría similares en toda la secuencia gnéissica. Algunas inclusiones fluidas, de posible origen primario, están espacialmente asociadas a las inclusiones fundidas, lo que indica que en algún momento de la historia supra-solidus de estas rocas los fundidos graníticos y los fluidos coexistieron. La modelización termodinámica y los cálculos de geotermobarometría convencional obtenidos usando la composición química de los gneises miloníticos y sus minerales establecen las condiciones del pico metamórfico a una temperatura de ≈ 850 ° C y a presiones de 12 a 14 kbar. Estas condiciones corresponden a las obtenidas usando la composición de los núcleos de los porfiroclastos de granate con inclusiones de cianita, rutilo y nano-granitos. Las condiciones posteriores a las condiciones del pico metamórfico ocurrieron a temperaturas de unos $\approx 800-850$ °C y presiones entre 5 y 6 kbar. Estas condiciones quedan registradas en la composición de los bordes de los porfiroclastos de granates con inclusiones de nano-granitos, sillimanita e ilmenita, coronas cordierita-cuarzo-biotita que sustituyen los bordes del granate, y la matriz con cristales orientados de sillimanita. Los estudios petrológicos anteriores a esta tesis doctoral, han propuesto que la anatexis cortical comenzó durante una descompresión cuasi-isotérmica desde las condiciones del pico metamórfico hasta las condiciones post-pico en el campo de sillimanita. El estudio de las inclusiones fundidas en esta tesis doctoral muestra, sin embargo, que las condiciones de fusión parcial ya estaban presentes en el pico metamórfico en condiciones de alta presión y temperatura, y que la mayoría de granate creció en presencia de fundidos graníticos.

Para restringir aún más la composición primaria y las condiciones de presión, temperatura y el contenido de elementos volátiles durante la fusión parcial registrada por las inclusiones de nano-granitos, he realizado un estudio experimental detallado de las mismas. Para ello, he separado trozos con inclusiones de nano-granitos tanto de los núcleos como de los bordes de los porfiroclastos de granate, que he fundido experimentalmente en un aparato tipo “piston-cylinder” durante 24 horas a presiones de 1.5 GPa, y temperaturas de 850, 825 y 800 °C, en ausencia de volátiles (i.e., sin adición de H₂O). Aunque todos los experimentos muestran vidrio dentro de las inclusiones fundidas, el grado de homogeneización de éstas dependió de la temperatura a la que se habían realizado los experimentos. Los experimentos realizados entre 850-825 °C muestran inclusiones con abundantes microestructuras de desequilibrio, mientras que los realizados a 800 °C muestran una proporción relativamente alta de nano-granitos homogeneizados, indicando que la fusión parcial y el atrapamiento de las inclusiones fundidas en los porfiroclastos y porfiroblastos de granate de los gneises de Jubrique se produjo probablemente entorno a los 800 °C. Los análisis de microsonda electrónica y de nanosonda iónica (NanoSIMS) muestran que los fundidos de las cargas experimentales tienen una composición de leucogranitos y son peraluminicos, aunque definen dos tipos composicionales bien diferenciados. Las inclusiones de Tipo I son ricas en K y Ca, y pobres en H₂O, mientras que las de Tipo II son pobres en K y Ca, y ricas en H₂O, con composiciones que varían entre granodioríticas a tonalíticas. Las inclusiones fundido de Tipo I y II se encuentran, respectivamente, mayoritariamente en los núcleos y los bordes de los porfiroclastos y porfiroblastos de granate. Deducimos que estos dos grupos composicionales se formaron durante dos eventos de fusión parcial a diferentes presiones y temperaturas y en condiciones contrastadas de presencia de fluidos. Nuestro estudio demuestra el gran potencial que tiene el estudio de las inclusiones fundidas en migmatitas y granulitas para desentrañar la historia de fusión parcial de la corteza inferior, especialmente en rocas fuertemente deformadas en donde la mayoría de las microestructuras anatécicas primarias han sido borradas por la deformación.

Uno de los principales problemas que impide la determinación de trayectorias de P-T-t fiables que nos permitan restringir mejor los posibles escenarios geodinámicos registrados en los gneises del basamento del dominio Alborán, es la dificultad de relacionar las edades absolutas obtenidas mediante la datación Th-U-Pb de las fases accesorias —tales como el circón y la monacita— con la cristalización metamórfica de

las principales asociaciones minerales. Debido a su importancia para la determinación de las condiciones de P y T de los gneises, es particularmente acuciante conocer la edad de la cristalización metamórfica del granate y sus inclusiones. Otra cuestión importante que es necesaria para desentrañar la evolución geodinámica de la litosfera del dominio de Alborán es establecer los vínculos temporales entre las trayectorias de P-T-t de las rocas del manto litosférico y las de los gneises corticales suprayacentes. Con el objetivo de determinar la edad de cristalización del granate en estas rocas, hemos analizado los isótopos de Lu-Hf en la roca total y en diferentes fracciones de los centros y bordes de granate en muestras de gneises de Jubrique y de piroxenitas con granate de las peridotitas de Ronda. Con estos datos, hemos calculado las isócronas Lu-Hf en cinco muestras de gneises porfiroclásticos y porfiroblásticos de Jubrique y en tres piroxenitas con granate de diferentes dominios de las peridotitas de Ronda.

Las isócronas de Lu-Hf obtenidas combinando los análisis de roca total y las diferentes fracciones de los centros y bordes de granate en los gneises de Jubrique proporcionan en su mayoría edades comprendidas entre los períodos Pérmico inferior y Jurásico inferior. Las isócronas multipunto de los gneises porfiroclásticos dan edades comprendidas entre el Pérmico inferior (289 Ma) y el Triásico medio a tardío (236 Ma), con la excepción de una muestra, que proporciona una isócrona de 193 Ma obtenida combinando la roca total y un borde del granate. Las isócronas multipunto de los gneises porfiroblásticos proporcionan edades correspondientes a los periodos Triásico inferior a medio (248 Ma) y Jurásico inferior (191 Ma), con la excepción de una isócrona obtenida combinando la roca total y un granate completo, que proporciona una edad de 129 Ma. Interpretamos las isócronas más antiguas como la edad de formación del granate durante la orogenia Varisca. Las edades comprendidas entre los ≈ 260 -190 Ma y la de ≈ 129 Ma son probablemente edades mínimas resultado de una perturbación del sistema isotópico de Lu-Hf causada por eventos tectono-metmórficos posteriores a la orogenia Varisca.

Los resultados de la geocronología Lu-Hf roca total-granate en los gneises de Jubrique y los estudios termocronológicos anteriores del sistema Th-U-Pb en fases accesorias ponen de relieve la naturaleza polimetamórfica de las rocas corticales de alto grado asociadas a las peridotitas de la Cordillera Bético-Rifeña. Las edades Lu-Hf de los núcleos de los porfiroclastos y porfiroblastos de granate confirman que el crecimiento del granate en los gneises de Jubrique se produjo en el Pérmico inferior

durante las últimas etapas de la orogenia Varisca. Esta inferencia plantea importantes problemas a las interpretaciones de las trayectorias de descompresión Alpina de los gneises de alto grado que se basen en las condiciones del pico metamórfico registradas en las inclusiones y/o la composición química de los núcleos de los granates. La presencia de inclusiones fundidas en los núcleos de los granate —que hemos demostrado experimentalmente que se formaron sobre los 800 °C— asociadas a distena y rutilo indican que el crecimiento de granate en el Hercínico tuvo lugar a altas presiones y temperaturas (1.2—1.4 GPa y \approx 800 °C). Estas condiciones de P y T son similares a las registradas en granulitas formadas en la base de una corteza continental engrosada durante una colisión continental. Como han deducido otros autores en sus estudios de los gneises de la Cordillera Rifeña, interpretamos que la anatexis cortical y la cristalización de los núcleos de granate en los gneises de Jubrique tuvieron lugar en una corteza engrosada durante el Pérmico inferior, probablemente en un contexto de convergencia y colisión continental.

A pesar de las numerosas dataciones del sistema Th-U-Pb en circones y monacitas de los gneises de Jubrique que ponen de manifiesto la existencia de una secuencia de eventos Alpinos, en nuestro estudio del sistema Lu-Hf roca total-granate de estos gneises no hemos obtenido isócronas de edad Alpina. Esto puede deberse bien a que los eventos Alpinos no han podido discernirse con las técnicas de muestreo y datación que hemos empleado, o a que el sistema isotópico Lu-Hf no se equilibró durante esta orogenia, registrando sólo los eventos Variscos. Una posible interpretación de nuestras isócronas Lu-Hf roca total-granate es que la mayor parte del granate y las microestructuras de la secuencia gnéisica de Jubrique es de edad Pérmica y/o Jurásica. Sin embargo, esta interpretación contradice, entre otras observaciones, las edades Th-U-Pb obtenidas en circones y monacitas incluidas en los bordes de los granates y en la matriz de los gneises. Estas dataciones proporcionan edades Alpinas comprendidas mayoritariamente entre los 34 Ma y 20 Ma. Estos resultados indican que el crecimiento del granate en los gneises de Jubrique es polimetamórfica y se produjo en al menos dos eventos geodinámicos diferentes. La presencia de inclusiones fundidas ricas en Ca en los bordes de los granates, implica que este último evento involucró también la anatexis de la corteza. La difusión extraordinariamente lenta de los elementos de las tierras raras y del Hf en el granate, puede ser la causa de la preservación de las edades Variscas de crecimiento de granate durante la orogenia Alpina. Para desentrañar el papel del evento

Alpino en la formación de las estructuras magmáticas y dúctiles de la secuencia gnéisica de Jubrique será necesario realizar estudios termocronológicos adicionales con una mayor resolución espacial y temporal.

Las isócronas de Lu-Hf combinando roca total y granate en las piroxenitas con granate de las peridotitas de Ronda proporcionan edades del límite Jurásico-Cretácico (144 Ma), el Paleógeno inferior-medio (53 Ma) y el Mioceno inferior (21 Ma). Interpretamos las edades del Mioceno inferior como el registro temporal de las etapas finales del evento Alpino que produjo la extensión del manto litosférico y la fusión parcial de la base del mismo, que fue el causante de la formación del frente de recristalización en este macizo, concluyendo con el emplazamiento intracortical de las peridotitas Bético-Rifeñas. Según esta interpretación, las edades de Lu-Hf de las piroxenitas con granate en el dominio de las milonitas con granate-espinela de las peridotitas de Ronda —que proporcionan edades más antiguas— no se requilibraron durante este evento térmico debido a que este dominio estaba más frío que el resto de la sección de la litosfera mantélica, lo que permitió la preservación de las edades Lu-Hf de eventos orogénicos más antiguos.

Una diferencia de primer orden entre los resultados geocronológicos de las peridotitas y los de las rocas gnéisica corticales es que las edades Lu-Hf de las piroxenitas del manto no registran en ningún caso el evento Varisco, mientras que este evento está registrado de forma generalizada por los termocronómetros Lu-Hf y Th-U-Pb en los gneises. Esto puede reflejar que las edades Lu-Hf Variscas —si existieron— de los granates del manto se requilibraron durante los eventos tectónicos posteriores, o que el granate en las rocas de manto se formó durante eventos geodinámicos posteriores al Varisco. Por otra parte, la coincidencia de las edades de Th-U-Pb en circones de las piroxenitas con granate del manto con las edades Lu-Hf de los granates de los gneisses corticales suprayacentes refleja, muy probablemente, un evento geodinámico extraordinario que afectó a toda la litosfera durante el Varisco, fundiendo parcialmente los protolitos de las piroxenitas en el manto litosférico, e induciendo la anatexis de la corteza suprayacente.

Résumé étendu

Le principal objectif de cette thèse est de découvrir les processus qui interviennent dans l'anatexie de la croûte inférieure à travers l'étude d'inclusions de nanogranites dans des minéraux métamorphiques présents dans les gneiss de la croûte inférieure, et leur relation avec les processus tectono-magmatiques du manteau lithosphérique subcontinental. Avec cet objectif et à travers de cette thèse de doctorat, j'ai étudié les gneiss de la séquence métamorphique crustale de Jubrique – une section complète – bien que amincie – dans les Alpujarrides occidentales (Cordillère Bétique, Espagne). Ces gneiss surmontent le massif ultrabasique de péridotites de Ronda – le plus large affleurement du manteau subcontinental sur Terre – et offre une opportunité unique d'investiguer la nature et l'âge des événements de fusion crustale et leur chronologie vis-à-vis des processus de manteau lithosphérique dans la Méditerranée occidentale.

L'étude de la composition des fondus primaires pendant l'anatexie des migmatites granulitiques de haute pression est importante pour comprendre la genèse et la différenciation de la croûte continentale. Les minéraux péricectiques dans les migmatites peuvent piéger des gouttelettes de roche fondue qui se forment via des réactions de fusion incongrue pendant l'anatexie crustale. Ces inclusions de fondu cristallisent communément et forment des nanogranitoïdes à travers un refroidissement lent du terrain anatectique. Afin d'obtenir des compositions primaires des fondus crustaux enregistrés dans ces nanogranitoïdes – incluant les concentrations volatiles et les informations sur les régimes fluides – ces inclusions doivent être refondues et rehomogénéisées avant d'être analysées.

Dans cette thèse, je décris l'existence d'inclusions de fondu dans les gneiss granulitiques polymétamorphiques de l'unité de Jubrique. La séquence de gneiss est composée dans sa base de gneiss mylonitiques et en contact avec les péridotites, et dans son toit de gneiss porphyroblastiques. Les gneiss mylonitiques sont des roches fortement déformées avec des grenats abondants et des biotites rares. A part la présence d'inclusions de fondu, les microstructures indiquant la présence antérieure de fondu sont rares ou absentes. Vers le haut de la séquence, la proportion modale du grenat diminue tandis que celle de la biotite augmente. Les inclusions de fondu sont présentes dans les cœurs et les bordures des grenats tout au long de la séquence. La majorité des

inclusions de fondu sont totalement cristallisées et correspondent aux nanogranites; tandis que certaines inclusions sont partiellement composées de verre, et plus rarement, sont totalement vitreuses. Elles montrent des formes cristallographiques négatives et varient en taille de ≈ 5 à 200 micromètres, avec une taille moyenne de $\approx 30-40$ micromètres. Les phases-filles dans les nanogranites et les inclusions de fondu partiellement cristallisées comprennent le quartz, le feldspath, biotite, muscovite; les minéraux accidentels incluent le disthène, le graphite, le zircon, la monazite, le rutile et l'ilménite; le verre a une composition granitique. Les inclusions de fondu sont en général similaires le long de la séquence de gneiss. Des inclusions fluides d'origine potentiellement primaire, sont associées spatialement avec des inclusions de fondu, indiquant qu'à un moment durant l'histoire du suprasolidus de ces roches, le liquide granitique et les fluides ont coexisté. La modélisation thermodynamique et la thermobarométrie conventionnelle des gneisses mylonitiques donnent des conditions de pic métamorphique de 850°C et 12-14 kbar, correspondant aux cœurs des grands grenats avec des inclusions de disthène et de rutile. Les conditions post-pic métamorphique de $\approx 800-850^{\circ}\text{C}$ et 5-6 kbar sont représentées par les bordures des grands grenats, et la matrice contenant la sillimanite orientée. Des études antérieures en pétrologie conventionnelle sur ces roches fortement déformées ont suggéré que l'anatexie a commencé pendant la décompression depuis les conditions de pic métamorphique aux conditions post-pic métamorphique et dans le domaine de la sillimanite. L'étude des inclusions de fondu montrent, pourtant, que le liquide magmatique était déjà présent dans le système dans les conditions de pic métamorphique, et que la majorité des grenats ont cristallisé dans la présence du fondu.

Afin de contraindre d'avantage les compositions primaires et les conditions P-T de la formation des nanogranitoides, j'ai entamé une étude expérimentale détaillée. Les nanogranitoides dans les puces de grenats séparées des cœurs et bordures des grands grenats ont été refondues à 15 kbar et 850 , 825 et 800°C et dans des conditions anhydriques (sans ajout de H_2O), durant 24 heures, utilisant l'appareil à piston cylindre. Bien que les essais montrent du verre (fusion ancienne) à l'intérieur des inclusions vitreuses, l'étendue de la réhomogénéisation dépend de la température expérimentale. Les essais à $850-825^{\circ}\text{C}$ montrent des microstructures de déséquilibre abondantes, tandis que ceux à 800°C montrent une proportion relativement haute de nanogranitoides réhomogénéisés, indiquant que l'anatexie et le piégeage des inclusions vitreuses dans

ces roches se sont éventuellement produits près de 800°C. La microsonde électronique et les analyses de NanoSIMS montrent que les verres expérimentaux sont des leucogranitoides et peralumineux, définissant toutefois deux groupes compositionnels distincts. Le type I correspond à des liquides leucogranitiques riches en potassium et en calcium et pauvres en H₂O, tandis que le type II représente des liquides granodioritiques à tonalitiques pauvres en potassium et en calcium et riches en H₂O. Les inclusions de fondu de type I et II sont trouvées dans la plupart des cas dans les cœurs et bordures des grands grenats, respectivement. Nous suggérons que ces anciennes migmatites ont subi deux événements de fusion sous des régimes de fluides différents, possiblement pendant deux périodes orogéniques différentes. Cette étude démontre que le grand potentiel des études des inclusions vitreuses dans les migmatites et les granulites dans le but est de révéler leur histoire anatectique, particulièrement dans des terrains fortement déformés où la majorité des microstructures anatectiques classiques ont été effacées.

L'une des principales problématiques qui empêche une détermination fiable des chemins P-T-t pour mieux contraindre les scénarios géodynamiques potentiels de l'évolution tectonique et métamorphique des gneiss de haut degré métamorphique du socle d'Alborán, est la difficulté de relier les âges termochronologiques du zircon et de la monazite avec la cristallisation des assemblages de minéraux majeurs, et en particulier, le grenat et ses inclusions de fondu. Dans le même dessein, une autre problématique importante est d'établir des liens temporels entre les chemins P-T-t de la section mantellique et ceux des roches qui forment son enveloppe crustale. Pour apporter quelques éclaircissements sur l'âge de la cristallisation, nous avons analysé Lu-Hf en roche totale et dans plusieurs fractions de cœur et bordure de grenats, and avons obtenu des isochrones de 5 échantillons de gneiss porphyroclastiques et porphyroblastiques de l'unité de Jubrique, et de 3 échantillons de pyroxénites à grenat appartenant aux mylonites à grenat et spinel et aux tectonites à spinel des péridotites de Ronda.

Les isochrones multipoints de Lu-Hf des roches totales et des différentes fractions cœur et bordures de grenats dans les gneisses mylonitiques et porphyroblastiques de l'unité de Jubrique ont donné des âges compris principalement entre le Permien Inférieur et le Jurassique Inférieur. Les isochrones multipoints des grenats dans les gneiss mylonitiques de Jubrique donnent des âges de Permien inférieur

(289 Ma) à Trias Moyen et Supérieur, sauf dans la combinaison roche totale et bordure de grenat, où l'âge obtenu est de 193 Ma. Les isochrones multipoints des grenats appartenant aux gneiss porphyroblastiques donnent des âges compris entre le Trias Moyen à Supérieur (248 Ma) et Jurassique Inférieur (191 Ma), sauf pour une isochrone à deux points représentant la roche totale et un grenat de JU-20, et qui a donné un âge de 129 Ma. Nous interprétons les âges les plus anciens comme étant des âges qui ont enregistré la formation des grenats pendant l'orogénèse Varisque. Nous interprétons les âges Lu-Hf compris entre ≈ 260 -190 Ma et ≈ 129 Ma comme dues à une réinitialisation partielle du système Lu-Hf par des événements tectono-métamorphiques post-varisques.

La géochronologie Lu-Hf des gneiss de Jubrique et les études thermochronologiques U-Pb antérieures sur des minéraux accessoires, mettent en évidence la nature polymétamorphique des roches de haut degré dans l'enveloppe crustale des péridotites Bético-Rifaines. Les âges Lu-hf des cœur des porphyroclastes et porphyroblastes de grenats confirment que la croissance des grenats dans les gneiss de Jubrique s'est passée pendant le Permien Inférieur durant les dernières étapes de l'orogénèse Varisque. Cette inférence pose un problème majeur dans l'interprétation des chemins P-T-t de décompression alpine dans les gneiss de haut degré de Jubrique, qui s'appuient sur les conditions de pic métamorphique enregistrées dans les inclusions et la chimie minérale des cœurs des grenats. La présence des inclusions de fondu dans les cœurs des grenats – en équilibre avec le disthène et le rutile, soutient fermement la présence d'un environnement de haute-P et haute-T (1.2-1.4 GPa and 850 °C) où le fondu est présent durant la croissance du grenat pendant l'Hercynien. Ces conditions correspondent à celles de roches granulitiques formées à la base d'une croûte continentale épaissie pendant une collision continentale. Comme déduit par des auteurs antérieurs concernant des gneiss équivalents dans la ceinture rifaine, nous interprétons que l'anatexis et la cristallisation des cœurs de grenat dans l'unité de Jubrique a pris place au Permien Inférieur dans un contexte de collision continentale et dans une croûte continentale épaissie.

Bien que les preuves thermochronologiques U-Pb-Th pointent vers la présence d'une séquence d'événements alpins dans l'unité de Jubrique, nous n'avons trouvé aucun âge Lu-H alpin indiquant que soit cet événement est non résolvable avec les techniques d'échantillonnage et de datation présentes, ou bien que le Lu-Hf des grenats

n'a pas été équilibré pendant l'orogénèse alpine. Une possible interprétation des isochrones Lu-Hf est que la plupart des grenats et fabriques constituant la séquence de gneiss de Jubrique est d'un âge Permien et/ou Jurassique. Toutefois, cette interprétation n'est pas en concordance avec les datations U-Th-Pb des zircons et monazites dans les bordures de grenat et dans la matrice des gneiss de Jubrique, qui ont donné des âges compris entre 30 et 20 Ma, ou plus jeunes. Ces résultats indiquent que la croissance du grenat dans les gneiss de Jubrique est polymétamorphique et a pris place durant au moins deux contextes géodynamiques différents ; le dernier événement implique aussi l'anatexie de la séquence, comme attesté par la présence d'inclusions riches en Ca dans les bordures de grenats. La lente diffusion des REE et Hf dans le grenat pourrait avoir préservé les âges de la croissance primaire de celui-ci sans avoir été réinitialisée pendant l'orogénèse alpine – du moins, à l'échelle que nous avons échantillonnée. D'avantage d'études reliant la microstructure avec une thermochronologie de haute résolution spatiale sont nécessaires afin de dénouer le rôle de l'orogénèse Alpine dans le développement des microstructures magmatique et ductile de la séquence de gneiss de Jubrique.

Les isochrones Lu-Hf de roche totale et de grenats dans les pyroxénites à grenat de Ronda donnent des âges de la limite Jurassique-Crétacé (144 Ma), du Paléogène Inférieur-Moyen (53 Ma) et du Néogène Inférieur (21 Ma). Nous interprétons les âges du Miocène Inférieur comme enregistrant les étapes de déclin de l'événement thermal relié à l'extension et qui a conduit à la fusion de la base des péridotites du manteau lithosphériques, le développement du front de cristallisation des péridotites de Ronda, et l'emplacement intracrustal final des péridotites des Bétiques et du Rif. Selon cette interprétation, les âges Lu-Hf des pyroxénites à grenat dans le domaine des mylonites à grenat et spinel de Ronda n'ont pas été réinitialisés pendant cet événement thermique car ce domaine était plus refroidi que le reste du massif de péridotites, ce qui a permis la préservation des âges Lu-Hf d'événements orogéniques plus anciens.

Une différence frappante entre les résultats géochronologiques des péridotites et leur enveloppe crustale est que les âges Lu-Hf dans les roches de la section du manteau n'enregistrent aucun événement Varisque, alors que celui-ci est enregistré d'une manière généralisée dans les roches crustales par les thermochronomètres Lu-Hf et U-Pb-Th. Cela pourrait d'un côté, refléter que ces âges Lu-Hf auraient été réinitialisés par

des événements mantelliques postérieurs, ou d'un autre, que les grenats dans les roches mantelliques sont grandi pendant des événements géodynamiques postérieur au Varisque. D'autre part, la coïncidence des âges U- Pb-Th dans les zircons des pyroxénites à grenat et ceux du Lu-Hf dans les grenats de la section crustale qui les superpose reflète, très probablement, un événement géodynamique extraordinaire qui aurait affecté à toute la lithosphère pendant le Varisque, engendrant une fusion partielle des pyroxénites à grenat dans la lithosphère mantellique et a induit à une anatexie dans la lithosphérique crustale superposée pendant l'orogénèse Varisque.

Part I

*Introduction, Thesis Aims,
Structure of the Thesis and
Methodology*

1 Introduction

1.1 Earth Structure: the Lower Continental Crust

Characterization of deep Earth systems is fundamental to increase our understanding of their processes. The Earth's crust is the outermost layer which extends vertically from the Earth's surface to the Mohorovičić discontinuity that marks the crust–mantle boundary (Fig. 1.1, 1.2). The lithosphere, known as the rigid outer layer of the Earth, is formed by the crust and upper mantle layers above the asthenosphere, and its depth extends to about 100 km. The Lithosphere is divided into several plates of different sizes, which move over the low velocity zone composed of relatively plastic layers of partially molten rocks, also known as the asthenosphere (100-200 km thick).

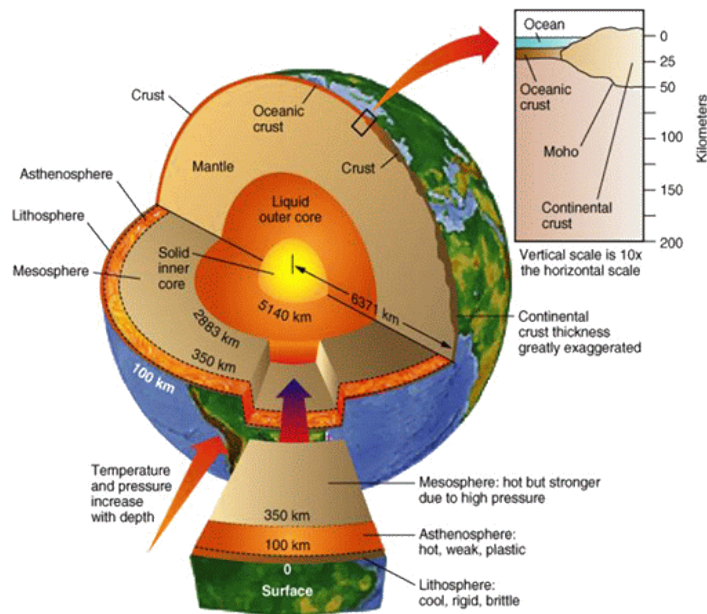


Figure 1.1. General internal structure of the Earth (source: <http://cosmiceaparty.org/blog/>)

There have been distinguished two types of crust; the oceanic thin crust (~7 km thick), composed of sediments and relatively dense lithologies such as basalt, gabbros and peridotites, always younger than ~200 Ma, and the continental crust that is thicker (~41.1 km on average), less dense, and much older than the oceanic crust (Rudnick and

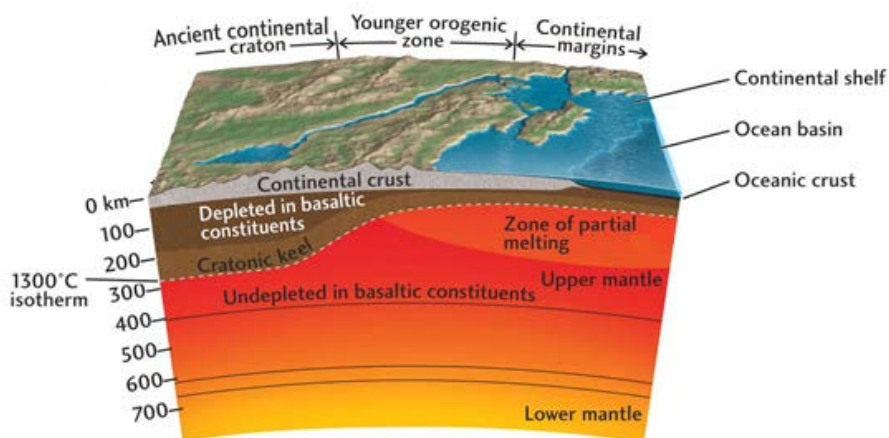


Figure 1.2. Detailed structure of the lithosphere at the surface and in depth. (source from Barth Matthias web page, Univ. Mainz)

Gao 2003). To know the origin and evolution of the continental crust, it is important to understand the relationships and degree of coupling between processes in the deep crust and underlying subcontinental lithospheric mantle. Isotopic data from zircon grains indicate that formation of the continental crust began more than 4.0 billion years ago. In a first stage, it formed as the mantle started differentiating, as thickened oceanic crust above “hotspots” and at shallow levels (~15 km) above convergent margins (Belousova et al. 2010; Harrison 2009). In a later stage, during the Archean (from ca 2.8 Ga), continental crust has mainly formed in magmatic arcs above subduction zones and 10 % was generated through mantle material added to existing crust by plumes and hotspots (Sawyer 2008). Its current composition is however not representative of mantle materials; the composition of the continental crust in the present day is andesitic, although have had fluctuations along time: during Archean (>2.5 Ga), it appears to have been slightly more felsic than during post-Archean era. Although having an andesitic mean composition, the continental crust is not uniform (Rudnick and Gao, 2003); while the upper crust is more silicic and richer in SiO_2 and K_2O , the lower crust is more mafic and is richer in Al_2O_3 , FeO , MgO and CaO (Brown, 2013). This adds to the complexity of its origin.

Seismic studies reveal that continental crust is highly heterogeneous in three dimensions. Most common models given by seismic refraction data show that the continental crust is structured in upper-, middle-, and lower major layers (Christensen and Mooney 1995; Holbrook et al. 1992). Rudnick and Fountain (1995) explain that P velocities increasing progressively with depth indicate increasing proportions of mafic lithologies and increasing metamorphic grade (Fig. 1.3).

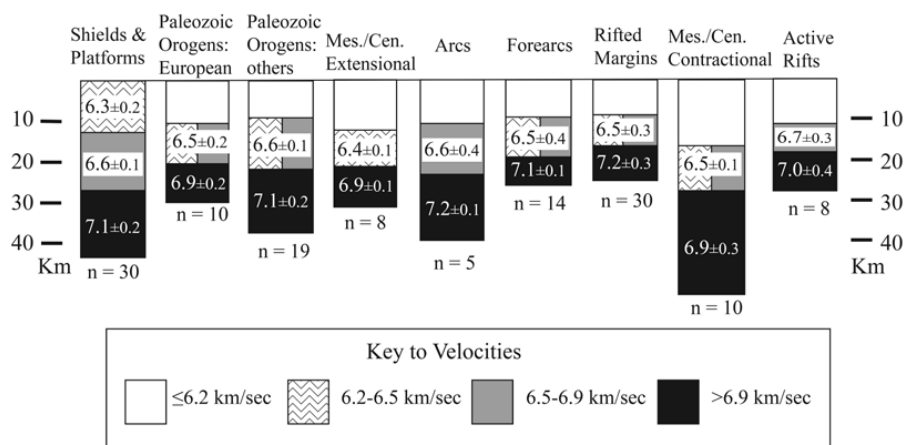


Figure 1.3. Seismic V_p data of crustal sections (modified after Rudnick and Fountain, 1995).

While the middle crust is formed of amphibolite facies rocks and has an intermediate bulk composition, enriched with K, Th and U contents, the lower crust is described as lithologically more heterogeneous due to its implication in different tectonic settings; the lower crust is composed of granulite facies rocks, its average bulk composition is originally mafic (approaching the composition of a primitive mantle-derived basalt) but can range to intermediate bulk compositions in some regions. Granulite terrains that experienced isobaric cooling are representative of middle to lower crust and have higher proportions of mafic rocks than granulite terrains that experienced isothermal decompressions. The latter are thought to be upper crustal rocks that endured orogenic phases. Although abundant among high grade metamorphic studies, metapelites constitutes only a small proportion of the lower crust for their limited occurrence in xenoliths and granulite terrains, and also for their high heat production (Rudnick and Fountain 1995). The upper crust has, on the other hand, an intermediate composition and is enriched with highly incompatible trace elements

budget (35-55%). For it being the best exposed on the surface, the upper crust is readily accessible to sampling, and solid estimates of its composition are available for most elements. These estimates show that the upper crust has a granodioritic bulk composition, is rich in incompatible elements, and is generally depleted in compatible elements. The deep crust is on the other hand harder to reach and therefore more difficult to study.

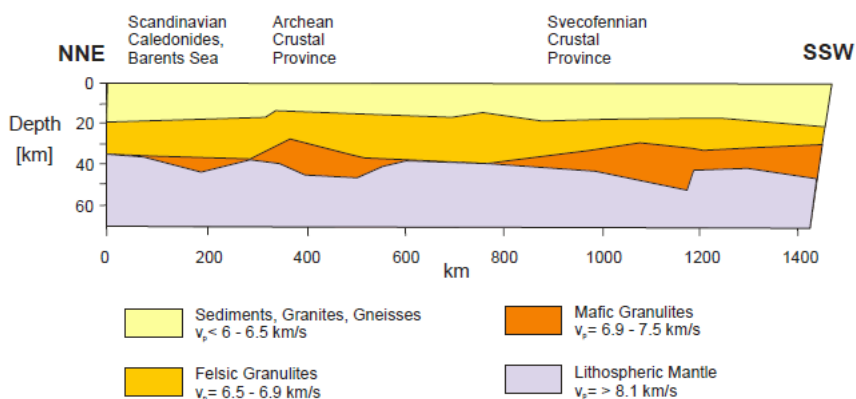


Figure 1.4. Structure of the continental crust. (Figure from Wedepohl, 1995)

1.2 Composition, Anatexis and Differentiation of the Continental Crust

In order to unravel the composition of the deep crust, three methods have been employed: (i) studies of high-grade metamorphic rocks (amphibolite or granulite facies rocks) exposed in surface outcrops (Bohlen and Mezger 1989) and, in some cases, in uplifted cross-sections of the crust reaching to depths of 20 km or more (Fountain et al. 1990; Hart et al. 1990; Ketcham 1996; Miller and Christensen 1994); (ii) studies of granulite-facies xenoliths (foreign rock fragments) that are carried from great depths to the Earth's surface by fast-rising magmas (see Rudnick 1992); and (iii) seismic investigations of lower crustal lithologies (Christensen and Mooney 1995; Holbrook et al. 1992; Rudnick and Fountain 1995; Smithson 1978) and surface heat flow studies.

Once formed, continental crust evolves in structure and composition (Fig. 1.4). Crustal anatexis is a fundamental process that controls the differentiation of the continental crust (Sawyer et al. 2011; Vielzeuf et al. 1990). Under normal circumstances

(stable 30-35 km thick continental crust that has not been involved in orogenic processes for a long time – e.g. cratons), the continental crust does not melt, as the average geothermal gradient heats the base of the crust up to a temperature of ca. 550°C. Crustal rocks can partially melt only when the metamorphic temperatures exceed 650°C (Sawyer et al. 2011). This can occur through either radiogenic heating due to thickening of the continental crust during continental collision or addition of mantle heat at the base of the crust, or mafic magmas intrusions during subduction and extension (Bea 2012). Some studies also point strain heating as a contributor to partial melting (Sawyer et al. 2011). There has been debate on the possibility of large melt production in the crust through radiogenic heating, based on the assumption that the concentration of K, Th, and U in the continental crust is not high enough to produce enough radiogenic heat to sustain such a degree of melting in the required timescale. However, recent studies (Bea 2012; Whittington et al. 2009) stress that the thermal diffusivity of rocks at high temperature is low; therefore heat retention in the middle and the lower crust is actually higher than previously thought. The role of the mantle in crustal anatexis is still under debate. Some authors argue that large volumes of melting require an additional source of heating coming from the asthenosphere upwelling during extension, or basaltic underplating, while some others consider that a fertile crust enriched with enough K, Th, U is capable of generating its own heating through radiogenic decay of these elements during thickening.

Production of large volumes of granitic melt in continental crust is assumed to occur mainly by fluid-absent incongruent melting of hydrous minerals such as micas, also known as dehydration melting because the lower crust is assumed to be dry melting (Stevens and Clemens 1993; Wannamaker 2000; Yardley 2009; Yardley and Valley 1997). However, but less frequently, it can also occur through introduction of large volumes of fluids to the rock system (Sawyer et al. 2011; Weinberg and Hasalova 2015; Whitney 1988). Water is therefore undoubtedly – in one form or the other, essential to generate large volumes of felsic melt in the continental crust.

During H₂O-rich fluid-present melting, crustal rocks will start to melt at 600 - 700 °C at most crustal pressures. In fluid-absent conditions, crustal rocks will start melting at temperatures above 700°C, and for hornblende-bearing protolith, melting will start at temperatures exceeding 900°C (Clemens 2006).

Melting reactions resulting from both types of melting give two types of products depending on the ferromagnesian components in the original rocks; fluid-saturated melting will yield to crystallization of micas and hornblende while fluid-undersaturated melting will produce anhydrous phases such as garnet, pyroxene and/or cordierite (Brown 2010); these minerals form through peritectic reactions that are known to occur in the presence of melt.

Although produced at great depths, melt tends to segregate and escape from its source to lower density environment in the shallower levels of the continental crust. When formed at grains boundaries, melt migrates towards low-P sites either through structural fabrics or ductile microcracks; it accumulates then in strain shadows or deformation bands. Leucosomes, melanosomes and peritectic minerals \pm leucosomes are recorders of these migration pathways. During its activity, melts migration network allows melt to be redistributed and to flow to shallower levels of the crust (Brown et al. 2011).

1.3 Approaches and Methodologies to Investigate Anatectic Rocks

1.3.1 Structural and Petrological Studies

Migmatites, or former partially melted rocks, are usually observed in internal domains of orogenic belts. Migmatitic complexes in granulitic terranes are the typical areas where it is possible to directly observe and study anatectic processes (e.g. Grant and Frost 1990; Sawyer 1998; Srogi et al. 1993). Structural and petrological studies of anatectic domains have provided a wealth of information on crustal anatexis. However, the study of anatectic terranes has some limitations. First, any former melt in the system has mixed and crystallized with residual mineral phases, and the rest has escaped the anatectic terranes. Secondly, deformation destroys anatectic microstructures and segregation networks of melts. Finally, the composition of anatectic melts is often investigated by focusing on migmatites, in particular on the leucosome produced by the crystallization of the melt. However, cumulus phenomena, entrainment of peritectic and residual minerals, and fractional crystallization may lead to a composition that is not representative of the primary liquid. Hence, characterizing melt through focus on leucosome is questionable: (Brown et al. 1995; Ellis and Obata 1992; Marchildon and Brown 2001; Sawyer 1996; Sawyer 2008).

1.3.2 Experimental Approach

Experiments have become a well-established approach in the investigation of anatectic rocks. Such studies have provided a basic framework for the knowledge and interpretation of anatectic processes and crustal reworking. These studies include determination of the first constraints on the melting process (e.g. Tuttle and Bowen 1958; Wyllie 1977), estimates of melt fertility of different rocks (e.g. Johannes and Holtz 1996; Patiño Douce and Beard, 1996) and constraints on the reactions that control melt production (e.g. Vielzeuf and Holloway 1988).

However, information from experiments is limited as they offer clues on microstructures or reactions paths (Qiang and Fuyuan 1994). Other limitations are (i) that conventional partial melting experiments do not consider compositional change in the bulk system, and (ii) that fluid-absent experiments are challenging and may not be representative of reality as they may overstep melting reactions because of lack of direct control of oxidation state (leading to growth of oxide phases, conversion of ferrous to ferric iron, reduction of the amount of water).

1.3.3 Thermodynamic Modeling Approach

The last fifteen years have known the evolvement of thermodynamic modeling with the development of more sophisticated activity models for both minerals and melts through large, internally consistent datasets and complex activity models. Thermodynamic modeling provides the opportunity to constrain more easily melting reactions by investigating –within the scope of the calibration limits of the models– a range of physical and chemical processes, such as the fractionation of components into porphyroblastic phases and the loss of melt from the rocks. Holland and Powell (1998) were the first to include melt end-members for the haplogranitic system in their internally consistent dataset, including the activity-composition relationship for melt published in Holland and Powell (2001) and extended in White et al. (2001). These advances promoted the development of quantitative thermodynamic calculations involving a range of melt-bearing equilibria produced in systems that are closer to the established model (i.e. broadly haplogranitic).

Despite the great utility of thermodynamic modelling, this approach has some limitation. First, there is still a limited understanding of the thermodynamic properties of some minerals and melts (particularly end-member thermodynamics and activity–

composition relationships). Furthermore, the assessment of the suitability of a given model calculation can only be done in a rather comparative and simplistic way; an example would be a comparison of mineral modes (abundances) and compositions with available natural and experimental examples. Finally, there are some inherent limits in the chemical systems that can be considered with the currently available thermodynamic database, as well as limits in the P–T–X range for which these existing models can be considered reasonably appropriate.

1.3.4 Study of Nanogranites and Melt inclusions

A recent new and powerful approach to the study of crustal anatexis, are melt inclusions in migmatites. Melt inclusions (MI) are small droplets of liquid, commonly a few to tens of micrometers across, trapped by minerals that grow in the presence of melt. Melt inclusions offer the possibility to gain a large amount of information on various processes in the Earth from early melting stages to plutons emplacement in the upper crust (Clocchiatti 1975; Lowenstern 1995; Roedder 1984; Student 1996; Webster and Thomas 2006). They were first described by Sorby (1858) in volcanic rocks, where they constitute a wealth of information on melt chemistry and volcanic processes (e.g. Webster et al. 1997; Gurenko et al. 2005; Wanless et al. 2014). Many of the assumptions concerning the interpretation of fluid inclusions (FI) have been applied to MI (Bodnar and Student 2006; Roedder 1984; Sorby 1858).

Despite the long-lasting interest in MI, a large amount of data only became available with the availability of new in situ microanalytical techniques. In particular, the development of the electron microprobe (EMP) analyses allowed the characterization of major and minor elements (e.g. Anderson 1974; Melson 1983) while more recently trace elements can be quantified using laser ablation ICP-MS (e.g. Halter et al. 2002). Moreover, infrared spectroscopy and ion microprobe now make it possible to characterize and quantify volatiles within the MI (see Sobolev 1996 and references therein).

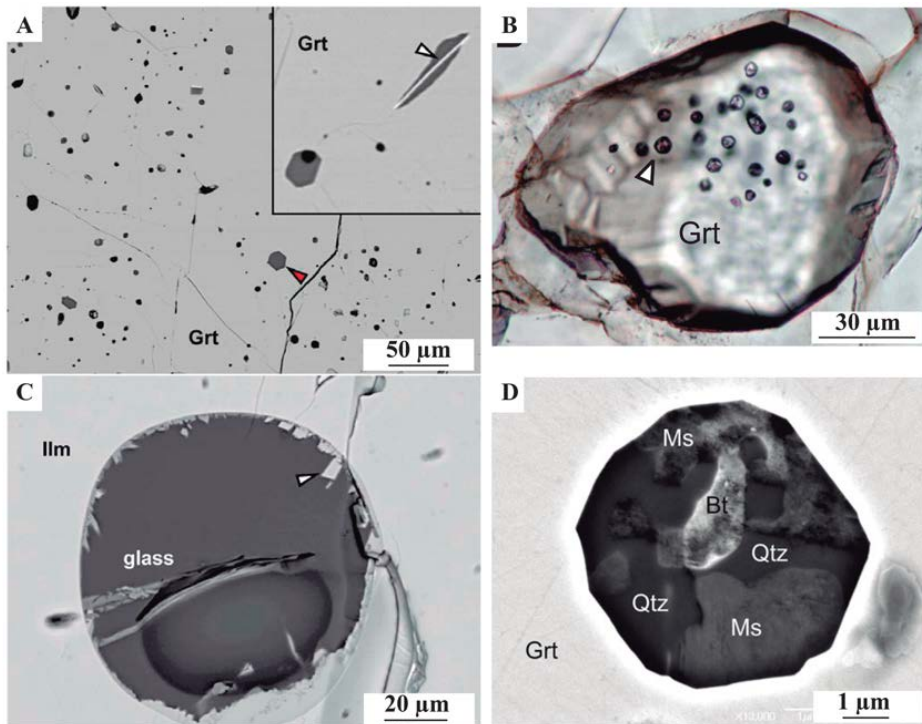


Figure 1.5. *a.* MI in garnet from an enclave of El Hoyazo (Spain). In the close-up of top-right two MI are enlarged: one with a well-developed negative crystal shape, the other with an ilmenite needle (arrow) that is probably a trapped mineral. (Cesare 2011). *b.* Primary melt inclusions (white arrow) in peritectic garnet (Grt). (Bartoli et al. 2013). *c.* A large MI hosted in ilmenite in an enclave from El Hoyazo. The inclusion walls are coated by ilmenite daughter crystallites (arrow). (Cesare 2011). *d.* FE-SEM BSE image of nanogranite inclusion in garnet (Grt) from the Ronda metatexite. The melt inclusion has a typical negative crystal shape and crystallized into an aggregate of quartz, biotite, muscovite, and plagioclase (not visible in this image) (Bartoli et al. 2013).

Recently, MI have also been reported in crustal crystalline anatectic rocks (Cesare et al. 1997; Hwanga et al. 2001; Stöckhert 2001). Most melting reactions during crustal anatexis are incongruent (e.g. Clemens 2006), i.e. produce melt and peritectic minerals, providing the opportunity that these minerals trap inclusions of the coexisting silicate liquid. Hence, MI trapped during melting can supply the composition of the primary anatectic melt (Cesare et al. 2011; Cesare et al. 2009), in contrast with MI trapped during crystallization and that provide the composition of fractionated (as opposed to primary) melts (Thomas and Davidson 2013; Webster et al. 1997) see also discussion in Bartoli et al. (2014).

Most MI reported in anatectic terranes appear partially or totally crystallized due to slow cooling at depth. Owing to the granitic phase assemblage made of micron to

submicron quartz, feldspars and micas, crystallized MI have been named “nanogranites” (Fig. 1.5) (Cesare et al. 2009). With the recent development of in-situ and high spatial resolution micro-analytical techniques, as well as appropriate methods to re-melt and re-homogenize nanogranites (Bartoli et al. 2013a; Bartoli et al. 2014), it is possible to characterize precisely MI, in order to relate their information to the process of anatexis of the host rock. Hence MI represent a new and powerful method to study anatexis, primarily because they can provide information on the primary melt compositions produced at the source region of crustal granites, including concentrations of H₂O and fluid regimes (Bartoli et al. 2013b; Bartoli et al. 2014; Cesare et al. 2011; Ferrero et al. 2012). This information can complement, and in some cases be more precise, than that provided by classical petrological and geochemical studies of anatectic terrains, for instance regarding the composition of the primary anatectic melt, which has been traditionally approximated by the composition of anatectic leucosomes. This is particularly important in cases where deformation has partially or totally erased the primary anatectic macro- and micro-structures. In these cases, the presence of MI may be the only evidence remaining in the rock for the presence and nature of melt (Cesare et al. 2011).

The number of MI occurrences in anatectic terranes reported in the literature is quite modest and, among those cases, only a few provide bulk compositional data from the MI (Bartoli et al. 2013b; Cesare et al. 2011; Ferrero et al. 2012). This is due to the relatively recent discovery of MI in crustal anatectic rocks (Cesare et al. 2011; Cesare et al. 2009; Cesare et al. 1997; Darling 2013; Gao et al. 2012; Hwanga et al. 2001; Korsakov and Hermann 2006; Liu et al. 2013; Stöckhert 2001; Stöckhert et al. 2009) and, more importantly, the very recent development of appropriate methodologies to recover the information encrypted within these former droplets of melt (Bartoli et al. 2013a; Bartoli et al. 2013b; Bartoli et al. 2014; Malaspina et al. 2006; Perchuk et al. 2008).

When reconstructing the metamorphic history of anatectic rocks, dating metamorphic assemblages and melting often constitutes one of the most important challenges. High grade metamorphic rocks, such as granulites and migmatites, often show a high heterogeneity and have, in many cases, experienced several metamorphic episodes. U-Pb on zircon and monazite is one of the most common methods of dating high-grade rocks. Polymetamorphic history of orogenic terrains is hard to unfold due to

the lack of possible correlations between textural information (reflecting peak and post-peak events) (Harley 1989) and geochronology; indeed, if most textural information reflects peak and post-peak events, it is hard to link the ages of the dated minerals with the processes that lead to the growth or modification of these minerals. Often, evidence of mineral growth is destroyed by recrystallization at high temperature and makes it hard to recover the prograde path in the studied rock (Greenfield et al. 1998; Harley 1989). Closure temperatures of some isotopic systems also limit the options of dating and geochemical correlations; if U-Pb geochronology in zircon is known to be the most efficient in terms of dating the oldest terrains on Earth (Valley et al. 2014) due to its high closure temperature (higher than 900°C) (Cherniak and Watson 2003; Dahl 1997; Lee et al. 1997). In fact, still it is difficult to link the crystallization of these accessory minerals and major minerals providing P-T conditions. However, minerals such as garnet have allowed a unique and successful bridging between thermobarometry and geochronology in high grade rocks. Growing over millions of years and in a wide range of P-T-X conditions, garnets are resistant minerals involved in a number of prograde reactions and are perfect recorders of tectono-metamorphic processes, especially at the prograde stage. Their enrichment in heavy rare earth elements (HREE) provides a potential for precise geochronology due to their high ratios of Sm/Nd (Thöni 2002; Van Breemen and Hawkesworth 1980) and Lu/Hf (Duchêne et al. 1997). Garnet's ability to fractionate Lu and Hf results in very high $^{176}\text{Lu}/^{177}\text{Hf}$ ratios and allows, together with slow diffusion rates and potential direct link with P-T information, to make this technique particularly suitable in dating high grade metamorphism. Some studies could successfully take it further by constraining the duration and rate of garnet growth through sampling cores and rims of zoned garnets (Anczkiewicz et al. 2004; Baxter et al. 2002; Burton and O'Nions 1992; Christensen et al. 1994; Christensen et al. 1989; Ducea et al. 2003; Pollington and Baxter 2010; Pollington and Baxter 2011; Sölvä 2003; Stowell et al. 2001; Vance and Harris 1999; Vance and O'Nions 1990). This approach is particularly crucial in the study of polymetamorphic terrains.

In this present study we showcase a thinned though complete continental crustal sequence that occurs in contact with the Ronda massif, which represents the largest outcrop of subcontinental lithospheric mantle determined so far. Anatectic fields and features occur throughout all the high grade facies rocks that constitute the Jubrique crustal sequence and that lie directly on the top of the Ronda peridotites. This offers a

unique opportunity to study in depth the anatectic history of these terrains and determine the common evolution of the lower continental crust and upper mantle in the Betic Cordillera region.

1.4 Geological Setting of the Study Case

The Betic Cordillera in southern Spain and the Rif in northern Morocco constitute an arcuate orogen formed during the N-S collision between Eurasian and African plates and the westward migration of the Alborán lithospheric domain, from Early-Middle Eocene to Early Miocene times (Fig. 1.6) (Andrieux J. 1971; Dewey et al. 1989; Platt et al. 2013). The Betic Cordillera is composed mainly of three stacked metamorphic nappe complexes, which are (from bottom to top): the Nevado-Filábride, the Alpujárride and the Maláguide (Tubia et al. 1992).

1.4.1 The Maláguide Complex

The Malaguide Complex is the highest part of the internal domains of the Betic Cordillera (Blumenthal 1930; Egeler and Simon 1969; Foucault 1971). It is made of Early Paleozoic to Eocene rocks and shows very low-grade metamorphism of Variscan age (Martin-Algarra et al. 2000). Discordance is observed between carboniferous formations and overlying Permo-Triassic layers. Below the discordance, rocks are affected by a very low grade metamorphism and several deformation structures. The absence of these deformation structures and metamorphism grade in the units postdating the discordance is attributed to the fact of the substratum is of a Hercynian age.

1.4.2 The Alpujarrides Complex and the Jubrique Unit

The Alpujarride units are typically constituted by, from top to bottom: Triassic carbonates, Permo-Triassic phyllites and quartzites (these lithologies constitute the post-Variscan sedimentary cover, e.g. (Martín 1987), and a pre-Mesozoic crystalline basement made of graphitic mica schists, gneisses and migmatites (e.g. Egeler and Simon 1969).

The metamorphic grade of the Alpujárride units increases from east to west in the orogen, such that in the western Betics, granulitic migmatites occur at the base of the sequence and appear spatially associated with slices of subcontinental mantle peridotites (i.e. the Ronda peridotites; Lundeen 1978; Obata 1980; Van der Wal and Vissers 1996;

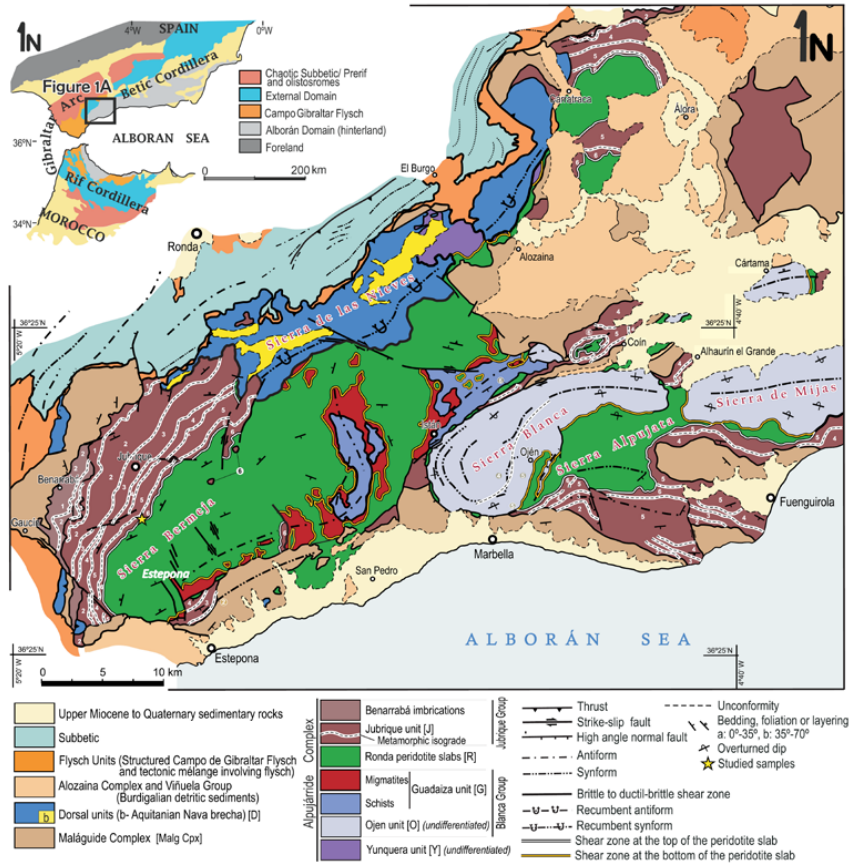


Figure 1.6. Geologic map of the Betic-Rif orogen (a) and the Western Betic Cordillera (b) (modified from Balanyá 1997; including data from Mart ín-Algarra 1987; Sanz de Galdeano and Andreo 1995; Mazzoli and Martín-Algarra 2011; Tubía et al. 2013), showing the location of the Jubrique unit and the studied samples.

Garrido et al. 2011; Précigout et al. 2013). Thus, in the vicinity of the Ronda peridotites, crustal rocks show systematically the highest metamorphic grade and extensive melting (Acosta-Vigil et al. 2001; Acosta-Vigil et al. 2014; Argles et al. 1999; Balanyá et al. 1997; Barich et al. 2014; Loomis 1972; Platt et al. 2003b; Torres-Roldán 1981; Torres-Roldán 1983; Tubía et al. 2013; Tubia et al. 1997).

The Alpujarride complex in the area of study is divided into two major tectonic units: the Jubrique unit, located on top of the peridotite massifs and constituting the highest Alpujarride unit below the Malaguide complex, and Blanca unit (composed of the Ojen and Guadaiza units) laying underneath the peridotite massifs (Balanyá et al. 1997; Tubia et al. 1997; Tubia et al. 1992). Metamorphism and deformation recorded

by Alpujarride rocks have been attributed to the Alpine crustal thickening of the Alborán domain during orogenic accretion (e.g. Platt et al. 2013 and references therein).

1.4.2.1 Structure and deformation

The imbricated stack of units that is observed at present is due to a contractional event that folded and thrust the original Alpujarride slab during the late metamorphic stages. The units show a top-to-the-N sense of displacements (Simancas and Campos 1993), a penetrative crenulation foliation (S1) generated by metamorphic recrystallization mainly at contact between units, and folding of older isotherms. Other authors however consider that the current structure of the Alpujarride complex in its central and oriental part in the Betic Cordillera is composed of a series of allochthonous units separated by a normal fault (García-Dueñas et al. 1992; Martínez-Martínez and Azañón 1997). Rocks are affected by a penetrative foliation parallel to the lithological contacts. This foliation postdates the medium-to-high-pressure mineral assemblage and is only present at folds hinges (P2). It predates a later low-pressure assemblage and is thought to be associated with pervasive ductile thinning of the Alpine orogenic pile, producing the contracting of the medium-to-high-pressure isotherms and associated apparently high thermal gradients (Azañón and Goffé 1997; Balanyá et al. 1997; Platt et al. 2003a; Torres-Roldán 1981).

The contact between Jubrique gneisses and Ronda peridotites is fragile and superimposed to a previous high temperature ductile shear zone (Balanyá et al. 1997; Loomis 1975; Loomis 1972; Torres-Roldán 1981). This contact is parallel to the mylonitic foliation of the crustal rocks (Balanyá et al. 1997; Lundeen 1978).

1.4.2.2 Metamorphism

Rocks in most of the Alpujarride units record nearly isothermal decompression P–T paths from medium-high- to low-pressure conditions (e.g. Azañón and Goffé 1997; García-Casco and Torres-Roldán 1996; Goffé et al. 1989; Torres-Roldán 1981; Tubia and Gil Iburguchi 1991).

In the thinned section of Los Reales (5 km-thick), carbonates and phyllites are at the top record pressures of 0.7–0.8 GPa, at 200–350 °C, followed by greenschist and amphibolite-facies schists towards the middle, and granulite-facies felsic gneisses at the bottom that record pressures up to 1.3–1.4 GPa, at 700–800 °C (Platt et al. 2003a; Torres-Roldán 1981).

1.4.3 The Ronda Peridotite Massif

The Ronda peridotite (Betic Cordillera, southern Spain) is the largest exposure of subcontinental mantle peridotite worldwide (Obata 1980). The Ronda peridotites belong to the internal zone of the Betic Cordillera in southern Spain. The Ronda peridotites and its thin overlying crustal sequence (Jubrique unit; Balanyá et al. 1997) belong to the upper part of the Alpujárride complex (“Los Reales” nappe; Tubia et al. 1992), which comprises three peridotite massifs: the Carratraca massif, the Ojen massif and the Ronda massif, which is the largest one. In this memoir, we will refer to the Sierra Bermeja massif as Ronda peridotite.

The western part of the Ronda massif is composed of four tectonic domains (Obata 1980; Van der Wal and Vissers 1996; Van der Wal and Vissers 1993) from south to north: Plagioclase (Pl)- bearing peridotite, granular peridotite, Spinel (Spl)- bearing tectonite and Garnet (Grt)/Spinel-bearing mylonite. The Ronda massif has suffered a first deformation stage marked by an almost adiabatic decompression (Frey et al. 1985), likely during the Jurassic Thetyan opening (Pearson et al. 1993; Van der Wal and Vissers 1993), which unroofed the massif from high depths to a thickened lower crust depth (~70 km) and produced graphitized diamonds (Davies et al. 1993; Garrido et al 2011).

P-T paths models (Garrido et al. 2011) suggest that the Ronda massif underwent at least three tectonic events during the Cenozoic period. The first was a decompression event due to an extensive stage (Balanyá et al. 1993; Balanyá et al. 1997; Obata 1980) that formed the spinel tectonite domain and the garnet-spinel mylonites; Lu-Hf cooling ages in Cpx-Grt pairs, with blocking temperature of ca. 800 °C, in garnet pyroxenite in the Beni Bousera yielded ages of 24 ± 3 Ma (Pearson and Nowell 2004). This closure age implies that Grt-Sp mylonites formed in the Oligocene by decompression and cooling from high-P and high-T primary conditions (Garrido et al. 2011). This was followed by a rapid uplift of asthenosphere, which induces partial melting of the lithospheric mantle and produces the granular peridotite bounded by a recrystallization front (Lenoir et al. 2001; Van der Wal and Vissers 1996). Finally, a compressive stage (Tubía et al. 2004; Hidas et al. 2013) caused the emplacement of the peridotite domain into the crust, and the formation of the plagioclase tectonite domain (Van der Wal and Vissers 1993, 1996; Hidas et al. 2013). The peridotite massif is intruded by acid dykes related to this compressive stage and dated at ca. 22 Ma (Esteban et al. 2011; Priem et

al. 1979; Sánchez-Rodríguez 1998). These dykes indicate that the end of the ductile deformation of the Ronda area occur approximately at 22 Ma.

2 Aims and Structure of the Thesis

Anatexis plays an important role in the reworking of the continental crust. Despite the numerous studies on crustal anatexis, the limitations of field, experimental and thermodynamic studies, in combination with the high deformation shown in many migmatitic terranes raise many challenges for petrologists as for the reconstruction of the anatectic process including the age of melting and the primary composition of anatectic melts.

2.1 Background and Problem Statement

As mentioned previously, volatile nature of melts prevents them from stabilizing at high depths; therefore they travel horizontally and vertically in the crust following the tectonic settings. This prevents the melt from keeping its original composition, especially if mixing with other fluids during its traveling. Deep crustal rocks that generated the melt either retain it as leucosome bands (migmatization) or completely lose melt in its matrix (e.g. strong mylonitization), becoming residual (restitic) rocks. For both cases, it becomes impossible to retrieve the original composition of the melt fractions. Studying melt inclusions in garnets offers a new possibility to study melt segregation in the deep crust even when the latter has endured a complex geodynamic history.

On the other hand, the problematic of relating age to metamorphism and anatexis is present in most of the published petro-chronological studies. While accessory minerals such as zircon and monazite can provide a high precision dating through U-Pb decay systems, it is difficult to successfully relate them to primary mineral assemblages in the rock. Thus, part of petrogenesis history of the rock remains unknown or poorly known. Garnet, however, is a major mineral that potentially provides at the same time ages (Lu-Hf, Sm-Nd) and P-T conditions of a rock.

The Jubrique unit is the case of a middle-lower crustal sequence that has endured a complex metamorphic and tectonic history. Its occurrence on the top of the Ronda peridotite massif has opened the way to several speculations as for the origin and age of its metamorphism and of the migmatization observed in the rocks at its contact with the

mantle. So far, studies have failed to determine in details the relationship between the high grade metamorphism and partial melting that has affected the Jubrique sequence and the mantle emplacement episode into the crust, and its regional implications.

2.2 Aims of the Thesis

This thesis aims to shed light on the processes of anatexis and age of a reworked lower continental crust. The Jubrique crustal sequence offers a unique opportunity to study continental crust evolution in the Alpujarrides complex (Betic Cordillera, Southern Spain). In order to investigate the process of anatexis in the lower continental crust of the Jubrique unit, I will combine detailed petrological study of the lithological sequence of the Jubrique unit including bulk and mineral major, trace analyses, with a detailed geochemical and experimental work on garnets in order to characterize on one hand the petrology and geochemistry of melt inclusions, and to perform Lu-Hf isotopic dating in the host mineral using state-of-the-art laboratory and instrumental techniques. The combination of petrographic and geochemical characterization of garnet-hosted MI and the Lu-Hf isotopic dating in MI-bearing garnets will allow us to link directly between the petrogenesis of garnets —and consequently major mineral assemblages— the age of high grade metamorphism and partial melting that occurred in these rocks. Its importance regionally will consist in reconstructing regionally thermal events that affected the lower crust and thus, situating in space and time the common evolution of the crust and the mantle in the Alpujarrides complex.

2.3 Outline of the Thesis

This Thesis memoir is divided into four parts. **Part I—Introduction, Aims & Thesis Structure and Methodology**, is subdivided in three chapters. In **Chapter 1—Introduction**, I provide some introductory notions to acquaint the reader with the main subject of the Thesis gaining a better grasp of the aims and motivation behind this work. It includes a summary of the basic notions of the continental crust structure and composition with an emphasis on the lower crust and partial melting processes. I also introduce the study of melt inclusions and nanogranites as a novel approach to investigate crustal anatexis. In the current chapter, **Chapter 2—Aims & Structure of the Thesis**, I present the main objectives and motivation of the Thesis and its structure. This section is followed by the description of the **Methodology in Chapter 3**. This

chapter summarizes the multidisciplinary approaches and the state-of-the-art instrumental analytical techniques and methodologies that I have used during my Thesis' research and that have provided a novel database to study melt inclusions in high-pressure migmatitic terrains. These approaches not only include the geochemical and cutting-edge instrumental techniques used (e.g. EDS-FEG-SEM, EPMA, LA-, MC-ICP-MS, NanoSIMS), but also the description of the experimental techniques using piston cylinder apparatus, and advanced geochronological methods based on the Lu-Hf isotopic system.

In **Part II—Results**, I present the main results of my Ph.D. Thesis, which are presented in four Chapters. In **Chapter 4**, I describe a new occurrence of melt inclusions (MI) in the granulitic gneisses of Jubrique, and their microstructural and petrological evolution along this migmatitic metamorphic sequence. This study sheds new lights on the nature of the anatectic processes that affected these strongly deformed and polymetamorphic rocks. The results of this chapter have been published in “Lithos”¹ —a journal ranked first in Mineralogy in the ISI-JCR— and have been presented in several international conferences such as the 2013 Goldschmidt Conference (Florence, Italy), and the 2013 Annual Meeting of the Geological Society of America (Denver, Colorado, USA). In **Chapter 5**, I present the experimental study of nanogranites from the gneisses of Jubrique, and the subsequent analysis of the major element compositions of experimental glasses. This study constitutes an effort towards building up the database of MI compositions, and towards the understanding of the significance and potential of the composition of MI from anatectic terrains, as well as their primary composition including volatile elements. The results of this chapter are part of a manuscript submitted to the JCR journal “Contributions to Mineralogy and Petrology”, which was accepted for publication pending corrections. The results of this chapter have been presented in international meetings such as the 2014 annual meeting of the European Geological Union (Vienna, Austria), and will be presented in the 2015 AGU Fall Meeting (San Francisco, CA, USA). The experimental part of this work has been carried out in collaboration with Earth Science Department of the University of Padova (Dr. Bernado Cesare y Dr. Omar Baroli) and the University of Milan (Dr.

¹ Barich, A., A. Acosta-Vigil, C. J. Garrido, B. Cesare, L. Tajčmanová, and O. Bartoli (2014), Microstructures and petrology of melt inclusions in the anatectic sequence of Jubrique (Betic Cordillera, S Spain): Implications for crustal anatexis, *Lithos*, 206–207(0), 303-320. doi: <http://dx.doi.org/10.1016/j.lithos.2014.08.003>.

Stefano Poli) during a short research secondment. In **Chapter 6**, I present the geochronology of garnet formation in the gneisses sequence of Jubrique and in garnet pyroxenites from the underlying Ronda peridotite using the Lu-Hf decay system. The analyzed crustal garnets are MI-bearing, their size allowed us to analyze them texturally and therefore to document ages of melting during the different stages of garnet growth. This research has been possible thanks to the collaboration with Dr. Robert Anczkiewicz of the Geological Institute in Krakow (Polish Academy of Sciences) during two short stays fellowships that took place respectively from 01/04/2014 to 30/06/2014 and from 01/04/2015 to 30/06/2015 and that were funded by the “Ministerio de Economía y Competitividad” (MINECO). The results of this chapter will be submitted to the JCR journal “Tectonics”.

Finally, **Part III—Conclusions** contains the main conclusion of my Thesis (**Chapter 7**), and **Part IV—References** presents the references and bibliography used in this Thesis (**Chapter 8**).

3 Methodology

3.1 Sampling and Sample Preparation

3.1.1 Sampling

Sampling was achieved along the whole crustal sequence of Jubrique on the top of the Sierra Bermeja peridotites massif. A total of 91 samples from different crustal lithologies including granulites (22), gneisses (14), schists (30), leucocratic material (20), quartzites (2), phyllites (3), were collected along the sequence. The minimum amount of material collected in the field for chemical analyses was about 8 to 10 kg per sample. Samples were selected on the basis of the absence of alteration at the outcrop and on their representativeness in terms of their macroscopic texture and modal composition. After petrographic study, only a few samples were selected for the detailed study of MI (cf. Chap. 4 and 5) and Lu-Hf geochronology (Chap. 6).

3.1.2 Preparation of Rock Thin and Thick Sections

All samples collected from the Jubrique sequence were cut into slabs with a diamond saw (Instituto Andaluz de Ciencias de la Tierra, UGR-CSIC, Spain). In each slab, one of several chips representative of the main textural and compositional features of the sampled lithologies were marked and cut. Thin section chips were grinded and then polished using 3 μm diamond grit using Buehler™ polishing pads, and then glued onto a 26x46 mm size thin-section glass with two-component petrological epoxy. Mounted thick sections were cut with a slow speed, high precision diamond saw to obtain ca. 80-100 μm thick section. The thick sections were subsequently grinded and polished using Buehler™ polysynthetic diamond at 3 and 1 μm grit steps; if necessary they were further polished using a 0.25 μm diamond grit step.

A total of 60 thin sections were used for petrographic study via conventional optical microscope (Instituto Andaluz de Ciencias de la Tierra) of all lithologies that constitute the Jubrique sequence.

3.1.3 Preparation of Whole-Rock Powders

For bulk rock chemical analysis, 5 to 10 kg samples were collected. The size of the samples depended on its grain size. After removal of altered surfaces using a diamond saw, the samples were cut into 3-4 cm cubic chips then were washed in water using an ultrasonic bath during 15 minutes. Once dried, chips were crushed and milled using a crusher with hardened still jaws and an agate ring mill, respectively in the petrology laboratory of the Instituto Andaluz de Ciencias de la Tierra. Representative samples of crushates for powdering were obtained using a riffle-splitter. The crushate was stored for subsequent mineral separation.

Powders with a grain size $\leq 2 \mu\text{m}$ were subsequently obtained for chemical analysis. Milling duration depended on the rock type and lithology. To avoid contamination between samples, the ring mills were cleaned using compressed air and alcohol after each sample.

3.2 Instrumental Analytical Techniques

3.2.1 Bulk Rock analyses: Energy Dispersive X-Ray Fluorescence (XRF)

Bulk rock major element analyses were conducted by X-Ray fluorescence spectrometry at the Instituto Andaluz de Ciencias de la Tierra, using a Bruker AXS S4 Pioneer instrument. The analyses were done on glass beads made by fusing the rock powder mixed with $\text{Li}_2\text{B}_4\text{O}_7$. The analytical detection limit and instrumental error were 0.1 % and $< 1 \%$, respectively.

3.2.2 Micro-analytical Spectroscopy Instrumental Analysis

3.2.2.1 Scanning Electron Microscopy (SEM)

The scanning electron microscope uses a focused beam of high-energy electrons to generate a variety of signals at the surface of solid specimens (Fig. 3.2). The signals, which derive from electron-sample interactions, show information about the sample including external morphology (texture), chemical composition, and crystalline structure and orientation of materials making up the sample. In most applications, data are collected over a selected area of the surface of the sample, and a 2-dimensional image is generated, which displays spatial variations in these properties. Areas ranging from approximately 1 cm to 5 microns in width can be imaged in a scanning mode

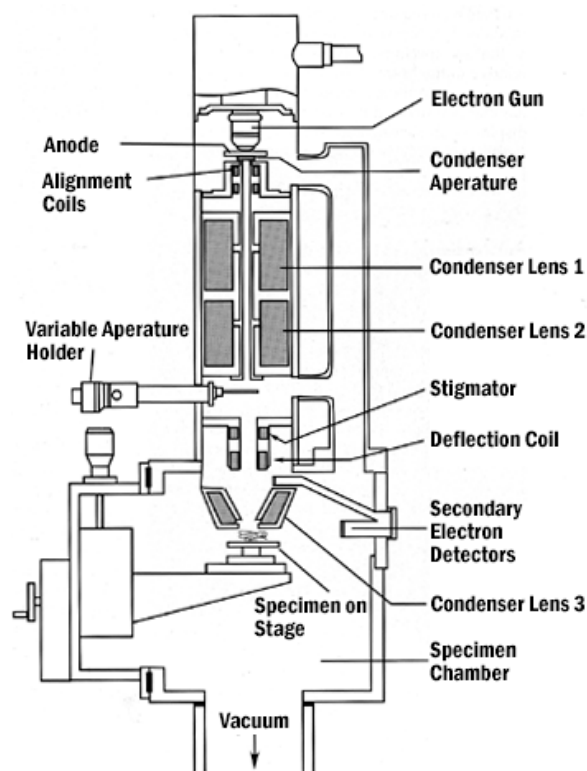


Figure 3.1. Schematic cartoon of a Scanning Electron Microscope (SEM). (image source: webpage of The University of Iowa <http://cmrf.research.uiowa.edu/scanning-electron-microscopy>.)

using conventional SEM techniques (magnification ranging from 20x to approximately 30,000x, spatial resolution of 50 to 100 nm) (Goldstein 2003). The SEM is also capable of performing analyses of selected point locations on the sample; this approach is especially useful in qualitatively or semi-quantitatively determining chemical compositions (using EDS), crystalline structure, and crystal orientations (using EBSD).

Scanning electron microscope (SEM) observations were performed by secondary and back-scattered electron imaging in carbon-coated, polished, thin sections, using LEO 1430-VP equipped with energy dispersive spectrometer (EDS) at the Centro de Instrumentación Científica (UGR, Granada, Spain; <http://cic.ugr.es>). EDS silicate inclusions (e.g. Melt Inclusions in Part 2) were identified using EDS spectrums and 2048x1886 pixel images under an acceleration voltage of 20 kV, a beam current of 20 nA, and a sample distance of 10 mm. Cathodoluminescent imaging was also performed to characterize accessory minerals and particularly zircons.

An energy dispersive detector is used to split the characteristic X-Rays of different elements into an energy spectrum, and EDS system with a given software is used to evaluate the energy spectrum in order to determine the abundance of specific elements. EDS can be used to find the chemical composition of materials down to a spot size of a few microns, and to create element composition maps. An EDS detector contains a crystal that absorbs the energy of incoming X-Rays by ionization, yielding free electrons in the crystal that become conductive and produce an electrical charge bias (Goldstein 2003). The X-Ray absorption thus converts the energy of individual X-Rays into electrical voltages of proportional size; the electrical pulses correspond to the characteristic X-Rays of the element (Fig. 3.1).

Microstructures of MI in non-coated thin sections were characterized using conventional microscope petrography and a QUANTA 400 environmental Scanning Electron Microscope at the Centro de Instrumentación Científica (CIC), Universidad de Granada, equipped with EDAX EDS (ultrathin window) and Li(Si) detectors. Back-scattered electron imaging and semi-quantitative energy dispersive spectroscopy (EDS) of the analyzed remelted MI were carried out using a CAM Scan MX2500 Scanning Electron Microscope (SEM) equipped with LaB₆ cathode, at the Dipartimento di Geoscienze of the Università di Padova (Italy).

3.2.2.2 Electron Micro-Probe Analysis (EMPA)

An electron probe microanalyzer is a microbeam instrument used primarily for the in situ non-destructive chemical analysis of minute solid samples. It is fundamentally the same as an SEM, with the added capability of chemical analysis (Reed 1995; Reed 2005). The primary importance of an EPMA is the ability to acquire precise, quantitative elemental analyses at very small spot sizes (as little as 1-2 microns), primarily by wavelength dispersive spectroscopy (WDS). The spatial scale of analysis, combined with the ability to produce detailed images of the sample, makes it possible to analyze geological materials in situ and to resolve complex chemical variation within single phases (Fig. 3.2).

3.2.2.2.1 Fundamentals

An electron microprobe runs under the principle that if an accelerated and focused electron beam attacks a solid material, the incident electron beam has sufficient energy

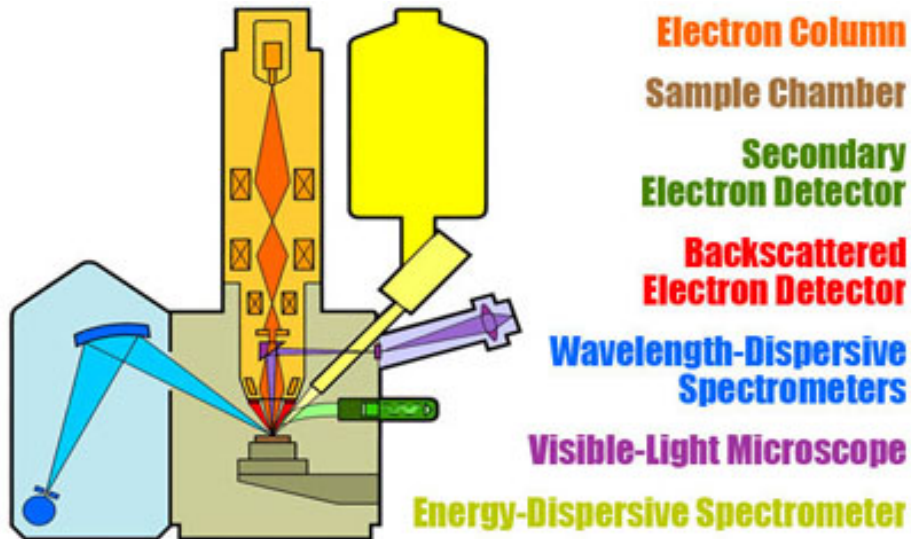


Figure 3.2. Schematic diagram of a typical microprobe (after John Goodge; source: http://serc.carleton.edu/research_education/geochemsheets/techniques/EPMA.html)

to release both matter and energy from the sample. These electron-sample interactions principally liberate heat, but they also yield both derivative electrons and X-Rays. Of most common interest in the analysis of geological materials are secondary and back-scattered electrons, which are practical for imaging a surface or obtaining an average composition of the material. X-Ray generation is produced by inelastic collisions of the incident electrons with electrons in the inner shells of atoms in the sample; when an inner-shell electron is ejected from its orbit, leaving a vacancy, a higher-shell electron falls into this vacancy and must shed some energy (as an X-Ray) to do so (Reed 2005). These quantized X-Rays are characteristic of the element. EPMA analysis is considered to be non-destructive; that is, X-Rays generated by electron interactions do not lead to volume loss of the sample, so it is possible to re-analyze the same materials more than one time.

EPMA consists of four major components that, from top to bottom, are (Reed 2005): (i) an electron source, regularly a W-filament cathode referred to as a ‘gun’; (ii) a series of electromagnetic lenses located in the column of the instrument, used to condense and focus the electron beam emanating from the source; this comprises the electron optics and operates in an analogous way to light optics; (iii) a sample chamber, with movable sample stage (x, y, z), that is under a vacuum to prevent gas and vapor

molecules from interfering with the electron beam on its way to the sample; a light microscope allows for direct optical observation of the sample; and (iv) a variety of detectors arranged around the sample chamber that are used to collect X-Rays and electrons emitted from the sample.

3.2.2.2.2 *Major element analyses*

Major element composition of minerals was obtained in ca. 30 μm thick thin sections, using a Cameca SX100 electron microprobe at the CIC. Natural and synthetic silicate oxides were used for calibration and ZAF correction was applied.

The major element composition of glass in remelted MI was analyzed with Jeol JXA 8200 and Cameca SX-50 Electron Microprobes (EMP) at the Dipartimento di Scienze della Terra (Università di Milano) and Dipartimento di Geoscienze (Università di Padova), respectively. To minimize alkali loss and changes in major elemental ratios, two analytical conditions were used as recommended by Morgan and London (2005); Morgan and London (1996). Sodium, K, Al and Si were analyzed first (and concurrently in the case of the Jeol JXA 8200), using a beam current and beam diameter of 2 nA and 1 μm , respectively, and accelerating voltages of 15 kV (Jeol JXA 8200) or 20 kV (Cameca SX-50). The elements Fe, Mn, Mg, Ti, Ca, P, F and Cl were analyzed afterwards with 15-kV, 20-nA, 1- μm (Jeol JXA 8200) or 20-kV, 20-nA, 1- μm (Cameca SX-50) beams. Counting times were 10 s on peak for all elements (except Fe, Mg and F with 20 s), and 10 s (Cameca SX-50) or 2 s (Jeol JXA 8200) on background. Matrix reduction used the PAP correction algorithm (Pouchou and Pichoir 1985). Analyses were corrected using anhydrous and hydrated haplogranite glasses of known composition as secondary standards (Morgan and London 2005). The standards were analyzed at the start and end of each analytical session using similar working conditions. Sodium loss was estimated as $\approx 20\%$ relative during these analyses. Initial estimates of water concentrations in glass were calculated by the difference of electron microprobe totals from 100%. Morgan and London (1996) and Acosta-Vigil et al. (2003) showed that using the above analytical methods on granitic glasses, the accuracy of H_2O by difference is better than $\pm 10\%$ relative for H_2O concentrations in the range of 2-10 wt%.

3.2.2.3 *Nanoscale Secondary Ion Mass Spectrometry (NanoSIMS)*

3.2.2.3.1 *Fundamentals*

Secondary Ion Mass Spectrometry (SIMS) (Richards et al. 2002) is an ion microprobe technology linking high-resolution microscopy with isotopic analysis, providing spatially resolved information on the molecular and isotopic compositions of materials (Pacholski and Winograd 1999). The basis for the technique was introduced in the 1960s by Castaing and Slodzian (1962), and two types of SIMS are available, defined as static and dynamic. Static SIMS is typically used to attain molecular and fine surface information (less than 1 nm depth) whereas dynamic SIMS is routinely used to acquire elemental and isotopic information from the upper few nm of the sample (for further details see Pacholski and Winograd, 1999; Adams et al. 2005). The Cameca® NanoSIMS-50s (Slodzian et al. 1992) currently represents the latest generation of ion microprobes designed for dynamic SIMS.

NanoSIMS is a nanoscopic scale resolution chemical imaging mass spectrometer based on secondary ion mass spectrometry. It works based on a coaxial optical design of the ion gun and the secondary ion extraction and on an original magnetic sector mass spectrometer with multi-collection (Fig. 3.3). NanoSIMS analysis is a destructive process that involves continuous bombardment of a sample with an energetic ion beam (either a Cs⁺ or O primary beam to enhance negative or positive ion formation, respectively), which results in sputtering of the upper sample surface and the consequent liberation of secondary ions.

These secondary ions are sorted on the basis of their energy in the instrument's electrostatic sector before being dispersed in a mass spectrometer according to their mass-to-charge ratios. By acquiring a series of spatially referenced spectra, via a raster-scanning process, a map can be produced for nearly any selected atomic mass, and information of isotopic ratios in the form of regions-of-interest, line scans and depth profiles can be obtained. The system is maintained permanently under ultra-high vacuum to prevent atmospheric interference with primary and secondary ions (typically 10⁻¹⁰Torr in the analysis chamber).

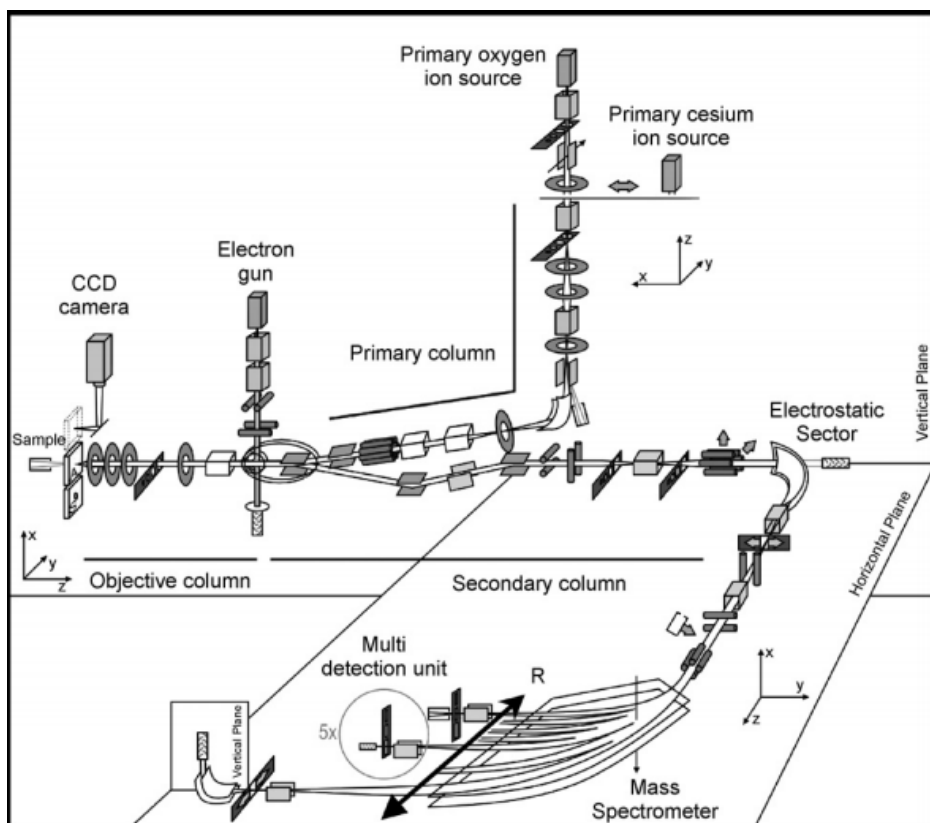


Figure 3.3. Schematics of Nano-SIMS Ion Optics. R $\frac{1}{4}$ Radius of the secondary ion trajectories (figure kindly provided by Frank J. Stadermann, Washington University, St. Louis, Missouri, <http://presolar.wustl.edu/nanosims/schematic.html>).

3.2.2.3.2 Analyses of melt inclusions

After a detailed optical and SEM investigation of the experimental run products to check for MI homogeneity and absence of cracks in the host garnets, we identified 26 remelted nanogranitoids within 8 garnet crystals appropriate to conduct a detailed determination of H₂O concentrations in experimental glasses. Analyses of H₂O were performed by Nano Secondary Ion Mass Spectrometry (NanoSIMS) using the Cameca NanoSIMS 50 at the Muséum National d'Histoire Naturelle of Paris.

Polished experimental capsules with MI exposed on the garnet surface and standard glasses were mounted in In to reduce H background in the analysis chamber (Aubaud et al. 2007). Melt inclusions were identified through images of $^{28}\text{Si}^-$, $^{39}\text{K}^{16}\text{O}^-$ and $^{56}\text{Fe}^{16}\text{O}^-$ secondary ions. For each of the analyses, we first performed a pre-

sputtering step on a $3 \times 3 \mu\text{m}^2$ surface area for 2 minutes with a 400 pA primary Cs^+ beam to remove the gold coating, surface contamination and to reach a steady state sputtering regime. Then a primary beam of 37 pA was used for data acquisition. Data were acquired by rastering a $3 \times 3 \mu\text{m}^2$ surface area and collecting only ions from the inner $1 \times 1 \mu\text{m}^2$ (beam blanking mode) to reduce surface contamination. Each analysis is a stack of 200 cycles, a cycle being 1.024 s long. $^{16}\text{OH}^-$ (used as a proxy for H_2O), $^{28}\text{Si}^-$, $^{39}\text{K}^{16}\text{O}^-$ and $^{56}\text{Fe}^{16}\text{O}^-$ were recorded simultaneously in multi-collection mode. We checked that the $^{16}\text{OH}^-/^{28}\text{Si}^-$ ratio was stable during MI analyses. Secondary ions were collected by electron multipliers with a dead time of 44 ns. Mass resolution was set to 8000 to resolve any mass interference on the selected ions. Several of the analyzed MI were large enough to conduct replicated analyses.

Three leucogranitic glasses with well-known H_2O concentrations, varying between ≈ 0 -7 wt%, were used for NanoSIMS calibration (Part II – Chapter 5): glass DL reported in (Acosta-Vigil et al. 2003) with $\text{H}_2\text{O}=6.5$ wt%; glass LGB1 from Behrens and Jantos (2001) with $\text{H}_2\text{O}=4.9$ wt% (uncertainties in these analyses are $\pm 13\%$ relative); and the almost anhydrous glass B from Morgan and London (2005) with $\text{H}_2\text{O}=300 \pm 42$ ppm. Data corrections using the aforementioned calibration, and error calculations, were performed using the R program (Graybill 1976). Although errors combine counting statistic and uncertainty of the calibration curve, the errors reported in Part II–Chapter 5 are dominated by the latter, which corresponds to a prediction interval at 68%. During the NanoSIMS sessions, the vacuum in the analysis chamber remained between 2.5 and 5×10^{-10} Torr. The detection limit for water was around 650 ppm.

The precise hydrogen concentrations of the three reference samples used in the calibration curve reported above were measured by Elastic Recoil Detection Analysis (ERDA). This method has been used as a reference for H determination in various materials, including geological samples with a large range of H_2O concentrations from several wt% to hundreds of ppm in nominally anhydrous minerals (Raepsaet et al. 2008; Aubaud et al. 2009; Bureau et al. 2009; Withers et al. 2012). Analyses were conducted at the Nuclear Microprobe of CEA Saclay (Khodja et al. 2001), using the 3.75 MV Van de Graaff single stage accelerator from HVEE which delivered a 3 MeV $^4\text{He}^+$ incident beam with a size of $12 \times 3 \mu\text{m}^2$ and a current of 950 pA, that impinged the target at a grazing angle of 15° . Ejected H atoms were collected in a silicon barrier detector placed at 30° from the incident beam and at 50 mm from the surface of the

sample, protected against the backscattered He ions by a 15 μm Al filter. Homogeneous regions of analysis, excluding cracks or bubbles in the glass, were selected by mapping the major components using Particle Induced X-Ray emission (PIXE) and backscattered helium ions spectroscopy (Rutherford Backscattering, RBS).

3.2.3 Mass Spectrometry Instrumental Techniques

3.2.4 Laser Ablation coupled with Inductively Coupled Plasma Source Mass Spectrometry (LA-ICP-MS)

In Laser Ablation Inductively Coupled Plasma Mass Spectrometry (LA-ICP-MS) the sample is directly analyzed by ablating with a pulsed laser beam (Fig. 3.4). In the latter, solid aerosols are transported into the core of inductively coupled argon plasma (ICP), which generates temperature of approximately 8000 $^{\circ}\text{C}$. The plasma in ICP-MS is used to generate ions that are afterward introduced to the mass analyzer. These ions are then separated and collected according to their mass to charge ratios. ICP-MS offers extremely high sensitivity to a wide range of elements. Depending on the analytical measurement system, very small amount of sample quantities may be sufficient for this technique. In addition, a focused laser beam allows spatial characterization of heterogeneity in solid samples, with typically micron resolution both in terms of lateral and depth conditions.

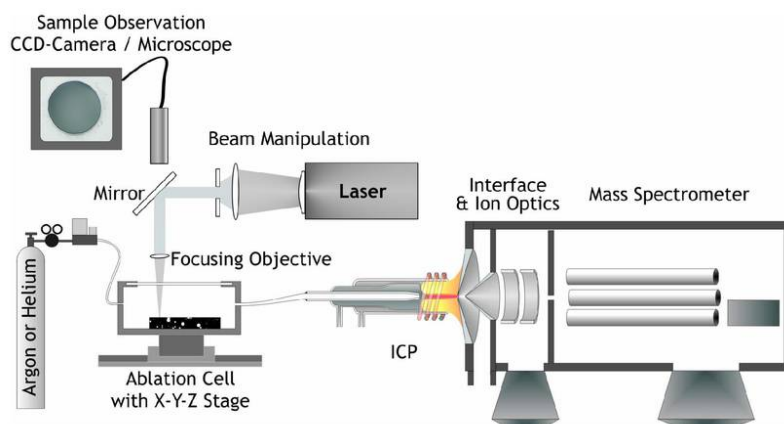


Figure 3.4. Schematic set-up of Laser Ablation Inductively Coupled Plasma Mass Spectrometer (LA-ICPMS) (after Günther and Hattendorf, 2005)

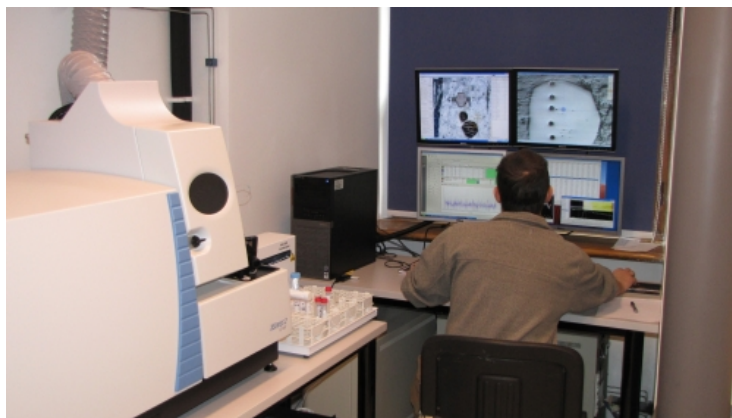
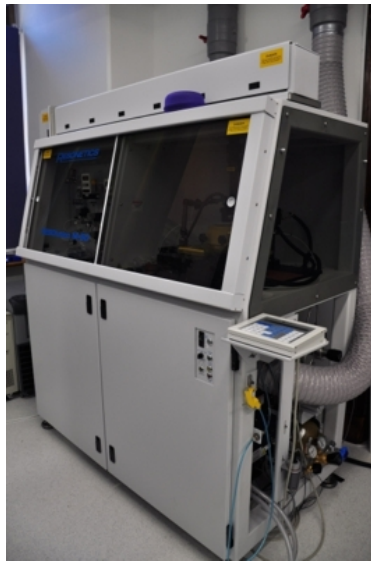


Figure 3.5. LA-ICP-MS Excimer laser of 193 nm (ArF) from Resonetics ® (upper image) coupled to an with quadrupole ICP mass spectrometer (lower image) and computer with Iolite software for data acquisition and reduction. Institute of Geological Sciences of Krakow, Polish Academy of Sciences, Poland (images sources: http://www.ing.pan.pl/Labs/Lab_GEO-IZO-GEO/Lab_Geo_Izo_04.htm).

Garnets from the mylonitic gneisses and porphyroblastic gneisses samples were at first subjected to trace element analyses by laser-ablation system RESolution M50 by Resonetics (Müller et al. 2009) coupled with quadrupole ICP-MS XSeries-II by Thermoelectron (Fig. 3.5). Spot size was 80 μm and the repetition rate 10 Hz. The ablation speed was of 5mm/s and the energy density of the laser beam was constant and homogeneous across the beam at 9 Jcm^{-2} for all analyses. Sample runs were bracketed

by measurements of NIST 612 glass using reference values of Jochum (2011). Silica content was used as internal standard.

3.2.5 Multicollector-ICP-MS: analyses of Lu-Hf isotopes in garnets

3.2.5.1 Separation of garnet cores and rims in thick sections

Using spatial distribution of Lu in the respective garnets, supported by the major elements profiles and the spatial distribution of inclusions in the garnets, a core-rim transition zoned was defined to proceed with the separation of garnet crystals.

Using a 2mm thick diamond saw, garnets cores and rims were cut out of the 1.5mm thick sections. Adhesive tape was used to avoid material loss and to stabilize the garnets during the cutting (Fig. 3.6). Samples cutting was made based on Lu profiles and according to the available garnet material, core and rims were subsequently separated in all samples except in the duplicate of sample JU18 (JU18-Grt2), where the garnet was too small to separate the two zones and was taken as one sample. In some other samples, according to the weight of the garnet material that should not exceed 0.1g per sample, pieces of the crystal were separated in several subsamples to keep the balance of the required quantity per analysis.



Figure 3.6. Cutting stage for the cutting and mechanical separation of garnet porphyroclasts and porphyroblasts and their cores/rims in thick sections. Diamond saw device (left), and a Jubrique garnet gneiss thick section ready to be cut for separation of garnet cores and rims from the gneiss matrix (right).

The following samples of gneisses were prepared for analyses. Sample JU08 is a typical mylonitic gneiss with stromatic metatextitic migmatite as described in Barich et

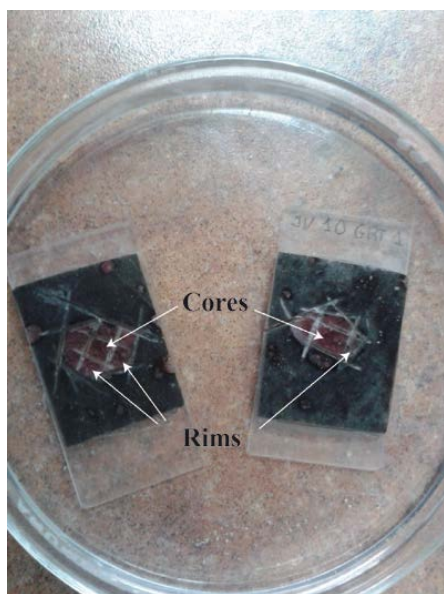


Figure 3.7. Thick section with the cuttings for separation of garnet cores and rims immersed in acetone in a Pétri box for the detachment of garnet parts for later digestion and dissolution.

al. 2014. It represents the closest sequence to the peridotite body. This sample in particular has been studied in details for melt inclusions occurrence and composition. Sample JU10 is the residual, highly deformed granulitic sequence of the Jubrique unit. It displays very fine dark matrix surrounding large garnet and kyanite porphyroclasts. Sample JU18 is the transition between the two types of gneisses in the sequence. Sample JU20 displays smaller garnet crystals opposed to an increase of biotite modal proportions, marking the complete transition to the upper levels of the gneiss sequence. Due to the small size of garnets, one out of two duplicates was considered for a whole

crystal cutting/crushing/analysis rather than a textural (core/rim) separation. Sample JU21 is a typical porphyroblastic gneiss with abundance of leucocratic veins and regular parallel layering (leucosome, paleosome, and mesosome).

3.2.5.2 Digestion and dissolution of samples

After laser ablation analysis and cutting of garnets, thick sections were then put in acetone to enable a good separation of the garnet pieces from the rest of the matrix (Fig. 3.7). After detaching garnet parts and weighing them, garnet fractions were recuperated and crushed in acetone by an agate mortar to $<50\mu\text{m}$ size. They were transferred into Teflon® beakers. They were rinsed by H_2O and leached using Sulfuric acid (ca. 96%). Prior to dissolution, garnet fractions were cleaned in ultrasonic bath of acetone and ethanol respectively, for 15 minutes each were subsequently washed lidless into 2ml of 2% HNO_3 (2%) on a 90°C plate for 30min, then evaporated to dryness. Between these steps, samples are rinsed by H_2O . Samples were then transferred into new beakers, and Sm-Nd and Lu-Hf spikes were added and evaporated.

Prior to dissolution, garnet samples were digested into a mixture of 3:1 HF-HNO₃ and left for two days on 120°C hot plate hosted in a HEPA-filtered laminar flow cabinet (Fig. 3.8). This step prevents fluorite formation and technically destroys silicate bonds.



Figure 3.8. Ultra-clean chemistry lab of the Institute of Geological Sciences in Krakow, Poland. (Top) Ultraclean lab with Picotrace® horizontal laminar flow cabinets; (middle) Graphite-Teflon hot plate with Savillex® beakers containing acid digested samples; (Bottom) Operator working with chromatographic columns for separation of Lu-Hf isotopes (top and bottom images from ; http://www.ing.pan.pl/Labs/Lab_GEO-IZO-GEO/Lab_Geo_Izo.htm).

Samples were then evaporated and 5-10 ml of 6NHCl:0.1HF was added to launch dissolution processes. They were left for 24 hours on 140°C hot plate then evaporated. Another 1-2ml of 6NHCl was added and immediately evaporated (Fig. 3.8).

3.2.5.3 Chromatography

Hf, Lu + Yb and light REE fractions were first separated on standard cation exchange columns (Fig. 3.9). Cleaning was achieved by using alternating 6N HCl and 6N HCl:1N HF. Final purification of Hf from other HFSE took place on a Lnspec® column. This Hf purification completely eliminates Lu and Yb interferences on ¹⁷⁶Hf. Sm and Nd were separated on a smaller size Lnspec® column (Fig. 3.9). The column was cleaned with 6N HCl and the sample loaded and eluted in 3N HCl. This method eliminates all interfering elements and also allows reduction of the Yb/Lu ratio to about 1:1 (Fig. 3.9).

3.2.5.4 Instrumental analysis

Lu-Hf isotope dilution analyses were conducted in the same laboratory using MC-ICP-MS Neptune (Fig. 3.9). Sample consumption was 10–80 ng for a static multi-collector analysis and 40–200 ng for a

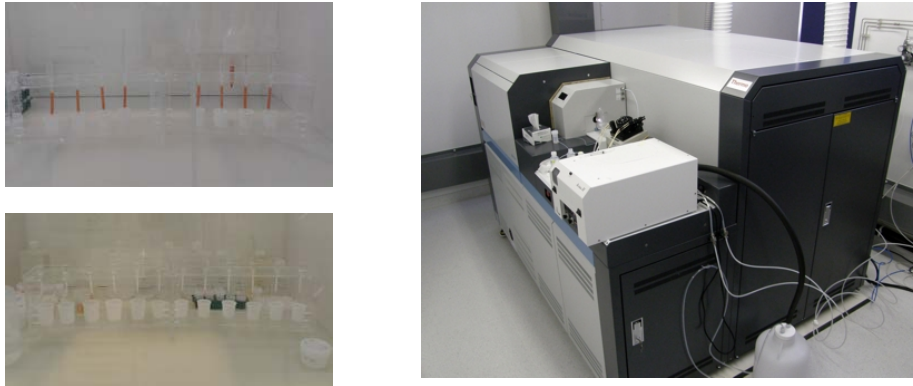


Figure 3.9. (left column images) Chromatographic columns: cation chromatographic columns (upper image) and anion chromatographic columns; (right image) Thermo-Fininningan Neptune II Multicollector-ICP-MS (MC-ICP-MS) at the Institute of Geological Sciences of Krakow, Poland (image source: http://www.ing.pan.pl/Labs/Lab_GEO-IZO-GEO/Lab_Geo_Izo_01.htm).

multi-dynamic analysis. Between samples the inlet system was cleaned with 5% HNO₃ followed by 5% HNO₃–5% HF after Hf analysis, which always extracted much more Hf from the inlet system. Subsequently, 2% HNO₃ was aspirated and used to measure on-peak zeroes (OPZ) for Nd or Yb, while 2% HNO₃–0.1% HF was used for Hf. Age and ¹⁷⁶Hf/¹⁷⁷Hf initial ratio calculations were conducted by Isoplot 4.15 (Ludwig 2008).

3.3 Experimental Techniques for the Remelting of Melt Inclusions

3.3.1 Sample preparation

Doubly polished ≈ 200-300 μm- and ≈ 3 mm-thick sections were used to obtain single MI-bearing garnet chips (≈ 2x2 mm) and fragments (up to ≈ 4x4 mm) containing complete and, except for the potential presence of late fractures affecting garnet, totally sealed MI. Remelted nanogranitoids come from four different thick sections of sample JU-8, from which several garnet crystals were selected. Garnet chips were separated by cutting manually under a binocular microscope. To investigate potential variations of MI composition with microstructural location, fragments of Garnet were collected from three different microstructural positions, including cores of large (≈6 mm) garnets, rims of large garnets, and small (≈1-2 mm) single garnets.

3.3.2 Piston-cylinder experiments

Remelting experiments of MI contained within fragments of garnet followed the methodology described by Bartoli et al. (2013), and were conducted using a single-stage, piston-cylinder apparatus (Fig. 3.10) at the Laboratory of Experimental Petrology, Dipartimento di Scienze della Terra (Università di Milano, Italy). Chips and fragments of garnets were loaded into Au capsules with external diameter of 3 mm and 5 mm, respectively, together with powdered silica to isolate garnet pieces from each other. No water was added to the capsules (Fig. 3.11), which were crimped and sealed by arc welding. We conducted four experiments (AB1 to AB4), each of them containing either three 3 mm capsules or one 5 mm capsule embedded in a low friction, 22 mm assembly composed of MgO-salts, a graphite heater and a NaCl sleeve. Capsules were accommodated within the crushable MgO-salt and a thermocouple was positioned above the samples at about the mid-point of the furnace assembly. Experiments were run for 24 hours at a constant pressure of 1.5 GPa and at temperatures of 850, 825 or 800 °C. The temperature range was chosen based on previous thermobarometric



Figure 3.10. Piston cylinder apparatus used for remelting experiments of partially crystallized and nanogranite inclusions (source: Bartoli, 2012)

estimates of peak and post-peak metamorphic conditions (Argles et al. 1999; Barich et al. 2014; Loomis 1972; Platt et al. 2003; Torres-Roldán 1981), whereas the temperature sequence (starting with 850 °C and continuing down to 825 °C and 800 °C) was dictated by the experimental results. Capsules after experiments (Fig. 3.11) were mounted in Epoxy, cut with a slow-speed diamond saw, and polished for SEM, EPMA and NanoSIMS analyses.

We chose the highest pressure value obtained in most of the previous thermobarometric studies, 1.5 GPa, in order to maintain a pressure on the garnet fragments equal or larger than



Figure 3.11. Au capsules containing garnet chips with re-melted nanogranites after high-pressure and high-temperature experiments in the piston cylinder apparatus.

the internal pressure in the remelted MI, and therefore to prevent MI decrepitation and volatile loss upon heating. Temperature was controlled by K-type (chromel-alumel) thermocouples and is considered accurate to ± 5 °C (Ferri et al. 2009). Using a Johannes-type piston cylinder, pressure can be directly measured by a load cell built into the frame (Johannes 1973) and is considered to be accurate to ± 0.03 GPa (Molina and Poli 2000). During each run, pressure was first increased to 1.5 GPa and then the assembly was isobarically heated at a constant heating rate (≈ 50 °C/min) until the target temperature was reached. After 24 h of run time, experiments were quenched isobarically by turning off power to the heater, at a rate of ≈ 50 °C/sec down to ≈ 50 °C. The confining pressure was released after quenching. Capsules were mounted in epoxy, and the inclusions in the garnet were exposed gradually by manual polishing, using first 4000- to 80- μm grits sizes, and 5- and 1- μm diamond suspensions for the final polishing stage.

Part II

Results

4 Microstructures and Petrology of Melt Inclusions in the Anatectic Sequence of Jubrique (Betic Cordillera, S Spain): Implications for Crustal Anatexis ¹

4.1 Introduction

Melt inclusions (MI) are small droplets of liquid, commonly a few to tens of micrometers across, trapped by minerals that grow in the presence of melt. They were first described by Sorby (1858) in igneous rocks, where they constitute a wealth of information on melt chemistry (e.g. (Gurenko et al. 2005; Wanless et al. 2014; Webster et al. 1997)). Many of the assumptions concerning the interpretation of fluid inclusions (FI) have been applied to MI (Bodnar and Student 2006; Roedder 1984; Sorby 1858). More recently, MI have also been reported in crustal crystalline rocks (Cesare et al. 1997) (Hwanga et al. 2001; Stöckhert 2001). Most melting reactions during crustal anatexis are incongruent (e.g. (Clemens 2006)), i.e. produce melt and peritectic minerals, providing the opportunity that these minerals trap inclusions of the coexisting silicate liquid. Hence, MI trapped during melting can supply the composition of the primary anatectic melt (Cesare et al. 2009; Cesare and Gomez-Pugnaire 2001), in contrast with MI trapped during crystallization of cooling igneous rocks that provide the composition of fractionated (as opposed to primary) melts (Thomas and Davidson 2013; Webster et al. 1997); see also discussion in Bartoli et al. (2014).

Most MI in anatectic terranes appear partially or totally crystallized due to slow cooling at depth. Owing to the granitic phase assemblage made of micron to submicron quartz, feldspars and micas, crystallized MI have been named “nanogranites” (Cesare et al. 2009). With the recent development of in-situ and high spatial resolution micro-analytical techniques, as well as appropriate methods to melt and rehomogenize

¹ *This chapter has been published in the JCR Journal LITHOS.*

nanogranites (Bartoli et al. 2013a; Bartoli et al. 2014), it is possible to characterize precisely MI, in order to relate their information to the process of anatexis of the host rock. Hence MI represent a new and powerful method to study anatexis, primarily because they can provide information on the parental melt compositions produced at the source region of crustal granites, including concentrations of H₂O and fluid regimes (Bartoli et al. 2013b; Bartoli et al. 2014; Cesare et al. 2011; Ferrero et al. 2012). This information can complement, and in some cases be more precise, than that provided by classical petrological and geochemical studies of anatectic terrains, for instance regarding the composition of the primary anatectic melt, which has been traditionally approximated by the composition of anatectic leucosomes. This is particularly important in cases where deformation has partially or totally erased the primary anatectic macro- and micro-structures. In these cases, the presence of MI may be the only evidence remaining in the rock for the presence and nature of melt (Cesare et al. 2011).

The number of MI occurrences in anatectic terranes reported in the literature is quite modest and, among those cases, only a few provide bulk compositional data from the MI (Bartoli et al. 2013b; Cesare et al. 2011; Cesare et al. 2009; Ferrero et al. 2012). This is due to the relatively recent discovery of MI in crustal anatectic rocks (Cesare et al. 2011; Cesare et al. 2009; Cesare et al. 1997; Darling 2013; Gao et al. 2012; Hwanga et al. 2001; Korsakov and Hermann 2006; Liu et al. 2013; Stöckhert 2001; Stöckhert et al. 2009) and, more importantly, the very recent development of appropriate methodologies to recover the information encrypted within these former droplets of melt (Malaspina et al. 2006) (Bartoli et al. 2013a; Bartoli et al. 2013b; Bartoli et al. 2014; Perchuk et al. 2008).

We report the presence and microstructures of MI in metasedimentary granulite-facies gneisses of the Jubrique unit, located in contact, and structurally above, the Ronda peridotite slab, in the hinterland of the Betic Cordillera (S Spain) (Fig. 4.1). Jubrique constitutes a complete though strongly thinned section (≤ 5 km) of upper to middle-lower continental crust. The studied gneisses, located at the bottom of the sequence, are strongly deformed and show a complex polymetamorphic history (Loomis 1972; Torres-Roldán 1981). Hence, Jubrique provides an exceptional opportunity to study partial melting in complex regional polymetamorphic and strongly deformed rocks by using the new approach of the MI (Cesare et al. 2011; Cesare et al. 2009). In addition, crustal anatexis is a fundamental process that controls the differentiation of the

continental crust (Sawyer et al. 2011), and this quite continuous section of continental crust offers the opportunity to characterize partial melting of middle-to-lower crustal levels, and study its potential effects on the compositional segregation of the crust. We start in this contribution by describing in detail the microstructures and phase assemblages of the MI present throughout the entire sequence of gneisses, and discuss their bearing on the process of partial melting of the gneisses. The fundamental aims of this study consist of: (i) describing a new occurrence of MI in the granulitic gneisses of Jubrique, and their microstructural evolution along the prograde metamorphic sequence; and (ii) to shed light on the timing and nature of the anatexis processes that affected these strongly deformed and polymetamorphic rocks.

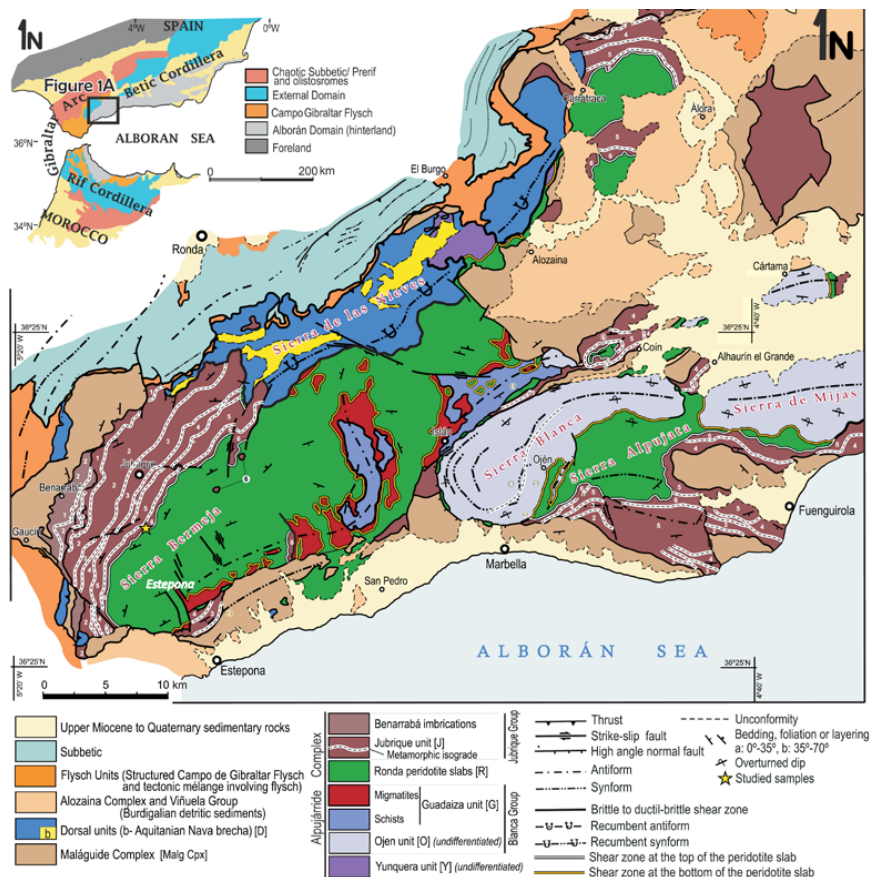


Figure 4.1. Geological maps of the Betic-Rif orogen and the studied area in the western Betic Cordillera of S Spain (modified from Balanyá et al., 1997; including data from Martín-Algarra, 1987; Sanz de Galdeano and Andreu, 1995; Mazzoli and Martín-Algarra, 2011; Tubía et al., 2013). The location of the studied sample JU-8 is shown as a yellow star.

4.2 Sampling, Petrography and Composition of Minerals

Most of the previous petrologic studies have divided the gneissic sequence of Jubrique into two major gneiss types, based either on the structures or mineral assemblages. Although structures, mineralogy and microstructures indicate that these rocks represent anatectic migmatites (see below), we have maintained the previous terminology of gneisses though have also provided the corresponding migmatitic terms. We have used field and petrographic criteria to distinguish two types of gneisses as well: (i) mylonitic gneisses at the bottom of the sequence and in contact with the underlying Ronda peridotites, and (ii) porphyroblastic gneisses on top of the mylonitic gneisses and right below the schists. Mylonitic gneisses constitute a $\approx 300\text{-}500$ m-thick sequence of rocks that, at the outcrop scale, appear as dark, Grt-rich rocks and rather massive rocks, except for the presence of frequent mm-to-cm Grt-bearing leucocratic bands that define a foliation and provides the rock with the appearance of a stromatic metatextitic migmatite (Fig. 4. 2a-b; see Sawyer (2008)) (mineral abbreviations are after Whitney and Evans (2010); except for silicate melt, Liq). This foliation is parallel to the contact with the peridotites. Leucocratic bands or leucosomes may occasionally reach up to several tens of cm in thickness and constitute tabular concordant Grt-rich leucocratic bodies (Fig. 2c); in this case, a foliation parallel to that affecting the host rock is clearly visible in the leucocratic bands at the outcrop scale. Some domains of the mylonitic gneisses are less affected by the deformation that produced the stromatic appearance, and appear to record a previous stage in the history of the rock, characterized by a dilatant structure (Fig. 4.2a; Sawyer (2008)). In these domains the proportion of leucosomes increases, appearing as mm-to-cm layers roughly parallel to the foliation, but also as veins or pods perpendicular to the foliation (Fig. 4.2a). These observations suggest that some melt has escaped from this rock during deformation and development of the stromatic migmatite. Garnet is always present within all the described leucocratic bands, veins and pods. However, there are also thin Grt-absent and Bt-Crd-bearing leucocratic dikes crosscutting the foliation at high angle, that in contrast with previously described Grt-bearing bands and veins, seem to develop under ductile-to-fragile conditions (Figs. 4.2a, 2d). The mylonitic gneisses are equivalent to the lower part of the gneiss series described by Loomis (1972), rocks belonging to the lower part of the Grt-Ky-Kfs zone of Torres-Roldán (1981), or the garnet gneiss of Platt et al. (2003c). Upper in the

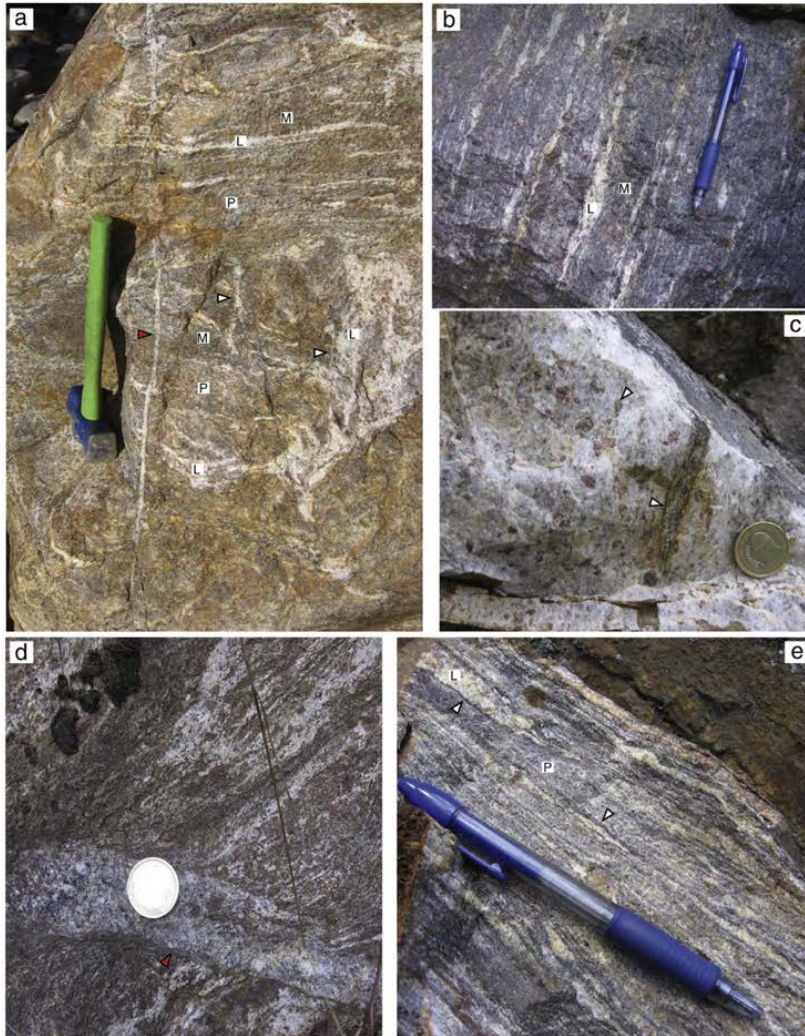


Figure 4.2. Field appearance of the mylonitic (a–d) and porphyroblastic (e–g) gneisses. (a–b) Mylonitic gneisses appear commonly as dark, massive and Grt-rich rocks except for the presence of millimeter-to-centimeter leucocratic bands that alternate with centimeter-to-decimeter mesocratic-to-melanocratic bands, defining a foliation. Based on this structure, and referred to the nomenclature of migmatites, these rocks can be classified as stromatic metatexitic migmatites, where leucocratic bands correspond to leucosomes (L), melanocratic bands to melanosome (M) and mesocratic bands to paleosome (P). Some domains are less affected by the deformation—central part of (a), appear to record a previous stage in the history of the rock, and are classified as dilatant metatexitic migmatites. These domains show a higher proportion of leucosome, which appear distributed within layers parallel to foliation, but also in veins and pods at high angle or perpendicular to the foliation (a; white arrows). The hammer and pen are 29 cm and 14 cm long, respectively. (c) Thick concordant Grt-rich leucocratic body affected by a foliation marked by scarce melanocratic minerals, elongated Grt and schlierens (white arrows), parallel to that in the host rock. The coin is 25mm across. (d) Thin Grt-absent and Bt-Crd-bearing leucocratic dikes crosscutting the foliation at high angle that seem to form under ductile-to-fragile conditions—see also red arrow in (a). (e) Porphyroblastic gneisses; based on the structure this rock can be classified as a stromatic metatexite. The foliation is defined by alternating mm-to-dm Grt-bearing leucosomes (L, leucocratic bands), paleosomes (P, mesocratic bands) and melanosomes (white arrows, melanocratic bands). Melanosomes around leucosomes are frequent and rather continuous.



Figure 4.2.(continued) (f) Porphyroblastic gneiss showing a thick concordant Grt-bearing leucocratic body (white arrow), and a thin Grt absent and Bt-Crd-bearing dike (red arrow) that crosscut the foliation at high angle and develop under ductile-to-fragile conditions. The hammer head is 12 cm across. (g). Porphyroblastic gneisses; based on the structure this rock can be classified as a schlieric diatexite.

sequence and further away from the contact with the peridotites, porphyroblastic gneisses are lighter, coarser-grained and more heterogeneous rocks, showing a clear layering defined by alternating mm-to-dm leucocratic and mesocratic-to-melanocratic bands (Fig. 4.2e-g). These bands are parallel to the mylonitic foliation of the underlying gneisses. Compared with the mylonitic gneisses, Grt decreases whereas Bt increases in abundance (Fig. 4.3). Biotite is aligned and defines schistosity parallel to the banding of the rock. Based on the structure, these rocks can be classified as stromatic metatexites (Figs. 2e-f) or schlieric diatexites (Fig. 4.2g). Leucocratic bands or leucosomes contain Grt and are separated from the paleosome by rather continuous mm-thick melanosomes. Occasionally leucosomes reach up to tens of cm in thickness and forms concordant tabular leucocratic bodies (Fig. 4.2f). As in the mylonitic gneisses, there are late Grt-absent and Crd-bearing thin dikes that seem to develop under ductile-to-fragile conditions (Fig. 4.2f). Porphyroblastic gneisses are likely equivalent to rocks belonging to the upper part of the Grt-Ky-Kfs zone of Torres-Roldán (1981) or the migmatites of Platt et al. (2003c).

We have conducted a systematic sampling of the gneissic sequence of Jubrique and collected a total of 40 samples. Seven samples of mylonitic (JU-6, JU-7, JU-8, JU-10) and porphyroblastic (JU-16, JU-21, JU-25) gneisses were chosen to study in detail the microstructures and phase assemblages of the MI (JU-6, JU-7, JU-16), bulk rock compositions (JU-7, JU-21) and mineral major element compositions (JU-6, JU-7, JU-10, JU-21, JU-25). In addition, we have also conducted a thermodynamic modeling of

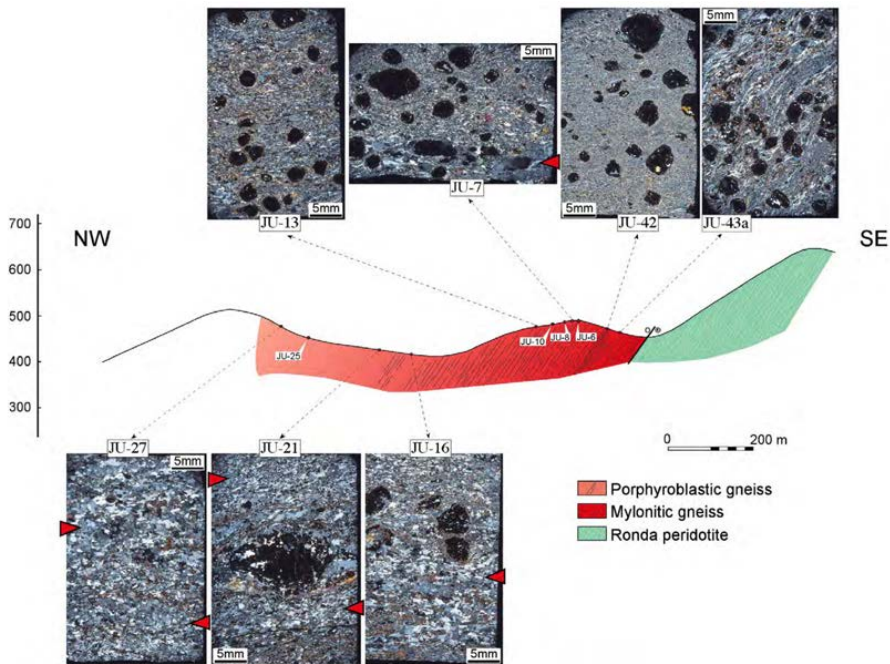
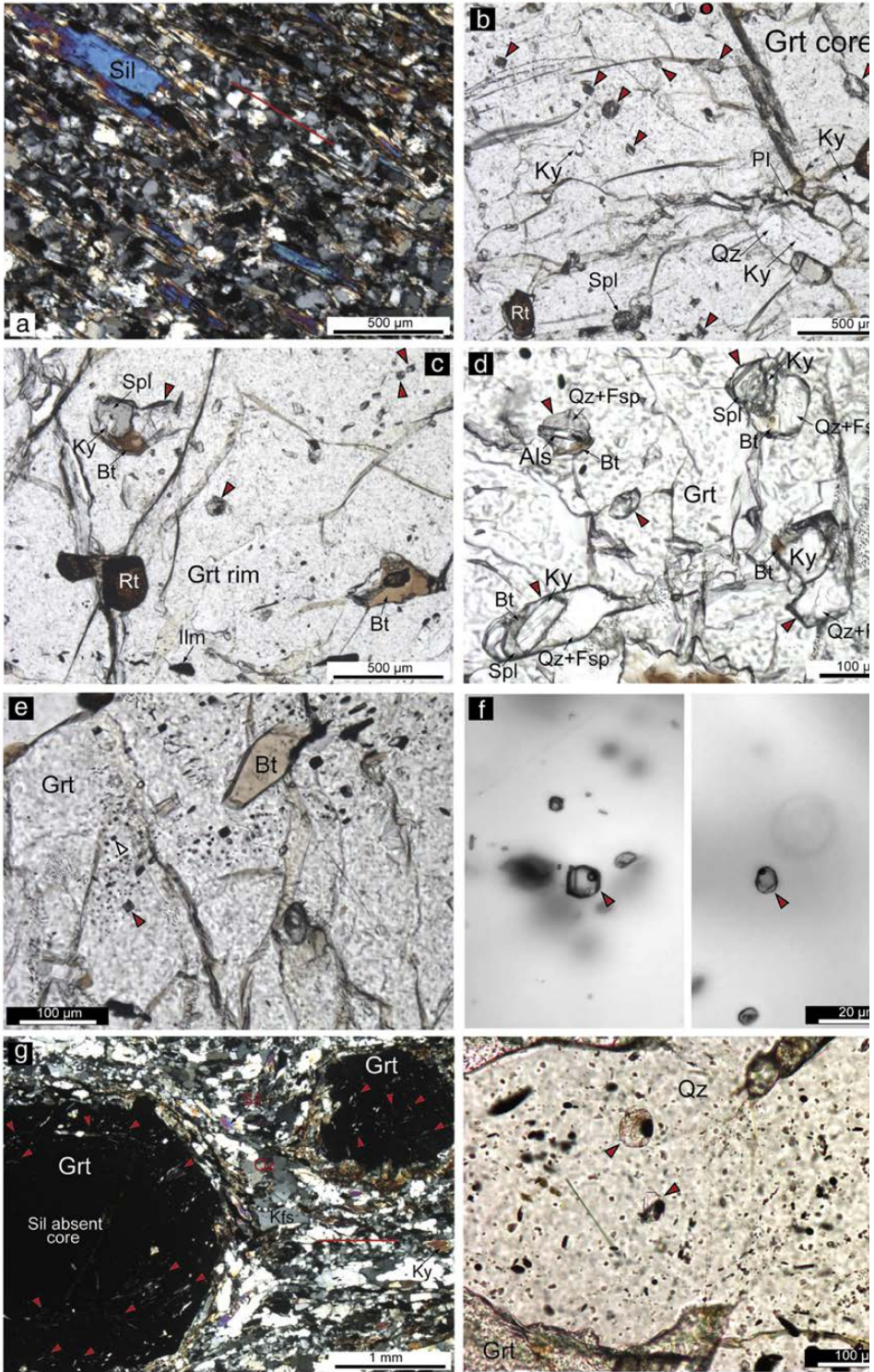


Figure 4.3. NW-SE cross-section of the contact between Ronda peridotites and Jubrique gneisses in the studied area (yellow star in Fig. 4.1), based on Olmo et al. (1980), Van der Wal and Vissers (1996), Balanyá et al. (1997), and data from this work. The cross-section shows the location of the studied samples, and the cross-polarized light photomicrographs show the microstructural evolution of gneisses as a function of distance to the top of the Ronda peridotite slab. Red arrows in the photomicrographs show the location of leucosomes at the thin-section scale. White lines in peridotites and black lines in gneisses show the traces of the mylonitic foliation. The traces of the schistosity in the porphyroblastic gneisses, parallel to the mylonitic foliation, have not been represented. See text for details.

the mylonitic gneiss JU-7, in order to shed light on the conditions of melt generation and entrapment. The location of these samples is shown in Figs. 4.1 and 4.3.

4.2.1 Petrography and Mineral Chemistry of Mylonitic Gneisses

Mylonitic gneisses are fine-grained rocks made of abundant to frequent Grt, Qz, Pl, Kfs, Ky, Sil and Crd, scarce to rare Bt, and accessory Spl, Gr, Ap, Rt, Ilm, Zrn, Mnz and rare Ep. These rocks show a mylonitic microstructure, with a fine-grained ($\approx 20\text{-}200\ \mu\text{m}$) matrix formed mostly by $\text{Qz}+\text{Pl}+\text{Kfs}+\text{Als}\pm\text{Crd}$, and porphyroclasts of Grt and, less frequently, Ky and Kfs (Figs. 4.3, 4.4). In addition to the banding observed at the outcrop scale, the main foliation (Sp) is defined by oriented ribbons of Qz, elongate Grt and Ky porphyroclasts, prisms of Ky and prisms/needles of Sil.



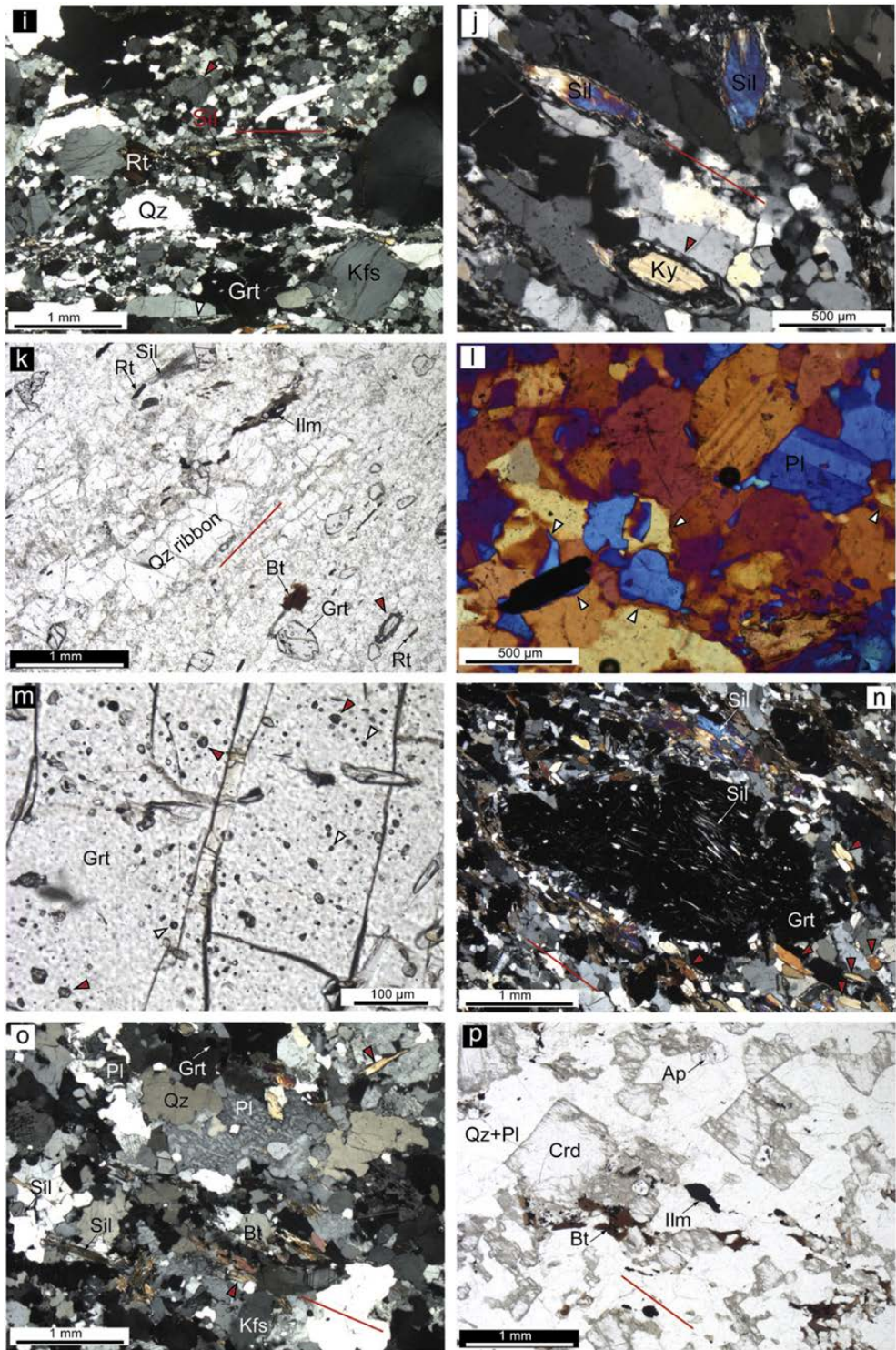


Figure 4.4 (continued)

< **Fig. 4.4.** Petrographic photomicrographs from mylonitic (a–l) and porphyroblastic (m–p) gneisses. (a) Prisms of Sil crystallized parallel to foliation in the matrix (hereafter marked by red line). Cross-polarized light (CPL). (b) Core of large Grt (≈6mm in diameter, center of the Grt is marked by red dot), showing mineral inclusions of Rt, Ky, Qz and Pl, and abundant MI (red arrows). Plane-polarized light (PPL). (c) Rim of the same large Grt from (b), showing single mineral inclusions of Rt, Ilm, Bt and abundant MI (red arrows) (PPL). Notice the large MI that includes Ky rimmed by Spl. (d) Melt inclusions in Grt of mylonitic gneisses show a large range in size. Compare the large MI shown in this figure (red arrows) with those in (b–c) and (e–f). These large MI include in all cases Ky (sometimes rimmed by Spl), in addition to Qz, feldspars and Bt (PPL). (e) Garnet showing coexisting MI (red arrow) and apparently primary FI (white arrow) (PPL). (f) Glassy MI with shrinkage bubble in Grt of mylonitic gneiss (PPL). (g) Garnet porphyroclasts in a matrix of Qz, feldspars and aluminosilicates (Ky and Sil) (CPL). The matrix foliation is defined by Qz ribbons and oriented Ky and Sil. Inclusions of Sil needles (red arrows) appear throughout the entire smaller Grt (≈1 mm) but only at the rims of the larger Grt (≈3 mm). Garnets show replacement coronas of Crd + Qz + Bt + Spl + Ilm ± Pl. (h) MI in Qz within Grt of mylonitic gneiss (PPL). (i) Deformed leucosome formed by a fine-grained quartzofeldspathic matrix, feldspar porphyroclasts and accessory Ky (white arrow), Sil, Grt and Rt (CPL). Kyanite is rimmed by an Spl + Pl ± Crd ± Kfs corona. Red arrow shows perthitic Kfs. The foliation in leucosomes is defined by oriented Qz ribbons, feldspar porphyroclasts, Ky and Sil. (j) Microstructures of aluminosilicates in the matrix of mylonitic gneisses (CPL). Relict Ky appears partially replaced by a corona of Spl + Pl ± Crd ± Kfs (red arrow). Sillimanite appears mostly as pseudomorphs after former Ky, constituting polycrystalline aggregates or single crystals with undulose extinction; it also forms small needles replacing former Ky (see fibers around Sil pseudomorphs). Matrix Ky and Sil are always oriented parallel or subparallel to foliation. (k) Concordant Grt-rich leucocratic body in mylonitic gneisses (see Fig. 2c) (PPL). This rock has a granitic mineral composition and a mylonitic microstructure, with a fine-grained matrix (≈50–200 μm) composed of Qz + Pl + Kfs, that encloses abundant Qz ribbons and Kfs and Grt porphyroclast up to ≈1 cm in diameter. Kyanite (red arrow) appears rimmed and partially replaced by Spl or Sil fibers. The foliation (red line) is defined by Qz ribbons and accessory Bt, Ky, Sil, Rt and Ilm. (l) Igneous microstructures in leucosome of mylonitic gneiss, such as cusped mineral terminations, melt films and subhedral microstructures (white arrows) (CPL plus quartz accessory plate). (m) Large elongated garnet (≈3 × 6mm) of porphyroblastic gneiss showing abundant coexisting MI (red arrow) and apparently primary FI (white arrow) (PPL). (n) Small elongated Grt in porphyroblastic gneiss showing abundant inclusions of Sil needles throughout the entire crystal (CPL). Sillimanite inclusions are mostly oriented parallel to the foliation in the matrix, defined by Ky prisms (red arrows), Sil pseudomorphs and Bt. (o) Granitic leucosome in porphyroblastic gneiss showing a subhedral to anhedral igneous microstructure and accessory Ky (red arrows), Sil, Grt and Bt (CPL). Notice Pl with antiperthites, and thin coronas around relict Ky. (p) Tonalitic leucosome in porphyroblastic gneiss with subhedral microstructure, formed by Qz, subhedral to anhedral Pl and Crd, and Bt (PPL). These leucosomes are oriented parallel to Sp; despite this, only Qz appears slightly deformed and shows undulose extinction, whereas subhedral Crd prisms are parallel to Sp.

The intensity of deformation varies within the sequence, and some dm-to-m domains may appear highly deformed, to the point that leucocratic and melanocratic bands become hardly distinguishable (Fig. 4.3); it is in these domains where Sil develops the largest (hundreds of μm) crystals (Fig. 4.4a). In spite of the strong deformation, mineral lineations are apparently absent in the field and at the scale of hand specimen or thin section. Garnet forms conspicuous rounded or elongated porphyroclasts ranging in size from ≤1 mm up to 2 cm, and are present within both leucocratic and melanocratic bands (Fig. 4.3). They often contain MI (Figs. 4.4b–f) as well as inclusions of Qz, Ky, Rt, Pl, Bt, Sil, Ilm, Zrn, Mnz, Gr and Spl (Figs. 4.3, 4b–e, 4.4g). Melt inclusions have also been observed within Qz included in Grt (Fig. 4.4h). Some FI, of possible primary origin, are

spatially associated with MI in clusters within Grt (Fig. 4.4e). Muscovite has never been observed. Considering large ($\geq 4\text{-}5$ mm) Grt porphyroclasts, MI, Ky and Rt are found both at cores and rims (Figs. 4.4b-c), whereas Sil and Ilm are only found at the rims (Fig. 4.4c, 4.4g). Mineral inclusions at the core are not oriented, whereas inclusions at rims (e.g. needles of Sil) may be oriented subparallel to Sp (Fig. 4.4g). Rims of Grt are variably replaced by undeformed coronas of Crd, Qz, Bt, Ilm, Kfs, Spl and rare Pl (Fig. 4.4g) (see also Platt et al. (2003b)). Garnets are rich in Alm and Prp ($\approx\text{Alm}66$, $\approx\text{Prp}28$), have low to very low concentrations of Grs and Sps ($\approx\text{Grs}4$, $\approx\text{Sps}2$) (Table 4.1, Fig. 4.5a), and show up to three compositional domains depending on crystal size. Crystals ≤ 3 mm show a central plateau in all components and increases in Grs and decreases in Prp and XMg at some hundreds of μm from, and towards the rim. The component spessartine is flat except at a few tens of μm from the rim where it increases. In addition to these compositional zones, larger crystals (≥ 5 mm) show a central domain with higher concentration of Grs with respect to the plateau (Fig. 4.5a).

Kyanite occurs both in Grt and in the matrix (Figs. 4.4b-d, 4.4g, 4.4i-j). Matrix Ky forms elongated porphyroclasts and small prisms, always parallel to Sp and metastable, partially replaced by either a Spl+Pl \pm Kfs \pm Crd corona (Fig. 4.4j) or a fringe of Sil. Frequently, former Ky appears also as polycrystalline aggregates with undulose extinction, apparently pseudomorphosed by Sil (Fig. 4.4f). Kyanite in Grt may also be rimmed by Spl coronas (Fig. 4.4c-d); however, Ky included at the cores of large Grt appear stable (Fig. 4.4b). In addition to needles included at the rims of Grt or replacing rims of Ky, Sil appears as small oriented prisms in the matrix (including leucocratic bands), and is particularly abundant in highly deformed rocks (Figs. 4.4a, 4.4g, 4.4i-k). Biotite occurs mostly in coronas ($\text{Mg}\# \approx 0.47$; $\text{Mg}\# = \text{mol.} [\text{MgO}/(\text{MgO} + \text{FeO})]$) around Grt (Fig. 4.4g), but also as inclusions within Grt ($\text{Mg}\# \approx 0.69$) (Figs. 4.4c, 4.4e) and, more rarely, in the matrix. Biotite included in Grt show the lowest Ti concentrations. Biotites of leucocratic and melanocratic bands are similar in composition ($\text{Mg}\# \approx 0.51$). Cordierite ($\text{Mg}\# \approx 0.61$) appears mostly in coronas partially replacing Grt, where it forms symplectic intergrowths with Qz; it may also appear in the fine-grained matrix of the rock. Plagioclase included in Grt ($\approx\text{An}50$) is richer in An with respect to Pl in leucocratic and melanocratic bands, which shows similar compositions ($\approx\text{An}40$). Plagioclase in leucocratic bands is either homogeneous or slightly zoned (inverse or direct), whereas Pl in melanocratic bands show a slight inverse zoning. Plagioclase in

coronas replacing matrix Ky shows intermediate compositions (\approx An45). K-feldspar shows a rather constant composition in all microstructural locations. Quartz appears frequently in the matrix as ribbons wrapping the porphyroclasts. Spinels are solid solutions between Spl, Hc and Ghn. Spinels included in Grt are closer to Spl and richer in Zn (Mg# \approx 0.41; ZnO \approx 6 wt%), whereas spinel in coronas around Grt is closer to Hc and has low concentrations of Zn (Mg# \approx 0.19; ZnO \approx 0.5 wt%).

Leucocratic bands are granitic and composed of Qz, Kfs, Pl (commonly Kfs>Pl; Kfs may appear with rod, string or patch perthites) and accessory Ky, Sil, Grt, Rt, Ilm and Gr (Fig. 4.4i). They are deformed but show larger grain size compared with the rest of the rock (Figs. 4.3, 4.4i); microstructures indicating the former presence of melt such as cusped mineral terminations, melt films and subhedral microstructures (Fig. 4.4i; e.g. Sawyer (2001); Vernon (2011)) are rare or absent, probably erased by deformation and high temperature annealing. Mesocratic-melanocratic bands are rich in Grt, Als and Pl. Leucocratic concordant bodies are similar to leucocratic bands: they show a mylonitic microstructure and have a granitic mineral composition (Qz+Pl+perthitic Kfs), with frequent Grt and accessory Ky, Sil, Bt, Rt, Ilm and Spl (Fig. 4.4k). Garnets have abundant MI and show many microstructural features similar to Grt of the host rock, suggesting that they are entrained crystals from the residue. The late leucocratic dikes crosscutting Sp are tonalitic medium-grained rocks made of Qz, Pl, Bt and Crd. They are almost undeformed and show a typically igneous subhedral microstructure. Hence they are different in composition and microstructure with respect to the leucogranitic bands/bodies parallel to Sp.

Pre-kinematic minerals (with respect to Sp) include the cores of large Grt porphyroclasts, inclusions of Ky, Bt, Rt and Pl in these cores (Fig. 4b), and porphyroclasts of Ky and Kfs. Syn-kinematic phases are oriented Sil within the rims of large Grt, in small Grt (Fig. 4.4g) or in the matrix (Fig. 4.4a), rims of large Grt and small Grt, and oriented Ilm and Bt in the matrix (Figs. 4.4g, 4.4i-j). Post-kinematic minerals include Crd, Bt, Ilm, Kfs, Spl and Pl replacing rims of Grt and Ky (Figs. 4.4g, 4.4j) (see also Loomis (1972); Torres-Roldán (1981); Balanyá et al. (1997); Argles et al. (1999); Platt et al. (2003b)).

4.2.2 Petrography and Mineral Chemistry of Porphyroblastic Gneisses

Porphyroblastic gneisses are fine-to-medium grained rocks characterized by a compositional layering at the mm-cm scale (leucosome, paleosome and melanosome, see Fig. 4.2e), parallel to a schistosity (Sp) defined by Bt, Als and Gr. Compared to mylonitic ones, porphyroblastic gneisses show lower modal proportions of Grt and Als, and higher amounts of Bt (Figs. 4.3 and 4.4). They also display a decrease in Grt and increase in Bt modal proportions towards upper structural levels. This, together with the similarity in mineralogy and many microstructures in both types of gneisses (particularly at their contact, see below), indicates a petrologic continuity throughout the entire sequence. Porphyroblastic gneisses are constituted by a fine-to-medium-grained matrix ($\approx 0.5\text{-}2$ mm) made of $\text{Qz}+\text{Pl}+\text{Kfs}+\text{Als}+\text{Bt}+\text{Grt}\pm\text{Crd}$, that enclose Grt and Kfs porphyroblasts. Quartz shows undulose extinction and/or development of subgrains, and Qz and feldspars develop sutured boundaries.

Garnet porphyroblasts reach in size up to 1.5 cm, and are in general smaller than in mylonitic gneisses. They also show replacement coronas of $\text{Crd}+\text{Qtz}+\text{Bt}+\text{Spl}$, and contain inclusions of melt (Fig. 4.4m), Qz, Ky, Sil, Pl, Bt, as well as Rt, Py, Gr, Zrn, Mnz, Ap and Ilm. Some FI seem primary as they appear regularly distributed throughout the entire Grt and spatially associated with MI (Fig. 4m); these may be filled with carbonates such as calcite and siderite. Garnets are rich in Alm and Prp ($\approx \text{Alm}66$, $\approx \text{Prp}22$) and show higher Grs and Sps ($\approx \text{Grs}8$, $\approx \text{Sps}4$) with respect to Grt in mylonitic gneisses. Crystals ≥ 5 mm show a central compositional plateau and, in contrast to mylonitic gneisses, a monotonic decrease in Sps and an irregular increase in Mg# towards the rims (Table 4.2, Fig. 4.5b); Grs also increases irregularly towards the rim. Crystals ≤ 2 mm lack the central plateau and show zoning patterns similar to rims of the large Grt.

Aluminosilicates are less abundant than in mylonitic gneisses, though their proportions vary throughout the sequence of porphyroblastic gneisses. Kyanite and Sil show similar microstructures to those in mylonitic gneisses. Besides included in Grt, Ky occurs in the matrix parallel to Sp and frequently rimmed by symplectite coronas of $\text{Spl}\pm\text{Pl}\pm\text{Crd}$ or by Sil (Fig. 4.4n). Sillimanite also appears as oriented inclusions at the rims of large Grt or throughout small Grt (Fig. 4.4n). Biotite occurs mostly as oriented crystals or crystal aggregates in the paleosome and melanosome, but also included within Grt porphyroblast (Mg# ≈ 0.44), in coronas partially replacing Grt porphyroblasts

Table 4.1 Bulk rock composition of mylonitic gneiss JU-7, and electron microprobe analyses (wt% of minerals of mylonitic gneisses JU-6, JU-7 and JU-10

Material No. analyses	JU-7 1	Grt mean 424	Crd 89	Bt inclusion 28	Bt matrix 15	Bt corona 44	Pl inclusion 13	Pl matrix 56	Pl corona 8	Kfs 8	Spl inclusion 1	Spl corona 3	Ilmenite 10
SiO ₂	57.9	37.69 (1.31)	48.75 (2.29)	36.55 (0.96)	34.96 (0.62)	35.21 (2.01)	54.39 (2.09)	57.84 (1.12)	56.99 (0.61)	63.69 (0.61)	0.05	0.02 (0.01)	0.03 (0.01)
Al ₂ O ₃	21.8	21.66 (0.88)	32.35 (1.42)	17.09 (0.91)	16.31 (0.29)	16.17 (2.49)	28.12 (1.36)	25.91 (0.68)	26.72 (0.37)	18.67 (0.27)	61.56	58.34 (0.18)	0.04 (0.01)
TiO ₂	1.27	0.03 (0.02)	0.01 (0.02)	4.67 (0.96)	5.10 (0.86)	5.26 (1.13)	0.01 (0.01)	0.01 (0.01)	0.01 (0.00)	0.03 (0.03)	0.02	0.09 (0.05)	53.38 (0.56)
FeO ^a	10.7	31.23 (2.44)	9.10 (0.86)	11.68 (1.36)	18.05 (0.83)	19.46 (1.79)	0.30 (0.06)	0.06 (0.09)	0.19 (0.08)	0.35 (0.41)	23.45	36.18 (0.32)	45.78 (1.28)
MnO	0.18	0.69 (0.23)	0.10 (0.02)	0.02 (0.02)	0.05 (0.04)	0.04 (0.02)	0.01 (0.01)	0.01 (0.01)	0.01 (0.01)	0.01 (0.00)	0.07	0.17 (0.01)	0.37 (0.04)
MgO	2.32	7.51 (1.49)	7.96 (0.65)	14.87 (1.58)	10.48 (0.87)	9.59 (0.75)	0.01 (0.00)	0.01 (0.02)	0.00 (0.00)	0.06 (0.11)	8.95	4.60 (0.10)	0.66 (0.25)
CaO	0.96	1.72 (0.83)	0.02 (0.01)	0.02 (0.02)	0.03 (0.04)	0.02 (0.03)	10.62 (1.63)	8.00 (0.86)	8.80 (0.42)	0.21 (0.32)	0.00	0.01 (0.01)	0.01 (0.02)
Na ₂ O	0.57	0.02 (0.04)	0.07 (0.02)	0.51 (0.25)	0.16 (0.03)	0.15 (0.04)	5.33 (0.88)	6.76 (0.55)	6.45 (0.23)	1.73 (0.32)	0.22	0.02 (0.01)	0.00 (0.01)
K ₂ O	2.39	0.02 (0.13)	0.03 (0.01)	9.03 (0.37)	9.37 (0.19)	8.89 (1.36)	0.25 (0.07)	0.41 (0.12)	0.27 (0.02)	13.77 (0.60)	0.01	0.01 (0.01)	0.01 (0.01)
P ₂ O ₅	n.d.	n.d.	n.d.	n.d.	n.d.	n.d.	n.d.	n.d.	n.d.	n.d.	n.d.	n.d.	n.d.
Cr ₂ O ₃	n.d.	0.03 (0.03)	0.01 (0.01)	0.06 (0.05)	0.06 (0.02)	0.20 (0.18)	0.01 (0.01)	0.01 (0.01)	0.01 (0.01)	0.01 (0.02)	0.29	0.41 (0.18)	0.04 (0.04)
ZrO	n.d.	0.03 (0.04)	0.03 (0.03)	0.12 (0.06)	0.04 (0.04)	0.04 (0.04)	0.02 (0.02)	0.02 (0.03)	0.02 (0.03)	0.01 (0.01)	5.56	0.57 (0.14)	0.05 (0.04)
F	n.d.	0.14 (0.04)	0.04 (0.03)	1.97 (1.31)	1.30 (0.83)	1.27 (0.72)	0.02 (0.02)	0.02 (0.02)	0.03 (0.03)	0.01 (0.01)	0.07	0.15 (0.03)	0.26 (0.03)
Cl	n.d.	0.01 (0.01)	0.01 (0.01)	0.04 (0.03)	0.04 (0.03)	0.03 (0.02)	0.01 (0.01)	0.01 (0.01)	0.00 (0.00)	0.01 (0.01)	0.00	0.00 (0.00)	0.01 (0.01)
LOI	1.79	100.8 (1.8)	98.5 (0.6)	96.61 (1.38)	95.93 (1.69)	96.32 (0.98)	99.08 (0.37)	99.05 (0.52)	99.48 (0.20)	98.57 (0.71)	100.25	100.56 (0.53)	
Total	ASI	4.14											
	Mg#	0.46											
	K#	0.73											
	Alm												
	Prp												
	Grs												
	Sps												
	Ab												
	An												
	Or												

^a Total Fe as FeO or Fe₂O₃
^b Water by difference (100-EMP total)

Table 4.2 Bulk rock composition of porphyroblastic gneiss JU-21, and electron microprobe analyses (wt%) of minerals of porphyroblastic gneisses JU-21 and JU-25

Mineral	JU-21	Grt mean	Grt core	Grt rim	Bt inclusion	Bt matrix	Bt corona	Pl matrix	Pl corona	Kfs
No. analyses	1	264	43	62	14	64	2	94	3	29
SiO ₂	62.5	36.98 (0.75)	36.24 (0.06)	37.08 (1.07)	34.19 (0.28)	34.99 (0.34)	34.76 (0.03)	55.94 (0.88)	52.30 (1.42)	63.02 (0.40)
Al ₂ O ₃	17.7	21.18 (0.30)	20.93 (0.04)	21.24 (0.44)	17.54 (0.80)	16.61 (0.49)	15.56 (0.15)	26.43 (0.62)	28.88 (0.89)	18.27 (0.18)
TiO ₂	1.02	0.03 (0.04)	0.02 (0.01)	0.03 (0.02)	5.54 (0.52)	5.00 (0.50)	6.17 (0.05)	0.01 (0.01)	0.01 (0.00)	0.02 (0.01)
Fe ₂ O ₃ *	7.83									
FeO*		30.18 (3.04)	33.96 (0.17)	29.02 (2.55)	18.88 (0.85)	15.96 (0.67)	17.40 (0.26)	0.10 (0.13)	0.35 (0.10)	0.08 (0.17)
MnO	0.13	2.02 (0.97)	2.64 (0.07)	1.48 (0.76)	0.07 (0.02)	0.03 (0.02)	0.02 (0.01)	0.01 (0.02)	0.01 (0.01)	0.01 (0.01)
MgO	2.20	5.63 (1.46)	3.94 (0.05)	6.16 (1.28)	8.35 (0.53)	11.30 (0.48)	10.31 (0.01)	0.01 (0.00)	0.01 (0.00)	0.00 (0.00)
CaO	2.16	3.02 (1.69)	1.48 (0.08)	3.78 (1.68)	0.01 (0.01)	0.02 (0.02)	0.02 (0.00)	8.92 (0.72)	11.67 (1.10)	0.22 (0.20)
Na ₂ O	1.00	0.02 (0.04)	0.02 (0.01)	0.02 (0.09)	0.20 (0.07)	0.17 (0.03)	0.17 (0.00)	6.09 (0.42)	4.55 (0.61)	1.39 (0.16)
K ₂ O	3.16	0.02 (0.03)	0.01 (0.01)	0.02 (0.05)	9.20 (0.21)	9.24 (0.16)	9.20 (0.00)	0.32 (0.08)	0.21 (0.04)	14.15 (0.33)
LOI	2.20									
Cr ₂ O ₃		0.02 (0.02)	0.02 (0.02)	0.03 (0.03)	0.05 (0.03)	0.06 (0.03)	0.14 (0.04)	0.01 (0.01)	0.01 (0.02)	0.01 (0.01)
ZnO		0.05 (0.04)	0.05 (0.04)	0.04 (0.04)	0.07 (0.06)	0.06 (0.05)	0.00 (0.00)	0.03 (0.03)	0.00 (0.00)	0.03 (0.04)
F		0.16 (0.04)	0.17 (0.03)	0.15 (0.04)	0.70 (0.17)	0.70 (0.08)	0.56 (0.02)	0.04 (0.03)	0.04 (0.04)	0.05 (0.03)
Cl		0.01 (0.01)	0.00 (0.01)	0.01 (0.01)	0.46 (0.22)	0.01 (0.01)	0.02 (0.00)	0.01 (0.01)	0.00 (0.00)	0.01 (0.01)
Total		99.30 (0.88)	99.47 (0.17)	99.04 (1.66)	95.27 (0.33)	94.12 (0.52)	94.31 (0.20)	97.90 (0.38)	98.04 (0.09)	97.26 (0.53)
ASI	1.97		0.17 (0.00)	0.28 (0.06)	0.44 (0.02)	0.56 (0.02)	0.51 (0.00)			
Mg#	0.53	0.25 (0.07)								
K#	0.67									
Alm		65.5 (7.2)	74.7 (0.5)	62.7 (5.9)						
Prp		21.7 (5.5)	15.3 (0.5)	23.7 (4.7)						
Grs		8.3 (4.6)	4.1 (0.4)	10.4 (4.6)						
Sps		4.5 (2.2)	6.0 (0.2)	3.4 (1.6)						
Ab									40.7 (5.0)	12.8 (1.5)
An								54.2 (3.5)	57.7 (5.5)	1.3 (0.9)
Or								43.9 (3.9)	1.0 (0.0)	86.0 (2.0)

* Total Fe as FeO or Fe₂O₃

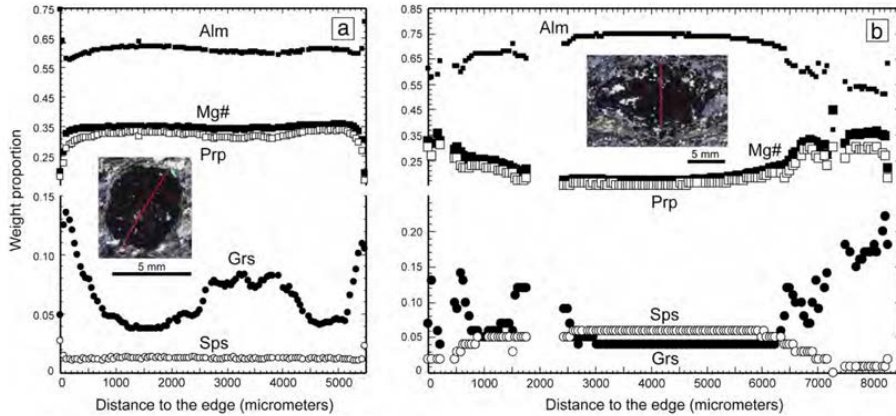


Figure 4.5. Major element concentration profiles (from EMP analyses) measured through the apparent center of large garnets from mylonitic gneisses (a) and porphyroblastic gneisses (b). Concentration scale for Grs and Sps is four times (a) or three times (b) that for Alm, Prp and Mg#.

(Mg# ≈ 0.51), replacing small Grt in the matrix, and as individual crystals within leucosomes. Biotites in paleosome, leucosomes and replacing small Grt show similar compositions (Mg# ≈ 0.56); Bt replacing Grt show the highest Ti concentrations, whereas Ti contents in Bt included in Grt is higher than those in matrix Bt. Plagioclase of paleosome and leucosome are similar in composition ($\approx \text{An}_{44}$), and either homogeneous or show slight inverse zoning ($\approx \text{An}_{38-44}$ at cores, An_{43-48} at rims). Plagioclase replacing small crystals of matrix Grt is richer in Ca ($\approx \text{An}_{58}$). K-feldspar show similar composition ($\approx \text{Ab}_{13}\text{Or}_{86}$) in all microstructural locations: as inclusions in Grt, in the paleosome, in leucosomes and as exsolutions within Pl of leucosomes.

Most of the observed leucosomes are granitic, composed of Qz, Pl, Kfs and accessory Ky, Sil, Grt, Rt and Ilm; Pl commonly shows patch to braid antiperthites (Fig. 4.4o). More rarely, leucocratic bands are tonalitic and composed of Qz, Pl, abundant subhedral to anhedral Crd and accessory Bt and Ilm (Fig. 4.4p). Anhedral Crd crystals include abundant aggregates of Sil needles and, more rarely, relicts of Grt. All leucosomes commonly show igneous microstructures such as euhedral to subhedral feldspars and Crd against a $\text{Qz} \pm \text{feldspar}$ matrix, and cusped mineral terminations, providing this domain with a subhedral microstructure (Fig. 4o-p); this indicates that they represent former melt-rich domains (Vernon 2011). The strong orientation of leucosomes parallel to Sp (Figs. 4.2e-g), together with the presence of igneous

microstructures (Figs. 4.4o-p), indicate pre-to-syn-kinematic melting with respect to Sp. The paleosome is rich in Grt, Bt, Als and Pl, and show porphyroblastic (Grt, Kfs) and anhedral to xenoblastic microstructures. Porphyroblastic gneisses may appear strongly deformed, particularly towards the contact with mylonitic gneisses, with a reduction in the matrix grain size ($\approx 50\text{-}200\ \mu\text{m}$) and development of Qz ribbons. Late Crd-bearing thin dikes perpendicular to foliation (Fig. 4.2f) are medium-to-coarse grained tonalitic rocks made of Qtz, Pl, Crd and Bt; they are similar in mineralogy and microstructures to the Crd leucosomes described above (Fig. 4.4p).

4.3 Microstructures of Melt Inclusions

Former MI have been observed within Grt present throughout the entire sequence of gneisses. Rarely, they also appear within Qz crystals included in Grt (Fig. 4.4h). Most of them correspond to nanogranites (i.e. totally crystallized polycrystalline inclusions), whereas only a few of them are partially crystallized and include some glass, or appear as totally glassy (Figs. 4.4, 4.6, 4.7). The abundance of MI varies between samples, even from the same outcrop. In gneisses with abundant MI ($\approx 10\text{-}20$ MI per mm^2 of Grt), they appear scattered throughout the entire host crystals; occasionally MI form clusters, particularly in porphyroblastic gneisses. In samples with scarce MI, they are isolated and apparently with a random distribution within the host. In general, MI are more abundant and larger in mylonitic gneisses. Melt inclusions are isometric, often show negative crystal shapes, range in size from ≈ 5 to $200\ \mu\text{m}$, and show a mean size of $\approx 30\text{-}40\ \mu\text{m}$. There is no pattern in the distribution of MI regarding their size, and small and large MI are observed next to each other. MI in the cores of large Grt occur in the vicinity of single inclusions of Ky and Rt, whereas MI at the rims of large Grt, or within small Grt, are often associated with inclusions of Ky, Sil, Rt and/or Ilm.

Nanogranites and partially crystallized MI from mylonitic and porphyroblastic gneisses are composed of daughter crystals of Qz, Kfs, Pl (albite to bytownite), ternary feldspar, Phl, Bt, Ms, rare calcite, and trapped crystals (see discussion) of Ky (\pm Spl), Gr, Phl, Zrn, Mnz, Rt, Ilm and Ap (Figs. 4.6 and 4.7). Crystals of Ky are present within most of the MI, and appear to be the main accidental mineral that favored the entrapment of the inclusions during Grt growth (Figs. 4.6a-e, 4.6g-h, 4.6k-l, 4.7a-b, 4.7e-, 4.7j). These Ky crystals are mostly anhedral and, in inclusions at the rims of large Grt, commonly appear partially replaced by a low-Zn, hercynitic Spl. Occasionally, in

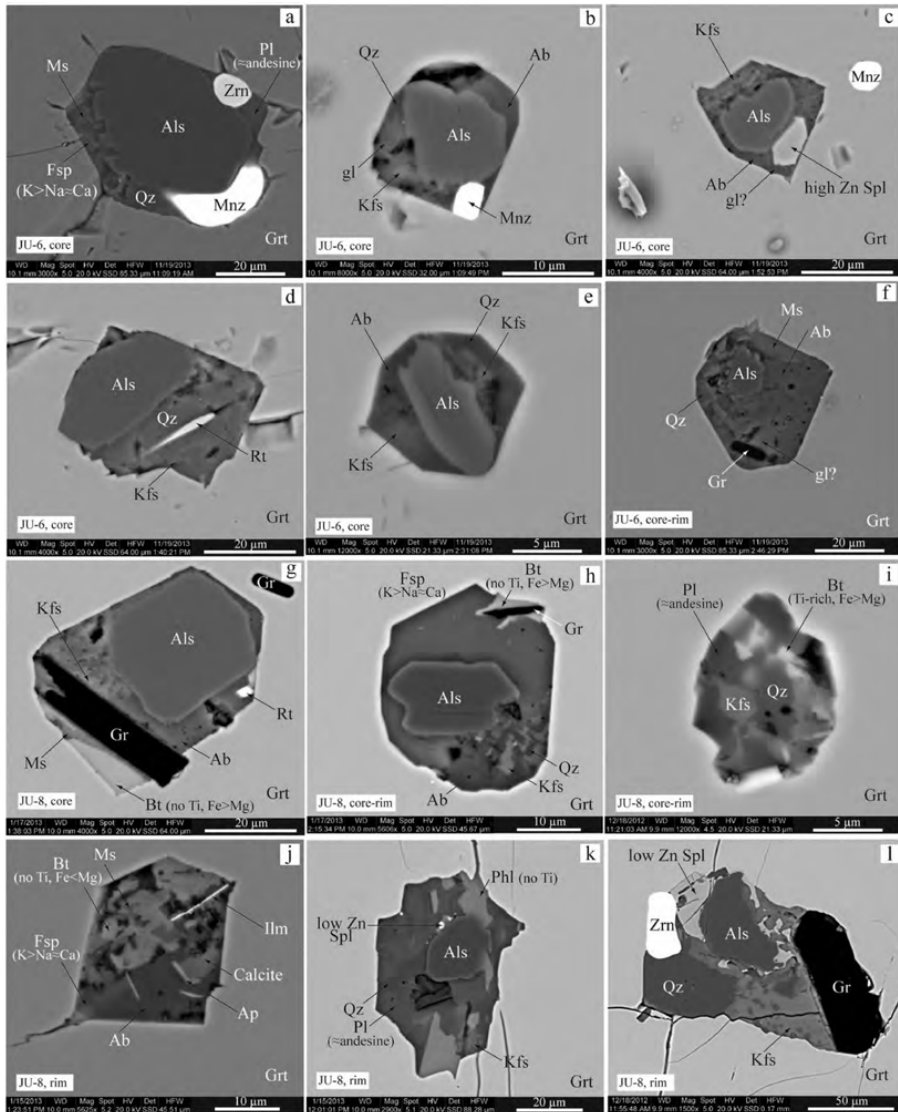


Figure 4.6. Backscattered electron images of selected nanogranites and partially crystallized melt inclusions in garnets of mylonitic gneisses JU-6 and JU-8, as a function of the region in the garnet (core, core-rim, and rim). See text for details.

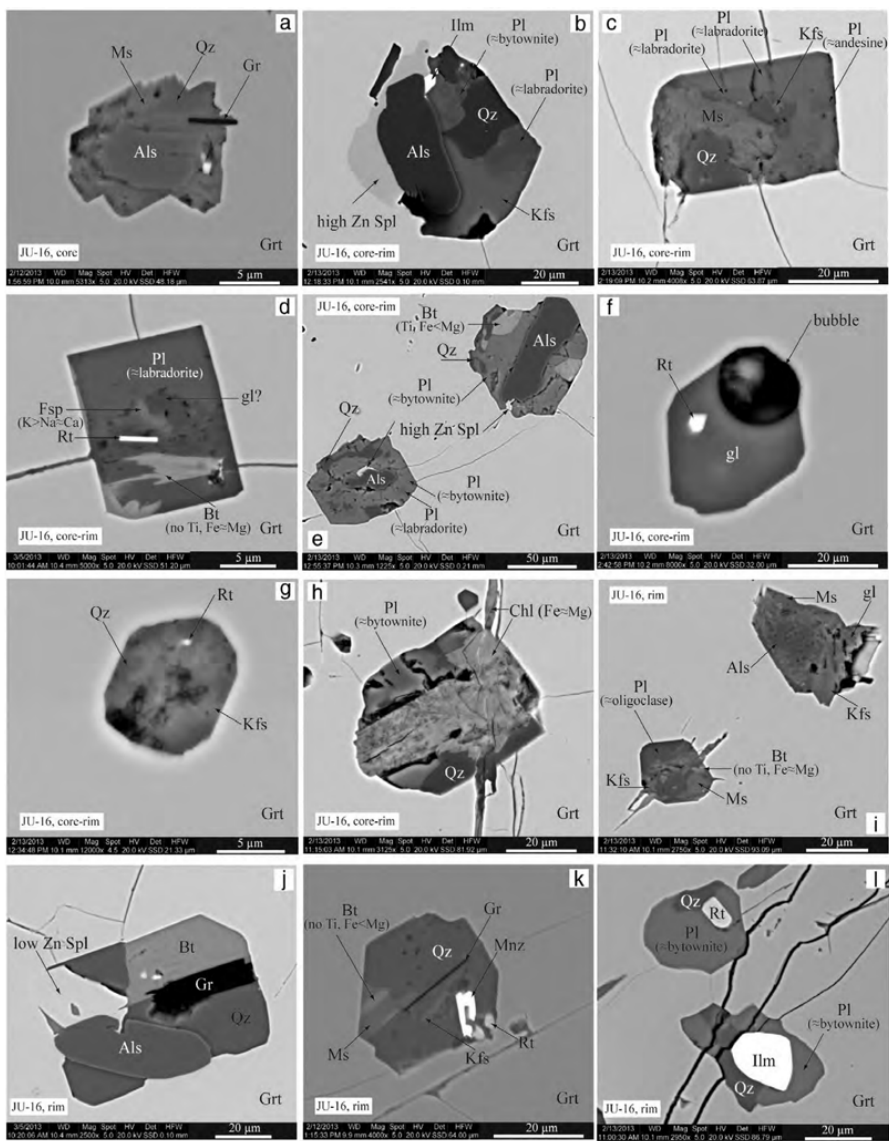


Figure 4.7. Backscattered electron images of selected nanogranites, partially crystallized melt inclusions, and glassy melt inclusions in garnets of porphyroblastic gneiss JU-16, as a function of the region in the garnet (core, core-rim, and rim). See text for details.

MI located at the core-rim region of large Grt, accidental Ky appear rimmed by Spl rich in Zn (Zn \approx Fe from EDS spectrum, Figs. 4.6c, 4.7b). Other solid inclusions include Gr, Zrn and Mnz (e.g. Figs. 4.6a-b, 4.6g, 4.6l). Ilmenite occurs only in MI located at the rim of large Grt (Figs. 4.6j, 4.7b, 4.7l), whereas Rt, Zrn and Mnz have been found throughout the entire host (Figs. 4.6a-b, 4.6d, 4.6g, 4.7d, 4.7f-g, 4.7k-l). Glassy MI may show some minor daughter minerals nucleated on the MI walls, and/or a shrinkage bubble (Fig. 4.7f). The glass present in partially crystallized MI (Figs. 4.6b-c, 4.6f, 4.7d, 4.7i) and glassy MI show typical granitic EDS spectra.

Offshoots around MI have been observed in a few cases; they are filled with daughter minerals, do not necessarily show a radial distribution and, compared with the diameter of the MI, they have similar to smaller lengths (Figs. 4.6a, 4.6j-k, 4.7c-d, 4.7i). Conversely, MI are commonly affected by late fractures crosscutting the entire Grt that may produce the retrogression and partial replacement of the primary mineral assemblage of nanogranites to a cryptocrystalline and low temperature assemblage that includes Chl (Fig. 4.6l, 4.7c, 4.7h, 4.7l). Among the daughter minerals of MI, Bt and Ms form euhedral to subhedral crystals, are frequently intergrown, and appear to be among the first minerals that crystallize from the melt (Fig. 4.6g, 4.6j, 4.6k, 4.7c, 4.7i, 4.7k). Although some Bt crystals appear to nucleate and grow from irregular Grt surfaces (Fig. 4.6k), crystallization of most MI started after development of negative crystal shapes (e.g. Figs. 4.6e, 4.7d), as found by Ferrero et al. (2012). In the MI, Qz and feldspars are subhedral to anhedral and are commonly intergrown (e.g. Figs. 4.6e, 4.6l, 4.7e, 4.7k). Some small cavities (e.g. Figs. 4.6f-g) can be interpreted as micro- to nano-porosity, and preliminary results of H analysis of remelted nanogranites (Bartoli et al., pers. com.) suggest that they were filled with the fluid dissolved in the former hydrous melt and exsolved upon crystallization (see also Fig. 4. in Bartoli et al., 2013b). One of the studied nanogranites contains calcite in an apparently primary context (i.e. either as a daughter or a trapped crystal; Fig. 4.6j). However, such rare, non-systematic occurrence prevents from allowing meaningful speculations. The microscopic observations show that MI in Grt of both types of gneisses have mostly similar characteristics regarding shape, size, degree of crystallization, mineralogy and distribution in the host, MI in porphyroblastic gneisses being slightly smaller (mean size of $\approx 30 \mu\text{m}$) and less abundant.

4.1 Phase Equilibria Modeling and Conventional Thermobarometry

All gneiss samples contain microstructures corresponding to several metamorphic stages. Furthermore, these gneisses show clear microstructures indicative of anatexis, and melt may have escaped from these deformed rocks during its metamorphic evolution (see above). Hence, the bulk rock composition of a given gneiss sample might not correspond to that of the protolith, which would influence the phase equilibria relationships and chemical compositions of minerals in the early stages of the metamorphic evolution. Inferring precise P - T conditions for such complex samples requires the use of particular equilibration volumes for each metamorphic stage. Only based on such a careful work we would be able to compare calculated compositional isopleths with observed mineral compositions and estimate precise P - T conditions. Such a detailed analysis is beyond the scope of this work. Here we have used the mylonitic gneiss sample JU-7 only to illustrate generalized P - T conditions recorded by these rocks, based on the comparison of microstructural observations with results from phase equilibria modeling. In order to make the modeled P - T conditions robust, we accompanied the phase equilibria modeling with results from conventional thermobarometry on mylonitic gneisses JU-6 and JU-7.

The model chemical system Na_2O - CaO - K_2O - FeO - MgO - Al_2O_3 - SiO_2 - H_2O - TiO_2 (NCKFMASHT) was used with the bulk rock composition obtained from XRF analysis. The bulk rock composition (in mol %) used for calculation is indicated in the upper left inset of the calculated P - T phase diagram pseudosection (Fig. 4.8). The amount of H_2O component involved in the calculation for the bulk rock composition was assumed as the loss of ignition of the XRF analysis. Graphite was neglected in the calculation due to its minor effect on the phase relationships under the P - T conditions of interest. All calculations were done by the Gibbs energy minimization (Connolly 2009) with the thermodynamic database of Holland & Powell (1998, as revised in 2003). We used the solution model of melt from White et al. (2007), garnet from Holland and Powell (2001), biotite from Tajčmanová et al. (2009), white mica from Coggon and Holland (2002) and ternary feldspar from Fuhrman and Lindsley (1988). An ideal model was used to account for the solution of cordierite.

Phase equilibria modeling provides peak P - T conditions of ≈ 850 °C and ≈ 12 -14 kbar (Grt-Bt-Fsp-Ky-Rt-Qz-Liq stability field; Fig. 4.8), recorded in the cores of large Grt

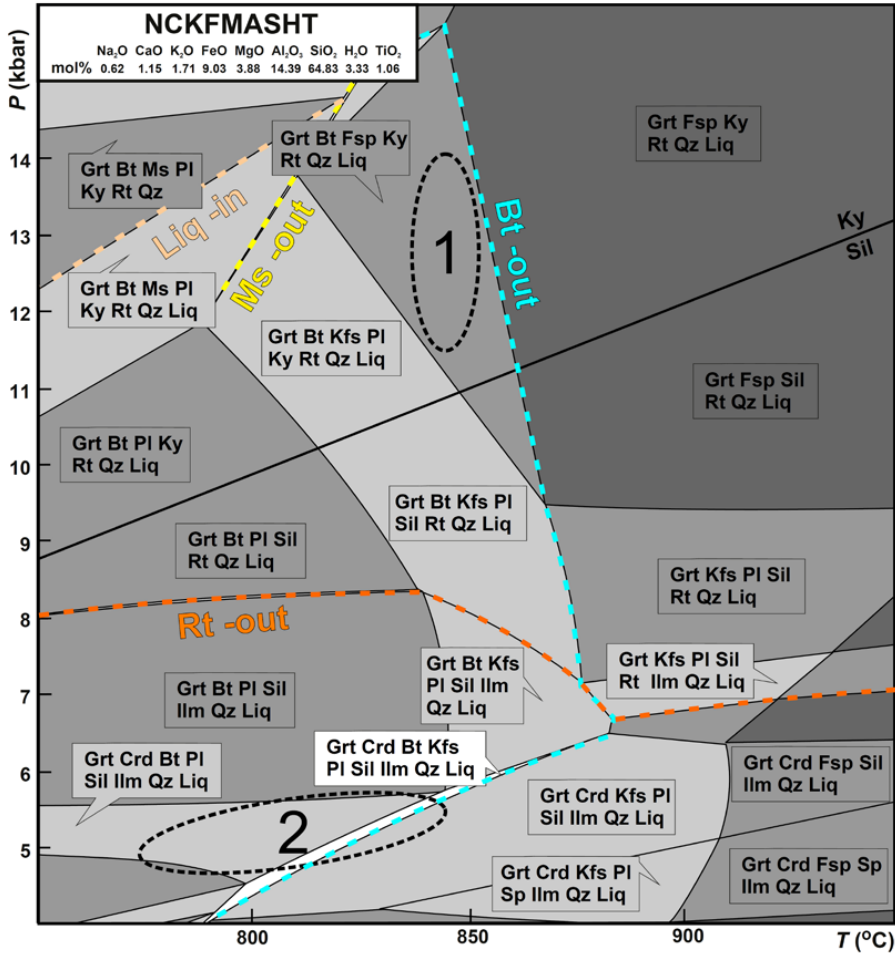


Figure 4.8. *P-T* section for the mylonitic gneiss JU-7 calculated in the system NCKFMASHT. Regions 1 and 2 indicate peak and post-peak *P-T* conditions, respectively, calculated based on phase equilibria modeling, conventional thermobarometry and microstructural observations. Liquid-in, Ms-out, Bt-out and Rt-out reactions are also shown. See text for details.

porphyroclasts and its inclusions of Ky, Pl, Bt, nanogranite and Rt. The post-peak *P-T* conditions, recorded in the rims of large Grt and its Sil and Bt inclusions, in the Crd coronas around Grt and in the matrix, are characterized by approximately similar *T* but much lower *P*, below the Rt-out reaction and in the cordierite stability field, at around $\approx 5\text{-}6$ kbar (Fig. 4.8). Both of these *P-T* conditions are at a higher temperature than the Ms fluid-absent melting reaction, and at slightly lower temperatures than the Bt fluid-absent melting reaction.

The GASP barometer (calibrations of Koziol, 1989 and Koziol and Newton, 1988), and the Grt-Bt (calibrations of Thompson, 1976; Ferry and Spear, 1978; Hodges and Spear, 1982) and Grt-Crd thermometers (calibrations of Bhattacharya et al. 1988; Holdaway and Lee, 1977; Thompson, 1976) have been used for thermobarometric calculations. Peak *T* of 740-840 °C (at 10-15 kbar) were calculated using cores of large (5-10 mm) Grt and inclusions of Bt in contact with the analyzed Grt cores. Peak *P*, calculated from cores of large Grt and inclusions of Pl in the cores, show a large variation between 8 and 12 kbar (at 750-850 °C). Post-peak *T* of 740-870 °C or 650-770 °C (at 4-6 kbar; Crd stability field in Fig. 4.8) were obtained using Grt rims and inclusions of Bt in the rims, or Grt rims and Crd coronas, respectively.

4.2 Discussion

4.2.1 Primary Nature and Significance of the MI: Comparison with Previous Studies

The study of MI in crustal anatectic rocks is a rather new subject and approach to the investigation of partial melting of the continental crust. Melt inclusions were first documented and studied in detail in partially melted metasedimentary enclaves in El Hoyazo dacite, where trapped melt solidified to glass due to rapid cooling upon ascent and extrusion of host magma (Cesare 2008; Cesare and Maineri 1999; Cesare et al. 2003; Cesare et al. 1997). The glassy nature and large size of these inclusions made possible its direct analysis by EMP and LA-ICP-MS. These MI represent primary anatectic melts generated during partial melting of the enclaves at depth, because: (i) they are trapped within minerals crystallized during anatexis at pressures of \approx 5-7 kbar (ii) they are primary inclusions based on their distribution in the host (following criteria from (Roedder, 1984); (iii) they have leucogranitic compositions similar to glasses generated in experimental studies of crustal anatexis, and close to the haplogranitic eutectics (Acosta-Vigil et al. 2010; Acosta-Vigil et al. 2007; Cesare et al. 2007; Cesare et al. 2003; Cesare et al. 1997).

Melt inclusions were also described in crustal crystalline rocks, such as UHP gneisses and eclogites associated with subduction of continental crust (Ferrando et al. 2005; Gao et al. 2012; Gao et al. 2013; Hwanga et al. 2001; Korsakov and Hermann 2006; Lang and Gilotti 2007; Liu et al. 2013; Zeng et al. 2013), and LP-to-MP anatectic

terrane associated with crustal thickening (Bartoli et al. 2013a; Cesare et al. 2011; Cesare et al. 2009; Darling 2013). In the case of UHP rocks, inclusions have been named as melt inclusions, multiphase inclusions, or polyphase inclusions, and have been interpreted as former melts or dense supercritical fluids. Several of these studies establish the primary nature of these inclusions based on either their random distribution (e.g. in Grt) or their preferred distribution along crystallographic directions (e.g. in Ky). Melt inclusions of LP-to-MP anatectic rocks contain either a polycrystalline granitic aggregate with typical igneous microstructures, or a polycrystalline granitic aggregate plus silicate glass, or only silicate glass, and hence have been named nanogranites, partially crystallized MI, and glassy MI, respectively (Ferrero et al. 2012). The primary nature of these inclusions was also established on the basis of their spatial distribution, as they show as rounded clusters of inclusions either in the center or randomly distributed throughout the host. The major elements concentrations of these MI have been precisely measured in some cases, either by the direct analysis of the glassy MI, or after the development of an appropriate experimental technique to remelt and homogenize nanogranites and partially crystallized MI (Bartoli et al. 2013a). In all cases these inclusions are leucogranitic in composition (Bartoli 2012; Bartoli et al. 2013b; Cesare et al. 2011; Cesare et al. 2009; Ferrero et al. 2012).

As in previous studies, we interpret MI in the gneisses of Jubrique as primary and representing primary melts generated during the anatexis of the host rock. This is based on their mostly random spatial distribution throughout the entire crystals (i.e. from core to rim) of a typical peritectic mineral such as Grt, as well as on the presence of a granitic mineral assemblage and/or glass with a typical granitic EDS spectrum (Figs. 4.6 and 4.7). Melt inclusions in these rocks may appear completely crystallized, partially crystallized, or constituted by glass without any crystalline phase. All these type of inclusions may be present in the same Grt crystal. The presence of glass in inclusions from deep crystalline rocks is a rather unexpected though apparently common feature, that has been attributed to, first, a pore size effect (crystallization is inhibited in the smaller inclusions) and, second, to factors that may inhibit nucleation such as the absence of preexisting nuclei or irregularities on the MI walls (Cesare et al. 2011; Ferrero et al. 2012). This study supports the hypothesis of the pore size effect, as glass has been found in relatively small ($\leq 20 \mu\text{m}$) MI. We interpret that Qz, Fsp, Kfs, Pl, Bt and Ms represent daughter minerals crystallized from the former melt, because: (i) they

constitute either the major or common minor minerals that crystallize from granite melts; (ii) Qz and feldspars show intergrowth microstructures typical of simultaneous crystallization from a melt (Figs. 4.6h, 4.6l); (iii) they nucleate on and crystallize from the planar walls, or adapt their shape to the negative crystal shape of MI; (iv) they fill the offshoots present in some MI (Fig. 4.7i). Conversely, Ky, Gr, Spl, Zrn, Rt, Ilm, Mnz and some crystals of Bt and Qz are interpreted as accidental minerals trapped with the melt, based on: (i) their relative large size compared with the size of MI and their low solubility in granitic melts (e.g. see Acosta-Vigil et al. (2003) for the case of aluminosilicates; Figs. 4.6a, 4.7b); (ii) the presence of indentations of these minerals within the walls of MI (Fig. 4.6g); (iii) presence of inclusions of these minerals in Grt. In particular, Ky is present within most of the studied MI, both at the cores and rims of Grt and, in addition to the above observations, Ky in MI from rims of Grt appears rimmed by low-Zn Spl as Ky crystals present in the matrix of the rock (Figs. 4.6k-1, 4.7j). The most frequent mineral that favored the trapping of MI in these gneisses was Ky, followed by Gr and more rarely Zrn, Rt, Ilm and Mnz.

Melt inclusions in this study show two remarkable features: a large size (mean of $\approx 30\text{-}40\ \mu\text{m}$ and maxima up to $\approx 200\ \mu\text{m}$) and the systematic presence of trapped Ky. This contrasts with MI in LP-to-MP anatectic rocks, which show a smaller size (mean and maximum diameters of $\approx 5\text{-}15\ \mu\text{m}$ and $\approx 50\ \mu\text{m}$, respectively) and were trapped in the P-T stability field of Sil. Sillimanite has not been observed as solid inclusion (trapped mineral) within MI at Jubrique. Instead, the main solid inclusion, in addition to Ky, are Gr, Zrn and Ilm. However, Sil has not been previously described as an accidental phase within MI. Instead, the main accidental phases that helped the entrapment of MI in LP-to-MP terranes are Gr and accessory minerals such as Zrn and Ilm. Melt inclusions in Jubrique show a few of the characteristics found in MI of UHP rocks. Reported MI in UHP terranes commonly show diameters of tens of micrometers, and some of them may reach up to 100-150 or even 200-250 μm . Also, some of the MI in UHP rocks contain Ky. However, our very detailed study did not identify minerals such as diamond, phengite and paragonite within MI of Jubrique, minerals that have only been described in MI from UHP rocks. Although diamond and coesite have been reported in Grt from gneisses of apparently similar composition and structural location in the Moroccan Rif (the southern branch of this arcuate Alpine orogen; (Ruiz-Cruz, 2012; Ruiz-Cruz, 2013), we have only identified graphite. Graphite occurs as euhedral

lamellae, and never as octahedral or rounded aggregates, which may instead suggest the presence of former diamond.

4.2.2 P-T Conditions of Melting and Implications of Nanogranites

Previous studies on the P - T conditions of these gneisses have mostly reported isothermal or near-isothermal decompression P - T paths, from ≈ 12 - 14 kbar at 730 - 800 °C to ≈ 3 - 4 kbar at 700 - 800 °C (Argles et al. 1999; Balanyá et al. 1997; Platt et al. 2003c; Torres-Roldán 1981). Among these, only Platt et al. (2003a) have placed the anatectic event in the P - T path: during decompression and growth of Grt rims in the field of Sil, at ≈ 6 - 7 kbar and 820 °C. For this, they have used the following arguments: (i) Grt rims, containing abundant Sil needles, show higher Grs contents than the cores, which they interpret to reflect partial melting in the matrix during this stage of growth; (ii) leucocratic bands, parallel to the main foliation, are assumed to represent anatectic leucosomes and to develop concomitantly to this main foliation, which is interpreted as decompressional. Partial melting has been associated with the breakdown of either white mica (Argles et al. 1999) or biotite (Platt et al. 2003b).

The recent report of diamond and coesite in Grt from gneisses of the Rif (Ruiz-Cruz and de Galdeano 2012; Ruiz-Cruz and Sanz de Galdeano 2013) have led these authors to propose that the earliest metamorphic event recorded by these rocks corresponds to UHP/UHT conditions of $P > 6$ GPa and $T > 1150$ °C, and that a first stage of melting occurred during this UHP/UHT event. During our detailed study, we have found no textural, mineralogical or petrologic evidence for UHP metamorphism in the investigated gneisses from the Betic Cordillera. In addition, pseudosection modeling and conventional thermobarometry place the peak P - T conditions of these rocks at ≈ 12 - 14 kbar and ≈ 800 - 850 °C, with post-peak conditions characterized by similar T and lower P of ≈ 5 - 6 kbar. The low pressure estimate is based on the first appearance of Crd in Fig. 4.8. The P - T estimates are in accordance with petrographic observations (relationships among Grt porphyroclasts, Ky, Sil, Rt and Ilm, see below) and most of the previous thermobarometric studies.

To interpret the information provided by the nanogranites and include it in the history of the rock, it is necessary to determine the timing of its entrapment within the host Grt. Nanogranites appear throughout the entire Grt crystals, from core to rim, including the largest Grt present in the studied thin sections (up to ≈ 1 cm in diameter).

Peak and post-peak P - T conditions were obtained from the cores and rims of these largest Grt, and hence (i) nanogranites were trapped, and melt was present, during both peak and post-peak P - T conditions, and (ii) most Grt in the gneisses grew in the presence of melt. These conclusions are also supported by the following microstructural observations. Nanogranites present at the cores of large Grt frequently include Ky; they may also include accidental Rt (Fig. 4.6). In addition, single mineral inclusions of Ky and Rt have been observed nearby nanogranites present at Grt cores. Nanogranites present at the rims of large Grt crystals frequently include also accidental Ky, although in this case Ky appears commonly rimmed by low-Zn Spl (Fig. 4.6k-l); nanogranites may include Rt but also Ilm (Fig. 4.6j). In addition, single mineral inclusions of Ky, Sil, Rt, Rt partially transformed to Ilm, and Ilm, may appear in the vicinity of nanogranites present at the rims. This indicates that during growth of Grt rims in the field of Sil and Ilm, they trapped droplets of melt present in the rock, together with relict Ky and Rt. We have not observed Sil within nanogranites, suggesting that this phase does not favor the trapping of MI as Ky does.

The above conclusions contrast with the previous hypothesis, based solely on petrographic observations and mineral compositions, that melting started during decompression and in the field of Sil (Platt et al. 2003b). This constitutes an example of the potential of the study of nanogranites in anatectic rocks. A preliminary study on the remelting of these nanogranites has provided leucogranitic compositions for the melt inclusions (Barich et al. 2014). Future detailed remelting studies will shed light on the precise compositions of the primary anatectic melts and the fluid regime during partial melting at Jubrique. In this regard, the coexistence of MI and apparently primary carbonate-bearing FI in some of the investigated Grt (Figs. 4.4h, 4.4k) suggests that during some time in the history of these rocks granitic melts and CO₂-bearing fluids coexisted. This uncommon coexistence of granitic melt and CO₂-bearing fluids during generation of crustal magmas has been previously reported in rapidly cooled crustal anatectic enclaves present within volcanic rocks (Cesare et al. 2007; Ferrero et al. 2011) and, more recently, in metamorphic enclaves within granodiorites (Ferrero et al. 2014).

Many of the previous studies have linked the two main P - T stages of equilibration recorded by these gneisses through an isothermal or near-isothermal decompression path (e.g. Argles, 1999; Balanyá, 1997; Platt, 2003; Torres-Roldán, 1981). However, several Zrn and Mnz geochronological studies conducted on these polymetamorphic

have associated the main mineral assemblages in the gneisses either to the Variscan, or the Alpine, or to both orogenic cycles (e.g. Michard, 1997; Montel et al. 2000; Whitehouse and Platt 2003; Rossetti et al. 2010). In this contribution we caution over the possibility that Grt cores and Grt rims, and therefore their associated P - T conditions and included nanogranites, formed during two separated events in time (e.g. see Montel, 2000; Whitehouse and Platt 2003). In relation with this, the reaction(s) responsible for the production of melt will depend on the P - T - t evolution of these rocks, as well as on the possibility that H₂O-rich fluids were present during anatexis. Pseudosection modeling and measured peak and post-peak conditions suggest, however, that Bt fluid-absent melting may have been important for the production of melt, as previously suggested by Argles et al. (1999) and Platt et al. (2003b).

5 The Composition of Nanogranitoids in Migmatites overlying the Ronda peridotites (Betic Cordillera, S Spain): the Anatectic History of a Polymetamorphic Basement

5.1 Introduction

Recent studies have demonstrated that melt inclusions (MI) constitute a new and powerful tool to investigate crustal anatexis (Cesare 2008; Cesare et al. 2009, 2011, under review). Studies of MI in crustal anatectic enclaves found within peraluminous dacites of SE Spain have shown that these trapped droplets of melt, now solidified to glass due to rapid ascent and extrusion, can provide precise information on the composition of primary anatectic melts during, and on the mechanisms of, crustal anatexis (Cesare et al. 1997, 2003; Acosta-Vigil et al. 2007, 2010, 2012a). In fact, MI represent a window into the suprasolidus prograde evolution of anatectic rocks (Acosta-Vigil et al. 2010).

Former MI were known to exist in deeply subducted, ultrahigh-pressure (UHP) crustal crystalline rocks, where they have been named as melt, polyphase, or multiphase inclusions (e.g. Hwang et al. 2001; Stockhert et al. 2001; Ferrando et al. 2005; Korsakov and Hermann 2006; Gao et al. 2012; Frezzotti and Ferrando 2015). However, detailed microstructural and, particularly, geochemical studies on these small data repositories in slowly cooled crystalline rocks, have only developed after the recent discovery of MI in low-to-medium P anatectic terranes (Cesare et al. 2009), building up on the previous studies of glassy MI of anatectic enclaves (Cesare et al. 1997, 2003; Cesare 2008; Acosta-Vigil et al. 2010, 2012a). Thus, detailed studies of MI in anatectic terranes have shown the great potential of this new approach, providing precise information on the primary compositions of melt from a particular terrane and lithology, including volatile concentrations and clues on the fluid regime during partial melting

(Cesare et al. 2009, under review; Bartoli et al. 2013a, 2014; Ferrero et al. 2015). Most of the MI in crystalline rocks, however, appear today crystallized to a granitic assemblage due to slow cooling at depth, with grain size commonly $<1 \mu\text{m}$; Cesare et al. (2009) named them as nanogranites. A previous and fundamental step for the detailed studies on these crystallized MI has been the development and further refinement of appropriate methodologies to rehomogenize them successfully under high P, in order to prevent MI decrepitation and interaction with the host mineral and matrix rock (Bartoli et al. 2013b; see also Malaspina et al. 2006; Perchuk et al. 2008). After application of this experimental methodology and subsequent analysis of several occurrences of nanogranites, Cesare et al. (under review) have observed that the studied MI have bulk compositions varying from granitic to granodioritic, trondhjemitic and tonalitic, and hence they have renamed them as nanogranitoids.

Barich et al. (2014) have documented the presence of crystallized MI in Grt from strongly deformed, former high P granulitic migmatites overlying the Ronda peridotite slab, in the Betic Cordillera of S Spain (hereafter mineral abbreviations after Kretz 1983). Despite the mylonitic microstructure of these former migmatites (hereafter referred to as porphyroclastic gneisses, after Barich et al. 2014), the microstructural study of MI has shown that they are present throughout the entire (up to 15-20 mm in diameter) Grt porphyroclasts, whose compositional profiles and mineral inclusion systematics attest for a polymetamorphic history (Barich et al. 2014, and references therein). Our study focuses on the experimental remelting of these MI, and the subsequent analysis of the major element compositions of the glass (quenched melt). Along with providing further constraints on the anatectic history and metamorphic evolution of the crustal units overlying the Ronda peridotite, this research constitutes an effort towards exploring the applications of the detailed study of MI in migmatites and granulites, and building up a composition database of MI in anatectic terranes, particularly for rocks such as these high P granulites. The latter are transitional between the two thermal environments registered by low-to-medium P and high P to UHP granulites, and are thought to form during continental collision at the base of thickened continental crust, or during subduction of the crust into the mantle (e.g. O'Brian and Rötzler 2003; Brown 2007). Since both environments are important regarding the investigation of crustal genesis and differentiation processes (e.g. Vielzeuf et al. 1990; Schmidt et al. 2004; Hermann and Spandler 2008; Hacker et al. 2011; Sawyer et al.

2011; Brown 2013), high P granulites are particularly relevant rocks for the study of MI.

5.2 Petrography and Microstructures of Melt inclusions

This study deals with the remelting and rehomogenization of MI in garnets of the porphyroclastic gneisses of Jubrique –equivalent to the lower gneiss series of Loomis (1972), granulites of Argles et al. (1999) and garnet gneiss of Platt et al. (2003). They constitute a \approx 300-500 m-thick sequence of dark, Grt-rich and rather massive rocks, except for the presence of frequent mm-to-cm (rarely dm) Grt-bearing leucocratic bands (former leucosomes) that defines the main foliation of the rock, Sp (Figs. 5.2a-b). Garnet is present in both leucocratic and mesocratic to melanocratic bands. Thin, Grt-absent and Bt-Crd-bearing leucocratic veins, intruded into the gneisses apparently under ductile-to-fragile conditions, are frequent and crosscut the main foliation at high angle (Barich et al. 2014).

Garnets from sample JU-8 of the porphyroclastic gneisses (Fig. 5.1) were selected as the starting material of this experimental study, due to their abundance in MI (Figs. 5.2c, d). The microstructures of these rocks have been described in detailed by Barich et al. (2014) and references therein; we summarize below the most relevant features. Porphyroclastic gneisses are mostly mylonitic rocks made of abundant to frequent Grt, Qz, Pl, Kfs, Ky, Sil and Crd, scarce to rare Bt, and accessory Spl, Gr, Ap, Rt, Ilm, Zrn and Mnz. They show a fine-grained (\approx 20-200 μ m) matrix of Qz+Pl+Kfs+Als \pm Crd, that includes porphyroclasts of Grt, Ky and Kfs. Based on microstructural criteria, these minerals have been grouped into three main assemblages. Cores of large (\approx 5-20 mm in diameter) Grt and their unoriented inclusions of Ky, Rt, Pl, Bt, Qz and melt represent the oldest, peak and pre-Sp high P mineral assemblage (\approx 850-800 $^{\circ}$ C, 1.4-1.2 GPa). Rims of large Grt and small (\leq 3 mm) Grt in the matrix, together with their inclusions of Sil, Ilm and melt, and oriented Sil, Qz, Pl, Kfs and Ilm in the matrix, constitute a pre-to-syn-Sp, medium-to-low P post-peak assemblage. Undeformed coronas of Sil or Spl+Pl \pm Crd \pm Kfs around relicts of oriented Ky in the matrix, and of Crd+Qz+Bt+Ilm \pm Kfs \pm Spl \pm Pl replacing Grt rims, constitute post-Sp assemblages formed at \approx 800-750 $^{\circ}$ C and 0.6-0.4 GPa. Leucocratic bands, parallel to Sp (Figs. 5.2a, b), are granitic and composed of Qz, Kfs, Pl and accessory Grt, Sil and Ilm,

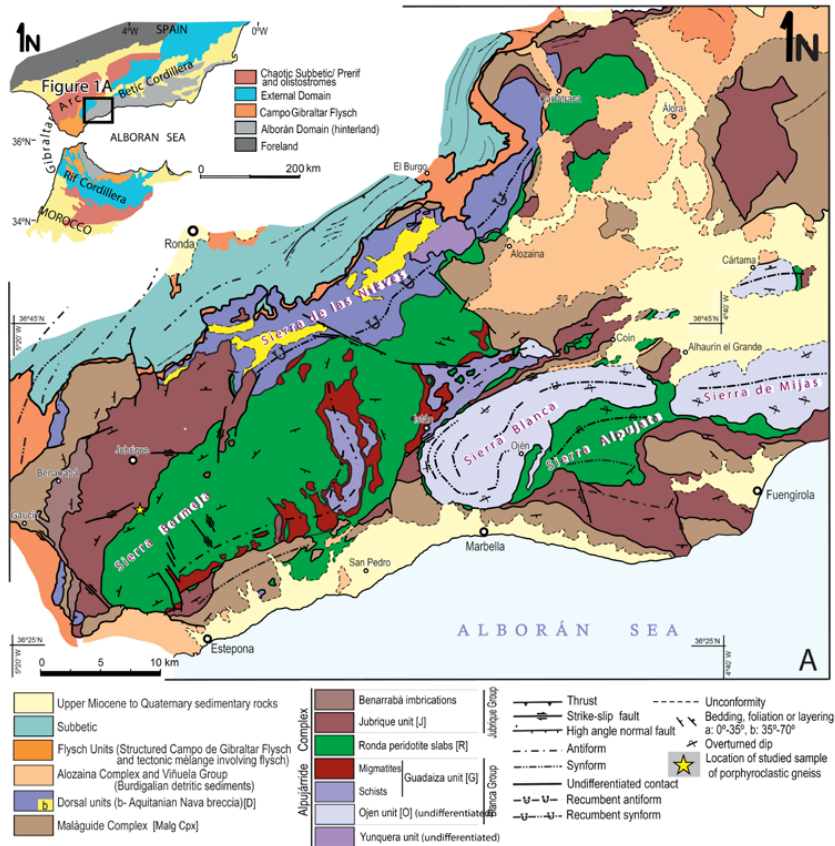


Figure 5.1. Geological maps of the Betic-Rif orogen and the studied area in the western Betic Cordillera of S Spain (modified from Balanyá *et al.* 1997; including data from Martín-Algarra 1987; Sanz de Galdeano and Andreu 1995; Mazzoli and Martín-Algarra 2011; Tubía *et al.* 2013). The location of the studied sample JU-8 is shown as a yellow star.

with relict Ky and Rt. Although deformed under ductile conditions, they still show some microstructures indicating the former presence of melt, and record melt-rich domains segregated before or during development of Sp. Biotite-Crd bearing leucocratic veins crosscutting Sp are undeformed, mostly made of Qz and Pl (i.e. tonalitic or trondhjemitic), have subhedral microstructure, and hence contrast in composition and microstructures with respect to former leucosomes.

Melt inclusions appear scattered from core to rim of large and small garnets (Figs. 5.2c, d). Due to the large proportion of Grt, presence of MI throughout the entire crystal and very small amount of Bt, Grt has been interpreted as a peritectic mineral formed together with the melt during Bt-breakdown melting reactions (see Barich *et al.* 2014). Most of the MI correspond to nanogranitoids, i.e. totally crystallized

polycrystalline inclusions (Cesare et al. 2009, under review). They are isometric, often have negative crystal shapes, range between ≈ 5 to 200 μm in diameter and have a mean size of ≈ 30 -40 μm (Figs. 5.2b, c). Melt inclusions in the cores of large Grt occur in the vicinity of single inclusions of Ky and Rt, whereas MI at the rims of large Grt, or in small Grt, are often associated with inclusions of Sil, Ilm and relict Ky and Rt. In general, MI towards the cores of large Grt are smaller (≈ 5 -15 μm) with respect to those at the rims (commonly ≥ 20 μm), where some of the crystallized minerals can be identified by optical microscope (Figs. 5.2c, d). Totally to partially crystallized MI are composed of daughter Qz, Pl (albite to bytownite), Kfs, ternary feldspar, Bt, Ms, rare calcite, and trapped crystals of Ky (\pm Spl), Gr, Phl, Zrn, Mnz, Rt, Ilm and Ap (Fig. 5.2e). Crystals of Ky are present within most of the MI, and represent the main solid inclusion that favored the entrapment of MI during Grt growth; they are mostly anhedral and, in MI at the rims of large Grt appear partially replaced by a low-Zn, hercynitic Spl. Ilmenite occurs only within MI located at the rim of large Grt, whereas Rt, Zrn and Mnz have been found throughout the entire host. Offshoots around MI have been observed in a few cases; they are filled with daughter minerals and do not necessarily show a radial distribution. Conversely, MI are commonly affected by late fractures crosscutting the entire Grt. Some small rounded cavities can be interpreted as micro- to nano-porosity; Raman micromapping conducted in similar microstructures from other MI study (Bartoli et al. 2013a) strongly suggest that they were filled with fluid dissolved in the former hydrous melt that exsolved upon crystallization. Some fluid inclusions, of possible primary origin, are spatially associated with MI in clusters within Grt.

5.3 Results

5.3.1 Microstructures of Remelted Nanogranitoids

All exposed MI from the experimental runs (850 to 800 $^{\circ}\text{C}$) show glass (former melt). The extent of melting, however, is variable regardless of temperature and microstructural location of MI. Exposed remelted MI vary in size from ≈ 5 to 200 μm and, in addition of glass, they commonly have Als and, less frequently Gr, Zrn, Rt, Sp and Mnz crystals. The large size of the crystals compared to the MI, and the low solubility of these minerals in granitic melts (e.g. Watson and Harrison 1983; Montel

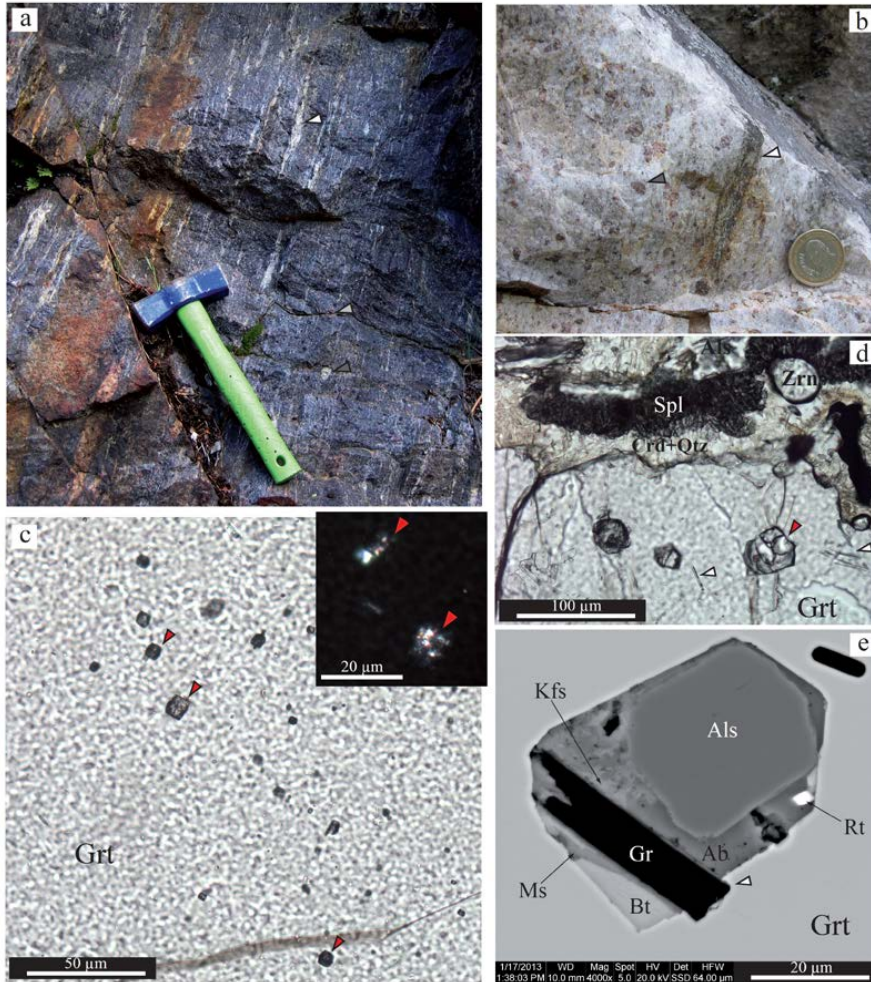


Figure 5.2. (a, b) Field appearance of the studied porphyroclastic gneiss (a, former migmatites; white arrow shows a cm-thick former leucosome; dark and light grey arrows show Kfs and Grt porphyroclasts, respectively; the hammer is 29 cm long) and a dm-thick leucocratic band parallel to the main foliation of the rock (b, former leucosome; grey and white arrows show Grt crystals and schlierens, respectively; the coin is 25 mm across; modified after Fig. 5.2c of Barich et al. 2014). (c, d) Plane-polarized light photomicrographs of small crystallized MI (c), mostly found towards the cores of large Grt crystals and in the vicinity of single Ky and Rt inclusions; and large crystallized MI (d), generally found towards the rims of large Grt crystals, and spatially associated with single Sil and Ilm inclusions. Although most of the inclusions in (c) and (d) correspond to crystallized MI, red arrows show those most clearly distinguishable. White arrows in (d) show inclusions of Sil needles. Notice that, in the case of the large MI, individual minerals are clearly visible and some of them can be identified under the optical microscope. This is not the case of the small MI, whose polycrystalline nature is clearly visible under cross-polarized light (small inset in Fig. 5.2c, representing an enlargement of two of the MI shown in Fig. 5.2c), though minerals cannot be identified under the microscope. (e) Backscattered electron (BSE) scanning electron microscope (SEM) image of a large crystallized MI in Grt (modified after Fig. 5.6g of Barich et al. 2014). Notice the indentation of Gr within the MI walls (white arrow), indicating the accidental nature of this mineral in this MI.

1993; Acosta-Vigil et al. 2003; Stepanov et al. 2012; Boehnke et al. 2013), indicates that they are solid inclusions (i.e. were already present during the entrapment of the MI) and hence are not expected to dissolve into the melt during the experiments (Table 5.1). In fact, these minerals are commonly present in most of the starting material, i.e. the unmelted MI, sometimes with clear microstructures indicating their accidental nature (Fig. 5.2e, and Barich et al. 2014). Among the potential daughter minerals (i.e. those that commonly constitute major or minor minerals in granitoid rocks), Bt and Qz are the most commonly present in the studied remelted MI (Table 5.1). Hereafter, “rehomogenized MI” refers to MI that after experimental remelting: (i) have negative crystal (or at least regular) shape with no decrepitation cracks; (ii) show no reaction with the host Grt, such as recrystallization of the Grt or crystallization of new minerals at the MI-Grt interface; and (iii) is formed by glass \pm accidental minerals, with no reactions between accidental minerals and melt, and no coexisting vapor –i.e. bubbles (Danyushevsky et al. 2002; Audetat and Lowenstern 2013). Conversely, “remelted MI” refers to MI having glass but lacking some or all of the above characteristics.

Table 5.1 Conditions and key information of all the conducted MI remelting experiments. All experiments were run at 1.5 GPa during 24 hrs

Experiment label	AB1-Rim8		AB1-SG8		AB3-Core8		AB3-Core8	
	850		850		825		825	
Run temperature	850		850		825		825	
Microstructural location of MI ^a	RIG		SG		CLG		CLG ²	
Type of MI	II		II		II		I	
No. of documented MI	14		13		22		2	
No. of rehomogenized MI	2		3		3		0	
% of rehomogenized MI	14		23		14		0	
No. of MI analyzed by EMP	13		7		12		2	
No. of MI analyzed by nanoSIMS	8		0		4		0	
Accidental minerals in remelted MI	Als ₁₀₀ St ₀ Gr ₀ Rt ₀ Spl ₀ Mnz ₀ Zrn ₀		Als ₀ Spl ₀ Rt ₀ Gr ₀ St ₀ Zrn ₀ Bt ₀ Qtz ₀		Als ₀ Zrn ₀ St ₀ Gr ₀ Rt ₀ Bt ₀ Spl ₀ Ap ₀		Bt ₀ Qtz ₀ Fsp ₀	
Daughter minerals in remelted MI	Bt ₀ Qtz ₀ Pl ₀		Bt ₀		Bt ₀ Qtz ₀ Cc ₀ Kfs ₀		Bt ₀ Qtz ₀ Fsp ₀	
No. of MI with offshots	3		4		4		0	
No. of MI with Ky rimed by St	5		1		4		0	
No. of MI with Grt recrystallization	2		3		1		0	
No. of MI showing irregular walls	3		4		4		0	
No. of MI showing bubbles	1		0		1		1	

^a CLG refers to Core of large Grt; RIG to rim of large Grt; SG to small Grt.

^b When a single experiment show MI of both leucogranitic and granodioritic-tonalitic compositions, we have separated the information corresponding to each of these two compositional types of MI.

The first experiments, conducted at 850 °C, showed few rehomogenized MI and abundant disequilibrium microstructures (Figs. 5.4a-d). Melt inclusions failed to rehomogenize as attested by the presence of: (i) frequent daughter crystals; (ii) reaction between accidental Als and melt to form St (Als is never rimmed by St in the starting materials, see Barich et al., 2014); (iii) irregular MI walls; and (iv) thin (\approx 1-10 μ m) recrystallized Grt domains at the Grt-MI boundary, indicated by variation of grey tone in BSE images with respect to the rest of the starting Grt (Table 5.1). Within MI, euhedral rims of St grow on, and replace Als after reaction with the melt, which may have produced a change in the composition of the originally trapped melt. This reaction,

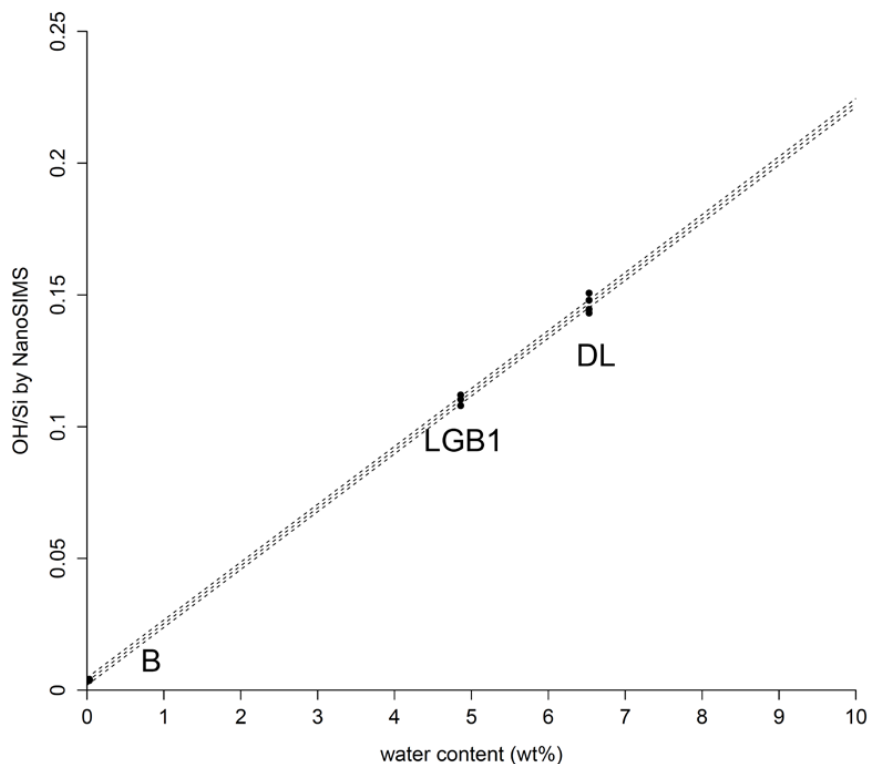


Figure 5.3. NanoSIMS calibration curve determined for the analytical session during which the experimental glasses in remelted and rehomogenized MI were analyzed. This linear calibration is based on the H₂O concentrations measured by Elastic Recoil Detection Analysis (ERDA) on the reference glasses B, LGB1 and DL. OH/Si stands for 16OH⁻/28Si⁻ determined by NanoSIMS. Replicates on each standard are reported. The spread shows the reproducibility during the analytical session. See text for details.

together with the presence of recrystallized Grt, decrepitation cracks and irregular MI boundaries, suggest that these inclusions were overheated.

Experiments conducted at 825 °C also show a low proportion of apparently rehomogenized MI and abundant disequilibrium microstructures as those described above, i.e. persistence of daughter minerals, reaction of Als+melt to St, irregular MI walls, presence of offshoots and recrystallization of Grt at the Grt-MI boundaries (Figs. 5.4e-h, Table 5.1). No clear differences between microstructures in remelted MI at the cores and rims of large Grt crystals have been observed, and hence 825 °C (at 1.5 GPa) is not the appropriate homogenization temperature for MI at any of the microstructural locations.

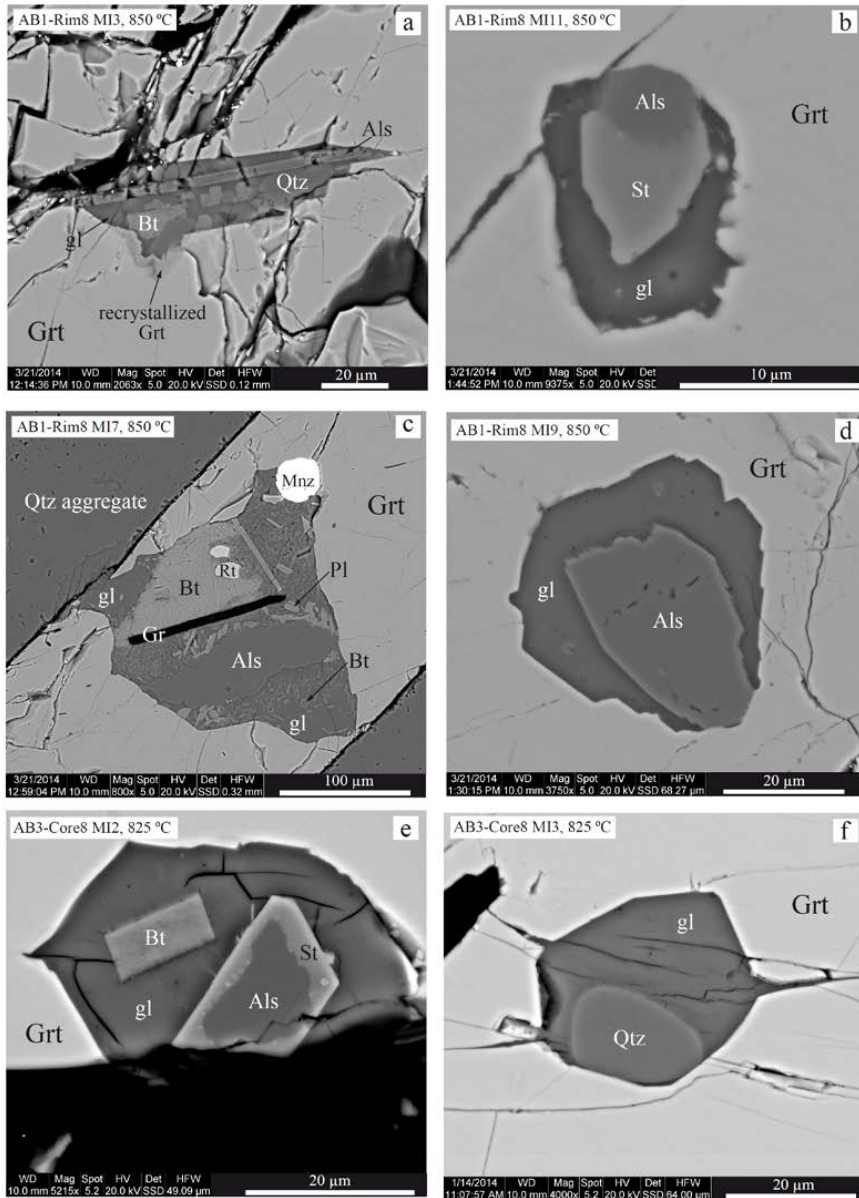


Figure 5.4. BSE-SEM images of remelted and rehomogenized nanogranitoids in several microstructural locations, after quenching of the 850 °C (a-d), 825 °C (e-h) and 800 °C (i-l) experiments. 850 °C and 825 °C experiments show a low proportion of rehomogenized MI (d, h), and abundant disequilibrium microstructures such as frequent partially dissolved daughter crystals (a, c, f, g), reaction between accidental Als and melt to form St (b, e), irregular MI walls (a, b, c, g), presence of offshoots (b, f) and recrystallized Grt at the boundary with the MI (a, g). 800 °C experiments show a larger number of rehomogenized MI (i-k), but also remelted MI (l).

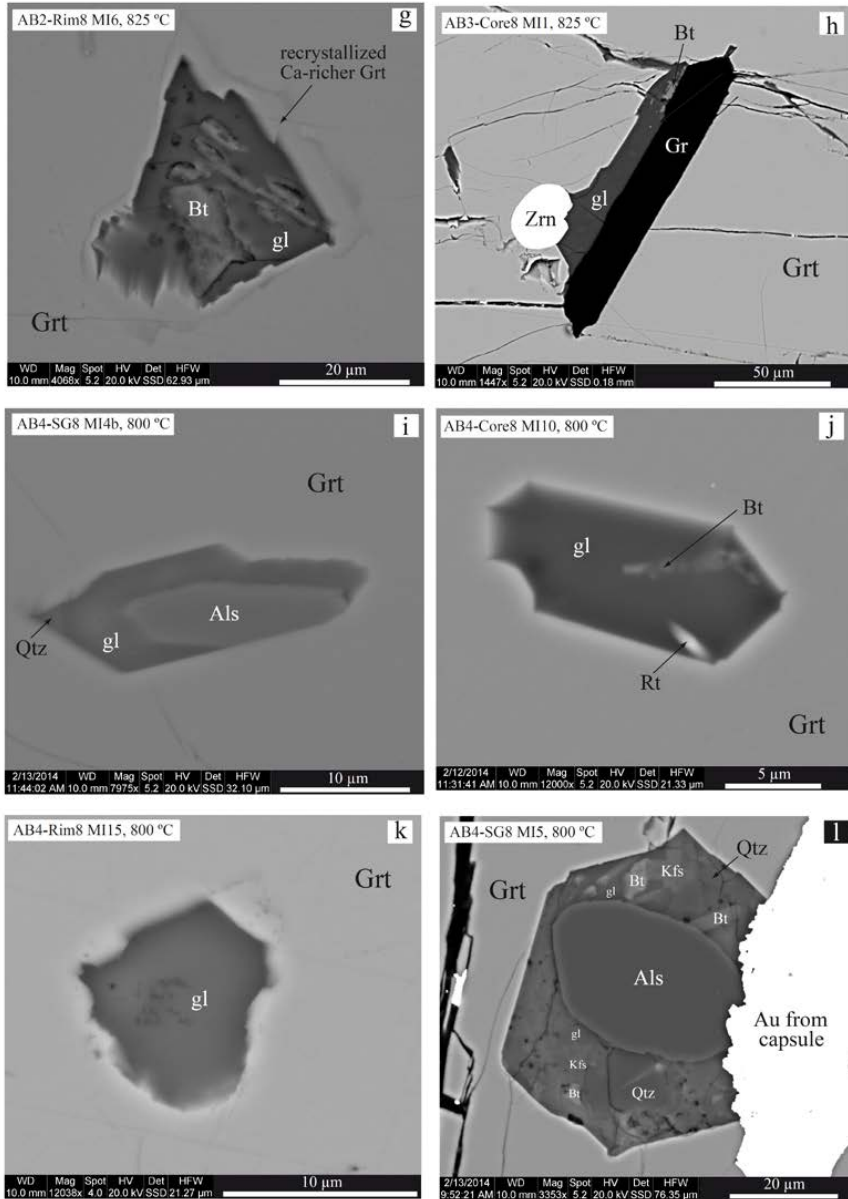


Figure 5.4 (continued) BSE-SEM images of remelted and rehomogenized nanogranitoids in several microstructural locations, after quenching of the 850 °C (a-d), 825 °C (e-h) and 800 °C (i-l) experiments. 850 °C and 825 °C experiments show a low proportion of rehomogenized MI (d, h), and abundant disequilibrium microstructures such as frequent partially dissolved daughter crystals (a, c, f, g), reaction between accidental Als and melt to form St (b, e), irregular MI walls (a, b, c, g), presence of offshoots (b, f) and recrystallized Grt at the boundary with the MI (a, g). 800 °C experiments show a larger number of rehomogenized MI (i-k), but also remelted MI (l).

Remelted nanogranitoids at 800 °C show a much closer approach to equilibrium (Figs. 5.4i-l). With respect to the higher T experiments, the proportion of apparently rehomogenized MI increases (up to ≈35 %), Als appears stable and is not replaced by St, walls of MI are mostly regular and many of them show negative crystal shapes, and offshoots are nearly absent (Table 5.1). No microstructural differences have been observed among the different locations, except for the case of MI within small Grt that seem somewhat further from equilibrium compared to MI at cores and rims or large Grt.

5.3.2 Composition of Glass in Remelted Nanogranitoids

The analyzed glasses from both remelted and rehomogenized MI have moderate to strongly peraluminous granitoid compositions [$ASI \approx 1.05-1.50$, $mean = 1.31$; $ASI = mol. Al_2O_3 / (CaO + Na_2O + K_2O)$], with mostly high SiO_2 ($\approx 65-73$ wt%, $mean = 66$ wt%), low $FeO + MgO + TiO_2$ ($\approx 0.7-3.0$ wt%, $mean = 1.8$ wt%), and variable CaO, alkalis and H_2O concentrations (Table 5.2). They distribute into two distinct compositional groups. Type I MI show low concentrations of CaO ($\approx 0.3-1.0$ wt%), variable though mostly low H_2O ($\approx 2-8$ wt%, $mean = 5$ wt%; H_2O by difference), higher K_2O ($\approx 3.5-6.5$ wt%) and K# [$mean = 0.55$; $K\# = mol. K_2O / (K_2O + Na_2O)$] and lower Mg# [≈ 0.30 ; $Mg\# = mol. MgO / (MgO + FeO)$] (Fig. 5.5). These glasses are granitic in composition (Fig. 5.6a) and, in Qz-Or-Ab normative pseudoternary diagrams, they plot in the vicinity of H_2O -undersaturated haplogranitic eutectics and Qz-Or cotectic lines (Fig. 5.6b), as most of the previously analyzed glassy MI and rehomogenized nanogranitoids reported in the literature (Cesare et al., under review). Type II MI have moderate to high CaO ($\approx 1.5-3.0$ wt%), high H_2O (8-14 wt%, $mean = 12$ wt%; H_2O by difference), lower K_2O ($\approx 1.0-2.5$ wt%) and K# (0.35) and higher Mg# (0.40). These glasses are granodioritic, trondhjemitic and tonalitic in composition (Fig. 5.6a) and, unlike most of the previously analyzed natural or experimental glasses coming from the partial melting of metasedimentary rocks, they plot far from the haplogranitic eutectics and surprisingly close to the Qz-Ab sideline of the normative Qz-Or-Ab pseudoternary diagram (Fig. 5.6b). In addition, they define a broad trend parallel to the Qz-Ab sideline.

When glass within large single MI is analyzed two or more locations, it shows a rather homogeneous composition, and hence each of the analyzed remelted and rehomogenized MI pertains to either type I or type II. The two compositional groups of MI are unrelated to the location of glass either in remelted or rehomogenized MI.

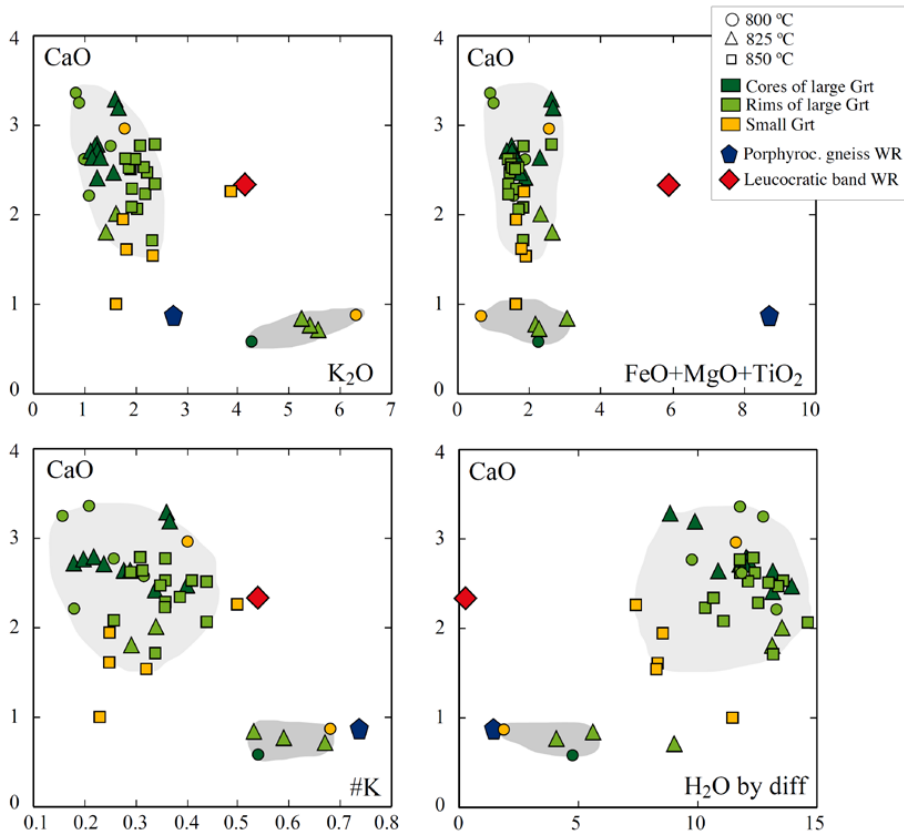


Figure 5.5. Harker diagrams of analyzed glasses in remelted and rehomogenized nanogranitoids. The complete EMP glass dataset (≈ 80 analyses, see Table 5.2) includes analyses affected by some contamination from host Grt and/or trapped minerals (shown by somewhat higher FeO, MgO and TiO₂ concentrations, and ASI values) and extensive Na loss (manifested by values of ASI > 1.5 after correction for Na loss). These values have not been considered when calculating mean concentrations (Table 5.2), and the corresponding analyses have not been included in Figs. 5.5 and 5.6. Dark and light grey areas represent the compositional domains corresponding to type I and type II MI, respectively. The bulk rock compositions of the studied porphyroclastic gneiss and the thick leucocratic band shown in Fig. 5.2b (former leucosome) are shown in blue and red symbols, respectively. Notice that the former leucosome contrasts in composition with respect to any of the analyzed MI. In particular, the leucosome is nominally anhydrous and show much higher FeO+MgO+TiO₂ concentrations (≈ 6 wt%).

Instead, these groups seem mostly related to the microstructural location of the MI. Thus, type I is mostly formed by MI coming from the cores of large Grt, whereas type II is mostly constituted by MI present at the rims of large Grt and within small Grt.

The H₂O concentrations of glass in remelted and rehomogenized MI determined by NanoSIMS span a wide range of values between ≈ 3 -14 wt% (Table 5.3). Figure 5.7 compares glass H₂O concentrations measured by NanoSIMS and estimated by EMP-difference. For the majority of analyzed MI (≈ 60 %) the two techniques provide quite

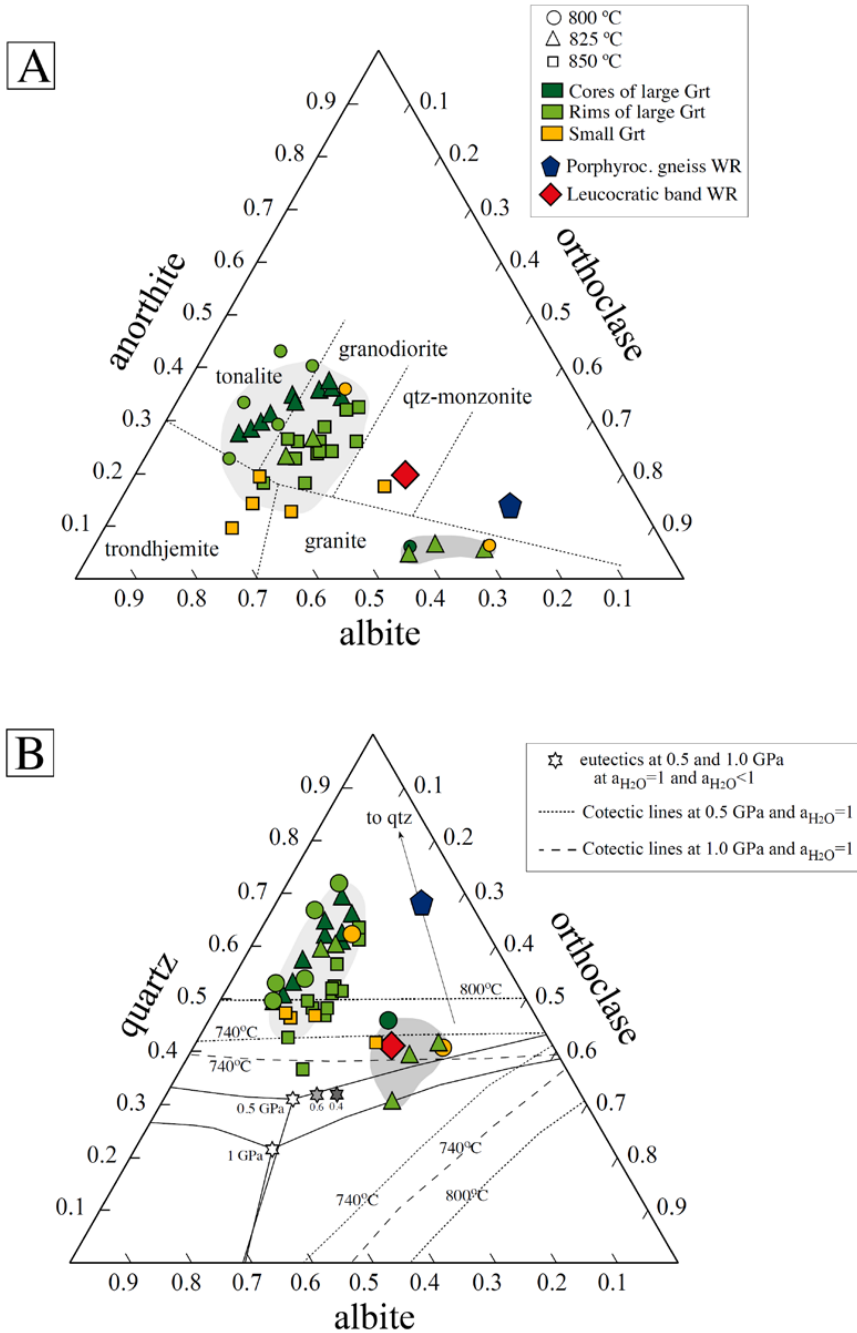


Figure 5.6. Anorthite-Or-Ab (a) and Qz-Or-Ab (b) pseudoternary normative diagrams (in wt%) for the analyzed glasses in remelted and rehomogenized nanogranitoids. Dark and light grey areas, and blue and red symbols, as in Fig. 5.5. Notice that although the analyzed leucosome have Qz-Or-Ab proportions similar to type I MI, leucosome and MI are different in composition (Fig. 5.5).

Table 5.2 Mean major element concentrations (wt%) and standard deviations of experimental glasses in all the conducted nanogranitoid remelting experiments

Experiment label	AB1-Rim8		AB1-SG8		AB3-Core8		AB3-Core8		AB2-Rim8		AB2-Rim8		AB4-Core8		AB4-Rim8		AB4-SG8	
	850	850	850	850	825	825	825	825	825	825	825	825	800	800	800	800	800	800
Run temperature	850		850		825		825		825		825		800		800		800	
Microstructural location of MI ^a	RLG	SG	CLG	CLG	CLG	CLG	CLG	CLG	RLG	RLG	RLG	RLG	CLG	CLG	RLG	RLG	SG	SG
	II	II	II	II	I	I	I	I	II	II	I	I	I	I	II	II	II	I
Type of MI	16 to 21; 10		5 to 7; 4		6 to 15; 5		2 to 3; 0		5 to 12; 2		3 to 4; 0		2 to 6; 8		3 to 6; 15		1 to 3; 3	
No. anal. by EMP; or by nanoSIM	16 to 21; 10		5 to 7; 4		6 to 15; 5		2 to 3; 0		5 to 12; 2		3 to 4; 0		2 to 6; 8		3 to 6; 15		1 to 3; 3	
SiO ₂	64.63 (1.17)	66.59 (0.57)	65.31 (1.36)	70.05 (1.46)	66.74 (1.44)	69.75 (2.83)	70.16 (1.29)	70.16 (1.29)	66.22 (2.26)	65.22 (2.26)	66.20 (0.04)	66.20 (0.04)	73.89	73.89	66.20 (0.04)	66.20 (0.04)	66.20 (0.04)	66.20 (0.04)
TiO ₂	0.12 (0.06)	0.10 (0.12)	0.08 (0.02)	0.04 (0.03)	0.09 (0.02)	0.02 (0.01)	0.07 (0.06)	0.07 (0.06)	0.07 (0.03)	0.07 (0.03)	0.06 (0.03)	0.06 (0.03)	0.01	0.01	0.06 (0.03)	0.06 (0.03)	0.06 (0.03)	0.06 (0.03)
Al ₂ O ₃	13.80 (0.31)	14.97 (0.60)	14.40 (0.75)	11.67 (0.78)	13.30 (0.67)	13.02 (1.84)	14.89 (0.98)	14.89 (0.98)	14.09 (0.84)	14.09 (0.84)	13.02 (0.28)	13.02 (0.28)	14.31	14.31	13.02 (0.28)	13.02 (0.28)	13.02 (0.28)	13.02 (0.28)
FeO*	1.31 (0.22)	1.29 (0.21)	1.23 (0.27)	2.79 (0.88)	1.49 (0.28)	2.24 (0.69)	2.14 (0.59)	2.14 (0.59)	1.44 (0.34)	1.44 (0.34)	1.71 (0.31)	1.71 (0.31)	0.62	0.62	1.71 (0.31)	1.71 (0.31)	1.71 (0.31)	1.71 (0.31)
MgO	0.48 (0.16)	0.35 (0.06)	0.64 (0.22)	0.67 (0.24)	0.66 (0.09)	0.54 (0.24)	0.46 (0.07)	0.46 (0.07)	0.42 (0.07)	0.42 (0.07)	0.69 (0.06)	0.69 (0.06)	0.03	0.03	0.69 (0.06)	0.69 (0.06)	0.69 (0.06)	0.69 (0.06)
MnO	0.02 (0.03)	0.04 (0.06)	0.02 (0.01)	0.04 (0.02)	0.02 (0.02)	0.04 (0.04)	0.09 (0.02)	0.09 (0.02)	0.03 (0.03)	0.03 (0.03)	0.01 (0.01)	0.01 (0.01)	0.00	0.00	0.01 (0.01)	0.01 (0.01)	0.01 (0.01)	0.01 (0.01)
CaO	2.24 (0.38)	1.64 (0.43)	2.73 (0.29)	0.65 (0.34)	1.65 (0.48)	0.76 (0.07)	0.48 (0.13)	0.48 (0.13)	2.46 (0.52)	2.46 (0.52)	2.94 (0.03)	2.94 (0.03)	0.87	0.87	2.94 (0.03)	2.94 (0.03)	2.94 (0.03)	2.94 (0.03)
Na ₂ O	2.53 (0.72)	3.64 (0.42)	2.59 (0.64)	2.20 (0.35)	2.22 (0.38)	2.44 (0.61)	2.88 (1.24)	2.88 (1.24)	1.75	1.75	2.94 (0.03)	2.94 (0.03)	1.94	1.94	2.94 (0.03)	2.94 (0.03)	2.94 (0.03)	2.94 (0.03)
K ₂ O	2.00 (0.29)	2.12 (0.84)	1.40 (0.19)	3.70 (0.78)	1.52 (0.19)	4.84 (1.17)	3.97 (1.00)	3.97 (1.00)	1.58 (0.28)	1.58 (0.28)	1.75	1.75	6.31	6.31	1.58 (0.28)	1.58 (0.28)	1.58 (0.28)	1.58 (0.28)
P ₂ O ₅	0.10 (0.08)	0.12 (0.10)	0.08 (0.07)	0.20 (0.28)	0.08 (0.04)	0.08 (0.09)	0.01 (0.01)	0.01 (0.01)	0.05 (0.02)	0.05 (0.02)	0.05 (0.02)	0.05 (0.02)	0.10	0.10	0.05 (0.02)	0.05 (0.02)	0.05 (0.02)	0.05 (0.02)
F	0.01 (0.02)	n.d.	0.00 (0.01)	0.02 (0.01)	0.00 (0.01)	0.00 (0.01)	0.01 (0.01)	0.01 (0.01)	0.00 (0.00)	0.00 (0.00)	0.00 (0.00)	0.00 (0.00)	0.01	0.01	0.00 (0.00)	0.00 (0.00)	0.00 (0.00)	0.00 (0.00)
Cl	0.10 (0.02)	n.d.	0.09 (0.02)	0.03 (0.01)	0.09 (0.03)	0.03 (0.02)	0.02 (0.01)	0.02 (0.01)	0.09 (0.04)	0.09 (0.04)	0.15 (0.02)	0.15 (0.02)	0.00	0.00	0.15 (0.02)	0.15 (0.02)	0.15 (0.02)	0.15 (0.02)
Total	87.47 (2.00)	91.29 (1.41)	88.22 (1.47)	92.75 (0.65)	87.96 (1.82)	93.74 (2.52)	96.77 (1.10)	96.77 (1.10)	87.22 (2.53)	87.22 (2.53)	87.74 (0.98)	87.74 (0.98)	98.09	98.09	87.74 (0.98)	87.74 (0.98)	87.74 (0.98)	87.74 (0.98)
H ₂ O by difference (100-EMP tota)	12.5 (2.0)	8.7 (1.4)	11.8 (1.5)	7.25 (0.65)	12.04 (1.82)	6.26 (2.52)	3.2 (1.1)	3.2 (1.1)	12.8 (2.5)	12.8 (2.5)	12.3 (1.0)	12.3 (1.0)	1.91	1.91	12.3 (1.0)	12.3 (1.0)	12.3 (1.0)	12.3 (1.0)
H ₂ O by nanoSIMS	9.95 (2.67)	9.3 (1.3)	7.35 (1.24)	n.d.	6.81 (0.83)	n.d.	6.13 (1.95)	6.13 (1.95)	10.31 (1.63)	10.31 (1.63)	9.74 (1.82)	9.74 (1.82)	n.d.	n.d.	9.74 (1.82)	9.74 (1.82)	9.74 (1.82)	9.74 (1.82)
ASI	1.36 (0.16)	1.36 (0.09)	1.35 (0.10)	1.38 (0.10)	1.50 (0.02)	1.18 (0.11)	1.42 (0.11)	1.42 (0.11)	1.39 (0.27)	1.39 (0.27)	1.27	1.27	1.23	1.23	1.27	1.27	1.27	1.27
#K	0.35 (0.06)	0.30 (0.10)	0.27 (0.08)	0.51 (0.11)	0.32 (0.04)	0.60 (0.07)	0.49 (0.15)	0.49 (0.15)	0.25 (0.07)	0.25 (0.07)	0.40	0.40	0.68	0.68	0.25 (0.07)	0.25 (0.07)	0.25 (0.07)	0.25 (0.07)
FeO†+MgO†+TiO ₂	1.91 (0.26)	1.80 (0.13)	1.94 (0.48)	3.49 (1.11)	2.24 (0.29)	2.80 (0.70)	2.66	2.66	1.93 (0.41)	1.93 (0.41)	2.46 (0.31)	2.46 (0.31)	0.66	0.66	2.46 (0.31)	2.46 (0.31)	2.46 (0.31)	2.46 (0.31)
#Mg	0.39 (0.08)	0.32 (0.06)	0.47 (0.03)	0.30 (0.04)	0.44 (0.06)	0.30 (0.10)	0.27 (0.02)	0.27 (0.02)	0.34 (0.02)	0.34 (0.02)	0.42 (0.06)	0.42 (0.06)	0.07	0.07	0.42 (0.06)	0.42 (0.06)	0.42 (0.06)	0.42 (0.06)

* Total Fe as FeO; n.d. not determined.

^a CLG refers to Core of large Grt; RLG to rim of large Grt; SG to small Grt.

^b When a single experiment show MI of both leucogranite and granodioritic-tonalitic compositions, we have separated the information corresponding to each of these two compositional types of MI.

^c Number of analyses used in the calculated mean concentrations and standard deviations.

Table 5.3 H₂O concentrations in experimental glasses (wt%) measured by NanoSIMS and EMP

Experiment_ML_Analysis no.	H ₂ O by NanoSIMS	1 sigma error	¹⁶ OH/ ²⁸ Si	H ₂ O by difference
800 °C, cores of large garnets				
AB4C8_MI1bis_1	5.66	0.07	1.28E-01	2.8
AB4C8_MI2_1	9.46	0.07	2.11E-01	9.4
AB4C8_MI5_1	3.42	0.06	7.84E-02	3.4
AB4C8_MI8_1	8.29	0.07	1.85E-01	5.9
AB4C8_MI8_2	5.99	0.07	1.35E-01	6.7
AB4C8_MI10_1	4.60	0.07	1.04E-01	n.d.
AB4C8_MI10_2	5.23	0.07	1.18E-01	n.d.
AB4C8_MI12_1	6.37	0.07	1.43E-01	4.8
Mean (standard deviation)	6,13 (1,95)			
800 °C, rims of large garnets				
AB4R8_MI1_1	11.26	0.08	2.50E-01	10.8
AB4R8_MI1_2	9.37	0.07	2.09E-01	11.8
AB4R8_MI5_1	12.12	0.08	2.69E-01	n.d.
AB4R8_MI5_2	10.51	0.08	2.34E-01	n.d.
AB4R8_MI7_1	13.08	0.08	2.91E-01	12.3
AB4R8_MI7_2	9.62	0.07	2.14E-01	15.9
AB4R8_MI10_1	8.73	0.07	1.95E-01	n.d.
AB4R8_MI10_2	10.23	0.08	2.28E-01	n.d.
AB4R8_MI10_3	9.39	0.07	2.09E-01	n.d.
AB4R8_MI12_1	9.55	0.07	2.13E-01	13.3
AB4R8_MI12_2	8.09	0.07	1.81E-01	12.7
AB4R8_MI12_3	7.99	0.07	1.79E-01	n.d.
AB4R8_MI15_1	11.70	0.08	2.60E-01	16.7
AB4R8_MI15_2	10.01	0.07	2.23E-01	n.d.
AB4R8_MI16_1	13.05	0.08	2.90E-01	n.d.
Mean (standard deviation)	10,31 (1,63)			
800 °C, small garnets				
AB4_SG8_MI4_1	7.65	0.07	1.71E-01	n.d.
AB4_SG8_MI4_2	10.99	0.08	2.45E-01	n.d.
AB4_SG8_MI4_3	10.58	0.08	2.36E-01	n.d.
Mean (standard deviation)	9,74 (1,82)			
825 °C, cores of large garnets				
AB3C8_MI3_1	6.90	0.07	1.55E-01	14
AB3C8_MI3_2	6.12	0.07	1.38E-01	11.5
AB3C8_MI9_1	7.60	0.07	1.70E-01	n.d.
AB3C8_MI28_1	9.36	0.07	2.09E-01	n.d.
AB3C8_MI28_2	6.77	0.07	1.52E-01	n.d.
Mean (standard deviation)	7,35 (1,24)			
825 °C, rims of large garnets				
AB2R8_MI1_1	6.22	0.07	1.40E-01	n.d.
AB2R8_MI3_1	7.40	0.07	1.66E-01	12.7
Mean (standard deviation)	6,81 (0,83)			
850 °C, rims of large garnets				
AB1R8_MI1_1	8.43	0.07	1.88E-01	n.d.
AB1R8_MI3_1	7.52	0.07	1.68E-01	13.6
AB1R8_MI5_2	14.19	0.09	3.15E-01	13.4
AB1R8_MI6_1	10.63	0.08	2.37E-01	11.3
AB1R8_MI6_2	9.81	0.07	2.19E-01	n.d.
AB1R8_MI9_1	5.30	0.07	1.20E-01	n.d.
AB1R8_MI9_2	10.46	0.08	2.33E-01	12.6
AB1R8_MI9_3	8.30	0.07	1.86E-01	13.6
AB1R8_MI11_2	12.93	0.08	2.87E-01	n.d.
AB1R8_MI13_1	11.96	0.08	2.66E-01	11.8
Mean (standard deviation)	9,95 (2,67)			
850 °C, small garnets				
AB1_SG8_MI9_5	10.1	0.12	2.78E-01	n.d.
AB1_SG8_MI9_6	10.7	0.12	2.95E-01	8.6
AB1_SG8_MI11_4	8.0	0.11	2.23E-01	7.44
AB1_SG8_MI11_1	8.3	0.11	2.29E-01	8.3
Mean (standard deviation)	9,3 (1,3)			

n.d. glass not analyzed by EMP

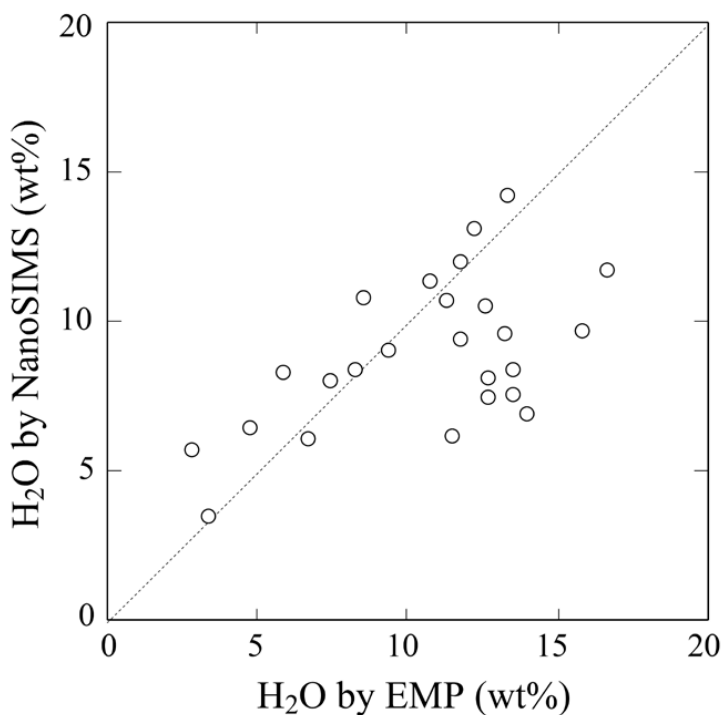


Figure 5.7. Comparison between H₂O concentrations estimated by the difference method (100-electron microprobe totals) and measured by NanoSIMS on experimental glass from the same MI.

similar results, as differences between both methods are $\leq 30\%$ relative, in good agreement with results from previous analyses of MI by NanoSIMS (Bartoli et al. 2014). However, a group of analyzed MI shows concentrations of H₂O by difference much higher ($\geq 40\%$ relative) than those by NanoSIMS (Fig. 5.7). This discrepancy has been mainly observed in MI located in the proximity of large Grt cavities produced during sample polishing. Because the ¹⁶OH⁻ and ²⁸Si⁻ signals were rather constant during analysis of MI away from these cavities, but variable during analysis of MI close to the cavities, we ascribe the large differences between H₂O concentrations by both methods to NanoSIMS instrumental instability associated with the presence of Grt cavities. Nevertheless, the NanoSIMS analyses confirm the EMP H₂O estimates, and in particular the high H₂O content of type II MI.

5.4 Discussion

5.4.1 P-T conditions of Anatexis at Jubrique

The microstructures of the experimental run products show that the frequency of disequilibrium features increases from 800 °C to 825-850 °C (Table 5.1, Fig. 5.4). Disequilibrium features include: (i) the presence of rather irregular and ragged boundaries between MI and host Grt, as opposed to straight, negative crystal shape boundaries; (ii) the change in composition of the host Grt at the boundaries with MI with respect to the starting composition, indicated by the variation in grey tones of BSE images and implying Grt-melt chemical interaction during the experiment (e.g. Perchuk et al., 2008); (iii) the destabilization of accidental Als to form St at the contact with melt; (iv) the presence of offshoots, suggesting decrepitation; and (v) the presence of abundant partially resorbed daughter minerals. Except for the presence of daughter minerals and rare offshoots, none of these features have been observed in the natural starting material (Barich et al. 2014). Concomitantly, there is a decrease in the proportion of apparently rehomogenized MI with increasing temperature, from 20-35% at 800 °C to 15-25% at 825 and 850 °C. In the only previous systematic study on the remelting of nanogranitoids from anatectic terranes, Bartoli et al (2013b) have found that the proportion of rehomogenized MI at the P-T conditions of anatexis of the rocks was ≈30-40%. They found equilibrium features in the rehomogenized MI such as negative crystal shape, absence of any daughter granitic minerals or bubbles, and presence of glass with typical leucogranitic compositions similar to those produced in experimental studies on crustal anatexis. The MI studied by Bartoli et al. (2013a, 2013b) are much smaller (≈5-15 μm across) than those studied from Jubrique. Considering the much larger size of MI in Jubrique, and the increase in rehomogenization timeframes with MI size found in previous studies on the remelting of crystallized MI (e.g. Thomas et al. 1996; Thomas and Klemm 1997; Bodnar and Student 2006; Zajacz et al. 2008), we conclude that: (i) the proportion of 20-35 % rehomogenized MI found at 800 °C is relatively high and likely large enough for the glass analyses to be representative of the trapped melt compositions; and (ii) the temperature of 800 °C is likely close to that of anatexis and MI entrapment in the studied rocks.

We have not considered variations in P during this experimental study. Among all the previously reported peak P for these rocks, including classical thermobarometric and phase equilibria modeling calculations (Loomis 1972; Torres-Roldán 1981; Balanyá et al. 1997; Argles et al. 1999; Platt et al. 2003; Barich et al. 2014; Massonne 2014), we have chosen the upper value of 1.5 GPa provided by most of these studies, expecting that this imposed external P on the Grt chips would prevent decrepitation of included MI due to increase in their internal P upon heating (e.g. Bartoli et al. 2013a). Following most of the previous petrologic studies, this P would correspond to that of generation of Grt cores (Loomis 1972; Torres-Roldán 1981; Argles et al. 1999; Platt et al. 2003; Barich et al. 2014). These experiments, conducted at a single P, cannot provide precise constraints on the P of anatexis of the host former migmatites. However, experimental results support that the P of anatexis should have been similar to or lower than 1.5 GPa, given that a relatively large number of studied MI did not decrepitate and rehomogenized at a combination of expected P-T anatexis conditions from previous thermobarometric studies, i.e. 800 °C and 1.5 GPa. It is unclear yet if departures of remelting experimental P above that of anatexis and MI entrapment would produce Grt-melt chemical interactions and hence lack of re-homogenization. Scarce experimental results on this issue suggest that departures of >0.5 GPa produce interaction of host Grt with melt and crystallization of new minerals (Ferrero et al. 2015). Nevertheless, further detailed experiments considering variations in P are required to investigate the effect of P on MI rehomogenization.

5.4.2 Significance of Glass Compositions in Remelted Nanogranitoids

The major element concentrations of analyzed glasses define two compositional groups corresponding to leucogranites (type I) and granodiorites-to-tonalites (type II) (Table 5.2, Figs. 5.6). Compared to the leucogranitic, granodioritic-to-tonalitic glasses represent the majority of the EMP analyses (80%), found within most (75%) of analyzed remelted/rehomogenized nanogranitoids. Most of them come from remelted MI located at the rims of large Grt or within small Grt, interpreted to record the latest stages in the evolution of the migmatites (Loomis 1972; Torres-Roldán 1981; Argles et al. 1999; Platt et al. 2003; Barich et al. 2014; Massonne 2014). On the other hand, the majority of leucogranitic glasses come from remelted/rehomogenized MI located at the cores of large Grt, interpreted to record the first documented stages in the evolution of

these rocks (op. cit.). Nevertheless, granodioritic-to-tonalitic glass has also been found in several MI within fragments of apparently large Grt cores (AB3-Core8, AB1-Core8), and leucogranitic glass was also found in a few MI within fragments of apparently large Grt rims or small Grt (AB4-SG8, AB2-Rim8; see Table 5.2).

Leucogranitic compositions have been so far the most frequently reported in (i) bulk rock analyses of leucosomes in metasedimentary/metagranitic migmatites (e.g. Sawyer 1996, 2008; and references therein), (ii) glass analyses from the relatively few reported studies of glassy MI in metasedimentary/metagranitic anatectic enclaves and rehomogenized nanogranitoids in migmatites and granulites (Cesare et al. 1997; 2003; 2009; 2011, and under review; Acosta-Vigil et al. 2007; Ferrero et al. 2012, 2014, 2015; Bartoli et al. 2013a, 2013b), and (iii) glass analyses in experimental studies on the fluid-absent anatexis of metasedimentary rocks (e.g. Vielzeuf and Holloway 1988; Patiño Douce and Johnston 1991; Montel and Vielzeuf 1997; Patiño Douce and Harris 1998; Schmidt et al. 2004; Hermann and Spandler 2008). The latter tell us that leucogranitic melts are produced during the dehydration melting of micas in metasedimentary/metagranitoid rocks, at moderate-to-low H₂O activities, within a wide range of mostly crustal P-T (\approx 750-900 °C, 0.1-1.3 GPa), but also at mantle conditions (up to 1000°C, 2.5-5 GPa) (op. cit.).

Compared to leucogranitic, granodioritic-to-tonalitic compositions are less frequently reported in bulk rock analyses of leucosomes and/or dikes/veins from metasedimentary anatectic terrains (e.g. Whitney and Irving 1994; García-Casco and Torres-Roldán 1996; Newton et al. 1998; Sawyer 2008; Morfin et al. 2013; Barich et al. 2014). A single study of rehomogenized MI in Grt from metasedimentary migmatites at the base of the Greater Himalayan Sequence (Kali Gandaki, Nepal) has recently reported tonalitic glass compositions (Carosi et al. 2015). Experimental granodioritic-to-tonalitic, CaO-rich, #K-low melts have been obtained during either the H₂O-saturated partial melting of metasedimentary rocks at \approx 675-775 °C and 0.6-1.4 GPa (Patiño Douce and Harris 1998; García-Casco et al. 2003; Ferri et al. 2009), or the fluid-absent partial melting of intermediate-to-basic rocks at \approx 825-1150 °C and 0.8-3.2 GPa (Rutter and Wyllie 1988; Hacker 1990; Rushmer 1991; Rapp et al. 1991; Rapp and Watson 1995; Schmidt et al. 2004). Accordingly, some of the studies of metasedimentary migmatites (Whitney and Irving 1994; García-Casco and Torres-Roldán 1996) and the recent study on the rehomogenization of MI by Carosi et al. (2015) have interpreted that

granodioritic-to-tonalitic compositions represent primary melts formed during H₂O-saturated anatexis.

5.4.3 Implications for the Geodynamic Evolution of Lower Continental Crust in the Betic Cordillera

The majority (75%) of the analyzed remelted/rehomogenized MI has granodioritic-to-tonalitic glass, and most of the reported analyses (Table 5.2, Figs. 5.6) come from apparently rehomogenized MI showing glass or glass plus solid inclusions such as Als or Zrn. We notice that, in addition to granodioritic-to-tonalitic MI, Barich et al. (2014) have described the presence of tonalitic veins crosscutting the main foliation of porphyroclastic gneisses, emplaced/segregated during the late history of these rocks. Based on experimental work (see above), one interpretation is that granodioritic-to-tonalitic melts at Jubrique may represent exotic liquids formed during the HP partial melting of a deeper intermediate-to-mafic source, and later segregated and intruded into metasedimentary rocks of upper crustal levels. However, the presence of granodioritic-to-tonalitic melt as inclusions within one of the major mineral components of these rocks, i.e. Grt, rather indicate anatexis of the host rock during growth of peritectic Grt. In addition, the existence of tonalitic veins is compatible in composition and timing with the presence of granodioritic-to-tonalitic MI at the rims of large garnets and within small garnets, recording the late magmatic history of these former migmatites. Hence we conclude that granodioritic-to-tonalitic glasses represent primary compositions of melt formed at some point during the anatectic history of these rocks, and particularly during partial melting under H₂O-rich fluid-present conditions (see above, and compare with Patiño-Douce and Harris 1998; García-Casco et al. 2003; Ferri et al. 2009).

Remelted/rehomogenized MI showing glass with leucogranitic composition are much less abundant, and their significance and meaning is more difficult to ascertain. On one hand, they may record former melts produced during partial melting of host migmatites under fluid-absent conditions (see above), and hence compositions of former MI may be compatible with two different melting scenarios of their host polymetamorphic metasedimentary rocks. On the other hand, leucogranitic glasses may result from some other processes, such as (i) the incomplete remelting of the MI (i.e. MI were not rehomogenized in all cases), or (ii) the entrapment of a compositionally heterogeneous melt present in the partially melted source (i.e. natural compositions

controlled by the kinetics of melting, and not by chemical equilibrium at constant P-T-X). We discuss below these two interpretations.

Although some leucogranitic glasses come from the analysis of partially crystalline MI (Fig. 5.4l), none of these partially remelted MI show any visible Ca-rich daughter mineral whose dissolution could produce, upon complete rehomogenization, a compositional shift towards Ca-rich, K-poor concentrations. In addition, the first melt fractions formed upon heating of a granitoid assemblage (i.e. the nanogranitoid) are expected to have the highest H₂O concentrations, as opposed to the lowest H₂O concentrations shown by leucogranitic glasses. Moreover, some of the leucogranitic glasses come from rehomogenized MI (Fig. 5.4j). Hence, and although the total number of rehomogenized leucogranitic MI is small, we conclude that leucogranitic melts have not been artificially produced during the experiments due to incomplete remelting of MI, but were present at some point during the anatectic history of the studied migmatites.

The trapping of a heterogeneous melt during a single, Grt-producing melting event in the migmatites is an explanation for the presence of leucogranitic and granodioritic-to-tonalitic melt compositions. The current experimental study has been conducted using a single rock sample (JU-8) but several (≈ 10) Grt crystals coming from a decimetric fragment of that sample. Distances between the studied Grt in this rock, therefore, are at least in the range of a few cm. Melt interconnection in partially melted metasedimentary rocks is expected to occur at the temperatures registered in the migmatites (≥ 800 °C; Laporte et al. 1997; Clemens 2006, and references therein). However, the interconnected melt is likely to be compositionally heterogeneous due to the sluggish diffusion of Si and Al in melt (Acosta-Vigil et al. 2006a, 2012b). Thus, melt in the vicinity of dissolving quartz crystals will be enriched in SiO₂ with respect to that close to feldspars, which will have higher Al₂O₃ concentrations (Acosta-Vigil et al. 2006b). Conversely, H₂O concentrations and, particularly, the ratio of alkalis throughout an interconnected melt network will show much lower concentration gradients, due to fast diffusion of these components in melt (Acosta-Vigil et al. 2002, 2006a, 2006b; Morgan et al. 2008). These diffusion systematics of granite melts can explain the linear trend shown by granodioritic-to-tonalitic glass compositions in the normative Qz-Or-Ab pseudoternary diagram (i.e. melts with very similar alkali ratios, but variable Si/Al ratios; compare with Fig. 10 of Acosta-Vigil et al. 2006b). However,

they cannot explain the coexistence of granodioritic-to-tonalitic and leucogranitic melts, constituting two well-defined clusters in the Qz-Or-Ab and Harker diagrams, and characterized by contrasting H₂O concentrations and alkali ratios (Figs. 5.6).

The above evidence, together with the distribution of most leucogranitic MI at the cores of large Grt, and most granodioritic-to-tonalitic MI at the rims of large Grt or within small Grt (Table 5.2), may suggest that former migmatites at Jubrique represented by the porphyroclastic gneisses underwent two melting events under contrasting fluid regimes. The first anatexis event occurred under fluid-absent and low aH₂O conditions, and was recorded by MI at the cores of large Grt. A second partial melting event took place in the presence of H₂O-rich fluids and was recorded by MI at the rims of large Grt and in small Grt of the matrix. Several geochronological studies have shown that basement rocks in the studied area of the Alpine Betic Cordillera still preserve Variscan minerals and/or fabrics (Acosta 1998; Sanchez-Rodríguez 1998; Zeck and Whitehouse 1999, 2002; Acosta-Vigil et al. 2014; Sánchez-Navas et al. 2014). In particular, studies of the porphyroclastic gneisses of Jubrique have shown that Grt cores likely formed during the Variscan orogeny, whereas Grt rims and the matrix of the rock may have crystallized during the Alpine (Whitehouse and Platt 2003; Massonne 2014; see also Montel et al. 2000; Rossetti et al. 2010). We tentatively suggest that the two reported glass compositions may reflect the anatexis of the host migmatites during two different orogenic events. Variscan anatexis formed the cores of large Grt and their leucogranitic MI, likely during the fluid-absent melting of Bt at ≈ 800 °C and 1.4-1.2 GPa. Alpine anatexis produced the growth of Grt rims on previous Variscan Grt and formed new small Grt in the matrix, together with the trapped granodioritic-to-tonalitic MI. This occurred during H₂O-rich fluid-present melting of the rock at similar T but lower P conditions (≈ 800 °C and 0.8-0.6 GPa), and associated with an incongruent melting reaction involving Grt growth.

5.4.4 Significance for Melt Inclusion Studies, Crustal Melting and Differentiation

Cesare et al. (1997) and Acosta-Vigil et al. (2007, 2010) have documented variations in the composition of glass (former melt) in metasedimentary anatexis enclaves (El Hoyazo, S Spain) as a function of microstructural location. Thus, glassy MI in Pl have different composition from glassy MI in Grt, which are also different in composition

from matrix glass. Acosta-Vigil et al. (2007, 2010, 2012a) have interpreted these variations as reflecting the evolution of melt composition during prograde anatexis and, on this basis, have provided information on the nature and mechanisms of anatexis in the enclaves during the prograde path, including melting reactions, fluid regimes, degree of melt homogeneity and extent of melt-residue equilibration. Later on, and during the novel studies of glassy and remelted MI in migmatites and granulites, Bartoli (2012) have documented variations in the composition of MI in Grt, this time as a function of the structural location of the host migmatite in the anatectic sequence of Ojén (Ronda, S Spain), and in turn of the T of formation. Thus, MI in Grt of lower T metatexites have different composition with respect to MI in Grt of higher T diatexites. The current study shows that MI composition may vary as a function of its microstructural location within a single mineral in the rock, i.e. Grt cores versus Grt rims. All the above indicates that MI compositions may vary systematically and at different scales: within a single mineral, among different minerals in the same rock, and among crystals of a single mineral present throughout a migmatitic sequence showing variations in T of formation. Hence, as in the studies of MI in anatectic enclaves (Acosta-Vigil et al. 2010), detailed investigation of MI in migmatites and granulites can supply information on the evolution of melt composition during the anatectic history of the rocks, as well as on the nature and mechanisms of the process of partial melting (see also Cesare et al. under review).

Recently, Aranovich et al. (2014) have discussed the potential role of the mantle as a source of extra heat and fluids to drive anatexis at deep crustal levels, melt ascent, and in turn differentiation of the continental crust. Among the problems raised by these authors against a pure fluid-absent incongruent melting model for anatexis and crustal differentiation, there is the presence of non-granitic –e.g. tonalitic– leucosomes in migmatites. The presence of low H₂O concentration leucogranitic MI at the cores of Grt in these former migmatites suggests that the bottom of a thickened continental crust partially melted under fluid-absent conditions. These observations are in accordance with a closed-system, fluid-absent melting model for anatexis and, in the case of melt extraction and ascent, crustal differentiation. However, based on the experimental results of Patiño Douce and Harris (1998), García-Casco et al. (2003) and Ferri et al. (2009), granodioritic-to-tonalitic MI at the rims of Grt also indicates that anatexis at mid-to-lower levels of an average continental crust took place in the presence of an

H₂O-rich fluid (see also Carosi et al., 2015). Aranovich et al. (2014) have proposed that CO₂-, Cl-rich fluids, coming from the outgassing of basaltic magmas, and later on split into carbonic and saline (alkalis- and halogens-rich) fractions as they cool and decompress, are important agents for open-system metamorphism and anatexis of deep crustal levels. The analyses of glass reported in this contribution show very low proportions of halogens and high concentrations of H₂O (Table 5.2), and do not support anatexis due to the presence of saline, but H₂O-rich fluids. Based on theoretical grounds, previous studies have concluded that the processes of crustal melting, genesis of granitoid magmas and crustal differentiation occurs in the absence of excess pervasive fluid (Clemens and Watkins 2001). However, the only direct available method to actually measure in situ the proportion and nature of volatiles in primary crustal melts, and hence to obtain precise information on the fluid regime during crustal anatexis, is the detailed study of MI (Cesare et al. 2011, under review; Bartoli et al. 2013a, 2014). And the current investigation tells us that H₂O-rich fluid-present partial melting did occur in metapelites of the middle-to-lower continental crust of the Ronda area. In fact, recent studies on anatexis are beginning to stress the importance of water-present melting in the continental crust (Sawyer 2010; and in particular Weinberg and Hasalová 2015). Another issue, beyond the scope of this contribution, is the origin of the fluids. Crustal rocks in general, and metapelites in particular, have only a very low proportion (<0.1 wt%) of free H₂O at temperatures slightly below their solidus, due to the strong reduction of porosity during prograde regional metamorphism (Yardley 2009). Hence, H₂O-rich fluid-present anatexis seems to indicate the influx of external fluids into the deep continental crust. Although previous investigations have provided some ways to introduce hydrous fluids of crustal origin into deep continental crust rocks (e.g. Brown 2010; Sawyer 2010; Weinberg and Hasalová 2014), the mechanisms of fluid infiltration during high-grade metamorphisms are not sufficiently understood yet (Brown 2013).

6 Unraveling the Age of the Polymetamorphic Evolution of the Alborán Basement: Garnet Lu-Hf Geochronology of Jubrique gneisses and Garnet Pyroxenites from the Ronda Peridotite ¹

6.1 Introduction

Accessory minerals, such as zircon and monazite, likely constitute the most suitable geochronometers in crustal rocks at amphibolite- and granulite-facies conditions (e.g. Hermann and Rubatto, 2003). One of the main issues that prevents from establishing reliable P-T-t paths and associated geodynamic scenarios for high-grade crustal rocks, is the difficulty of relating zircon and monazite ages with the crystallization of the P-T dependent major mineral assemblages in the rock. A clear example of this are the contradictory conclusions obtained by several zircon and monazite geochronological studies on the age of metamorphism in basement rocks of the highest-grade Alpujarride units (Fig. 6.1), and in particular on the Jubrique (or Beni Bousera, Rif) unit (Sánchez-Rodríguez, 1998; Platt and Whitehouse, 1999; Montel et al., 2000; Whitehouse and Platt, 2003; Rossetti et al., 2010; Ruiz-Cruz and Sanz de Galdeano, 2014; Massonne, 2014). To shed light on this problematic, we have dated large garnet crystals in samples from porphyroclastic and porphyroblastic gneisses from the basal crustal sequence of Jubrique, and from garnet pyroxenites in the underlying Ronda peridotite massif (Sierra Bermeja) near the contact with the Jubrique unit. Based on these new Lu-Hf garnet geochronology data and previously published data on zircon and monazite ages, we discuss the age of metamorphism and associated geodynamic scenarios recorded in the gneisses, and the geological relationships between the crustal sequence and the underlying peridotite slab.

¹ This chapter is part of a draft paper to be submitted to TECTONICS.

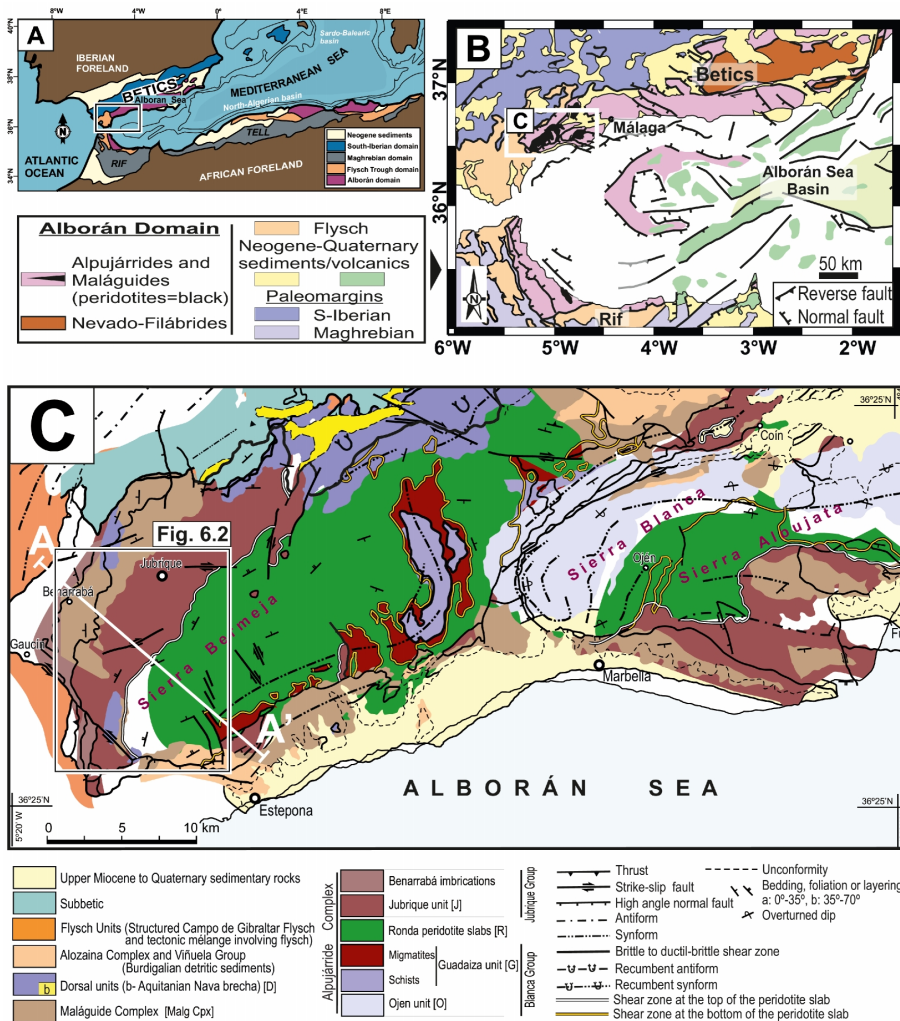


Figure 6.1. *a.* Sketch of the main tectonic units of the Betic-Rif-Tell Alpine orogenic belt and the Betic-Rif Gibraltar arc in the westernmost Mediterranean. The black and white rectangular frame shows the location of Fig. 6.1.b. *b.* Simplified geological map (modified after Comas et al. 1999 and Booth-Rea et al. 2007) with the main tectonic domains forming the Betic-Rif orogenic belt. Also shown is the location of the Ronda Peridotite in Betics and Beni Bousera Peridotite in the Rif mountains. The white rectangular frame shows the location of Fig. 6.1.c. *c.* Detailed geological map of the internal parts of the western Betic Cordillera of S. Spain (modified from Balanyá et al., 1997 and including data from Martín-Algarra, 1987; Sanz de Galdeano and Andreu, 1995; Mazzoli and Martín-Algarra, 2011; Tubía et al., 2013). The black and white rectangular frame indicates the location of the study area shown Fig. 6.2; the A-A' white solid line shows the location of the geological cross-section of the westernmost Alpujarrides shown in the Fig. 6.2.

6.2 Geological Setting

Here, we will provide a summary of the main structure of the study area (Fig. 6.1). For more details about the Regional Geology the reader is referred to Chapter 1. The study area is located in the Betic-Rif-Tell Alpine orogenic belt in the westernmost Mediterranean (Fig. 6.1a). The internal units of the Betic are composed of the Alboran domain, constituted by the Maláguide and the underlying Alpujarride complexes (Fig. 6.1b, c), and their Rif analogues the Sebtime and the Ghomaride complexes. The Alpujarrides and Sebtime complexes, which host, respectively, the Ronda and Beni Bousera peridotites, are two large slabs of subcontinental mantle peridotites (Fig. 6.1).

From top to bottom, a complete Alpujarride sequence is composed of non-metamorphic to greenschist-facies Triassic carbonates and Permo-Triassic phyllites and quartzites (e.g. Martín and Braga, 1987), graphitic micaschists, gneisses, migmatites and mylonites (deformed former migmatites) (e.g. Egeler and Simons, 1969; Tubía et al., 1997) (Fig. 6c). Carbonates, phyllites and quartzites constitute the post-Variscan sedimentary cover and therefore their metamorphism and deformation occurred during the Cenozoic associated with the Alpine orogeny (Martín and Braga, 1987). Schists, gneisses, migmatites and mylonites are pre-Mesozoic rocks and represent a crystalline basement during the Alpine orogeny (e.g. Egeler and Simons, 1969; Michard et al., 1997; Acosta, 1998; Sánchez-Rodríguez, 1998; Platt and Whitehouse, 1999; Zeck and Whitehouse, 1999, 2001; Montel et al., 2000; Acosta-Vigil et al., 2014).

The study area is located in the westernmost Alpujarrides, where it crops out the Jubrique section, a highly attenuated—but complete—crustal section that constitutes the crustal envelope of the Ronda peridotite slab (Fig. 6.1c). From top to bottom, the Jubrique crustal section (≤ 5 km) is composed of carbonates, low-grade phyllites with relict HP-LT assemblages followed by late andalusite, graphitic mica schists with prekinematic garnet, staurolite, and kyanite as well as synkinematic sillimanite and late andalusite schists, and kyanite and sillimanite garnet porphyroclastic and garnet-rich porphyroclastic to mylonitic gneisses along the contact with the peridotites (Figs. 6.1 & 6.2). A high temperature ductile shear zone separates the gneisses from the underlying the Ronda peridotites; this contact is parallel to the mylonitic foliation of the crustal rocks (Fig. 6.2).

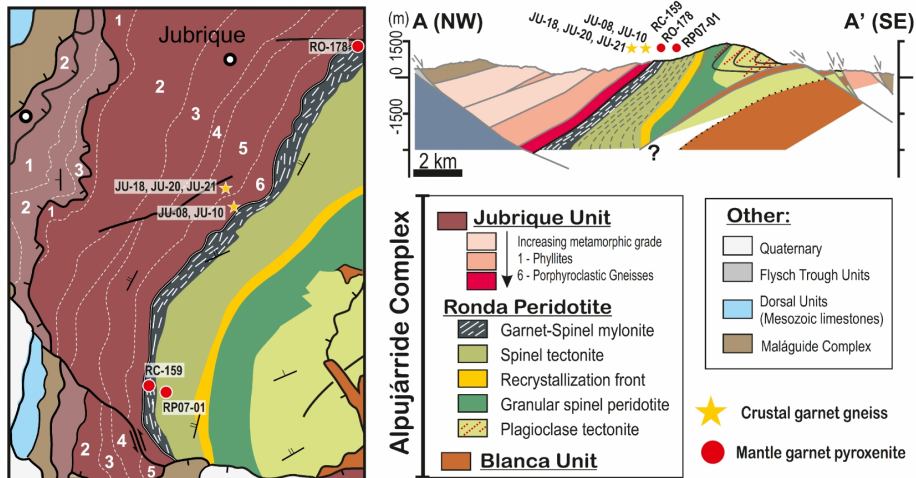


Figure 6.2. Simplified geological map showing the sample location in the Jubrique crustal unit and the westernmost part of the Ronda peridotite of the western Alpujarrides (see Fig. 6.1 for location in the realm of the Betic orogen). Isograd distribution is after Balanyá et al. (1997). Also shown are the tectono-metamorphic domains and internal structures of the western Ronda Peridotite (Van der Wal & Vissers 1996; Lenoir et al. 2001; Précigout et al. 2007; Soustelle et al. 2009). The Ronda Peridotite is outlined in black. The A–A' is the cross-section (shown in Fig. 6.1) the cross-section of the westernmost Alborán Domain in the Betic after Hidas et al. (2013), showing the approximate location of samples relative to the main tectono-metamorphic domains of the Ronda peridotite in this area.

In this area, the Ronda peridotite massif constitutes a coherent lithospheric mantle section that is zoned into four kilometer-scale petrological, geochemical and structural domains that, from the top to the bottom of the section (and from NNW to SSE), are (Fig. 6.2): (1) the garnet-spinel mylonite; (2) the spinel tectonite domain; (3) the granular spinel peridotite domain, which is separated from the overlying spinel tectonite by a sharp recrystallization front; and the basal (4) plagioclase tectonite domain (Fig. 6.2) (Van der Wal and Vissers, 1996; Lenoir et al., 2001; Précigout et al., 2007; Soustelle et al., 2009; Hidas et al., 2013).

6.3 Sampling and Sample Description

To investigate the age of garnet crystallization in the Jubrique crustal and the Ronda peridotite rocks, we have selected five samples of gneisses from the Jubrique unit and three garnet pyroxenites from the garnet-spinel mylonites and the spinel tectonite domain of the Ronda peridotite (Fig. 6.2; Table 6.1).

The samples from the Jubrique crustal section are three porphyroblastic gneisses (JU-18, JU-20 and JU-21) and two porphyroclastic gneisses (JU-08 and JU-10). Barich et al. (2014) provided a detailed petrological study of these samples (cf. Ch. 4). Sample JU-08 is porphyroclastic gneiss located near the contact of the Jubrique unit with the garnet-spinel mylonites of the Ronda peridotite (Fig. 6.2). Barich et al. (2014) have provided a detailed petrological study of this sample and its nano-granite inclusions in garnet, which conditions of equilibrations and composition have been determined experimentally (Acosta-Vigil *et al.*, submitted; cf. Ch. 4 & 5). Sample JU-10 is a residual porphyroclastic gneiss made up of a very fine-grained matrix of neoblasts surrounding large garnet and kyanite porphyroclasts. JU-18 is a sample of porphyroblastic gneiss close to the transition zone with the underlying porphyroclastic gneisses (Fig. 6.2). JU-20 and JU-21 are representative samples of the Jubrique porphyroblastic-mylonitic gneisses; they have the typical metatexitic microstructure characteristic of these gneisses, which is constituted by sharp leucosomes, melanosomes and paleosomes domains (Barich et al., 2014; Ch. 4).

From the underlying Ronda peridotite slab, we have selected three samples of garnet pyroxenites from the garnet-spinel mylonites (samples RC-159 and RO-178) and the spinel tectonite domain (sample RP07-1) of this massif (Fig. 6.2) (Van der Wal and Visser, 1993; Garrido et al., 2011; Précigout et al., 2007). The outcrops of the selected pyroxenites have been studied previously for their microstructure, petrology and geochemistry (Garrido & Bodinier, 1999; Morishita et al., 2001). Sample RC-159 is a coarse-grained garnet pyroxenite, composed of coarse garnets hosted by very coarse clinopyroxenes. Clinopyroxenes show exsolutions of orthopyroxene and garnet. Garnets are mostly inclusion-free, and only contain occasional rutile needle inclusions. Sample RO-178 is a porphyroclastic plagioclase-bearing garnet pyroxenite composed of large porphyroclasts of clinopyroxene and garnet immersed in a very fine matrix of clinopyroxene, plagioclase and garnet neoblasts. Previous studies have reported the presence of corundum and sapphirine in this outcrop of layered pyroxenites interlayered with garnet and garnet-spinel peridotites (Morishita et al., 2001). Sample RP07-1 is a porphyroclastic garnet pyroxenite composed of large clinopyroxene and garnet porphyroclasts in a matrix of clinopyroxene and garnet neoblasts —mostly transformed to kelyphite aggregates. All garnet pyroxenites samples show a strong imprint of high-

temperature ductile deformation similar to those described in the garnet pyroxenites from the Beni Bousera peridotite (Frets et al., 2012).

6.4 Sample Preparation and Analytical Procedures

Samples from all the Jubrique gneisses were cut into several ≈ 1 -2 cm thick slabs in order to expose the central domains of the largest garnet crystals. From each sample, one to two ≈ 1.5 mm thick polished sections of the central section of large garnet crystals (≈ 1 to 1.5 mm in diameter) were prepared. All garnets were analyzed for trace elements by LA-ICP-MS along two perpendicular profiles. Separation between rims and cores was based on the trace element analytical profiles and the systematics of mineral inclusions in garnets (cf. Chapter 2 and below).

Large garnets were cut from their matrix and divided into several fragments, which at least included a core and a rim domain (except for JU-20 with a single analysis of the entire garnet). Due to the high Lu and Hf concentration of most of the studied garnets (cf. Sec. 6.5), high-precision Lu-Hf isotopic analysis only required ≈ 0.1 g of garnet allowing the analysis of several subsamples from the same crystal. In samples where garnet crystals were large enough to be split into several ≈ 0.1 g subsamples, two or more core and rim domains were obtained from each garnet (cf. chapter 2). Lu-Hf analyses of the bulk rock, and core and rim subsamples are useful to test for the homogeneity—or variability—of Lu-Hf ages throughout the entire garnet crystal. Due to the small size of the crystals and their homogeneity, garnet fractions from the Ronda garnet pyroxenite were obtained by crushing the host rock and handpicking crystal fragments under a binocular microscope.

The trace element zoning profiles in garnets and Lu–Hf isotope dilution analyses were measured at the Institute of Geological Sciences, Polish Academy of Sciences, Kraków, Poland. Trace elements were measured using a Resonetics® ArF excimer laser-ablation system RESOLUTION M50 (Müller et al., 2009) coupled with a ThermoFinnigan® XSeries II quadrupole ICP-MS II. Sample runs were bracketed by measurements of NIST 612 glass using reference values of Jochum et al. (2011). Silica content was used as an internal standard. Data were processed using IgorPro-Iolite Software (Paton et al., 2015).

Lu–Hf isotope dilution analyses were conducted in the same laboratory using MC ICP-MS Neptune. Details on short and long term precision as well as constants used for

data reduction are reported in the footnote to Table 6.1. The description of chemical protocols is presented in Anczkiewicz et al. (2004) and mass spectrometry procedures are similar to those given in Thirlwall and Anczkiewicz (2004). Age and $^{176}\text{Hf}/^{177}\text{Hf}$ initial ratio calculations were conducted by Isoplot 4.15 (Ludwig, 2008). Age errors are given at 95% confidence level. More details regarding the Lu-Hf isotopic analysis of both garnet and bulk rock are described in Chapter 3. Table 6.1 lists all the analyzed samples according to their lithology, grains and aliquots. Analytical and mass spectrometry procedures follow those of Anczkiewicz et al. (2012).

6.5 Results

6.5.1 Garnet Core to Rim Lu and Hf concentration profiles

Selected Lu-Hf concentration profiles in garnet are shown in Figure 6.3. The Lu concentrations in garnets from porphyroclastic gneisses vary strongly from core to rim. Lu concentrations at or towards cores are very high (mostly ≈ 20 to 50, sometimes up to 70-80 ppm, maintained throughout a ≈ 5 to 8 mm diameter), whereas rims are mostly depleted in Lu (down to ≈ 1 -5 ppm, maintained throughout a ≈ 2 to 8 mm diameter). The transition from high-Lu cores to low-Lu rims is either progressive (e.g. profile 1 from Grt1 of JU-10; Fig. 6.3) or sharp and abrupt (e.g. profile 3A from JU-21; Fig. 6.3). Sharp transitions are more common, although both kinds of transitions can be found within a single garnet (e.g. Grt1 of JU-8 and Grt1 of JU-10). Although high-Lu domains can be found around the geometrical center of the crystal (e.g. Grt1 of JU-10; ellipsoidal crystal), more commonly they appear displaced towards garnet rims (Grt2 of JU-10; ellipsoidal to rectangular-elongated crystal), or even at a few tens to hundred micrometers of the rims (Grt1 and Grt2 of JU-8; elongated-rectangular crystals showing a straight –planar in 3D– face with high-Lu domains located next to it, and where the low-Lu domain is missing). The displacement of high-Lu domains towards garnet rims seems related to crystal shape (ellipsoidal versus elongated-rectangular crystals delimited by some planar face). Hafnium is mostly flat and low (≈ 0.4 - 0.6 ppm, sometimes < 0.1 ppm) throughout the entire garnet profiles, except for spikes due to inclusions (I in Fig. 6.3).

Although major element concentration profiles were not obtained from the analyzed garnet crystals, representative profiles of relatively large (≈ 0.6 mm) garnet in porphyroclastic gneisses are described in Chapter 4 and Barich et al. (2014). Overall, there seems to be a close correlation between major element and Lu concentration profiles, and the distribution of mineral inclusions within the garnet as well (see Chap. 4). Thus, garnet cores have moderate to high concentrations of Ca and very high concentrations of Lu, and show Ky and Rt single mineral inclusions. Garnet rims, instead, have very low Lu and high to very high Ca concentrations, and show inclusions of Sil and Ilm, together with relict and partially resorbed Ky and Rt. Melt inclusions are found throughout the entire garnet crystals, from core to rim (cf. Chap. 4). Sometimes an intermediate rim of Qz inclusions within garnet delimitate high-Lu cores from low-Lu rims. All these criteria have been used when separating garnet cores and rim fractions for Lu-Hf isotopic analysis. In addition, most garnet crystals in porphyroclastic gneisses are variably resorbed, as shown by the presence of cordierite-quartz-biotite-plagioclase coronas replacing Grt rims and increase in Mn concentration at the very rim (≈ 100 μm from the crystal edge).

Analyzed garnets from porphyroblastic gneisses are comparable in size (1 to 1.5 mm in diameter) and general distribution of Lu (high-Lu cores versus low-Lu rims) and Hf (low and flat) to those of mylonitic gneisses, though there are some clear differences. High-Lu domains have lower Lu concentrations (mostly ≈ 6 to 10, sometimes up to 20-25 ppm, maintained throughout a ≈ 4 to 9 mm diameter), constitute wider domains (e.g. Grt1 of JU-18, Grt1 of JU-21) and mostly occupy geometrical centers. Low-Lu rims are narrower (≈ 1 -2 mm wide) and in many cases absent (e.g. Grt1 of JU-18, Grt1 and Grt2 of JU-20), with mostly sharp transitions from high-Lu cores to low-Lu rims. Comparing these profiles with major element concentration profiles of a large garnet ($\approx 1 \times 1.5$ mm) described in Chapter 4 and Barich et al. (2014) suggests high-Lu cores are also higher in Alm and Sps and lower in Grs and #Mg (having inclusions of Ky and Rt), whereas low-Lu rims are higher in Prp and #Mg and high to very high in Grs (having inclusions of Sil and Ilm).

Yttrium concentration profiles closely match those of Lu, both in mylonitic and porphyroblastic gneisses. Concentrations mostly range from 1000-1500 ppm at the cores and 100-200 ppm at the rims of Grt porphyroclast of mylonitic gneisses, and from 300-500

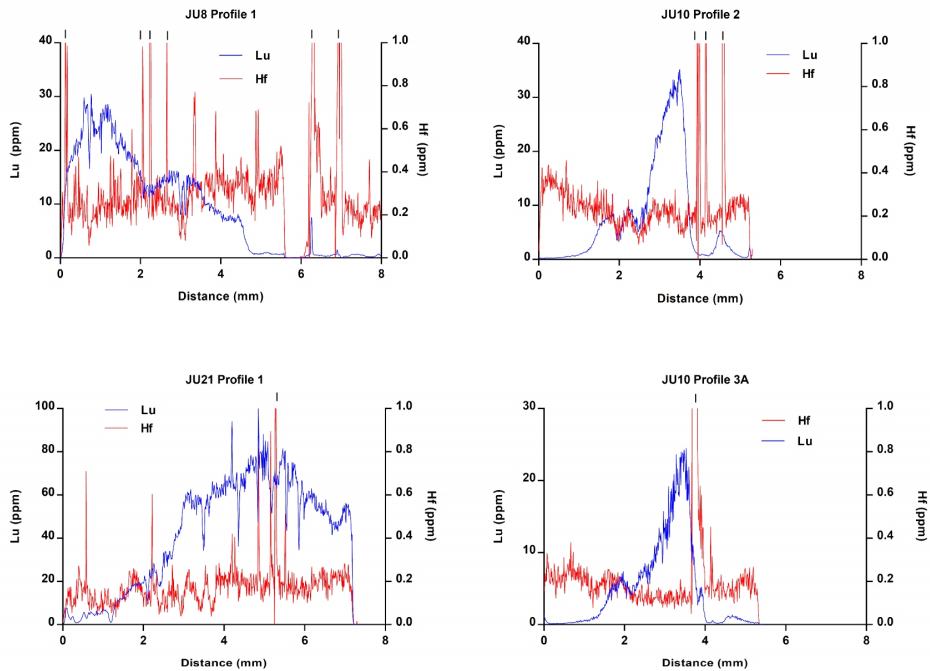


Figure 6.3. Representative core-to-rim Lu and Hf concentration profiles in garnets from Jubrique porphyroclastic (JU8 and JU10) and porphyroblastic gneisses (JU21). The “I” in the spikes of the Hf concentration profiles indicate inclusions.

(sometimes up to 800) ppm at cores versus 20-100 (up to 200-300) ppm at rims of Grt in porphyroblastic gneisses. Ti, Zr and U concentrations are very low to null. Garnets from Ronda garnet pyroxenites were not analyzed, but previous studies have shown they had a very homogeneous composition and lack inclusions (Obata, 1980; Morishita et al., 2001; Garrido et al., 2011).

6.5.2 Lu-Hf isochrons

6.5.2.1 Jubrique Gneisses

We have calculated ages from the Lu-Hf isotopic analyses using the software Isoplot (Ludwig, 2008) combining either of whole rock and garnet cores, or whole rock and garnet rims, or whole rock plus garnet cores and rims. Data are listed in Table 6.1 and isochrons shown in Fig. 6.4. The Lu-Hf age of garnets from Jubrique gneisses range

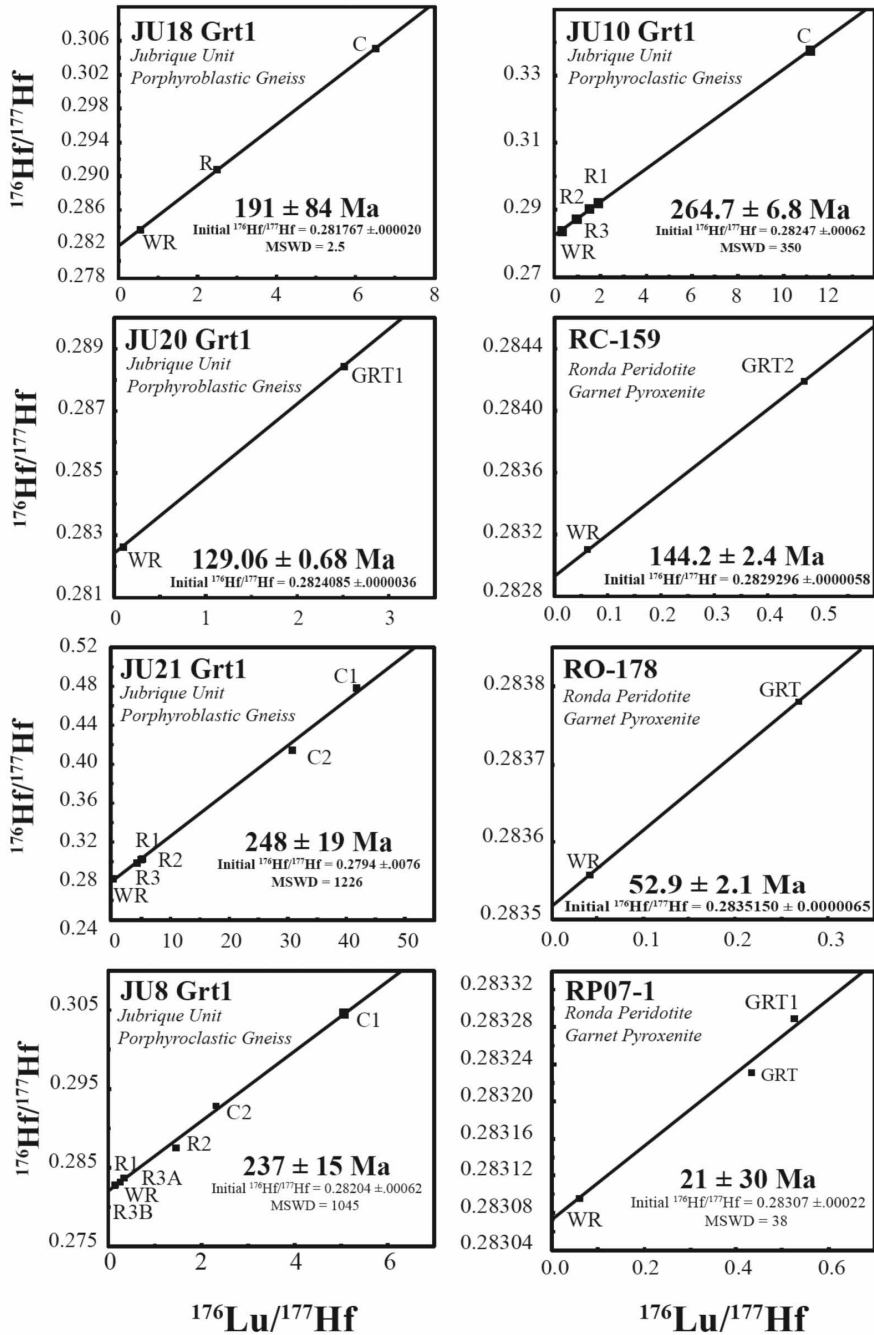


Figure 6.4. Lu–Hf isochron diagrams of garnet crystals and whole rocks. See Fig. 6.2 and Table 6.1 for sample location and further details of parameters. Garnet fractions are labelled with sequential numbers; error bars are smaller than symbol size. Abbreviations: WR – whole rock, Grt/GRT – garnet, C – core, R – rim.

mostly between the Early Permian (289 Ma) to Early Jurassic (191 Ma) Periods, with a single age in the Early Cretaceous (129 Ma) (Table 6.1). Ages of garnets from mylonitic and porphyroblastic gneisses are in general similar, although there is a higher proportion of younger ages in porphyroblastic gneisses. In nearly all cases the Mean Square of Weighted Deviates (MSWD) is high to very high (≈ 70 -1200), indicating that scatter of points is not due to analytical causes but to the lack of initial isotopic equilibrium at the time of garnet crystallization in all analyzed samples (i.e., whole rock and garnet domains), and/or that some of the samples were open systems with respect to parent and daughter element (e.g. Baxter and Scherer, 2013). Therefore, the reported multipoint isochrones only provide approximate ages. The only exception to this is sample JU-18 with a Lu-Hf age of 192 ± 1 and MSWD= 2.5.

Multipoint isochrones for garnets in mylonitic gneisses provide Early Permian (289 Ma) to Middle-Late Triassic (236 Ma) ages, except for the combination of whole rock and 3 rims of Grt1 from JU-8, that yields an age of 193 Ma. In the case of JU-10, the combination of whole rock and a core provides a younger age (266 Ma) than whole rock and three rims (289 Ma), suggesting differential mobility of Lu and Hf after crystallization.

Multipoint isochrones for garnets in porphyroblastic gneisses provide Early-Middle Triassic (248 Ma) to Early Jurassic (191 Ma) ages, except for the two-point isochron made of whole rock and a single garnet from JU-20, yielding an age of 129 Ma.

6.5.2.2 Ronda Garnet Pyroxenites

Ages of garnets analyzed from Ronda garnet pyroxenites range from Jurassic-Cretaceous limit (144 Ma), Lower-Middle Paleogene (53 Ma) and Lower Neogene (21 Ma) Periods. All of these ages are provided by two-point isochrones, except for the 21 Ma obtained from a 3-point (whole rock and two garnet concentrates) isochron with a MSWD of 38. Further analyses of whole rock would be required to improve the precision of Lu-Hf.

Table 6.1. Summary of the Lu-Hf results

Sample ID	Fraction	amount (mg)	Lu (ppm)	Hf (ppm)	$^{176}\text{Lu}/^{177}\text{Hf}$	2se	$^{176}\text{Hf}/^{177}\text{Hf}$	2se	Age
<i>JU18 - Porphyroblastic gneiss, Jubrique crustal section. Lat. 36° 31' 31.38" N Long. 5° 12' 49.14" W</i>									
	JU18 GRT1 - C	66.30	16.730	0.366	6.4953	0.0325	0.305135	0.000013	
	JU18 GRT1 - R	69.17	5.281	0.300	2.4950	0.0125	0.290693	0.000013	
	WR	99.65	0.476	0.122	0.5499	0.0027	0.283743	0.000013	191 ± 84
	JU20-GRT1	31.04	10.790	0.608	2.5109	0.0126	0.288466	0.000007	
	WR	100.32	0.557	0.805	0.0980	0.0005	0.282645	0.000003	129.06 ± 0.68
<i>JU21 - Porphyroblastic gneiss, Jubrique crustal section. Lat. 36° 31' 32.22" N Long. 5° 12' 49.98" W</i>									
	JU21 GRT1 - C1	94.57	69.881	0.246	41.6717	0.2084	0.478321	0.000011	
	JU21 GRT1 - C2	72.85	42.679	0.200	30.9041	0.1545	0.415154	0.000010	
	JU21 GRT1 - R1	28.39	3.431	0.100	4.8629	0.0243	0.301649	0.000016	
	JU21 GRT1 - R2	66.38	12.358	0.419	4.1872	0.0209	0.297710	0.000010	
	JU21 GRT1 - R3	45.31	11.148	0.315	5.0304	0.0252	0.303195	0.000010	
	WR	100.01	0.391	0.358	0.1544	0.0008	0.282831	0.000007	248 ± 19
<i>JU8 - Porphyroclastic gneiss, Jubrique crustal section. Lat. 36° 31' 30.84" N Long. 5° 12' 36.6" W</i>									
	JU8-Grt1 - C1	82.00	14.295	0.401	5.0573	0.0253	0.304481	0.000004	
	JU8-Grt1 - C2	80.00	7.715	0.473	2.3115	0.0116	0.292828	0.000004	
	JU8-Grt1 - R1	65.25	1.145	0.473	0.3423	0.0017	0.283707	0.000005	
	JU8-Grt1 - R2	70.49	6.672	0.653	1.4457	0.0072	0.287524	0.000003	
	JU8-Grt1 - R3A	74.19	0.864	0.469	0.2607	0.0013	0.283190	0.000004	
	JU8-Grt1 - R3B	66.30	1.340	1.371	0.1383	0.0007	0.282790	0.000002	
	WR	100.63	0.557	0.526	0.1500	0.0007	0.282811	0.000004	237 ± 15
<i>JU10 - Porphyroclastic gneiss, Jubrique crustal section. Lat. 36° 31' 30.84" N Long. 5° 12' 36.6" W</i>									
	JU10 GRT2 - C	75.83	15.484	0.198	11.1561	0.0558	0.337667	0.000008	
	JU10 GRT2 - R1	110.19	2.034	0.309	0.9326	0.0047	0.287098	0.000006	
	JU10 GRT2 - R2	118.78	3.366	0.311	1.5304	0.0077	0.290329	0.000004	
	JU10 GRT2 - R3	122.38	3.763	0.278	1.9207	0.0096	0.292223	0.000004	
	WR	100.40	0.403	0.180	0.3169	0.0016	0.283577	0.000008	264.7 ± 6.8
<i>RC 159 - Garnet pyroxenite, Grt-Sp mylonites, Ronda peridotite. Lat. 36° 28' 7.00" N Long. 5° 14' 35.00" W</i>									
	RC 159 A - GRT2	83.41	0.182	0.055	0.4678	0.0023	0.284190	0.000017	
	WR	100.55	0.439	0.987	0.0629	0.0003	0.283099	0.000004	144.2 ± 2.4
<i>RO-178 - Plagioclase-bearing, garnet pyroxenite, Grt-Sp mylonites, Ronda peridotite. Lat. 36° 33' 37.03" N Long. 5° 10' 50.88" W</i>									
	RO-178 - GRT	105.21	0.210	0.110	0.2691	0.0013	0.283781	0.000007	
	WR	100.28	0.071	0.234	0.0426	0.0002	0.283557	0.000005	52.9 ± 2.1
<i>RP07-1 - Garnet pyroxenite, Spinel tectonite domain, Ronda peridotite. Lat. 36° 28' 1.00" N Long. 5° 14' 9.00" W</i>									
	RP 07-1A - GRT	111.64	0.915	0.299	0.4331	0.0022	0.283231	0.000005	
	RP 07-1B - GRT1	87.06	1.057	0.285	0.5252	0.0026	0.283289	0.000005	
	WR	100.58	0.336	0.834	0.0570	0.0003	0.283096	0.000004	21 ± 30

Grt: Garnet; C: Core; R: Rim; se: Standard Error. All errors are 2 se. $^{176}\text{Lu}/^{177}\text{Hf}$ errors are 0.5%, JMC475 yielded 0.282161 ± 10 ($n=34$) over the period of analyses, which is the same as the long term reproducibility (four-year period calculated) of 0.282159 ± 13 ($n=133$) at the MC-ICP-MS of the Institute of Geological Sciences, Kraków (Poland). Where in run errors were smaller than the external precision, the errors were propagated. Mass bias correction to $^{179}\text{Hf}/^{177}\text{Hf} = 0.7325$. Decay constant $\lambda^{176}\text{Lu} = 1.865 \times 10^{-11} \text{yr}^{-1}$ (Scherer et al., 2001).

6.6 Discussion

6.6.1 Comparison with Previous Geochronological Studies

Figure 6.5 shows a compilation of geochronological ages obtained using different thermo-chronometers in the Alpujárrides and Sebtides in the Rif units. These geochronological studies have brought forward two main groups of ages corresponding to the Variscan and Alpine orogenies. Alpine ages (≈ 15 -50 Ma) have been mostly obtained by isotopic systems with medium to low closure temperatures (≤ 600 -650 °C): mostly Rb-Sr, K-Ar and ^{40}Ar - ^{39}Ar analyses on whole rock, muscovite, biotite and hornblende, as well as U-Pb-Th dating of zircon and monazite (see caption of Fig. 6.2 for references). U-Pb-Th dating of monazite and zircon has yielded a range of Variscan ages from ≈ 280 -320 Ma, and older ages interpreted as inherited from the source rocks of the Alpujárride sequence: ≈ 560 -640 Ma (Cadomian or Pan-African), 940-1020 Ma (Grevillian), and Early Proterozoic to Early Archean (Zeck and Whitehouse, 1999; Sánchez-Rodríguez, 1998; Acosta-Vigil et al. 2014; Sánchez-Navas et al. 2014).

6.6.1.1 Western Alpujárrides high-grade gneisses

Lu-Hf ages from mylonitic and porphyroblastic gneisses of Jubrique unit are mostly comprised between the Early Permian and Early Jurassic Periods (Fig. 6.4). We interpret Lu-Hf ages between ≈ 260 -190 Ma (samples JU-21, JU-10, and JU-8) and ≈ 129 Ma (samples JU-20 and JU-18) (Fig. 6.4) as due to partial reset of the Lu-Hf system after the Variscan. The younger ages provided by the garnet core JU-10 compared to older ages in the rims of the same garnet (Table 6.1) may be explained as due to modifications of the parent isotope/stable reference isotope ratio after garnet crystallization caused by the diffusional fractionation between faster-diffusing Lu and very slow-diffusing Hf.

As pointed out previously, Variscan thermochronological ages are commonplace in western Alpujárrides rocks (Fig. 6.59). The Lu-Hf garnet ages of approximately 250 Ma (JU-21; JU-8, and JU-10; Fig. 6.4) recorded in Jubrique gneisses are slightly younger than the SHRIMP U-Th-Pb ages of 290-300 Ma (Sánchez-Rodríguez, 1998) obtained in oscillatory-zoned domains of euhedral zircons from leucocratic zones in Jubrique porphyroclastic gneisses, and interpreted as recording the age of anatexis and high-grade

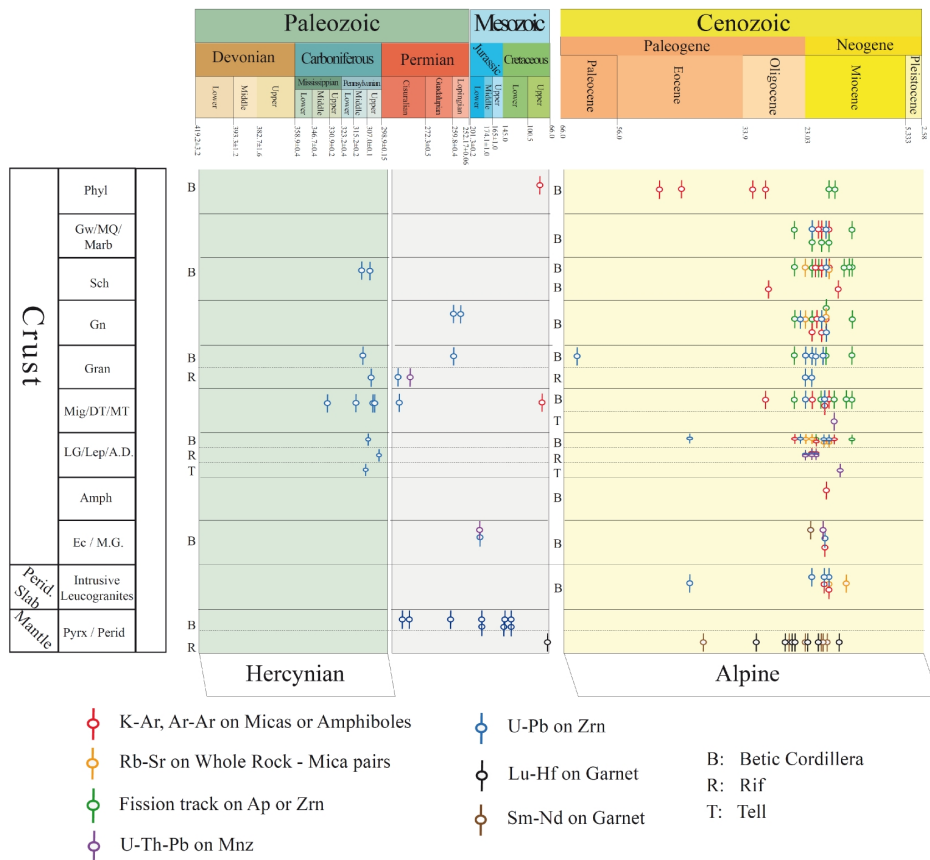


Figure 6.5. Compilation of geochronological ages obtained using different thermo-chronometers in the Alpujarrides and Sebtides in the Rif units as a function of geographical location, lithology, isotopic method and mineral. Ages in the Jubrique crustal sequence and in leucogranites intruding the peridotite slabs encompass: (1) U-Pb-Th ages on zircon and monazite (Acosta, 1998; Sanchez-Rodriguez, 1998; Platt and Whitehouse, 1999; Zeck and Whitehouse, 1999, 2002; Montel et al., 2000; Sanchez-Rodriguez and Gebauer, 2000; Zeck and Williams, 2001; Platt et al., 2003b; Whitehouse and Platt, 2003; Janots et al., 2006; Rossetti et al., 2010; Esteban et al., 2011a, 2011b; Acosta-Vigil et al., 2014; Massonne, 2014; Ruiz-Cruz and Sanz de Galdeano, 2014); (2) Rb-Sr on whole rock, biotite and muscovite (Priem et al., 1979; Zeck et al. 1989a, 1989b; Zeck et al. 1992; Acosta, 1998); (3) K-Ar and ^{40}Ar - ^{39}Ar on whole rock, amphibole, biotite, muscovite, white mica and K-feldspar (Loomis, 1975; Priem et al., 1979; Monié et al., 1991, 1994; Zeck et al., 1992; Platt et al., 1998, 2003a, 2005; Sosson et al., 1998; Michard et al., 2006; Rossetti et al., 2010); and (4) fission-track on zircon and apatite (Andriessen and Zeck, 1996; Sosson et al., 1998; Platt et al., 1998, 2003a, 2005). Ages in the Ronda peridotite comes from U-Pb-Th ages on zircon from garnet pyroxenites from the Ronda Peridotite (Sanchez-Rodriguez and Gebauer, 2000), Sm-Nd isochron in garnet pyroxenites, and two point Lu-Hf isochrons in garnet pyroxenites from the Beni Bousera (Pearson and Nowell, 2004; Blichert-Toft et al., 1999). Abbreviations: Phyl – Phyllite; GW/MQ/Marb – Quartzite/Metaquartzite/Marble; Sch – Schist; Gn – Gneiss; Gran – Granulite; Mig/DT/MT – Migmatite/Diatexite/Metatexite; LG/Lep/A.D. – Leucogranite/Leptinite/Acid Dyke; Amph – Amphibolite; Ec/M.G. – Eclogite/Mafic Granulite; Pyrx/Perid – Pyroxenite/Peridotite.

mineral associations during the Variscan orogeny (Sánchez-Rodríguez, 1998). These zircons show overgrowths of thin (up to 10-15 μm) structureless rims that yielded Early Miocene ages corresponding to the Alpine orogeny (Sánchez-Rodríguez, 1998). Ruiz-Cruz and Sanz de Galdeano (2014) found zircons with similar oscillatory zoned overgrowths and SHRIMP U-Pb-Th dating yielded Late Carboniferous-Early Permian ages (≈ 330 and ≈ 265 , respectively). The youngest event was ascribed to the anatexis of the crust during the Variscan orogeny, and the Pre-Variscan ages of c. 400 Ma (390-470 Ma) —which are similar to U-Pb-Th zircon ages in migmatitic gneisses from the central Alpujarrides (427-467 Ma; Zeck and Whitehouse, 1999)— to an Ultra High Pressure (UHP) metamorphic stage that preceded the anatexis. On the basis of a detailed phase equilibria and metamorphic study and U-Pb-Th monazite geochronology, Massonne (2014) casted serious doubts about the UHP pressure event, and found arbitrary the choice of the two events and their relation to metamorphic high-grade assemblages. This author dated monazite in garnet cores [287 ± 9 (2σ) Ma] that he interpreted as the record of high-grade metamorphism during the Variscan orogeny, and two other monazite populations which yielded ages of c. 34 Ma and early Miocene times (around 20 Ma) interpreted as reflecting two Alpine events.

U-Pb-Th zircon Variscan ages (Fig. 6.5) are also reported in the Blanca Unit — constituting the sole of the Ronda peridotite in the western Alpujarrides (Fig. 6.2) — (≈ 290 -300 Ma; Acosta, 1998; Sánchez-Rodríguez, 1998; Acosta-Vigil et al. 2014), and in eclogite-facies mafic boudins in this unit (≈ 184 Ma; Sánchez-Rodríguez, 1998; Sánchez-Rodríguez and Gebauer, 2000). Blanca unit low-pressure migmatites were interpreted as produced during the emplacement of the Ronda peridotite (Platt et al. 2013; and references therein); however, the combination of Variscan ages in the Blanca unit and the younger Mesozoic to Alpine Lu-Hf ages in Ronda garnet pyroxenites (this study) indicate that the main anatexis event in the crustal sole of the Ronda peridotite was temporally unrelated to the intracrustal emplacement of peridotites (see also Massonne, 2014). Although the provenance of units constituting the sole of peridotites is yet uncertain (i.e., Iberia foreland vs. an exotic Alboran provenance; Platt et al. 2013, and references therein), these units share many features with the Jubrique crustal units overlying the peridotite in terms of their thermochronological record.

Similar U-Pb-Th ages in zircon (Rossetti et al. 2010) and monazite have been reported in garnet cores (Montel et al. 2000) from gneisses of the crustal envelop of the Beni Bousera peridotite in the Rif Mountains. Rossetti et al. (2010) dated zircons and

monazites from both leucosomes and sheets of slightly discordant peraluminous granites within porphyroclastic gneisses. They concluded that the Variscan sector- and oscillatory-zoned domains of zircons from leucosomes and granitic dikes were coeval to the tectonic fabrics, metamorphism and anatexis in the host granulites. Structureless zircon rims with Alpine (≈ 22 Ma) ages were observed in some samples, and interpreted as re-equilibration of Variscan domains during early Miocene metamorphism. In the porphyroclastic gneisses of Beni Bousera, Montel et al. (2000) obtained Variscan (≈ 300 Ma) and Alpine (≈ 22 Ma) U-Pb-Th ages for monazite crystals included in Grt or in the matrix of the rock, respectively. They interpreted that Grt crystallized during the Variscan, whereas the matrix of the rock formed during the Alpine. Interestingly, and to our best knowledge, no Mesozoic thermochronological ages have ever been reported in the crustal envelop of peridotites in the Rif Mountains (Fig. 6.5).

The Lu-Hf garnet geochronology in the Jubrique units and previous thermochronological studies of the crustal envelope of Betic-Rif highlight the polymetamorphic nature of these units (Acosta, 1998; Sánchez-Rodríguez, 1998; Montel et al. 2000; Rossetti et al. 2010; Massonne, 2014; Sánchez-Navas et al. 2014). The prevalence of Late Carboniferous to Early Permian ages in the Western Alpujarrides high-grade rock points to the Variscan orogeny as a main thermal event. Despite the thermochronological evidence for a sequence of Alpine events in the Jubrique units, we have found no Alpine Lu-Hf ages indicating either that this event is not resolvable with the present sampling and dating techniques, or that garnet was not equilibrated during the Alpine. This result may have important repercussions for the P-T-t evolution of high-grade rocks in the crustal envelope of Betic-Rif peridotites and will be discussed in detail in a later section.

6.6.1.2 Ronda and Beni Bousera peridotites

The present study is the first report of Lu-Hf whole rock-garnet isochrons for Ronda garnet pyroxenites. Lu-Hf ages yielded Jurassic-Early Cretaceous [144 ± 2 (2 SE) Ma; sample RC-159], Eocene [53 ± 2 (2 SE) Ma; sample RO-178] and Miocene [21 ± 30 (2 SE) Ma; sample RP07-1] ages (Fig. 6.4). The latter Miocene age requires further Lu-Hf whole rock analyses to increase its precision, but, at this stage, we consider it as a valid result. Certainly, further Lu-Hf and Sm-Nd isochrons, as well as trace elements in garnets, in Ronda garnet pyroxenites are necessary to better constrain the geodynamic

meaning of these ages; however, we can make some preliminary inferences from the present dataset.

Early Cretaceous age in the garnet pyroxenite RC159 is similar to Early Jurassic and Late Jurassic-Early Cretaceous ages reported from magmatic oscillatory-zoned domains in zircons from three Ronda garnet pyroxenites [143 ± 16 and 131 ± 3 Ma] (Sánchez-Rodríguez and Gebauer, 2000). Together with an older age of 178 ± 2 (2 SE), these authors interpreted these ages as recording the formation of the pyroxenite protoliths during extensional/transensional events related to the breakup of Pangea. According to these authors, this event also formed the basaltic protoliths of the eclogitic boudins in the underlying Blanca unit (Sánchez-Rodríguez and Gebauer, 2000). Their U-Pb-Th zircon age of 131 ± 3 Ma was obtained in a Ronda corundum-bearing garnet pyroxenite from the same outcrop as our sample RO-178, which yielded a (Eocene) garnet Lu-Hf age of 53 ± 2 (2 SE) Ma (Fig. 6.4). Eocene ages in the Alpujarrides realm are interpreted as recording the onset of convergence, HP subduction metamorphism (Azañon et al. 1998) and the accretion of the Alboran lithospheric domain (Platt et al. 2013; and references therein). Ar-Ar ages of approximately 50 Ma on white mica from the low-grade Alpujarrides phyllites may date the initiation of this contractional event (Platt et al. 2005) (Fig. 6.5). The Early Miocene Lu-Hf age obtained in the garnet pyroxenite RP07-1 is similar to the three point Sm-Nd isochrons (22 ± 2 Ma) in one Ronda garnet pyroxenite (Zindler et al. 1983). Similar Early Miocene ages of approximately 21 Ma were obtained in the rim of magmatic zircons from Ronda garnet pyroxenites (Sánchez-Rodríguez and Gebauer, 2000). We interpret these Early Miocene ages as recording the waning stages of the extensional-related thermal event leading to the melting of the base of the lithospheric mantle peridotites, the development of the Ronda peridotite recrystallization front (Van der Wal and Vissers, 2003; Lenoir et al. 2001; Soustelle et al. 2009), and the final intracrustal emplacement of the Betic-Rif peridotites (Hidas et al. 2013) (Fig. 6.2). In this interpretation, the Lu-Hf ages of garnet pyroxenites in the Ronda garnet-spinel mylonite domain (Fig. 6.2) were not reset during this event because this domain was substantially cooler than the rest of the peridotite massif (Obata, 1980; Garrido et al. 2011; Précigout et al. 2013; Johanesen et al. 2014), which allowed the preservation of Lu-Hf ages from early orogenic events since the Mesozoic. In this respect the results of the Lu-Hf geochronology in Ronda garnet pyroxenites highly differ from those obtained in garnet pyroxenites from the Beni Bousera peridotite in the Rif belt. Blichert-Toft et al. (1999) and Pearson and Nowell

(2004) obtained exclusively Oligocene to Early Miocene Lu-Hf ages in many samples of garnet pyroxenites from the Beni Bousera peridotite (Blichert-Toft et al. 1999; Pearson and Nowell, 2004). The mean of eight Lu-Hf isochrons in Beni Bousera garnet pyroxenites yielded an age of 24 ± 8.6 (2 SE) Ma (Pearson and Nowell, 2004). The most precise Lu-Hf isochrons in Beni Bousera garnet pyroxenites provided ages of 22.5 ± 1.1 Ma (Pearson and Nowell, 2004) and of 25.3 ± 1.2 Ma. These ages are interpreted as “the best estimate when the Beni Bousera massif passed through the Lu-Hf blocking temperature for the garnet-clinopyroxene assemblage” (Pearson and Nowell, 2004). Similarly to the case of the Ronda peridotite, we interpret these ages as recording the extensional and thermal event that lead to incipient partial lithospheric melting before the emplacement of the Beni Bousera into the crust during the Alpine orogeny (Afiri et al. 2011; Frets et al. 2014).

A striking first order difference between the geochronological results in peridotites and their crustal envelop rocks is that the Lu-Hf ages in the mantle section do not record any Hercynian/Variscan event, which is otherwise widespread in the Lu-Hf and U-Pb-Th thermochronological record of the high-grade crustal rocks (Fig. 6.5). This may reflect that, if this event was ever present, these Lu-Hf ages were reset during later mantle events or that mantle garnet grew in geodynamic events later than the Variscan. It is worth noting that Ronda garnet pyroxenites with U-Pb-Th zircons ages of 178 ± 3 Ma (sample RDA24 of Sánchez-Rodríguez and Gebauer, 2000) and 131 ± 3 Ma (sample CA1 of Sánchez-Rodríguez and Gebauer, 2000) also contain populations of magmatic zircons that yielded Late Carboniferous to Early Permian ages (c. 285 Ma, 260 ± 11 and 282 ± 11 Ma (1s); concordant within errors) (Sánchez-Rodríguez and Gebauer, 2000). These Late Carboniferous–Early Permian ages are, within error, coincident with the Lu-Hf ages of c. 290 Ma recorded in the Jubrique unit garnets (this work) and similar to SHRIMP U-Th-Pb ages of 290-300 Ma obtained in oscillatory-zoned domains of euhedral zircons from leucocratic zones in Jubrique porphyroclastic gneisses, and it is interpreted as recording the age of anatexis and/or high-grade mineral associations during the Variscan orogeny (Sánchez-Rodríguez, 1998). Sánchez-Rodríguez and Gebauer (2000) interpreted this pollution of zircons in Ronda garnet pyroxenites as inherited before the formation of the garnet protoliths, but the arguments for such interpretations is not clear. The physical mechanisms by which Carboniferous-Permian zircon or even older zircons (> 1.7 Ga; Sánchez-Rodríguez and Gebauer

(2000); Marchesi et al. unpublished results) were inherited in mantle pyroxenite is uncertain. It is most likely that garnet pyroxenite protoliths are as old as the foundation of the Ronda subcontinental lithospheric mantle as attested by the coincidence between peridotite Re-Os and pyroxenite model ages, which are older than 1.1 Ga (Pearson and Nowell, 2004; Marchesi et al. 2010). The coincidence of U-Pb-Th age in mantle pyroxenites and of U-Pb-Th and Lu-Hf ages in the overlying crustal sections most likely reflects extraordinary thermal events that partially melted garnet pyroxenite in the mantle lithosphere and induced anatexis in the overlying lithospheric crustal section.

6.6.2 Unraveling the P-T-time Evolution of Jubrique Gneisses

Despite the wealth of U-Pb-Th data now available in the western Alpujarrides units (Fig. 6.5<) much uncertainty still exists about the timing and significance of the peak and post-peak P-T metamorphic conditions recorded by the highest grade in the crustal envelop of the peridotites (Platt et al. 2013; and references therein).

Figure 6.6 shows a recent compilation by Platt et al. (2013) of the pressure-temperature paths (P-T-t) for different units in the Alpujarride Complex. This figure highlights two features that are characteristic of the P-T evolution of the Alpujarride crustal units: (i) the presence of a condensed metamorphic sequences showing apparent downward steep temperature gradient towards the peridotite sequence (Fig. 6.2); and (ii) the nearly isothermal or heating with decompression P-T-t typically recorded by these units. This P-T-t evolution is thought to record some combination of vertical ductile thinning and excision along low-angle normal faults or ductile shear zones during extension in the Alpine orogeny (Balanyá et al. 1997; Argles et al. 1999; Azañon & Crespo-Blanc, 2000; Soto & Platt 1999; Platt et al. 2013). Isothermal—or accompanied by some increase in temperature— decompression resulted in localized metamorphism that produced assemblages including andalusite or sillimanite, and the breakdown of early-formed minerals (García-Casco & Torres-Roldán 1996; Balanyá et al. 1997; Argles et al. 1999). Gneisses from the crustal envelope of the Ronda, Ojen and Carratraca peridotites record the highest metamorphic grade of the Alpujarride units (Argles et al. 1999; Platt et al. 2013; Barich et al. 2014; Massonne, 2014; Ruiz-Cruz & Sanz de Galdeano, 2014) (Fig. 6.6). In these units, metamorphism locally reached high grade with the breakdown of muscovite and the initiation of partial melting (Argles et al. 1999, García-Casco et al. 1993). Similar high-grade gneisses are found in the crustal

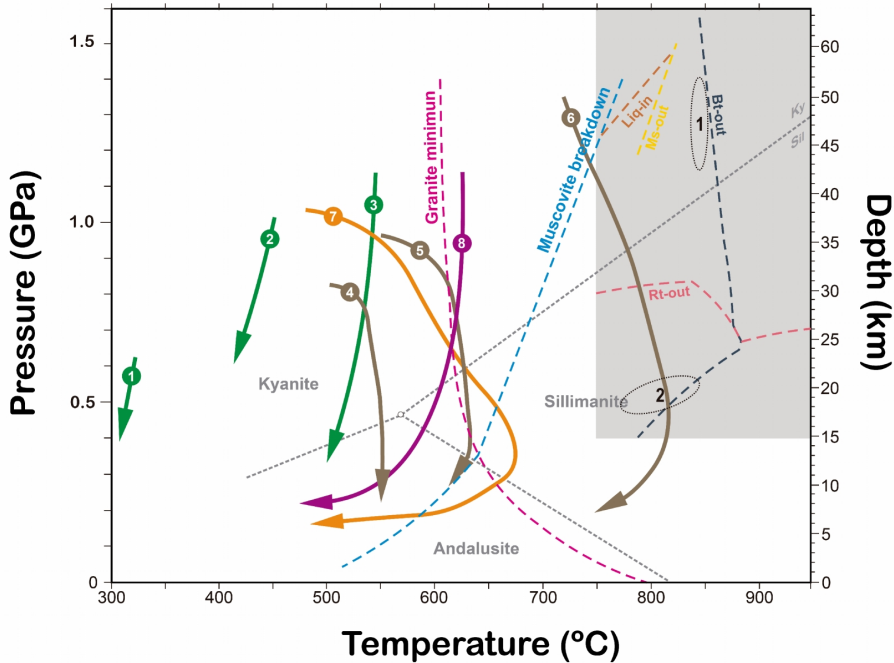


Figure 6.6. Compilation after Platt et al. (2013) of the pressure-temperature paths for different units in the Alpujarrides Complex: (1–3) south-central Alpujarrides (Azañon & Crespo-Blanc, 2000); (4–8) central and western Alpujarrides: (4–6) crustal envelope of the Carratraca peridotite massif (Argles et al. 1999), (7) ODP Site 976 in the Alborán Sea (Soto & Platt 1999), and (8) the Torrox unit (García-Casco & Torres-Roldán 1996). The shadow area shows the Liquid-in, Ms-out, Bt-out and Rt-out reactions calculated in the system NCKFMASHT by Barich et al. (2014) for a porphyroclastic gneiss JU-7 of the Jubrique unit. This gneiss samples is similar to sample JU-8 from the present study. Ellipses 1 and 2 indicate peak and post-peak P-T conditions, respectively, calculated by Barich et al. (2014) based on phase equilibria modeling, conventional thermobarometry and microstructural and nanograins microstructural observations.

envelope of the Beni Bousera peridotite in the Rif Mountains (Bouybaouene et al. 1998; Montel et al. 2001).

Ruiz-Cruz & Sanz de Galdeano (2014) have reported the occurrence of nanodiamonds in Alpujarrides gneisses—including the Jubrique unit—as evidence for an ultrahigh pressure (UHP) metamorphic event. Massonne (2014) demonstrated that rocks from the Jubrique unit never reached P–T conditions of the diamond stability field and concluded that the reported nanodiamonds either grew in metastable equilibrium or were artificially introduced into rock thin sections. Previous studies have obtained similar P–T conditions on the basis of phase equilibria modeling, conventional thermobarometry and microstructural observations (Balanyá et al. 1997; Argles et al.

1999; Barich et al. 2014; Massonne, 2014; Platt et al. 2013). Further studies are necessary to confirm the UHP nature of these units, and therefore, we will not speculate here about the cause and timing of this event.

6.6.2.1 Timing and geodynamic setting of peak P-T metamorphic conditions

Peak P-T conditions in western Alpujarrides gneisses are recorded in the core of garnet porphyroclasts and porphyroblasts that contain abundant kyanite, rutile and MI inclusions (García-Casco et al. 1993; Balanyá et al. 1997; Bouybaouene et al. 1998; Argles et al. 1999; Barich et al. 2014). In our previous thermodynamic phase diagram modeling and conventional thermobarometric study of Jubrique mylonitic gneisses we determined peak P-T conditions of 1.2–1.4 GPa and ≈ 850 °C (Fig. 6.6) (Barich et al. 2014; Chap. 5). These P-T conditions are broadly in good agreement with previous works (Bouybaouene et al. 1998; Argles et al. 1999), though our estimated equilibration temperature is hotter than that reported previously. The presence of MI inclusions in garnet cores in equilibrium with kyanite and rutile (see below) (Fig. 6.6) (Barich et al. 2014), which have demonstrated experimentally to be formed at 850 °C (Chap. 5; Acosta-Vigil et al. submitted), strongly supports a high-T, melt-present (c. 850 °C) environment during the onset of garnet growth at the peak P-T conditions of equilibration of Jubrique gneisses.

Lu-Hf ages of cores or garnet porphyroclasts and porphyroblasts confirm that the growth of garnet in Jubrique gneisses occurred in the Early Permian during the latest stages of the Variscan orogeny (Table 6.1; Fig. 6.4). This inference poses major problems to the interpretation of Alpine decompression P-T-t paths (Fig. 6.6) that rely on peak metamorphic conditions retrieved in garnet inclusions and the mineral chemistry of garnet cores in high-grade Jubrique gneisses (Balanyá et al. 1997; Argles et al. 1999). These Lu-Hf ages are in good agreement with U-Pb-Th dating of monazite enclosed in garnet cores of Jubrique gneisses and that yielded late Hercynian ages (287 ± 9 Ma) (Massonne, 2014). According to this author, the high-Y content of this Hercynian population of monazite indicates they grew slightly before garnet crystallization, which could explain the slightly younger Lu-Hf garnet ages. Massonne (2014) estimated P–T granulite-facies conditions —as recorded in the garnet Ca-poor cores— of 0.7 GPa and 800 °C. These pressure conditions are significantly lower than previous estimates of peak pressure conditions obtained from garnet core in the Jubrique

gneisses (García-Casco et al. 1993; Balanyá et al. 1997; Bouybaouene et al. 1998; Argles et al. 1999). This author ascribed high-pressure conditions of 1.3 GPa and temperatures above 650 °C to a later Alpine event recorded by the growth of Ca-rich rims in garnet associated with a monazite population that yielded ages of approximately 34 Ma. We think that our thermodynamic phase diagram modelling and mineral chemistry of Jubrique gneisses is robust (Barich et al. 2014; Chap. 4), and indicates that high-pressure peak conditions were predominant during the growth of low-Ca garnet cores in the presence of melt, kyanite and rutile. The main consequence of these differing P-T conditions is that anatexis during the Variscan orogeny either occurred at low-to-intermediate pressures (Massonne, 2014) or in an overthickened hot continental crust (Bouybaouene et al. 1998).

As discussed above, Variscan zircons in the Jubrique gneissic sequence have been cited as evidence that the high-grade metamorphism is Variscan, and they certainly suggest that granitic melt was pervasive at the time of garnet growth. Previous studies have proposed that anatexis started during decompression from peak to post-peak conditions and in the field of sillimanite. The study of MI shows, however, that melt was already present in the system at peak conditions, and that most garnet grew in the presence of melt (Barich et al. 2014; Acosta-Vigil et al. submitted; cf. Chap. 4 & 5). There are several potential mechanisms for large extent of melting of the lower continental crust (Thompson and Connolly, 1995; Brown, 2007; Bea, 2012; and references therein): (1) the supply of H₂O at temperatures above their H₂O-saturated solidi; (2) decompression melting through dehydration (fluid-absent) melting reactions; (3) increasing heat flux at the base of thickened crust, mostly due to asthenospheric upwelling or mantle wedge convection, or by heat advection of hot mantle magmas emplaced within the crust; and (4) accumulation of radiogenic heat by the decay of heat producing elements such as ⁴⁰K, ²³⁰Th and ²³⁵U. According to Brown (2007), the apparent thermal gradient associated with peak P-T conditions recorded in garnet cores from the Jubrique unit is transitional between low-to-medium-P and high-P to UHP granulites. These granulitic rocks are thought to form during continental collision at the base of thickened continental crust, or during subduction of the crust (Brown 2007 and references therein). Thermal modeling shows that P-T conditions recorded in garnet cores of Jubrique gneisses can be reached at the base of overthickened continental crust during continental collision (Thompson and Connolly, 1995). As previously suggested

by Bouybaouene et al. (1998) for equivalent gneisses in the Rif belt, we interpret that the anatexis and crystallization of garnet cores in the Jubrique unit took place in the Early Permian in a context of continental collision and overthickened continental crust. Lower Carboniferous high-grade metamorphic rocks and migmatites, as well as Upper Carboniferous to Lower Permian voluminous felsic magmatism, occurred in the Variscan orogen of the Iberian Peninsula. They have been interpreted as caused by anatexis and melt extraction during crustal thickening and continental collision (Villaseca et al. 1999; Bea et al. 2003, 2007). Partial melting of these rocks, however, took place at similar temperatures (800–850 °C) but lower pressures (0.4–0.6 GPa) than Jubrique granulitic gneisses.

6.6.2.2 Timing and geodynamic setting of post-peak P-T metamorphic conditions

Post-peak P-T conditions in the Jubrique gneissic sequence are recorded in the rims of garnet and matrix assemblages, which yield P-T conditions of 5–6 kbar and 800–850 °C (Fig. 6.6) (Barich et al. 2014). Similar P-T conditions have been reported in previous studies (Fig. 6.6; Argles et al. 1999). Garnet rims contain inclusions of Ca-rich MI, sillimanite and ilmenite, and the garnet outermost rim is commonly broken down to a symplectite of cordierite and spinel (García-Casco et al. 1993; Balanyá et al. 1997; Argles et al. 1999; Barich et al. 2014; Massonne, 2014).

Lu-Hf ages of garnet rims in Jubrique gneisses are indistinguishable from Lu-Hf ages in garnet cores, yielding both ages corresponding to the Early Permian or Early Jurassic Periods (Table 6.1; Fig. 6.4). A possible interpretation of the Lu-Hf garnet core-rim ages is that most of the garnet and fabric of the Jubrique gneissic sequence is Permian and/or Jurassic in age (e.g., Rossetti et al. 2010). However, this interpretation is at odd with U-Pb-Th dating of zircon and monazite in garnet rims and matrix of the Jubrique gneissic sequence that yielded Alpine ages ranging from 34 to 20 Ma, or younger (Platt and Whitehouse, 1999; Whitehouse and Platt, 2003; Massonne, 2014). Similar results are found in zircon and monazite in the Sebtiides gneissic sequence in the Rif Mountains (Bouybaouene et al. 1998; Montel et al. 2000). These results indicate that garnet growth in Jubrique gneisses is polymetamorphic and occurred at least in two different geodynamic events; the latest event involved anatexis as attested by the presence of Ca-rich inclusions in garnet rims (Barich et al. 2014; Acosta-Vigil et al. submitted; Chap. 4 & 5). As sampled and recorded by Lu-Hf thermochronology, we do

not see much possibility of the presence of a younger Alpine event in garnet rims of Jubrique gneisses. There has been certainly partial resetting of Lu-Hf isotopes in garnet after the Early Permian crystallization event, likely in the Early Jurassic and/or the Cenozoic during the Alpine orogeny. The full resetting of Lu-Hf ages ($\geq 95\%$) in a crystal of ≈ 10 mm in diameter at $850\text{ }^{\circ}\text{C}$ would take ≈ 300 Ma (Baxter and Scherer, 2013; and references therein). Slow diffusion of REE and Hf in garnet then implies that primary garnet growth ages should be well preserved, except for the case of the smallest grains or outermost growth zones of garnet porphyroclasts and porphyroblasts. If present, Lu-Hf rims equilibrated in the Alpine event are much thinner than our sampling (Chap. 3), which might have been too broad to unravel the Alpine events compared with the higher spatial resolution of SHRIMP and EMP U-Pb-Th geochronology in zircon and monazite. Sm-Nd garnet isochron thermochronology in the same samples (ongoing work) will shed some light into this issue as the diffusivity of the parent-daughter isotopes of this isotopic system is faster than that of the Lu-Hf system.

Previous studies of U-Pb-Th zircon and monazite geochronology have reported younger Alpine events in the Jubrique gneissic sequence. Massonne (2014) interpreted the 34 Ma age of a monazite population found in Ca-richer zones that surrounded garnet cores as the record of an Alpine high-P event at P-T conditions of c. 1.3 GPa and above $650\text{ }^{\circ}\text{C}$. To our best knowledge, this result would be the first report of a high-P and high-T event of late Eocene age in the western Betics. An early contractional stage of deformation (likely in the early Eocene; Platt et al. 2013) in the Alpujarrides was accompanied by HP-LT metamorphism, which produced assemblages including carpholite and chloritoid, garnet, kyanite, and staurolite at higher grades, in aluminous pelites (Azañon et al. 1998; Platt et al. 2013 and references therein). The presence of eclogite boudins in the underlying Blanca unit has also been claimed as the record of an Alpine HP subduction metamorphism (Tubía and Gil Ibarguchi, 1991), but the age of this event is uncertain. As discussed in Chapter 5, the growth of Ca-rich rims in garnets of the Jubrique gneissic sequence was likely an open system process as attested by the presence of abundant Ca-rich melt inclusions (Acosta-Vigil et al. submitted). In our view, the interpretation of the metamorphic P-T conditions recorded in high-Ca garnet rims would require pseudosection thermodynamic modelling based on local equilibrium considering that at these stages the system was open to Ca and other elements. Therefore, bulk rock pseudosections may provide a wrong estimate of the P-T

conditions of high-Ca rim; therefore, confirmation of this event would require further consideration of this matter.

On the basis of SHRIMP U-Pb-Th dating of structureless rounded soccer-ball zircons, Platt and Whitehouse (1999) and Whitehouse and Platt (2003) concluded that metamorphism in Jubrique porphyroblastic (their migmatites) and porphyroclastic (their granulites) gneisses was Alpine ($\approx 20\text{-}23$ Ma). Platt and Whitehouse (1999) did not provide a clear description of the textural relationships between the age of zircon and the metamorphic crystallization of major minerals. Whitehouse and Platt (2003) reported ages and trace element contents of zircons in the gneisses as a function of their microstructural position —i.e. matrix versus crystals hosted in Grt cores and rims— and concluded that structureless zircons of Early Miocene age were equilibrated with garnet rims and garnet neoblasts in the gneiss matrix. Massonne (2014) reached a similar conclusion on the basis of the presence of an Early Miocene population of low-Y monazite in the matrix of Jubrique gneisses. This Early Miocene low-P and high-T event occurred at peak temperatures of $740\text{ }^{\circ}\text{C}$ and was characterized by crystallization of late sillimanite in the outermost Ca-poor garnet rims (Massonne, 2014). This geochronological evidence will place P-T conditions of the latest growth of garnet in the Jubrique gneissic sequence at low pressure and high-temperature conditions during the latest stage of Alpine ductile deformation in the Alboran domain (Fig. 6.6). Although this is a likely scenario, this sequence of events cannot fully account for the textural occurrence of MI in the rims of large garnet porphyroblasts and in small peritectic garnet in the matrix of porphyroblastic gneisses. Leucocratic bands —likely former leucosomes— show peritectic MI-bearing garnets (Chap. 4; Barich et al. 2014). Relict, partially transformed kyanite (by spinel) and rutile (by ilmenite) at the rims of garnets are microstructurally undistinguishable from relict kyanite and rutile in the rock matrix. In addition, where inclusions of sillimanite occur at the rims of garnet they are oriented and broadly parallel to the main foliation and to sillimanite in the matrix, indicating that they formed synchronically. Further detailed studies relating microstructure with high spatial resolution absolute thermochronological ages are obviously needed to unravel the real extent of the late Alpine orogeny event in the development of the magmatic and ductile microstructures of the Jubrique gneissic sequence.

Part III

Conclusions

7 Conclusions

The main objective of this thesis has been to investigate the anatexis of the lower continental crust through the petrological and experimental study of the microstructure and composition of nanogranite inclusions in garnet and garnet Lu-Hf geochronology in high-pressure anatectic terrains. The case study of this thesis has been gneisses from the Jubrique unit overlying the Ronda peridotite massif in S. Spain. This thesis has provided new information on the petrological and compositional nature of anatectic melts in the lower continental crust as preserved in nanogranitoid inclusions in garnets from high-pressure granulitic migmatites, has shed new light on the age of crystallization of the anatexis, and established the (temporal) relationships between the garnet thermochronology of the lithospheric mantle and the overlying crust. The following main conclusions can be drawn from this thesis:

- I. The lower Jubrique gneissic sequence is composed of a lower sequence of mylonitic to porphyroclastic gneisses—in contact with the peridotites—and porphyroblastic gneisses on top. Except for the presence of melt inclusions, anatectic microstructures indicating the former presence of melt are rare or absent. The anatectic structures and microstructures in the mylonitic gneisses were strongly obliterated by deformation, whereas the porphyroblastic gneisses preserve some anatectic microstructures.
- II. Thermodynamic modeling and conventional thermobarometry of mylonitic gneisses provide peak conditions of ≈ 850 °C and 1.2-1.4 GPa, corresponding to cores of large garnets with inclusions of kyanite and rutile. Post-peak conditions of ≈ 800 -850 °C and 0.5-0.6 GPa are represented by rim regions of large garnets with inclusions of sillimanite and ilmenite, cordierite-quartz-biotite coronas replacing garnet rims, and the matrix with oriented sillimanite. The P-T conditions are similar in porphyroblastic and mylonitic gneisses.
- III. Melt inclusions (MI) are widespread in the granulitic gneisses of the Jubrique unit and are similar throughout the entire sequence. Melt inclusions are present in cores and rim of garnets—mostly in large porphyroblast and

porphyroclasts—. Most of the former melt inclusions are now totally recrystallized and correspond to “nanogranitoids” inclusions, whereas some of them are partially made of glass or, more rarely, are totally glassy. The entrapment of several pre-anatectic minerals, and high pressure phases such as kyanite and rutile, indicate they formed at high-pressure conditions.

- IV. The presence of MI in large garnet crystals indicate that garnet porphyroblasts and porphyroclasts in the Jubrique sequence grew in the presence of anatectic melts, which were entrapped in this mineral at the peak and post-peak P-T metamorphic conditions. This conclusion places important constraints on the relative timing of anatexis and garnet growth in the Jubrique gneissic sequence; in previous studies anatexis in this sequence has been ascribed to post-peak P-T conditions and caused by crustal extension and near isobaric —or slightly increase temperature— decompression in the field of sillimanite. We conclude that anatexis was already widespread at the peak metamorphic conditions.
- V. High pressure (1.5 GPa) and (variable) high temperature melting experiments in nanogranite inclusions in garnet, confirms that anatexis and entrapment of melt inclusions in the Jubrique anatectic rocks occurred at temperatures of approximately 800 °C, as evidenced by the relatively high proportion of rehomogenized nanogranitoids at this temperature.
- VI. Experimental glasses show that anatectic melts —as recorded in nanogranite inclusions— were leucogranitic and peraluminous in composition, with two distinct compositional groups formed at peak and post-peak metamorphic conditions in two melting events under contrasting fluid regimes:
 - a. *Type I melt inclusions* are mostly found in the core of large garnet porphyroclasts and porphyroblasts, and formed at high-P and high-T. They are K-rich, and Ca- and H₂O-poor leucogranitic melts.
 - b. *Type II melt inclusions* are mostly found in the rims of large garnet porphyroclasts and porphyroblasts, and formed at lower-P and high-T

conditions. They are K-poor, Ca- and H₂O-rich granodioritic to tonalitic melts.

- VII. Lu-Hf isochrons combining whole-rock and cores of garnet porphyroclasts and porphyroblasts confirm that the growth of garnet in Jubrique gneisses occurred in the Early Permian (289 Ma) during the latest stages of the Variscan orogeny. This inference poses major problems to the interpretation of the Alpine decompression P-T-t paths in the high-grade Jubrique gneisses, which rely on peak metamorphic conditions registered in the inclusions and the mineral chemistry of garnet cores.
- VIII. The presence of MI in garnet cores in equilibrium with kyanite and rutile at high-P and high-T (1.2–1.4 GPa and \approx 850 °C) indicate P-T conditions akin to that of granulitic rocks formed at the base of thickened continental crust during continental collision. As deduced by previous authors in equivalent gneisses of the Rif belt, we interpret that the anatexis and crystallization of garnet cores in the Jubrique unit took place in the Early Permian in a context of continental collision and overthickened continental crust.
- IX. Despite the U-Pb-Th thermochronological evidence for a sequence of Alpine events in the Jubrique units, we have found no Alpine Lu-Hf ages indicating either that this event is not resolvable with the present sampling and dating techniques, or that the Lu-Hf of garnet was not equilibrated during the Alpine orogeny. The slow diffusion of REE and Hf in garnet may have preserved primary garnet growth ages without being reset in the Alpine orogeny at least at the scale we sampled them.
- X. The Lu-Hf whole rock and garnets isochrons of Ronda garnet pyroxenites indicate a complex multistage evolution of the lithospheric mantle of the Alboran domain recording main events in the Jurassic-Cretaceous limit (144 Ma), the Lower-Middle Paleogene (53 Ma) and the Lower Neogene (21 Ma) Periods. Early Miocene ages record the waning stages of the extensional-related thermal event leading to the melting of the base of the lithospheric mantle peridotites, the development of the Ronda peridotite recrystallization front, and the final intracrustal emplacement of the Betic-Rif peridotites.

Preservation of Lu-Hf ages from early orogenic events since the Mesozoic in the Ronda garnet-spinel mylonite occurred because this domain was substantially cooler than the rest of the peridotite massif.

- XI. Lu-Hf ages in rocks of the mantle section do not record any Variscan event, which is otherwise widespread in the Lu-Hf and U-Pb-Th thermochronological record of the overlying high-grade crustal rocks. This may reflect either that this Lu-Hf ages in mantle rock might have been reset by later mantle events or that garnet in mantle rocks grew during geodynamic events later than the Variscan.
- XII. The coincidence of U-Pb-Th age in zircons of mantle pyroxenites and the garnet Lu-Hf ages in gneisses from overlying Jubrique crustal sections reflects lithospheric-scale extraordinary thermal event during the Variscan orogeny; this event partially melted garnet pyroxenites in the mantle lithosphere and induced pervasive anatexis in the overlying lithospheric crustal section of the Alboran domain.

7.1 Perspectives and future work

The combined study of the petrology of melt inclusions and garnet geochronology in this thesis has opened a new perspective to study crustal anatexis in terms of the composition of granitoid “embryos” —as named by Bartoli and co-workers— and their entrapment age. Melt inclusions study in the present work is a pioneer investigation in the Jubrique unit and, to some extent, in high-pressure, highly deformed anatectic terranes. Microstructural and petrological observations suggest that anatexis underwent through at least two melting events under two fluid regimes; one leucogranitic and the second granodioritic-to-tonalitic. Moreover, melt inclusions were observed alongside with primary fluid inclusions which suggest that MI and FI were contemporaneous. Further detailed studies are therefore necessary to confirm the systematic distribution of leucogranitic and granodioritic-to-tonalitic MI at the cores and rims of large garnet crystals, respectively. This contribution demonstrates the potential of detailed studies of MI in migmatites and granulites for the investigation of crustal anatexis and continental crust generation and differentiation.

Our observations and interpretations bring, to our knowledge, the evidence that a large part of the studied rocks formed during a multiphase anatectic event that started during the Variscan and continued to the late Jurassic. The evidence that this crustal sequence, although displaying a normal, continuous and complete metamorphic gradient, shows a clear polymetamorphic history and brings to our attention the importance of further petrological and geochronological work with higher temporal and spatial resolution. The absence of a recorded Alpine event in Jubrique gneisses garnets by Lu-Hf system questions the effect of the Alpine metamorphism on the primary assemblages and general phase equilibria in these rocks. This raises more interrogations about the coupling and decoupling of the crust and the mantle in this deeply complex orogenic area. There is undoubtedly a strong need for more detailed geochronology, especially on large garnet rims and small garnets as an attempt to detect any Alpine growth and to possibly establish a correlation with the matrix that is known to have recorded the Alpine metamorphism. In order to unravel the role of the Alpine orogenic event in the development of the magmatic and ductile microstructure of the Jubrique gneiss sequence, further detailed studies relating microstructure with high spatial thermochronology are needed. Besides, for a better understanding of the early anatectic history in the region, an analogic approach to this work should be extended to Jubrique's counterpart in the Rif Mountains (Northern Morocco), the Beni Bousera peridotite massif and its overlying crustal sequence.

The geochemistry of analyzed garnets in the Jubrique gneiss sequence, points to particular features that need further investigation. One of these observations is the particularly high concentrations in Lu that are above 70 ppm in porphyroblastic gneisses and above 40 ppm in porphyroclastic gneisses. While such concentrations are extremely unusual in this mineral and their cause is not well known, the difference in concentrations between the two gneisses raises questions concerning their petrogenesis and should be investigated in depth. This approach could be extended to a more detailed scale including other trace elements and other major minerals in these rocks.

Part fV

References

8 References

- Acosta-Vigil, A., M. D. Pereira, D. M. Shaw, and D. London (2001), Contrasting behaviour of boron during crustal anatexis, *Lithos*, 56(1), 15-31. doi: 10.1016/S0024-4937(00)00057-8.
- Acosta-Vigil, A., D. London, G. B. Morgan Iv, and T. A. Dewers (2003), Solubility of excess alumina in hydrous granitic melts in equilibrium with peraluminous minerals at 700-800 °C and 200 MPa, and applications of the aluminum saturation index, *Contributions to Mineralogy and Petrology*, 146(1), 100-119. doi: 10.1007/s00410-003-0486-6.
- Acosta-Vigil, A., B. Cesare, D. London, and G. B. Morgan (2007), Microstructures and composition of melt inclusions in a crustal anatectic environment, represented by metapelitic enclaves within El Hoyazo dacites, SE Spain, *Chemical Geology*, 237(3-4), 450-465. doi: 10.1016/j.chemgeo.2006.07.014.
- Acosta-Vigil, A., I. Buick, B. Cesare, D. London, and G. B. Morgan (2012), The extent of equilibration between melt and residuum during regional anatexis and its implications for differentiation of the continental crust: A study of partially melted metapelitic enclaves, *Journal of Petrology*, 53(7), 1319-1356. doi: 10.1093/petrology/egs018.
- Acosta-Vigil, A., I. Buick, J. Hermann, B. Cesare, D. Rubatto, D. London, and G. B. Morgan Vi (2010), Mechanisms of crustal anatexis: A geochemical study of partially melted metapelitic enclaves and host dacite, SE Spain, *Journal of Petrology*, 51(4), 785-821. doi: 10.1093/petrology/egp095.
- Acosta-Vigil, A., D. Rubatto, O. Bartoli, B. Cesare, S. Meli, A. Pedrera, A. Azor, and L. Tajčmanová (2014), Age of anatexis in the crustal footwall of the Ronda peridotites, S Spain, *Lithos*, 210-211, 147-167. doi: 10.1016/j.lithos.2014.08.018.
- Acosta, A. (1998), Estudio de los fenómenos de fusión cortical y generación de granitoides asociados a las peridotitas de Ronda, Ph.D. thesis, 305 pp, Universidad de Granada, unpublished.
- Adams, F., L. Van Vaeck, and R. Barrett (2005), Advanced analytical techniques: platform for nano materials science, *Spectrochimica Acta Part B: Atomic Spectroscopy*, 60(1), 13-26. doi: 10.1016/j.sab.2004.10.003.
- Afiri, A., F. Gueydan, P. Pitra, A. Essaifi, and J. Précigout (2011), Oligo-Miocene exhumation of the Beni-Bousera peridotite through a lithosphere-scale extensional shear zone, *Geodinamica Acta*, 24(1), 49-60. doi: 10.3166/ga.24.49-60.
- Anczkiewicz, R., J. P. Platt, M. F. Thirlwall, and J. Wakabayashi (2004), Franciscan subduction off to a slow start: evidence from high-precision Lu-Hf garnet ages on high grade-blocks, *Earth and Planetary Science Letters*, 225(1-2), 147-161. doi: 10.1016/j.epsl.2004.06.003.
- Anczkiewicz, R., M. Thirlwall, O. Alard, N. W. Rogers, and C. Clark (2012), Diffusional homogenization of light REE in garnet from the Day Nui Con Voi Massif in N-Vietnam:

- Implications for Sm-Nd geochronology and timing of metamorphism in the Red River shear zone, *Chemical Geology*, 318, 16-30. doi: 10.1016/j.chemgeo.2012.04.024.
- Anderson, A. T. (1974), Evidence for a picritic, volatile-rich magma beneath Mt. Shasta, California, *Journal of Petrology*, 15(2), 243-267. doi: 10.1093/petrology/15.2.243.
- Andriessen, P. A. M., and H. P. Zeck (1996), Fission-track constraints on timing of Alpine nappe emplacement and rates of cooling and exhumation, Torrox area, Betic Cordilleras, S Spain, *Chemical Geology*, 131(1-4), 199-206. doi: 10.1016/0009-2541(95)00148-4.
- Andrieux, J., J.-M. Fontboté, and M. Mattauer (1971), Sur un modele explicatif de l'arc de Gibraltar, *Earth and Planetary Science Letters*, 12(1), 191-198. doi: 10.1016/0012-821X(71)90077-X.
- Argles, T. W., J. P. Platt, and D. J. Waters (1999), Attenuation and excision of a crustal section during extensional exhumation: The Carratraca Massif, Betic Cordillera, southern Spain, *Journal of the Geological Society*, 156, 149-162.
- Aubaud, C., A. C. Withers, M. H. Hirschmann, Y. Guan, L. A. Leshin, S. J. Mackwell, and D. R. Bell (2007), Intercalibration of FTIR and SIMS for hydrogen measurements in glasses and nominally anhydrous minerals., *American Mineralogist*, 92, 811-828.
- Azañón, J. M., and A. Crespo-Blanc (2000), Exhumation during a continental collision inferred from the tectonometamorphic evolution of the Alpujarride Complex in the central Betics (Alboran Domain, SE Spain), *Tectonics*, 19(3), 549-565.
- Azañón, J. M., and B. Goffé (1997), Ferro- and magnesiocarpholite assemblages as record of high-P, low-T metamorphism in the Central Alpujarrides, Betic Cordillera (SE Spain), *European Journal of Mineralogy*, 1035-1052.
- Azañón, J. M., V. García-Dueñas, and B. Goffé (1998), Exhumation of high-pressure metapelites and coeval crustal extension in the Alpujarride complex (Betic Cordillera), *Tectonophysics*, 285(3-4), 231-252.
- Balanyá, J. C., J. M. Azañón, M. Sánchez-Gómez, and V. García-Dueñas (1993), Pervasive ductile extension, isothermal decompression and thinning of the Jubrique unit in the Paleogene (Alpujarride Complex, western Betics Spain), *Comptes Rendus de l'Académie des Sciences de Paris: Série II*, 316(11), 1595-1601.
- Balanyá, J. C., V. García Dueñas, J. M. Azañón, and M. Sánchez Gómez (1997), Alternating contractional and extensional events in the Alpujarride Nappes of the Alboran domain (Betics, Gibraltar arc), *Tectonics*, 16(2), 226-238.
- Barich, A., A. Acosta-Vigil, C. J. Garrido, B. Cesare, L. Tajčmanová, and O. Bartoli (2014a), Microstructures and petrology of melt inclusions in the anatectic sequence of Jubrique (Betic Cordillera, S Spain): Implications for crustal anatexis, *Lithos*, 206-207(0), 303-320. doi: 10.1016/j.lithos.2014.08.003.
- Barich, A., O. Bartoli, A. Acosta-Vigil, S. Poli, B. Cesare, and C. J. Garrido (2014b), Remelting of nanogranites in peritectic garnet from granulites of Jubrique, Betic Cordillera, Southern Spain, paper presented at EGU General Assembly Conference Abstracts.

- Bartoli, O. (2012), When the Continental Crust Melts: A Combined Study of Melt Inclusions and Classical Petrology on the Ronda Migmatites, Ph.D. thesis, 128 pp, Università degli Studi di Parma, unpublished.
- Bartoli, O., B. Cesare, L. Remusat, A. Acosta-Vigil, and S. Poli (2014), The H₂O content of granite embryos, *Earth and Planetary Science Letters*, 395, 281-290.
- Bartoli, O., B. Cesare, S. Poli, R. J. Bodnar, A. Acosta-Vigil, M. L. Frezzotti, and S. Meli (2013), Recovering the composition of melt and the fluid regime at the onset of crustal anatexis and S-type granite formation, *Geology*, 41(2), 115-118.
- Bartoli, O., B. Cesare, S. Poli, A. Acosta-Vigil, R. Esposito, A. Turina, R. Bodnar, R. Angel, and J. Hunter (2013), Nanogranite inclusions in migmatitic garnet: Behavior during piston-cylinder remelting experiments, *Geofluids*, 13(4), 405-420.
- Baxter, E. F., J. Ague, and D. DePaolo (2002), Prograde temperature–time evolution in the Barrovian type–locality constrained by Sm/Nd garnet ages from Glen Clova, Scotland, *Journal of the Geological Society*, 159(1), 71-82. doi: 10.1144/0016-76901013.
- Bea, F. (2012), The sources of energy for crustal melting and the geochemistry of heat-producing elements, *Lithos*, 153, 278-291. doi: 10.1016/j.lithos.2012.01.017.
- Bea, F., P. Montero, and T. Zinger (2003), The nature, origin, and thermal influence of the granite source layer of Central Iberia, *Journal of Geology*, 111(5), 579-595. doi: 10.1086/376767.
- Bea, F., P. Montero, F. González-Lodeiro, and C. Talavera (2007), Zircon inheritance reveals exceptionally fast crustal magma generation processes in central iberia during the cambro-ordovician, *Journal of Petrology*, 48(12), 2327-2339. doi: 10.1093/petrology/egm061.
- Behrens, H., and N. Jantos (2001), The effect of anhydrous composition on water solubility in granitic melts, *American Mineralogist*, 86(1-2), 14-20.
- Belousova, E. A., Y. A. Kostitsyn, W. L. Griffin, G. C. Begg, S. Y. O'Reilly, and N. J. Pearson (2010), The growth of the continental crust: Constraints from zircon Hf-isotope data, *Lithos*, 119(3-4), 457-466. doi: 10.1016/j.lithos.2010.07.024.
- Bhattacharya, A., A. Mazumdar, and S. Sen (1988), Fe-Mg mixing in cordierite; constraints from natural data and implications for cordierite-garnet geothermometry in granulites, *American Mineralogist*, 73(3-4), 338-344.
- Blichert-Toft, J., F. Albarède, and J. Kornprobst (1999), Lu-Hf isotope systematics of garnet pyroxenites from Beni Bousera, Morocco: Implications for basalt origin, *Science*, 283(5406), 1303-1306.
- Blumenthal, M. (1930), Beiträge zur Geologie der betischen Kordilleren beiderseits des Rio Guadalhorce (Prov. Malaga), *Eclogae Geologicae Helvetiae*, 23, 41-289.
- Bodnar, R. J., and J. J. Student (2006), Melt inclusions in plutonic rocks: petrography and microthermometry, in *Melt Inclusions in Plutonic Rocks*, edited by J. D. Webster, pp. 1-26, Mineralogical Association of Canada, Short Course.

- Bohlen, S. R., and K. Mezger (1989), Origin of granulite terranes and the formation of the lowermost Continental Crust, *Science*, 244(4902), 326-329. doi: 10.1126/science.244.4902.326.
- Booth-Rea, G., C. R. Ranero, J. M. Martínez-Martínez, and I. Grevenmeyer (2007), Crustal types and Tertiary tectonic evolution of the Alborán sea, western Mediterranean, *Geochemistry, Geophysics, Geosystems*, 8(10), Q10005. doi: 10.1029/2007GC001639.
- Bouybaouène, M., A. Michard, and B. Goffé (1998), High-pressure granulites on top of the Beni Bousera peridotites, Rif belt, Morocco: A record of an ancient thickened crust in the Alboran domain, *Bulletin de la Societe Geologique de France*, 169(2), 153-162.
- Brown, M. (2007), Crustal melting and melt extraction, ascent and emplacement in orogens: mechanisms and consequences, *Journal of the Geological Society*, 164, 709-730. doi: 10.1144/0016-76492006-171.
- Brown, M. (2010), The spatial and temporal patterning of the deep crust and implications for the process of melt extraction, *Philosophical transactions. Series A*, 368(1910), 11-51. doi: 10.1098/rsta.2009.0200.
- Brown, M. (2013), Granite: from genesis to emplacement, *Geological Society of America Bulletin*, 125(7-8), 1079-1113. doi: 10.1130/b30877.1.
- Brown, M., and T. Rushmer (1997), The role of deformation in the movement of granitic melt: views from the laboratory and the field, in *Deformation-enhanced fluid transport in the Earth's crust and mantle*, edited by M. B. Holness, pp. 111-144, Springer Science & Business Media.
- Brown, M., T. Rushmer, and E. W. Sawyer (1995), Introduction to special section: Mechanisms and consequences of melt segregation from crustal protoliths, *Journal of Geophysical Research: Solid Earth*, 100(B8), 15551-15563. doi: 10.1029/95JB01253.
- Brown, M., K. Schulmann, and R. W. White (2011), Granulites, partial melting and the rheology of the lower crust, *Journal of Metamorphic Geology*, 29(1), 1-6. doi: 10.1111/j.1525-1314.2010.00917.x.
- Burton, K. W., and R. K. O'Nions (1992), The timing of mineral growth across a regional metamorphic sequence, *Nature*, 357(6375), 235-238.
- Caddick, M. J., J. Konopásek, and A. B. Thompson (2010), Preservation of garnet growth zoning and the duration of prograde metamorphism, *Journal of Petrology*, 51(11), 2327-2347. doi: 10.1093/petrology/egq059.
- Castaing, R., and S. Slodzian (1962), Microanalyse par émission ionique secondaire, *Journal de Microscopie*, 1, 395-410.
- Cesare, B. (2008), Crustal melting: working with enclaves, in *Working with Migmatites*, edited by E. W. Sawyer and M. Brown, pp. 37-55, Mineralogical Association of Canada, Short Course.
- Cesare, B., and C. Maineri (1999), Fluid-present anatexis of metapelites at El Hoyazo (SE Spain): constraints from Raman spectroscopy of graphite, *Contributions to Mineralogy and Petrology*, 135(1), 41-52. doi: 10.1007/s004100050496.
- Cesare, B., and M. T. Gómez-Pugnaire (2001), Crustal melting in the Alboran domain: Constraints from xenoliths of the Neogene volcanic province, *Physics and Chemistry of*

- the Earth, Part A: Solid Earth and Geodesy*, 26(4-5), 255-260.
- Cesare, B., E. Salvioli-Mariani, and G. Venturelli (1997), Crustal anatexis and melt extraction during deformation in the restitic xenoliths at El Joyazo (SE Spain), *Mineralogical Magazine*, 61(1), 15-27.
- Cesare, B., C. Marchesi, J. Hermann, and M. T. Gómez-Pugnaire (2003), Primary melt inclusions in andalusite from anatectic graphitic metapelites: Implications for the position of the Al_2SiO_5 triple point, *Geology*, 31(7), 573-576. doi: 10.1130/0091-7613(2003)031.
- Cesare, B., A. Acosta-Vigil, S. Ferrero, and O. Bartoli (2011), Melt inclusions in migmatites and granulites, *Journal of the Virtual Explorer*, 38, 1441-8142.
- Cesare, B., C. Maineri, A. Baron Toaldo, D. Pedron, and A. Acosta Vigil (2007), Immiscibility between carbonic fluids and granitic melts during crustal anatexis: A fluid and melt inclusion study in the enclaves of the Neogene Volcanic Province of SE Spain, *Chemical Geology*, 237(3-4), 433-449. doi: 10.1016/j.chemgeo.2006.07.013.
- Cesare, B., S. Ferrero, E. Salvioli-Mariani, D. Pedron, and A. Cavallo (2009), "Nanogranite" and glassy inclusions: The anatectic melt in migmatites and granulites, *Geology*, 37(7), 627-630.
- Clemens, J. D. (1990), The granulite — granite connexion, in *Granulites and Crustal Evolution*, edited by D. Vielzeuf and P. Vidal, pp. 25-36, Springer Netherlands.
- Clemens, J. D. (2006), Melting of the continental crust: fluid regimes, melting reactions and source-rock fertility, in *Brown, M. and Rushmer, T. (eds) Evolution and Differentiation of the Continental Crust*, Cambridge University Press, 397-331. doi: 10.2277/0521782376.
- Clemens, J. D., and K. Benn (2010), Anatomy, emplacement and evolution of a shallow-level, post-tectonic laccolith: the Mt Disappointment pluton, SE Australia, *Journal of the Geological Society*, 167(5), 915-941. doi: 10.1144/0016-76492009-120.
- Clemens, J. D., P. A. Helps, and G. Stevens (2010), Chemical structure in granitic magmas – a signal from the source?, *Geological Society of America Special Papers*, 472, 159-172. doi: 10.1130/2010.2472(11).
- Clocchiatti, R. (1975), Les inclusions vitreuses des cristaux de quartz. Etude optique, thermo-optique et chimique. Application géologique, Université de Paris VI, Mémoires de la Société Géologique de France, Nouvelle Série, n 125.
- Coggon, R., and T. J. B. Holland (2002), Mixing properties of phengiticmicas and revised garnet–phengite thermobarometers, *Journal of Metamorphic Geology*, 20, 683–696.
- Collins, W. J., R. H. Flood, R. H. Vernon, and S. E. Shaw (1989), The Wuluma granite, Arunta Block, central Australia: An example of in situ, near-isochemical granite formation in a granulite-facies terrane, *Lithos*, 23(1), 63-83. doi: 10.1016/0024-4937(89)90023-6.
- Comas, M. C., J. P. Platt, J. I. Soto, and A. B. Watts (1999), The origin and tectonic history of the Alborán Basin: insights from Leg 161, *Proceedings of the Ocean Drilling Program, Scientific Results*, 161, 555-579.
- Connolly, J. A. D. (2009), The geodynamic equation of state: What and how, *Geochemistry, Geophysics*,

- Geosystems*, 10(10), Q10014. doi: 10.1029/2009GC002540.
- Chappell, B. W. (1996), Magma mixing and the production of compositional variation within granite suites: Evidence from the granites of southeastern Australia, *Journal of Petrology*, 37(3), 449-470. doi: 10.1093/ptrology/37.3.449.
- Chappell, B. W. (1999), Aluminium saturation in I- and S-type granites and the characterization of fractionated haplogranites, *Lithos*, 46(3), 535-551. doi: 10.1016/S0024-4937(98)00086-3.
- Chappell, B. W., and A. J. R. White (1974), Two contrasting granite types, *Pacific Geology*, 8, 173-174.
- Cherniak, D. J., and E. B. Watson (2001), Pb diffusion in zircon, *Chemical Geology*, 172(1-2), 5-24. doi: 10.1016/S0009-2541(00)00233-3.
- Cherniak, D. J., and E. B. Watson (2003), Diffusion in zircon, *Reviews in Mineralogy and Geochemistry*, 53, 113-143. doi: 10.2113/0530113.
- Christensen, J., J. Selverstone, J. Rosenfeld, and D. DePaolo (1994), Correlation by Rb-Sr geochronology of garnet growth histories from different structural levels within the Tauern Window, Eastern Alps, *Contributions to Mineralogy and Petrology*, 118(1), 1-12. doi: 10.1007/BF00310607.
- Christensen, J. N., J. L. Rosenfeld, and D. J. DePaolo (1989), Rates of tectonometamorphic processes from Rubidium and Strontium isotopes in garnet, *Science*, 244(4911), 1469. doi: 10.1126/science.244.4911.1465.
- Christensen, N. I., and W. D. Mooney (1995), Seismic velocity structure and composition of the continental crust: A global view, *Journal of Geophysical Research: Solid Earth*, 100(B6), 9761-9788. doi: 10.1029/95JB00259.
- Dahl, P. S. (1997), A crystal-chemical basis for Pb retention and fission-track annealing systematics in U-bearing minerals, with implications for geochronology, *Earth and Planetary Science Letters*, 150(3-4), 277-290. doi: 10.1016/S0012-821X(97)00108-8.
- Darling, R. S. (2013), Zircon-bearing, crystallized melt inclusions in peritectic garnet from the western Adirondack Mountains, New York State, USA, *Geofluids*, 13(4), 453-459. doi: 10.1111/gfl.12047.
- Davies, G. R., P. H. Nixon, D. G. Pearson, and M. Obata (1993), Tectonic implications of graphitized diamonds from the Ronda, peridotite massif, southern Spain, *Geology*, 21(5), 471-474.
- Deniel, C., P. Vidal, A. Fernandez, P. Le Fort, and J.-J. Peucat (1987), Isotopic study of the Manaslu granite (Himalaya, Nepal): Inferences on the age and source of Himalayan leucogranites, *Contributions to Mineralogy and Petrology*, 96(1), 78-92. doi: 10.1007/BF00375529.
- Dewey, J. F., M. L. Helman, S. D. Knott, E. Turco, and D. H. W. Hutton (1989), Kinematics of the western Mediterranean, *Geological Society, London, Special Publications*, 45(1), 265-283. doi: 10.1144/gsl.sp.1989.045.01.15.
- Dougan, T. W. (1982), Melting reactions and trace element relationships in selected specimens of migmatitic pelites from New Hampshire and Maine, *Contributions to Mineralogy and Petrology*, 78(3), 337-344.
- Ducea, M. N., J. Ganguly, E. J. Rosenberg, P. J. Patchett, W. Cheng, and C. Isachsen (2003), Sm-Nd

- dating of spatially controlled domains of garnet single crystals: a new method of high-temperature thermochronology, *Earth and Planetary Science Letters*, 213(1–2), 31–42. doi: 10.1016/S0012-821X(03)00298-X.
- Duchêne, S., J. Blichert-Toft, B. Luais, P. Telouk, J. M. Lardeaux, and F. Albarède (1997), The Lu–Hf dating of garnets and the ages of the Alpine high-pressure metamorphism, *Nature*, 387(6633), 586–589.
- Duggen, S., K. Hoernle, P. van den Bogaard, and D. Garbe-Schönberg (2005), Post-collisional transition from subduction- to intraplate-type magmatism in the westernmost Mediterranean: Evidence for continental-edge delamination of subcontinental lithosphere, *Journal of Petrology*, 46(6), 1155–1201. doi: 10.1093/petrology/egi013.
- Duke, E. F., J. J. Papike, and J. C. Laul (1992), Geochemistry of a boron-rich peraluminous granite pluton: the Calamity Peak layered granite-pegmatite complex, Black Hills, South Dakota, *Canadian Mineralogist*, 30, 811–833.
- Egeler, C. G., and O. J. Simon (1969), Sur la tectonique de la zone Bétique: étude basée sur les recherches dans le secteur compris entre Almería et Vélez Rubio, *Verhandelingen der Koninklijke Nederlandse akademie van wetenschappen, afd. natuurkunde*, XXV(3), 1–90.
- Eggins, S. M. (2003), Laser ablation ICP-MS analysis of geological materials prepared as Lithium Borate glasses, *Geostandards Newsletter*, 27(2), 147–162. doi: 10.1111/j.1751-908X.2003.tb00642.x.
- Eggins, S. M., R. L. Rudnick, and W. F. McDonough (1998), The composition of peridotites and their minerals: a laser-ablation ICP-MS study, *Earth and Planetary Science Letters*, 154(1–4), 53–71. doi: 10.1016/S0012-821X(97)00195-7.
- Ellis, D. J., and M. Obata (1992), Migmatite and melt segregation at Cooma, New South Wales, *Geological Society of America Special Papers*, 272, 95–106. doi: 10.1130/SPE272-p95.
- Esteban, J. J., L. Sánchez-Rodríguez, D. Seward, J. Cuevas, and J. M. Tubía (2004), The late thermal history of the Ronda area, southern Spain, *Tectonophysics*, 389(1–2), 81–92. doi: 10.1016/j.tecto.2004.07.050.
- Esteban, J. J., J. Cuevas, J. M. Tubía, S. Sergeev, and A. Larionov (2011a), A revised Aquitanian age for the emplacement of the Ronda peridotites (Betic Cordilleras, southern Spain), *Geological Magazine*, 148(1), 183–187. doi: 10.1017/S0016756810000737.
- Esteban, J. J., J. M. Tubía, J. Cuevas, N. Vegas, S. Sergeev, and A. Larionov (2011b), Peri-Gondwanan provenance of pre-Triassic metamorphic sequences in the western Alpujarride nappes (Betic Cordillera, southern Spain), *Gondwana Research*, 20(2–3), 443–449. doi: 10.1016/j.gr.2010.11.006.
- Evensen, J., and D. London (2003), Experimental partitioning of Be, Cs, and other trace elements between cordierite and felsic melt, and the chemical signature of S-type granite, *Contributions to Mineralogy and Petrology*, 144(6), 739–757. doi: 10.1007/s00410-002-0426-x.
- Evensen, J. M., and D. London (2002), Experimental silicate mineral/melt partition coefficients for beryllium and the crustal Be cycle from migmatite to pegmatite, *Geochimica et Cosmochimica Acta*, 66(12), 2239–

2265. doi: 10.1016/S0016-7037(02)00889-X.
- Fernández-Suárez, J., F. Corfu, R. Arenas, A. Marcos, J. R. Martínez Catalán, F. Díaz García, J. Abati, and F. J. Fernández (2002), U-Pb evidence for a polyorogenic evolution of the HP-HT units of the NW Iberian Massif, *Contributions to Mineralogy and Petrology*, 143(2), 236-253. doi: 10.1007/s00410-001-0337-2.
- Ferrando, S., M. L. Frezzotti, L. Dallai, and R. Compagnoni (2005), Fluid-Rock interaction in UHP phengite-kyanite-epidote eclogite from the Sulu orogen, eastern China, *International Geology Review*, 47(7), 750-774. doi: 10.2747/0020-6814.47.7.750.
- Ferrero, S., R. J. Bodnar, B. Cesare, and C. Viti (2011), Re-equilibration of primary fluid inclusions in peritectic garnet from metapelitic enclaves, El Hoyazo, Spain, *Lithos*, 124(1), 117-131.
- Ferrero, S., R. Braga, M. Berkesi, B. Cesare, and N. Laridhi Ouazaa (2014), Production of metaluminous melt during fluid-present anatexis: an example from the Maghrebic basement, La Galite Archipelago, central Mediterranean, *Journal of Metamorphic Geology*, 32(2), 209-225.
- Ferrero, S., O. Bartoli, B. Cesare, E. Salvioli-Mariani, A. Acosta-Vigil, A. Cavallo, C. Groppo, and S. Battiston (2012), Microstructures of melt inclusions in anatexitic metasedimentary rocks, *Journal of Metamorphic Geology*, 30(3), 303-322. doi: 10.1111/j.1525-1314.2011.00968.x.
- Ferri, F., L. Burlini, B. Cesare, and R. Sassi (2007), Seismic properties of lower crustal xenoliths from El Hoyazo (SE Spain): Experimental evidence up to partial melting, *Earth and Planetary Science Letters*, 253(1-2), 239-253. doi: 10.1016/j.epsl.2006.10.027.
- Ferri, F., B. Gibert, M. Violay, F. R. Schilling, and B. Cesare, 4) (2009), Electrical conductivity in a partially molten lower crust from laboratory measurements on xenoliths (El Hoyazo, SE Spain), *Geophysical Research Abstracts, EGU General Assembly 2009*, 11.
- Ferry, J. M., and F. S. Spear (1978), Experimental calibration of the partitioning of Fe and Mg between biotite and garnet, *Contributions to Mineralogy and Petrology*, 66(2), 113-117. doi: 10.1007/BF00372150.
- Foucault, A., and J. Paquet (1971), Sur l'importance d'une tectogénèse hercynienne dans la région centrale des Cordillères bétiques (Sud de la Sierra Arana, Province de Grenade, Espagne), *Comptes Rendus de l'Académie des Sciences de Paris*, 272, 2756-2758.
- Fountain, D., J. Percival, and M. Salisbury (1990), Exposed Cross Sections of the Continental Crust - Synopsis, in *Exposed Cross-Sections of the Continental Crust*, edited by M. Salisbury and D. Fountain, pp. 653-662, Springer Netherlands.
- Frets, E., A. Tommasi, C. J. Garrido, J. A. Padrón-Navarta, I. Amri, and K. Targuisti (2012), Deformation processes and rheology of pyroxenites under lithospheric mantle conditions, *Journal of Structural Geology*, 39, 138-157. doi: 10.1016/j.jsg.2012.02.019.
- Frets, E. C., A. Tommasi, C. J. Garrido, A. Vauchez, D. Mainprice, K. Targuisti, and I. Amri (2014), The Beni Bousera peridotite (Rif Belt, Morocco): an oblique-slip low-angle shear zone thinning the

- Subcontinental Mantle Lithosphere, *Journal of Petrology*, 55(2), 283-313. doi: 10.1093/petrology/egt067.
- Frey, F. A., C. John Suen, and H. W. Stockman (1985), The Ronda high temperature peridotite: Geochemistry and petrogenesis, *Geochimica et Cosmochimica Acta*, 49(11), 2469-2491. doi: 10.1016/0016-7037(85)90247-9.
- Frezzotti, M. L., A. Peccerillo, V. Zanon, and I. Nikogosian (2004), Silica-rich melts in quartz Xenoliths from Vulcano Island and their bearing on processes of crustal anatexis and crust–magma interaction beneath the Aeolian Arc, Southern Italy, *Journal of Petrology*, 45(1), 3-26. doi: 10.1093/petrology/egg080.
- Fuhrman, M. L., and D. H. Lindsley (1988), Ternary-feldspar modeling and thermometry, *American Mineralogist*, 73(3-4), 201-215.
- Fujimaki, H. (1986), Partition coefficients of Hf, Zr, and REE between zircon, apatite, and liquid, *Contributions to Mineralogy and Petrology*, 94(1), 42-45. doi: 10.1007/BF00371224.
- Fyfe, W. S. (1973), The generation of batholiths *Tectonophysics*, 17, 273-283.
- Gao, L., L. Zeng, and K. Xie (2012), Eocene high grade metamorphism and crustal anatexis in the North Himalaya Gneiss Domes, Southern Tibet, *Chinese Science Bulletin*, 57(6), 639-650. doi: 10.1007/s11434-011-4805-4.
- Gao, X. Y., Y. F. Zheng, Y. X. Chen, and Z. Hu (2013), Trace element composition of continentally subducted slab-derived melt: Insight from multiphase solid inclusions in ultrahigh-pressure eclogite in the Dabie orogen, *Journal of Metamorphic Geology*, 31(4), 453-468. doi: 10.1111/jmg.12029.
- García-Casco, A., and R. L. Torres-Roldán (1996), Disequilibrium induced by fast decompression in St-Bt-Grt-Ky-Sil-And metapelites from the Betic belt (Southern Spain), *Journal of Petrology*, 37(5), 1207-1239.
- García-Casco, A., A. Sánchez Navas, and R. L. Torres Roldán (1993), Disequilibrium decomposition and breakdown of muscovite in high P-T gneisses, Betic Alpine belt (Southern Spain), *American Mineralogist*, 78(1-2), 158-177.
- García-Dueñas, V., J. C. Balanyá, and J. M. Martínez-Martínez (1992), Miocene extensional detachments in the outcropping basement of the northern Alboran Basin (Betics) and their tectonic implications, *Geo-Marine Letters*, 12(2-3), 88-95. doi: 10.1007/BF02084917.
- Garrido, C. J., and J. L. Bodinier (1999), Diversity of mafic rocks in the Ronda peridotite: Evidence for pervasive melt-rock reaction during heating of subcontinental lithosphere by upwelling asthenosphere, *Journal of Petrology*, 40(5), 729-754.
- Garrido, C. J., F. Gueydan, G. Booth-Rea, J. Précigout, K. Hidas, J. A. Padron-Navarta, and C. Marchesi (2011), Garnet lherzolite and garnet-spinel mylonite in the Ronda peridotite: Vestiges of Oligocene backarc mantle lithospheric extension in the western Mediterranean, *Geology*, 39(10), 927-930. doi: 10.1130/G31760.1.
- Goffé, B., A. Michard, V. García-Dueñas, F. González-Lodeiro, P. Monié, J. Campos, J. Galindo-Zaldívar, A. Jabaloy, J. M. Martínez-Martínez, and J. F. Simancas (1989), First evidence of high-pressure, low-

- temperature metamorphism in the Alpujarride nappes, Betic Cordillera (SE Spain), *European Journal of Mineralogy*, 1, 139-142.
- Goldstein, J. (2003), Scanning Electron Microscopy and X-ray Microanalysis, Springer, New York
- Gómez-Pugnaire, M. T., J. Galindo-Zaldívar, D. Rubatto, F. González-Lodeiro, V. López Sánchez-Vizcaíno, and A. Jabaloy (2004), A reinterpretation of the Nevado-Filábride and Alpujarride Complexes (Betic Cordillera): Field, petrography and U-Pb ages from orthogneisses (western Sierra Nevada, S Spain), *Schweizerische Mineralogische und Petrographische Mitteilungen*, 84(3), 303-322.
- Grant, J. A., and B. R. Frost (1990), Contact metamorphism and partial melting of pelitic rocks in the aureole of the Laramie anorthosite complex, Morton Pass, Wyoming, *American Journal of Science*, 290(4), 425-472.
- Graybill, F. A. (1976), *Theory and Application of the Linear Model*, Duxbury Press, Massachusetts.
- Greenfield, J. E., G. L. Clarke, and R. W. White (1998), A sequence of partial melting reactions at Mt Stafford, central Australia, *Journal of Metamorphic Geology*, 16(3), 363-378. doi: 10.1111/j.1525-1314.1998.00141.x.
- Guillot, S., and P. Le Fort (1995), Geochemical constraints on the bimodal origin of High Himalayan leucogranites, *Lithos*, 35(3-4), 221-234. doi: 10.1016/0024-4937(94)00052-4.
- Gurenko, A. A., R. B. Trumbull, R. Thomas, and J. M. Linsday (2005), A melt inclusion record of volatiles, trace elements and Li-B isotope variations in a single magma system from the Plat Pays Volcanic Complex, Dominica, Lesser Antilles, *Journal of Petrology*, 46(12), 2495-2526. doi: 10.1093/petrology/egi063.
- Halter, W. E., T. Pettke, C. A. Heinrich, and B. Rothen-Rutishauser (2002), Major to trace element analysis of melt inclusions by laser-ablation ICP-MS: methods of quantification, *Chemical Geology*, 183(1-4), 63-86. doi: 10.1016/S0009-2541(01)00372-2.
- Hanson, G. N. (1989), An approach to trace element modeling using a simple igneous system as an example, *Reviews in Mineralogy and Geochemistry*, 21(1), 79-97.
- Harley, S. (1989), The origins of granulites - A metamorphic perspective, *Geological Magazine*, 215-247.
- Harrison, T. M. (2009), The Hadean crust: evidence from >4 Ga Zircons, *Annual Review of Earth and Planetary Sciences*, 37, 479-505. doi: 10.1146/annurev.earth.031208.100151.
- Hart, R. J., M. A. G. Andreoli, M. Tredoux, and M. J. De Wit (1990), Geochemistry across an exposed section of Archean crust at Vredefort, South Africa: with implications for mid-crustal discontinuities, *Chemical Geology*, 82, 21-50. doi: 10.1016/0009-2541(90)90072-F.
- Hidas, K., G. Booth-Rea, C. J. Garrido, J. M. Martínez-Martínez, J. A. Padrón-Navarta, Z. Konc, F. Giaconia, E. Frets, and C. Marchesi (2013), Backarc basin inversion and subcontinental mantle emplacement in the crust: kilometre-scale folding and shearing at the base of the proto-Alborán lithospheric mantle (Betic Cordillera, southern Spain), *Journal of the Geological Society*, 170(1), 47-55. doi: 10.1144/jgs2011-151.

- Higuchi, H., and H. Nagasawa (1969), Partition of trace elements between rock-forming minerals and the host volcanic rocks, *Earth and Planetary Science Letters*, 7(3), 281-287. doi: 10.1016/0012-821X(69)90066-1.
- Hodges, K. V., and F. S. Spear (1982), Geothermometry, geobarometry and the Al₂SiO₅ triple point at the Mt. Moosilauke, New Hampshire, *American Mineralogist*, 67, 1118-1134.
- Holbrook, W. S., G. M. Purdy, J. A. Collins, R. E. Sheridan, D. L. Musser, L. Glover, M. Talwani, J. I. Ewing, R. Hawman, and S. B. Smithson (1992), Deep velocity structure of rifted continental crust, U.S. Mid-Atlantic Margin, from wide-angle reflection/refraction data, *Geophysical Research Letters*, 19(16), 1699-1702. doi: 10.1029/92GL01799.
- Holdaway, M. J., and S. Lee (1977), Fe-Mg cordierite stability in high-grade pelitic rocks based on experimental, theoretical, and natural observations, *Contributions to Mineralogy and Petrology*, 63(2), 175-198. doi: 10.1007/BF00398778.
- Holland, T., and R. Powell (2001), Calculation of phase relations involving haplogranitic melts using an internally consistent thermodynamic dataset, *Journal of Petrology*, 42(4), 673-683. doi: 10.1093/petrology/42.4.673.
- Holland, T. J. B., and R. Powell (1998), An internally consistent thermodynamic data set for phases of petrological interest, *Journal of Metamorphic Geology*, 16(3), 309-343. doi: 10.1111/j.1525-1314.1998.00140.x.
- Hwanga, S., P. Shenb, H. Chuc, T. Yuid, and C. Lind (2001), Genesis of microdiamonds from melt and associated multiphase inclusions in garnet of ultrahigh-pressure gneiss from Erzgebirge, Germany, *Earth and Planetary Science Letters*, 188(1), 9-15. doi: 10.1016/S0012-821X(01)00314-4.
- Icenhower, J., and D. London (1995), An experimental study of element partitioning among biotite, muscovite, and coexisting peraluminous silicic melt at 200 MPa (H₂O), *American Mineralogist*, 80(11-12), 1229-1251.
- Icenhower, J., and D. London (1996), Experimental partitioning of Rb, Cs, Sr, and Ba between alkali feldspar and peraluminous melt *American Mineralogist*, 81, 719-734.
- Inger, S., and N. Harris (1993), Geochemical constraints on leucogranite magmatism in the Langtang Valley, Nepal Himalaya, *Journal of Petrology*, 34(2), 345-368. doi: 10.1093/petrology/34.2.345.
- Jakobsen, H., N. C. Munksgaard, and H. P. Zeck (1983), Pre-Dalslandian deformation and recrystallization in the basement of the Dalslandian supracrustals, Grenvillian (Sveconorwegian) belt, south-west Sweden, *Geologiska Foreningens i Stockholm Forhandlingar*, 105(3), 205-212.
- Janots, E., F. Negro, F. Brunet, B. Goffé, M. Engi, and M. L. Bouybaouène (2006), Evolution of the REE mineralogy in HP-LT metapelites of the Sebide complex, Rif, Morocco: Monazite stability and geochronology, *Lithos*, 87(3-4), 214-234. doi: 10.1016/j.lithos.2005.06.008.
- Jochum, K. P., U. Weis, B. Stoll, D. Kuzmin, Q. Yang, I. Raczek, D. E. Jacob, A. Stracke, K. Birbaum, and D. A. Frick (2011), Determination of reference values for NIST SRM 610-

- 617 glasses following ISO guidelines, *Geostandards and Geoanalytical Research*, 35(4), 397-429.
- Johanesen, K., J. P. Platt, M. S. Kaplan, and A. J. Ianno (2014), A revised thermal history of the Ronda peridotite, S. Spain: New evidence for excision during exhumation, *Earth and Planetary Science Letters*, 393, 187-199. doi: 10.1016/j.epsl.2014.01.024.
- Johannes, W. (1973), A simplified piston-cylinder apparatus of high precision, *Neues Jahrbuch fuer Mineralogie Monatshefte*, 7(8), 337-351.
- Johannes, W., and F. Holtz (1992), Melting of plagioclase in granite and related systems: composition of coexisting phases and kinetic observations, *Earth and Environmental Science Transactions of the Royal Society of Edinburgh*, 83(1-2), 417-422. doi: 10.1017/S0263593300008087.
- Johannes, W., and F. Holtz (1996), Petrogenesis and Experimental Petrology of Granitic Rocks, *New York: Springer*, 22, 335. doi: 10.1007/978-3-642-61049-3.
- Ketchum, R. A. (1996), Distribution of heat-producing elements in the upper and middle crust of southern and west central Arizona: Evidence from the core complexes, *Journal of Geophysical Research: Solid Earth*, 101(B6), 13611-13632. doi: 10.1029/96JB00664.
- Khodja, H., E. Berthoumieux, L. Daudin, and J.-P. Gallien (2001), The Pierre Süe Laboratory nuclear microprobe as a multi-disciplinary analysis tool, *Nuclear Instruments and Methods in Physics Research Section B: Beam Interactions with Materials and Atoms*, 181(1-4), 83-86. doi: 10.1016/S0168-583X(01)00564-X.
- Klemme, S., D. Günther, K. Hametner, S. Prowatke, and T. Zack (2006), The partitioning of trace elements between ilmenite, ulvospinel, armalcolite and silicate melts with implications for the early differentiation of the moon, *Chemical Geology*, 234(3-4), 251-263. doi: 10.1016/j.chemgeo.2006.05.005.
- Korsakov, A. V., and J. Hermann (2006), Silicate and carbonate melt inclusions associated with diamonds in deeply subducted carbonate rocks, *Earth and Planetary Science Letters*, 241(1-2), 104-118. doi: 10.1016/j.epsl.2005.10.037.
- Kosler, J. (2001), Laser-ablation ICPMS study of metamorphic minerals and processes, in *Laser-ablation ICPMS in Earth Sciences*, edited by P. Sylvester, pp. 185-202, Mineralogical Society of Canada, Short Course.
- Koziol, A. M. (1989), Recalibration of the garnet-plagioclase- Al_2SiO_5 -quartz (GASP) geobarometer and applications to natural parageneses, *Eos, Transactions American Geophysical Union*, 70, 943.
- Koziol, A. M., and R. C. Newton (1988), Redetermination of the anorthite breakdown reaction and improvement of the plagioclase-garnet- Al_2SiO_5 -quartz geobarometer, *American Mineralogist*, 73, 216-223.
- Kretz, R. (1983), Symbols for rock-forming minerals, *American Mineralogist*, 68(1-2), 277-279.
- Lang, H. M., and J. A. Gilotti (2007), Partial melting of metapelites at ultrahigh-pressure conditions, Greenland Caledonides, *Journal of Metamorphic Geology*, 25(2), 129-147. doi: 10.1111/j.1525-1314.2006.00687.x.

- Lavina, B., B. Cesare, A. M. Álvarez-Valero, H. Uchida, R. T. Downs, A. Koneva, and P. Dera (2009), Closure temperatures of intracrystalline ordering in anatectic and metamorphic hercynite, $\text{Fe}^{2+}\text{Al}_2\text{O}_4$, *American Mineralogist*, 94(5-6), 657. doi: 10.2138/am.2009.3031.
- Le Fort, P. (1981), Manaslu leucogranite: A collision signature of the Himalaya: A model for its genesis and emplacement, *Journal of Geophysical Research: Solid Earth*, 86(B11), 10545-10568. doi: 10.1029/JB086iB11p10545.
- Le Fort, P., M. Cuney, C. Deniel, C. France-Lanord, S. M. F. Sheppard, B. N. Upreti, and P. Vidal (1987), Deep Seated Processes in Collision Zones Crustal generation of the Himalayan leucogranites, *Tectonophysics*, 134(1), 39-57. doi: 10.1016/0040-1951(87)90248-4.
- Lee, J. K. W., I. S. Williams, and D. J. Ellis (1997), Pb, U and Th diffusion in natural zircon, *Nature*, 390(6656), 159-162.
- Lenoir, X., C. Garrido, J. Bodinier, J. Dautria, and F. Gervilla (2001), The recrystallization front of the Ronda peridotite: Evidence for melting and thermal erosion of subcontinental lithospheric mantle beneath the Alboran basin, *Journal of Petrology*, 42(1), 141-158. doi: 10.1093/petrology/42.1.141.
- Liu, Q., J. Hermann, and J. Zhang (2013), Polyphase inclusions in the Shuanghe UHP eclogites formed by subsolidus transformation and incipient melting during exhumation of deeply subducted crust, *Lithos*, 177, 91-109. doi: 10.1016/j.lithos.2013.06.010.
- Loomis, T. (1975), Reaction of zoning of garnet, *Contributions to Mineralogy and Petrology*, 52(4), 285-305. doi: 10.1007/BF00401458.
- Loomis, T. P. (1972), Contact metamorphism of pelitic rock by the Ronda ultramafic intrusion, southern Spain, *Geological Society of America Bulletin*, 83(8), 2449-2474. doi: 10.1130/0016-7606(1972)83[2449:cmopr]2.0.co;2.
- López Ruiz, J., and E. Rodríguez Badiola (1980), La region volcánica Neógena del sureste de España, *Estudios geológicos*, (1-2), 5-63.
- Lowenstern, J. B. (1995), Applications of silicate melt inclusions to the study of magmatic volatiles, In: J.F.H. Thompson (ed). *Magmas, Fluids and Ore Deposits. Mineralogical Association of Canada Short Course*, 23, 71-99.
- Ludwig, K. R. (2008), Isoplot: A geochronological toolkit for Microsoft Excel, *Berkley Geochronology Centre, Special Publication*, 4, 77.
- Lundeen, M. T. (1978), Emplacement of the Ronda peridotite, Sierra Bermeja, Spain, *Geological Society of America Bulletin*, 89(2), 172-180. doi: 10.1130/0016-7606(1978)89<172:eotrps>2.0.co;2.
- Luo, Y., and J. C. Ayers (2009), Experimental measurements of zircon/melt trace-element partition coefficients, *Geochimica et Cosmochimica Acta*, 73(12), 3656-3679. doi: 10.1016/j.gca.2009.03.027.
- Mahood, G., and W. Hildreth (1983), Large partition coefficients for trace elements in high-silica rhyolites, *Geochimica et Cosmochimica Acta*, 47(1), 11-30. doi: 10.1016/0016-7037(83)90087-X.
- Malaspina, N., J. Hermann, M. Scambelluri, and R. Compagnoni (2006), Polyphase inclusions in

- garnet-orthopyroxenite (Dabie Shan, China) as monitors for metasomatism and fluid-related trace element transfer in subduction zone peridotite, *Earth and Planetary Science Letters*, 249(3-4), 173-187. doi: 10.1016/j.epsl.2006.07.017.
- Marchesi, C., W. L. Griffin, C. J. Garrido, J.-L. Bodinier, and N. J. Pearson (2010), Persistence of mantle lithospheric Re-Os signature during asthenospherization of the subcontinental lithospheric mantle: insights from in situ isotopic analysis of sulfides from the Ronda peridotite (Southern Spain), *Contributions to Mineralogy and Petrology*, 159(3), 315-330. doi: 10.1007/s00410-009-0429-y.
- Marchildon, N., and M. Brown (2001), Melt segregation in late syn-tectonic anatectic migmatites: an example from the Onawa contact aureole, Maine, USA, *Physics and Chemistry of the Earth, Part A: Solid Earth and Geodesy*, 26(4-5), 225-229. doi: 10.1016/S1464-1895(01)00049-7.
- Martín-Algarra, A. (1987), Evolución geológica alpina del contacto entre las Zonas Internas y las Zonas Externas de las Cordilleras Béticas, Ph.D. thesis, 1171 pp, University of Granada, unpublished.
- Martín-Algarra, A., A. Messina, V. V. Perrone, S. Russo, A. Maate, and M. Martín-Martín (2000), A lost realm in the internal domains of the Betic-Rif orogen (Spain and Morocco): Evidence from conglomerates and consequences for Alpine geodynamic evolution, *Journal of Geology*, 108(4), 447-467.
- Martin, H. (1980), Comportement de quelques elements en traces au cours de l'anatexie: exemple du Massif de Saint-Malo (Bretagne, France), *Canadian Journal of Earth Sciences*, 17(7), 927-941. doi: 10.1139/e80-089.
- Martín, J. M., Braga, J.C. (1987), Alpujárride carbonate deposits (southern Spain)—marine sedimentation in a Triassic Atlantic, *Palaeogeography, Palaeoclimatology, Palaeoecology*, 59, 243-260.
- Martínez-Martínez, J. M., and J. M. Azañón (1997), Mode of extensional tectonics in the southeastern Betics (SE Spain): Implications for the tectonic evolution of the peri-Alborán orogenic system, *Tectonics*, 16(2), 205-225. doi: 10.1029/97TC00157.
- Martínez-Martínez, J. M., G. Booth-Rea, J. M. Azañón, and F. Torcal (2006), Active transfer fault zone linking a segmented extensional system (Betics, southern Spain): Insight into heterogeneous extension driven by edge delamination, *Tectonophysics*, 422(1-4), 159-173. doi: 10.1016/j.tecto.2006.06.001.
- Massonne, H.-J. (2014), Wealth of P-T-t information in medium-high grade metapelites: Example from the Jubrique Unit of the Betic Cordillera, S Spain, *Lithos*, 208-209(0), 137-157. doi: 10.1016/j.lithos.2014.08.027.
- Mazzoli, S., and A. Algarra (2011), Deformation partitioning during transpressional emplacement of a 'mantle extrusion wedge': the Ronda peridotites, western Betic Cordillera, Spain, *Journal of the Geological Society*, 168(2), 373-382. doi: 10.1144/0016-76492010-126.
- McLennan, S. M., S. R. Taylor, and S. R. Hemming (2006), Composition, differentiation, and evolution of continental crust: constraints from sedimentary rocks and heat flow (Evolution and Differentiation of the Continental Crust), 92-134.

- Mehnert, K. R., and W. Büsch (1982), The initial stage of migmatite formation, *Neues Jahrbuch für Mineralogie - Abhandlungen*, 145, 211-238.
- Melson, W. G. (1983), Monitoring the 1980-1982 eruptions of Mount St. Helens: Compositions and abundances of glass, *Science*, 221(4618), 1387-1391. doi: 10.1126/science.221.4618.1387.
- Michard, A., B. Goffé, M. L. Bouybaouene, and O. Saddiqi (1997), Late Hercynian-Mesozoic thinning in the Alboran domain: Metamorphic data from the northern Rif, Morocco, *Terra Nova*, 9(4), 171-174. doi: 10.1046/j.1365-3121.1997.d01-24.x.
- Michard, A., F. Negro, O. Saddiqi, M. L. Bouybaouène, A. Chalouan, R. Montigny, and B. Goffé (2006), Pressure-temperature-time constraints on the Maghrebide mountain building: evidence from the Rif-Betic transect (Morocco, Spain), Algerian correlations, and geodynamic implications, *Comptes Rendus de l'Académie des Sciences de Paris. Série II*, 338(1-2), 92-114. doi: 10.1016/j.crte.2005.11.011.
- Miller, C. F., S. M. McDowell, and R. W. Mapes (2003), Hot and cold granites? Implications of zircon saturation temperatures and preservation of inheritance, *Geology*, 31(6), 529-532. doi: 10.1130/0091-7613(2003)031<0529:hacgio>2.0.co; 2.
- Miller, D. J., and N. L. Christensen (1994), Seismic signature and geochemistry of an island arc: A multidisciplinary study of the Kohistan accreted terrane, northern Pakistan, *Journal of Geophysical Research: Solid Earth*, 99(B6), 11623-11642. doi: 10.1029/94JB00059.
- Molina, J. F., and S. Poli (2000), Carbonate stability and fluid composition in subducted oceanic crust: an experimental study on H₂O-CO₂-bearing basalts, *Earth and Planetary Science Letters*, 176(3-4), 295-310. doi: 10.1016/S0012-821X(00)00021-2.
- Monié, P., R. L. Torres-Roldán, and A. García-Casco (1994), Cooling and exhumation of the western Betic Cordilleras, Ar⁴⁰-Ar³⁹ thermochronological constraints on a collapsed terrane, *Tectonophysics*, 238(1-4), 353-379.
- Monié, P., J. Galindo-Zaldívar, F. G. Lodeiro, B. Goffé, and A. Jabaloy (1991), ⁴⁰Ar/³⁹Ar geochronology of Alpine tectonism in the Betic Cordilleras (southern Spain), *Journal of the Geological Society*, 148(2), 289-297.
- Montel, J. M. (1993), A model for monazite/melt equilibrium and application to the generation of granitic magmas, *Chemical Geology*, 110(1-3), 127-146. doi: 10.1016/0009-2541(93)90250-M.
- Montel, J. M., J. Kornprobst, and D. Vielzeuf (2000), Preservation of old U-Th-Pb ages in shielded monazite: Example from the Beni Bousera Hercynian kinzigites (Morocco), *Journal of Metamorphic Geology*, 18(3), 335-342.
- Morgan, G. B., and D. London (2005), Effect of current density on the electron microprobe analysis of alkali aluminosilicate glasses, *American Mineralogist*, 90(7), 1131-1138. doi: 10.2138/am.2005.1769.
- Morgan, G. B. V., and D. London (1996), Optimizing the electron microprobe analysis of hydrous alkali aluminosilicate glasses, *Journal Name: American Mineralogist*, 81(9-10), 1176-1185.

- Morishita, T., S. Arai, and F. Gervilla (2001), High-pressure aluminous mafic rocks from the Ronda peridotite massif, southern Spain: significance of sapphirine- and corundum-bearing mineral assemblages, *Lithos*, 57(2-3), 143-161.
- Müller, W., M. Shelley, P. Miller, and S. Broude (2009), Initial performance metrics of a new custom-designed ArF excimer LA-ICPMS system coupled to a two-volume laser-ablation cell, *Journal of Analytical Atomic Spectrometry*, 24(2), 209-214. doi: 10.1039/B805995K.
- Mungall, J. E. (2002), Empirical models relating viscosity and tracer diffusion in magmatic silicate melts, *Geochimica et Cosmochimica Acta*, 66(1), 125-143. doi: 10.1016/S0016-7037(01)00736-0.
- Munksgaard, N. (1984), High $\delta^{18}\text{O}$ and possible pre-eruptional Rb-Sr isochrons in cordierite-bearing Neogene volcanics from SE Spain, *Contributions to Mineralogy and Petrology*, 87(4), 351-358. doi: 10.1007/BF00381291.
- Munksgaard, N. C. (1985), A non-magmatic origin for compositionally zoned euhedral garnets in silicic Neogene volcanics from SE Spain., *Neues Jahrbuch für Mineralogie, Monatshefte*, 2, 73-82.
- Nabelek, P. I., C. Russ-Nabelek, and J. R. Denison (1992), The generation and crystallization conditions of the Proterozoic Harney Peak Leucogranite, Black Hills, South Dakota, USA: Petrologic and geochemical constraints, *Contributions to Mineralogy and Petrology*, 110(2-3), 173-191. doi: 10.1007/BF00310737.
- Nabelek, P. I., M. D. Glascock, and M. D. GLASCOCK (1995), REE-depleted leucogranites, Black Hills, South Dakota: A consequence of disequilibrium melting of monazite-bearing schists, *Journal of Petrology*, 36(4), 1055-1071. doi: 10.1093/petrology/36.4.1055.
- Nagasawa, H., and C. C. Schnetzler (1971), Partitioning of rare earth, alkali and alkaline earth elements between phenocrysts and acidic igneous magma, *Geochimica et Cosmochimica Acta*, 35(9), 953-968. doi: 10.1016/0016-7037(71)90008-1.
- Nash, W. P., and H. R. Crecraft (1985), Partition coefficients for trace elements in silicic magmas, *Geochimica et Cosmochimica Acta*, 49(11), 2309-2322. doi: 10.1016/0016-7037(85)90231-5.
- Norman, M. D., W. L. Griffin, N. J. Pearson, M. O. García, and S. Y. O'reilly (1998), Quantitative analysis of trace element abundances in glasses and minerals: A comparison of laser ablation inductively coupled plasma mass spectrometry, solution inductively coupled plasma mass spectrometry, proton microprobe and electron microprobe data, *Journal of Analytical Atomic Spectrometry*, 13(5), 477-482. doi: 10.1039/A707972I.
- Obata, M. (1980), The Ronda peridotite: Garnet-, spinel-, and plagioclase-lherzolite facies and the P-T trajectories of a high-temperature mantle intrusion, *Journal of Petrology*, 21(3), 533-572. doi: 10.1093/petrology/21.3.533.
- Olmo, A., J. G. Pablo, F. Aldaya, J. Campos, J. Chacón, V. García-Dueñas, L. García-Rosell, C. Sanz de Galdeano, M. Orozco, and R. L. Torres-Roldán (1980), Mapa y memoria explicativa de la hoja 1064 (Cortes de la Frontera) del Mapa Geológico Nacional a escala

- 1:50.000, *Instituto Geológico y Minero de España*.
- Pacholski, M. L., and N. Winograd (1999), Imaging with mass spectrometry, *Chemical Reviews*, 99(10), 2977-3006.
- Patiño Douce, A. E., and J. S. Beard (1996), Effects of P, f(O₂) and Mg/Fe ratio on dehydration melting of model metagreywackes, *Journal of Petrology*, 37(5), 999-1024. doi: 10.1093/petrology/37.5.999.
- Paton, C., J. Hellstrom, B. Paul, J. Woodhead, and J. Hergt (2011), Iolite: Freeware for the visualisation and processing of mass spectrometric data, *Journal of Analytical Atomic Spectrometry*, 26(12), 2508-2518.
- Pearce, N. J. G., W. T. Perkins, J. A. Westgate, M. P. Gorton, S. E. Jackson, C. R. Neal, and S. P. Chenery (1997), A Compilation of new and published major and trace element data for NIST SRM 610 and NIST SRM 612 glass reference materials, *Geostandards Newsletter*, 21(1), 115-144. doi: 10.1111/j.1751-908X.1997.tb00538.x.
- Pearson, D. G., and G. M. Nowell (2004), Re–Os and Lu–Hf isotope constraints on the origin and age of pyroxenites from the Beni Bousera peridotite massif: Implications for mixed peridotite–pyroxenite mantle sources, *Journal of Petrology*, 45(2), 439-455. doi: 10.1093/petrology/egg102.
- Pearson, D. G., G. R. Davies, and P. H. Nixon (1993), Geochemical constraints on the petrogenesis of diamond facies pyroxenites from the Beni Bousera peridotite massif, North Morocco, *Journal of Petrology*, 34(1), 125-172. doi: 10.1093/petrology/34.1.125.
- Perchuk, A. L., M. Burchard, W. V. Maresch, and H. P. Schertl (2008), Melting of hydrous and carbonate mineral inclusions in garnet host during ultrahigh pressure experiments, *Lithos*, 103(1–2), 25-45. doi: 10.1016/j.lithos.2007.09.008.
- Perini, G., B. Cesare, M. T. Gómez-Pugnaire, L. Ghezzi, and S. Tommasini (2009), Armouring effect on Sr–Nd isotopes during disequilibrium crustal melting: the case study of frozen migmatites from El Hoyazo and Mazarrón, SE Spain, *European Journal of Mineralogy*, 21, 117-131.
- Platt, J. P., and M. J. Whitehouse (1999), Early Miocene high-temperature metamorphism and rapid exhumation in the Betic Cordillera (Spain): evidence from U–Pb zircon ages, *Earth and Planetary Science Letters*, 171(4), 591-605.
- Platt, J. P., S. P. Kelley, A. Carter, and M. Orozco (2005), Timing of tectonic events in the Alpujarride Complex, Betic Cordillera, southern Spain, *Journal of the Geological Society*, 162, 451-462.
- Platt, J. P., W. M. Behr, K. Johannesen, and J. R. Williams (2013), The Betic-Rif arc and its orogenic hinterland: A review, *Annual Review of Earth and Planetary Sciences*, 41, 313-357. doi: 10.1146/annurev-earth-050212-123951.
- Platt, J. P., J. I. Soto, M. J. Whitehouse, A. J. Hurford, and S. P. Kelley (1998), Thermal evolution, rate of exhumation, and tectonic significance of metamorphic rocks from the floor of the Alboran extensional basin, western Mediterranean, *Tectonics*, 17(5), 671-689.
- Platt, J. P., M. J. Whitehouse, S. P. Kelley, A. Carter, and L. Hollick (2003a), Simultaneous extensional exhumation across the Alboran Basin: Implications for the causes of

- late orogenic extension, *Geology*, 31(3), 251-254.
- Platt, J. P., T. W. Argles, A. Carter, S. P. Kelley, M. J. Whitehouse, and L. Loneragan (2003b), Exhumation of the Ronda peridotite and its crustal envelope: constraints from thermal modelling of a P-T-time array, *Journal of the Geological Society*, 160, 655-676.
- Platt, J. P., S. Allerton, A. Kirker, C. Mandeville, A. Mayfield, E. S. Platzman, and A. Rimi (2003c), The ultimate arc: Differential displacement, oroclinal bending, and vertical axis rotation in the External Betic-Rif arc, *Tectonics*, 22(3).
- Pollington, A. D., and E. F. Baxter (2010), High resolution Sm–Nd garnet geochronology reveals the uneven pace of tectonometamorphic processes, *Earth and Planetary Science Letters*, 293(1–2), 63-71. doi: 10.1016/j.epsl.2010.02.019.
- Pollington, A. D., and E. F. Baxter (2011), High precision microsampling and preparation of zoned garnet porphyroblasts for Sm–Nd geochronology, *Chemical Geology*, 281(3–4), 270-282. doi: 10.1016/j.chemgeo.2010.12.014.
- Pouchou, J. L., and F. Pichoir (1985), “PAP” ($\varphi \rho Z$) correction procedure for improved quantitative microanalysis, in *Microbeam Analysis*, edited by J. T. Armstrong, pp. 104-106, San Francisco Press, San Francisco.
- Précigout, J., F. Gueydan, D. Gapais, C. J. Garrido, and A. Essaifi (2007), Strain localisation in the subcontinental mantle - a ductile alternative to the brittle mantle, *Tectonophysics*, 445(3-4), 318-336. doi: 10.1016/j.tecto.2007.09.002.
- Précigout, J., F. Gueydan, C. J. Garrido, N. Cogné, and G. Booth-Rea (2013), Deformation and exhumation of the Ronda peridotite (Spain), *Tectonics*, 32(4), 1011-1025. doi: 10.1002/tect.20062.
- Pressley, R. A., and M. Brown (1999), The Phillips pluton, Maine, USA: evidence of heterogeneous crustal sources and implications for granite ascent and emplacement mechanisms in convergent orogens, *Lithos*, 46(3), 335-366. doi: 10.1016/S0024-4937(98)00073-5.
- Priem, H. N. A., N. A. I. M. Boelrijk, E. H. Hebeda, I. S. Oen, E. A. T. Verdurmen, and R. H. Verschure (1979), Isotopic dating of the emplacement of the ultramafic masses in the Serrania de Ronda, Southern Spain, *Contributions to Mineralogy and Petrology*, 70(1), 103-109. doi: 10.1007/BF00371876.
- Prowatke, S., and S. Klemme (2006), Trace element partitioning between apatite and silicate melts, *Geochimica et Cosmochimica Acta*, 70(17), 4513-4527. doi: 10.1016/j.gca.2006.06.162.
- Qiang, L., and W. Fuyuan (1994), Experimental studies on partial melting of massive samples of granite, *Chinese Journal of Geochemistry*, 13(4), 363-370. doi: 10.1007/BF02838525.
- Reagan, M. K., O. Ishizuka, R. J. Stern, K. A. Kelley, Y. Ohara, J. Blichert-Toft, S. H. Bloomer, J. Cash, P. Fryer, B. B. Hanan, R. Hickey-Vargas, T. Ishii, J.-I. Kimura, D. W. Peate, M. C. Rowe, and M. Woods (2010), Fore-arc basalts and subduction initiation in the Izu-Bonin-Mariana system, *Geochemistry Geophysics Geosystems*, 11. doi: 10.1029/2009gc002871.
- Reed, S. J. B. (1995), Electron Microprobe Microanalysis, in *Microprobe Techniques in the Earth Sciences*, edited by P. J. Potts, J. F.

- Bowles and S. J. B. Reed, pp. 49–90, The Mineralogical Society of America.
- Reed, S. J. B. (2005), *Electron Microprobe Analysis and Scanning Electron Microscopy in Geology*, 212 pp., Cambridge University Press, Cambridge.
- Reid, M. R. (1990), Ion probe investigation of Rare Earth Element distribution and partial melting of metasedimentary granulites, in *Granulites and Crustal Evolution*, edited by D. Vielzeuf and P. Vidal, pp. 507-522, Springer Netherlands.
- Richards, J. P., A. E. J. Crafford, P. Wannamaker, and P. Sims (2002), Deep crustal controls on mineral trends, *Ore Geology Reviews*, 21(3-4), 125-126.
- Roedder, E. (1984), Fluid inclusions, Mineralogical Society of America, Reviews in Mineralogy, 12, 644.
- Rossetti, F., T. Theye, F. Lucci, M. L. Bouybaouene, A. Dini, A. Gerdes, D. Phillips, and D. Cozzupoli (2010), Timing and modes of granite magmatism in the core of the Alboran Domain, Rif chain, northern Morocco: Implications for the Alpine evolution of the western Mediterranean, *Tectonics*, 29(2), TC2017. doi: 10.1029/2009tc002487.
- Rubatto, D., and J. Hermann (2007), Experimental zircon/melt and zircon/garnet trace element partitioning and implications for the geochronology of crustal rocks, *Chemical Geology*, 241(1-2), 38-61. doi: 10.1016/j.chemgeo.2007.01.027.
- Rudnick, R. L., and D. M. Fountain (1995), Nature and composition of the continental crust: A lower crustal perspective, *Reviews of Geophysics*, 33(3), 267-309. doi: 10.1029/95RG01302.
- Rudnick, R. L., and S. Gao (2003), Composition of the Continental Crust, in *Treatise on Geochemistry*, edited by H. D. Turekian and K. K. Holland, pp. Vol. 3, pp. 1-64, Pergamon Press, Oxford.
- Ruiz-Cruz, M. D., and C. Sanz de Galdeano (2012), Diamond and coesite in ultrahigh-pressure–ultrahigh-temperature granulites from Ceuta, Northern Rif, northwest Africa, *Mineralogical Magazine*, 76(3), 683-705. doi: 10.1180/minmag.2012.076.3.17.
- Ruiz-Cruz, M. D., and C. Sanz de Galdeano (2013), Coesite and diamond inclusions, exsolution microstructures and chemical patterns in ultrahigh pressure garnet from Ceuta (Northern Rif, Spain), *Lithos*, 177, 184-206. doi: 10.1016/j.lithos.2013.06.004.
- Ruiz-Cruz, M. D., and C. Sanz de Galdeano (2014), Garnet variety and zircon ages in UHP meta-sedimentary rocks from the Jubrique zone (Alpujarride Complex, Betic Cordillera, Spain): Evidence for a pre-Alpine emplacement of the Ronda peridotite, *International Geology Review*, 56(7), 845-868. doi: 10.1080/00206814.2014.904759.
- Sánchez-Navas, A., A. García-Casco, and A. Martín-Algarra (2014), Pre-Alpine discordant granitic dikes in the metamorphic core of the Betic Cordillera: tectonic implications, *Terra Nova*, 26(6), 477-486. doi: 10.1111/ter.12123.
- Sánchez-Rodríguez, L., and D. Gebauer (2000), Mesozoic formation of pyroxenites and gabbros in the Ronda area (southern Spain), followed by Early Miocene subduction metamorphism and emplacement into the middle crust: U-Pb sensitive high-resolution ion microprobe dating of

- zircon, *Tectonophysics*, 316(1-2), 19-44.
- Sánchez-Rodríguez, L. (1998), Alpine evolution of the Ronda Ultramafic Complex and its country-rocks (Betic chain, southern Spain): U–Pb SHRIMP zircon and fission-track dating, Ph.D. thesis, 170 pp, ETH, Zürich, unpublished.
- Sano, Y., K. Terada, and T. Fukuoka (2002), High mass resolution ion microprobe analysis of rare earth elements in silicate glass, apatite and zircon: lack of matrix dependency, *Chemical Geology*, 184(3–4), 217-230. doi: 10.1016/S0009-2541(01)00366-7.
- Sanz de Galdeano, C., and B. Andreo (1995), Structure of Sierra Blanca (Alpujarride Complex, West of the Betic Cordillera), *Estudios geológicos*, 51, 43-55.
- Sawyer, E. (2010), Migmatites formed by water-fluxed partial melting of a leucogranodiorite protolith: microstructures in the residual rocks and source of the fluid, *Lithos*, 116(3), 273-286.
- Sawyer, E. W. (1991), Disequilibrium melting and the rate of melt–residuum separation during migmatization of mafic rocks from the Grenville Front, Quebec, *Journal of Petrology*, 32(4), 701-738. doi: 10.1093/petrology/32.4.701.
- Sawyer, E. W. (1996), Melt segregation and magma flow in migmatites: implications for the generation of granite magmas, *Earth and Environmental Science Transactions of the Royal Society of Edinburgh*, 87(1-2), 85-94. doi: 10.1017/S0263593300006507.
- Sawyer, E. W. (1998), Formation and evolution of granite magmas during crustal reworking: the significance of diatexites, *Journal of Petrology*, 39(6), 1147-1167. doi: 10.1093/petrology/39.6.1147.
- Sawyer, E. W. (2001), Melt segregation in the continental crust: Distribution and movement of melt in anatectic rocks, *Journal of Metamorphic Geology*, 19(3), 291-309. doi: 10.1046/j.0263-4929.2000.00312.x.
- Sawyer, E. W. (2008), *Atlas of Migmatites*, 387 pp., NRC Research Press and Mineralogical Association of Canada, Québec.
- Sawyer, E. W., B. Cesare, and M. Brown (2011), When the Continental Crust melts, *Elements*, 7(4), 229-234. doi: 10.2113/gselements.7.4.229.
- Scaillet, B., C. France-Lanord, and P. Le Fort (1990), Badrinath-Gangotri plutons (Garhwal, India): petrological and geochemical evidence for fractionation processes in a high Himalayan leucogranite, *Journal of Volcanology and Geothermal Research*, 44(1), 163-188. doi: 10.1016/0377-0273(90)90017-A.
- Scherer, E., C. Münker, and K. Mezger (2001), Calibration of the Lu–Hf clock, *Science*, 293, 683-687.
- Searle, M. P., R. R. Parrish, K. V. Hodges, A. Hurford, M. W. Ayres, and M. J. Whitehouse (1997), Shisha Pangma leucogranite, South Tibetan Himalaya: Field relations, geochemistry, age, origin, and emplacement, *J Geol*, 105(3), 295-318. doi: 10.1086/515924.
- Simancas, J. F., and J. Campos (1993), Compresión NNW-SSE tardi a postmetamórfica y extensión subordinada en el Complejo Alpujarride (Dominio de Alborán, Orógeno bético), *Revista de la Sociedad Geológica de España*, 6, 23-26.
- Sisson, T. W., and C. R. Bacon (1992), Garnet/high-silica rhyolite trace

- element partition coefficients measured by ion microprobe, *Geochimica et Cosmochimica Acta*, 56(5), 2133-2136. doi: 10.1016/0016-7037(92)90336-H.
- Slodzian, G., B. Daigne, F. Girard, F. Boust, and F. Hillion (1992), Scanning secondary ion analytical microscopy with parallel detection, *Biology of the Cell*, 74, 43-50. doi: 10.1016/0248-4900(92)90007-N.
- Smithson, S. B. (1978), Modeling continental crust: Structural and chemical constraints, *Geophysical Research Letters*, 5(9), 749-752. doi: 10.1029/GL005i009p00749.
- Sobolev, A. (1996), Melt inclusions in minerals as a source of principle petrological information, *Petrology*, 4(3), 209-220.
- Sölva, H. T., Martín; Habler, Gerlinde (2003), Dating a single garnet crystal with very high Sm/Nd ratios (Campo basement unit, Eastern Alps), *European Journal of Mineralogy*, 15(1), 35 - 42. doi: 10.1127/0935-1221/2003/0015-0035.
- Sorby, H. C. (1858), On the microscopical, structure of crystals, indicating the origin of minerals and rocks, *Quarterly Journal of the Geological Society*, 14(1-2), 453-500, NP-NP. doi: 10.1144/gsl.jgs.1858.014.01-02.44.
- Sosson, M., A. C. Morillon, J. Bourgois, G. Feraud, G. Poupeau, and P. Saint-Marc (1998), Late exhumation stages of the Alpujarride Complex (western Betic Cordilleras, Spain): new thermochronological and structural data on Los Reales and Ojen nappes, *Tectonophysics*, 285(3-4), 253-273.
- Soto, J. I., and J. P. Platt (1999), Petrological and structural evolution of high-grade metamorphic rocks from the floor of the Alboran Sea basin, western Mediterranean, *Journal of Petrology*, 40(1), 21-60.
- Soto, J. I., F. Fernández-Ibáñez, M. Fernández, and A. García-Casco (2008), Thermal structure of the crust in the Gibraltar Arc: Influence on active tectonics in the western Mediterranean, *Geochemistry, Geophysics, Geosystems*, 9(10). doi: 10.1029/2008GC002061.
- Soustelle, V., A. Tommasi, J. L. Bodinier, C. J. Garrido, and A. Vauchez (2009), Deformation and reactive melt transport in the mantle lithosphere above a large-scale partial melting domain: the Ronda Peridotite massif, Southern Spain, *Journal of Petrology*, 50(7), 1235-1266. doi: 10.1093/petrology/egp032.
- Srogi, L., M. E. Wagner, and T. M. Lutz (1993), Dehydration, partial melting and disequilibrium in the granulite-facies Wilmington complex, Pennsylvania-Delaware Piedmont, *American Journal of Science*, 293(5), 405-462.
- Stern, C. R., R. Kligfield, D. Schelling, N. S. Virdi, K. Futa, Z. E. Peterman, and H. Amini (1989), The Bhagirathi leucogranite of the High Himalaya (Garhwal, India); Age, petrogenesis, and tectonic implications, *Geological Society of America Special Papers*, 232, 33-46. doi: 10.1130/SPE232-p33.
- Stevens, G., and J. D. Clemens (1993), Fluid-rock interaction in the deeper continental lithosphere fluid-absent melting and the roles of fluids in the lithosphere: a slanted summary?, *Chemical Geology*, 108(1), 1-17. doi: 10.1016/0009-2541(93)90314-9.
- Stevens, G., A. Villaros, and J.-F. Moyen (2007), Selective peritectic garnet entrainment as the origin of geochemical diversity in S-type

- granites, *Geology*, 35(1), 9-12. doi: 10.1130/g22959a.1.
- Stöckhert, B., C. A. Trepmann, and H. J. Massonne (2009), Decrepitated UHP fluid inclusions: about diverse phase assemblages and extreme decompression rates (Erzgebirge, Germany), *Journal of Metamorphic Geology*, 27(9), 673-684. doi: 10.1111/j.1525-1314.2009.00835.x.
- Stöckhert, B., Duyster, J., Trepmann, C., Massonne, H.-J. (2001), Microdiamond daughter crystals precipitated from supercritical CO₂ plus silicate fluids included in garnet, Erzgebirge, Germany, *Geology*, 29, 391-394.
- Stowell, H. H., D. L. Taylor, D. L. Tinkham, S. A. Goldberg, and K. A. Ouderkirk (2001), Contact metamorphic P-T-t paths from Sm-Nd garnet ages, phase equilibria modelling and thermobarometry: Garnet Ledge, south-eastern Alaska, USA, *Journal of Metamorphic Geology*, 19(6), 645-660. doi: 10.1046/j.0263-4929.2001.00337.x.
- Student, J. J., & Bodnar, R. J. (1996), Melt inclusion microthermometry: Petrologic constraints from the H₂O-saturated haplogranite system, *Petrology*, 4(3), 291-306.
- Sun, S. S., and G. N. Hanson (1975), Origin of Ross Island basanitoids and limitations upon the heterogeneity of mantle sources for alkali basalts and nephelinites *Contributions to Mineralogy and Petrology*, 52, 77-106.
- Tajčmanová, L., J. Connolly, and B. Cesare (2009), A thermodynamic model for titanium and ferric iron solution in biotite, *Journal of Metamorphic Geology*, 27(2), 153-165.
- Thomas, J. B., R. J. Bodnar, N. Shimizu, and A. K. Sinha (2002), Determination of zircon/melt trace element partition coefficients from SIMS analysis of melt inclusions in zircon, *Geochimica et Cosmochimica Acta*, 66(16), 2887-2901. doi: 10.1016/S0016-7037(02)00881-5.
- Thomas, R., and P. Davidson (2013), The missing link between granites and granitic pegmatites, *Journal of Geosciences*, 58(2), 183-200.
- Thompson, A. B. (1976), Mineral reactions in pelitic rocks: II, Calculation of some P-T-X(Fe-Mg) phase relations, *American Journal of Science*, 276(4), 425-454. doi: 10.2475/ajs.276.4.425.
- Thompson, A. B., and J. A. D. Connolly (1995), Melting of the continental crust: Some Thermal and petrological constraints on anatexis in continental collision zones and other tectonic settings, *Journal of Geophysical Research-Solid Earth*, 100(B8), 15565-15579.
- Thöni, M. (2002), Sm-Nd isotope systematics in garnet from different lithologies (Eastern Alps): age results, and an evaluation of potential problems for garnet Sm-Nd chronometry, *Chemical Geology*, 185(3-4), 255-281. doi: 10.1016/S0009-2541(01)00410-7.
- Torres-Roldán, R. L. (1981), Plurifacial metamorphic evolution of the Sierra Bermeja peridotite aureole (Southern Spain), *Estudios geológicos*, 37(3-4), 115-134.
- Torres-Roldán, R. L. (1983), Fractionated melting of metapelite and further crystal-melt equilibria—The example of the Blanca unit migmatite complex, north of Estepona (Southern Spain), *Tectonophysics*, 96(1), 95-123. doi: 10.1016/0040-1951(83)90246-9.
- Tubía, J. M., and J. Cuevas (1986), High-temperature emplacement of the

- Los Reales peridotite nappe (Betic Cordillera, Spain), *Journal of Structural Geology*, 8(3-4), 473-482. doi: 10.1016/0191-8141(86)90064-7.
- Tubía, J. M., and J. I. Gil Ibarra (1991), Eclogites of the Ojén nappe: a record of subduction in the Alpujarride complex (Betic Cordilleras, southern Spain), *Journal of the Geological Society*, 148(5), 801-804. doi: 10.1144/gsjgs.148.5.0801.
- Tubía, J. M., J. Cuevas, and J. I. Gil Ibarra (1997), Sequential development of the metamorphic aureole beneath the Ronda peridotites and its bearing on the tectonic evolution of the Betic Cordillera, *Tectonophysics*, 279(1-4), 227-252.
- Tubía, J. M., J. Cuevas, and J. J. Esteban (2004), Tectonic evidence in the Ronda peridotites, Spain, for mantle diapirism related to delamination, *Geology*, 32(11), 941-944. doi: 10.1130/g20869.1.
- Tubía, J. M., J. Cuevas, and J. J. Esteban (2013), Localization of deformation and kinematic shift during the hot emplacement of the Ronda peridotites (Betic Cordilleras, southern Spain), *Journal of Structural Geology*, 50, 148-160. doi: 10.1016/j.jsg.2012.06.010.
- Tubía, J. M., J. Cuevas, F. Navarro-Vila, F. Alvarez, and F. Aldaya (1992), Tectonic evolution of the Alpujarride complex (Betic Cordillera, Southern Spain), *Journal of Structural Geology*, 14(2), 193-203. doi: 10.1016/0191-8141(92)90056-3.
- Tuttle, O. F., and N. L. Bowen (1958), Origin of granite in the light of experimental studies in the system $\text{NaAlSi}_3\text{O}_8\text{-KAlSi}_3\text{O}_8\text{-SiO}_2\text{-H}_2\text{O}$, *Geological Society of America Memoirs*, 74, 1-146. doi: 10.1130/MEM74-p1.
- Valley, J. W., A. J. Cavosie, T. Ushikubo, D. A. Reinhard, D. F. Lawrence, D. J. Larson, P. H. Clifton, T. F. Kelly, S. A. Wilde, D. E. Moser, and M. J. Spicuzza (2014), Hadean age for a post-magma-ocean zircon confirmed by atom-probe tomography, *Nature Geoscience*, 7(3), 219-223. doi: 10.1038/ngeo2075.
- Van Breemen, O., and C. J. Hawkesworth (1980), Sm-Nd isotopic study of garnets and their metamorphic host rocks, *Earth and Environmental Science Transactions of the Royal Society of Edinburgh*, 71(02), 97-102. doi: 10.1017/S0263593300013535.
- Van der Wal, D., and R. L. M. Vissers (1993), Uplift and Emplacement of Upper-Mantle Rocks in the Western Mediterranean, *Geology*, 21(12), 1119-1122.
- Van der Wal, D., and R. Vissers, L. M. (1996), Structural petrology of the Ronda peridotite, SW Spain: deformation history, *Journal of Petrology*, 37(1), 23-43. doi: 10.1093/petrology/37.1.23.
- Vance, D., and R. K. O'Nions (1990), Isotopic chronometry of zoned garnets: growth kinetics and metamorphic histories, *Earth and Planetary Science Letters*, 97(3-4), 227-240. doi: 10.1016/0012-821X(90)90044-X.
- Vance, D., and N. Harris (1999), Timing of prograde metamorphism in the Zaskar Himalaya, *Geology*, 27(5), 395-398. doi: 10.1130/0091-7613(1999)027.
- Vernon, R. H. (2007), Problems in identifying restite in S-Type granites of southeastern Australia, with speculations on sources of magma and enclaves, *The Canadian*

- Mineralogist*, 45(1), 147-178. doi: 10.2113/gscanmin.45.1.147.
- Vernon, R. H. (2011), Microstructures of melt-bearing regional metamorphic rocks, *Geological Society of America Memoirs*, 207, 1-11. doi: 10.1130/2011.1207(01).
- Vidal, P., A. Cocherie, and P. Le Fort (1982), Geochemical investigations of the origin of the Manaslu leucogranite (Himalaya, Nepal), *Geochimica et Cosmochimica Acta*, 46(11), 2279-2292. doi: 10.1016/0016-7037(82)90201-0.
- Vielzeuf, D., and J. Holloway (1988), Experimental determination of the fluid-absent melting relations in the pelitic system, *Contributions to Mineralogy and Petrology*, 98(3), 257-276. doi: 10.1007/BF00375178.
- Vielzeuf, D., J. D. Clemens, C. Pin, and E. Moinet (1990), Granites, Granulites, and Crustal Differentiation, in *Granulites and Crustal Evolution*, edited by D. Vielzeuf and P. Vidal, pp. 59-85, Springer Netherlands.
- Villarros, A., G. Stevens, and I. S. Buick (2009), Tracking S-type granite from source to emplacement: Clues from garnet in the Cape Granite Suite, *Lithos*, 112(3-4), 217-235. doi: 10.1016/j.lithos.2009.02.011.
- Villaseca, C., H. Downes, C. Pin, and L. Barbero (1999), Nature and composition of the lower continental crust in central Spain and the granulite-granite linkage: Inferences from granulitic xenoliths, *Journal of Petrology*, 40(10), 1465-1496.
- Wanless, V. D., M. D. Behn, A. M. Shaw, and T. Plank (2014), Variations in melting dynamics and mantle compositions along the Eastern Volcanic Zone of the Gakkel Ridge: Insights from olivine-hosted melt inclusions, *Contributions to Mineralogy and Petrology*, 167(5), 1-22. doi: 10.1007/s00410-014-1005-7.
- Wannamaker, P. E. (2000), Comment on "The petrologic case for a dry lower crust" by Bruce W. D. Yardley and John W. Valley, *Journal of Geophysical Research-Solid Earth*, 105(B3), 6057-6064. doi: 10.1029/1999jb900324.
- Watson, E. B. (1996), Surface enrichment and trace-element uptake during crystal growth, *Geochimica et Cosmochimica Acta*, 60(24), 5013-5020. doi: 10.1016/S0016-7037(96)00299-2.
- Watson, E. B., and T. H. Green (1981), Apatite/liquid partition coefficients for the rare earth elements and strontium, *Earth and Planetary Science Letters*, 56, 405-421. doi: 10.1016/0012-821X(81)90144-8.
- Watson, E. B., and T. M. Harrison (1983), Zircon saturation revisited: temperature and composition effects in a variety of crustal magma types, *Earth and Planetary Science Letters*, 64(2), 295-304. doi: 10.1016/0012-821X(83)90211-X.
- Watson, E. B., and T. M. Harrison (1984), Accessory minerals and the geochemical evolution of crustal magmatic systems: a summary and prospectus of experimental approaches, *Physics of the Earth and Planetary Interiors*, 35(1), 19-30. doi: 10.1016/0031-9201(84)90031-1.
- Watson, E. B., and Y. Liang (1995), A simple model for sector zoning in slowly grown crystals; implications for growth rate and lattice diffusion, with emphasis on accessory minerals in crustal rocks, *American Mineralogist*, 80(11-12), 1179-1187.
- Watt, G. R., and S. L. Harley (1993), Accessory phase controls on the geochemistry of crustal melts and restites produced during water-

- undersaturated partial melting, *Contributions to Mineralogy and Petrology*, 114(4), 550-566. doi: 10.1007/BF00321759.
- Watt, G. R., I. M. Burns, and G. A. Graham (1996), Chemical characteristics of migmatites: accessory phase distribution and evidence for fast melt segregation rates, *Contributions to Mineralogy and Petrology*, 125(1), 100-111. doi: 10.1007/s004100050209.
- Weber, C., and P. Barbey (1986), The role of water, mixing processes and metamorphic fabric in the genesis of the Baume migmatites (Ardèche, France), *Contributions to Mineralogy and Petrology*, 92(4), 481-491. doi: 10.1007/BF00374430.
- Weber, C., P. Barbey, M. Cuney, and H. Martín (1985), Trace element behaviour during migmatization. Evidence for a complex melt-residuum-fluid interaction in the St. Malo migmatitic dome (France), *Contributions to Mineralogy and Petrology*, 90(1), 52-62. doi: 10.1007/BF00373041.
- Webster, J. D., and R. Thomas (2006), Silicate melt inclusions in felsic plutons: a synthesis and review, in *Melt Inclusions in Plutonic Rocks*, edited by J. D. Webster, pp. 165-188, Mineralogical Association of Canada, Short Course.
- Webster, J. D., R. Thomas, D. Rhede, H.-J. Förster, and R. Seltmann (1997), Melt inclusions in quartz from an evolved peraluminous pegmatite: geochemical evidence for strong tin enrichment in fluorine-rich and phosphorus-rich residual liquids, *Geochimica et Cosmochimica Acta*, 61(13), 2589-2604.
- Wedepohl, K. H. (1995), The composition of the continental crust, *Geochimica et Cosmochimica Acta*, 59(7), 1217-1232. doi: 10.1016/0016-7037(95)00038-2.
- Weinberg, R. F., and P. Hasalova (2015), Water-fluxed melting of the continental crust: a review, *Lithos*, 212, 158-188. doi: 10.1016/j.lithos.2014.08.021.
- White, A. J. R., and B. W. Chappell (1977), Experimental petrology related to extreme metamorphism Ultrametamorphism and granitoid genesis, *Tectonophysics*, 43(1), 7-22. doi: 10.1016/0040-1951(77)90003-8.
- White, R. W., R. Powell, and T. J. B. Holland (2001), Calculation of partial melting equilibria in the system Na₂O-CaO-K₂O-FeO-MgO-Al₂O₃-SiO₂-H₂O (NCKFMASH), *Journal of Metamorphic Geology*, 19(2), 139-153. doi: 10.1046/j.0263-4929.2000.00303.x.
- White, R. W., R. Powell, and T. J. B. Holland (2007), Progress relating to calculation of partial melting equilibria for metapelites, *Journal of Metamorphic Geology*, 25(5), 511-527. doi: 10.1111/j.1525-1314.2007.00711.x.
- Whitehouse, M. J., and J. P. Platt (2003), Dating high-grade metamorphism - constraints from rare-earth elements in zircon and garnet, *Contributions to Mineralogy and Petrology*, 145(1), 61-74. doi: 10.1007/s00410-002-0432-z.
- Whitehouse, M. J., and J. P. Platt (2003), Dating high-grade metamorphism—constraints from rare-earth elements in zircon and garnet, *Contributions to Mineralogy and Petrology*, 145(1), 61-74. doi: 10.1007/s00410-002-0432-z.
- Whitney, D. L., and B. W. Evans (2010), Abbreviations for names of rock-forming minerals, *American Mineralogist*, 95(1), 185-187. doi: 10.2138/am.2010.3371.

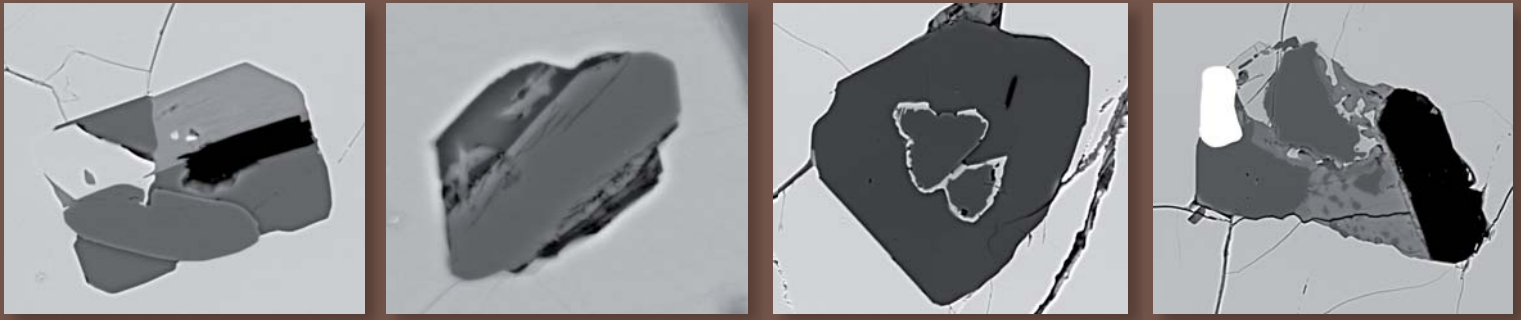
- Whitney, J. A. (1988), The origin of granite: The role and source of water in the evolution of granitic magmas, *Geological Society of America Bulletin*, 100(12), 1886-1897. doi: 10.1130/0016-7606(1988)100<1886:toogtr>2.3.co;2
- Whittacker, E. J. W., and R. Muntus (1970), Ionic radii for use in geochemistry *Geochimica et Cosmochimica Acta*, 34, 945-956.
- Whittington, A. G., A. M. Hofmeister, and P. I. Nabelek (2009), Temperature-dependent thermal diffusivity of the Earth's crust and implications for magmatism, *Nature*, 458(7236), 319-321. doi: 10.1038/nature07818.
- Wickham, S. M. (1987), The segregation and emplacement of granitic magmas, *Journal of the Geological Society*, 144(2), 281-297. doi: 10.1144/gsjgs.144.2.0281.
- Wyllie, P. J. (1977), Crustal anatexis: An experimental review, *Tectonophysics*, 43(1-2), 41-71. doi: 10.1016/0040-1951(77)90005-1.
- Yardley, B. W. D. (2009), The role of water in the evolution of the continental crust, *Journal of the Geological Society*, 166, 585-600. doi: 10.1144/0016-76492008-101.
- Yardley, B. W. D., and J. W. Valley (1997), The petrologic case for a dry lower crust, *Journal of Geophysical Research: Solid Earth*, 102(B6), 12173-12185. doi: 10.1029/97JB00508.
- Yurimoto, H., E. F. Duke, J. J. Papike, and C. K. Shearer (1990), Are discontinuous chondrite-normalized REE patterns in pegmatitic granite systems the results of monazite fractionation?, *Geochimica et Cosmochimica Acta*, 54(7), 2141-2145. doi: 10.1016/0016-7037(90)90277-R.
- Zeck, H. P. (1968), Anatectic origin and further petrogenesis of almandine-bearing biotite-cordierite-labradorite-dacite with many inclusions of restite and basaltoid material, Cerro del Hoyazo, SE Spain. , Ph.D. thesis, 161 pp, unpublished.
- Zeck, H. P. (1970), An erupted migmatite from Cerro del Hoyazo, SE Spain, *Contributions to Mineralogy and Petrology*, 26(3), 225-246. doi: 10.1007/BF00373202.
- Zeck, H. P. (1992), Restite-melt and mafic-felsic magma mixing and mingling in an S-type dacite, Cerro del Hoyazo, southeastern Spain, *Transactions of the Royal Society of Edinburgh: Earth Sciences*, 83(1-2), 139-144. doi: 10.1130/SPE272-p139.
- Zeck, H. P., and M. J. Whitehouse (1999), Hercynian, Pan-African, Proterozoic and Archean ion-microprobe zircon ages for a Betic-Rif core complex, Alpine belt, W Mediterranean - Consequences for its P-T-t path, *Contributions to Mineralogy and Petrology*, 134(2-3), 134-149.
- Zeck, H. P., and I. S. Williams (2001), Hercynian metamorphism in nappe core complexes of the Alpine Betic-Rif belt, Western Mediterranean - A SHRIMP zircon study, *Journal of Petrology*, 42(7), 1373-1385.
- Zeck, H. P., and I. S. Williams (2002), Inherited and magmatic zircon from Neogene Hoyazo cordierite dacite, SE Spain - Anatectic source rock provenance and magmatic evolution, *Journal of Petrology*, 43(6), 1089-1104.
- Zeck, H. P., F. Albat, B. T. Hansen, R. L. Torres-Roldán, and A. García-Casco (1989a), Alpine tourmaline-bearing muscovite leucogranites,

intrusion age and petrogenesis, Betic Cordilleras, SE Spain, *Neues Jahrbuch Fur Mineralogie-Monatshefte*(11), 513-520.

Zeck, H. P., F. Albat, B. T. Hansen, R. L. Torres-Roldán, A. García-Casco, and A. Martín-Algarra (1989b), A 21 ± 2 Ma age of the termination of the ductile Alpine deformation in the internal zone of the Betic Cordillera, South Spain, *Tectonophysics*, 169(1-3), 215-220. doi: 10.1016/0040-1951(89)90196-0.

Zeng, L., Z. Chen, and J. Chen (2013), Metamorphic solid salt (KCl-NaCl) in quartzo-feldspathic polyphase inclusions in the Sulu ultrahigh-pressure eclogite, *Chinese Science Bulletin*, 58(8), 931-937. doi: 10.1007/s11434-012-5373-y.

Zindler, A., H. Staudigel, S. R. Hart, R. Endres, and S. Goldstein (1983), Nd and Sr isotopic study of a mafic layer from Ronda ultramafic complex, *Nature*, 304(5923), 226-230.



Partial melting (anatexis) plays a fundamental role in the generation, differentiation and the rheology of Earth's continental crust. "Migmatitic" terranes constitute the main geological record of crustal anatexis throughout Earth's history. Unravelling the mechanisms of crustal anatexis from these terranes has proven to be challenging particularly when it comes to unveiling the primary chemical composition of anatectic melts. The main aim of this thesis is to better understand lower crustal anatexis through the study of "nanogranite inclusions" — microscopic droplets of melt that formed via incongruent melting reactions— in metamorphic minerals, and its relationship with lithospheric scale tectonomagmatic processes. The originality of my Thesis resides in the combination of a petrological, thermodynamical and experimental study of anatexis on the basis of the study of nanogranite inclusions in garnets from high-pressure granulitic migmatites. The case study is migmatitic gneisses from the Jubrique unit, a complete —though strongly thinned— crustal section in the westernmost Alpujarrides (Betic Cordillera, S. Spain). These gneisses overlie the Ronda peridotites —the largest exposure of subcontinental lithospheric mantle on Earth— and provide a unique opportunity to investigate the nature and age of crustal melting events and their timing with mantle processes in the westernmost Mediterranean.

Melt inclusions ($\approx 30\text{-}40\ \mu\text{m}$) —now recrystallized to nanogranites— in Jubrique gneisses are present in garnet cores and rims throughout the entire sequence. Thermodynamic modeling and conventional thermobarometry provide peak conditions of $\approx 850\ \text{°C}$ and $1.2\text{-}1.4\ \text{GPa}$, corresponding to garnet cores with kyanite and rutile inclusions. Post-peak conditions of $\approx 800\text{-}850\ \text{°C}$ and c. $0.5\ \text{GPa}$ are recorded in rims of garnet porphyroblast/clasts. The study of nanogranite inclusions shows that most garnet grew in the presence of melt. To constrain the primary composition and the P-T conditions of formation of nanogranitoids, we have carried out an experimental study of nanogranitoids in garnets, which were melted at $1.5\ \text{GPa}$ and $850, 825$ and $800\ \text{°C}$ in a piston cylinder apparatus. Experiments show that anatexis and entrapment of nanogranites occurred at c. $800\ \text{°C}$. Electron microprobe and NanoSIMS analyses indicate that experimental glasses are leucogranitic and peraluminous and define two compositional groups: Type I corresponds to K-rich, Ca- and H_2O -poor leucogranitic melts, whereas type II represents K-poor, Ca- and H_2O -rich granodioritic to tonalitic melts. They are found, respectively, at cores and rims of garnet porphyroblasts/clasts, and show that Jubrique migmatites underwent two anatectic events under contrasting fluid regimes.

To determine the age of crustal melting events and their timing with lithospheric mantle processes, we have analyzed Lu-Hf in whole rocks and garnets of Jubrique gneisses and garnet pyroxenites from the Ronda peridotite. The Lu-Hf isochrons confirm that the growth of garnet in Jubrique gneisses occurred in the Early Permian (c. 289 Ma) during the latest stages of the Variscan orogeny, most likely in a context of continental collision and overthickened continental crust. We found no Alpine Lu-Hf ages indicating either that this event is not resolvable with our sampling and dating techniques, or that the Lu-Hf of garnet was not equilibrated in the Alpine orogeny. The Lu-Hf whole rock-garnet isochrons of mantle garnet pyroxenites provide Jurassic-Cretaceous (144 Ma), Paleogene (53 Ma) and Miocene (21 Ma) ages. We interpret early Miocene ages as recording the waning stages of an Alpine extensional-related thermal event before emplacement of peridotites. Mantle garnet pyroxenites do not record Lu-Hf Variscan ages that may point that this system was reset by later mantle events or that garnet in mantle rocks grew in geodynamic events later than the Variscan orogeny.

